Thèse n° 9589

Many-body physics with strongly interacting fermions coupled to light

Présentée le 5 mai 2023

Faculté des sciences de base
Chaire Fondation Sandoz en physique des gaz quantiques
Programme doctoral en physique

pour l'obtention du grade de Docteur ès Sciences

par

Victor Youri HELSON

Acceptée sur proposition du jury

Prof. M. Wyart, président du jury
Prof. J.-Ph. Brantut, directeur de thèse
Prof. H. Moritz, rapporteur
Dr F. Piazza, rapporteur
Prof. T. Esslinger, rapporteur

École
polytechnique
fédérale
de Lausanne

2023

To those who made this work possible and will never read it.

Plût au ciel que le lecteur, enhardi et devenu momentanément féroce comme ce qu'il lit, trouve, sans se désorienter, son chemin abrupt et sauvage, à travers les marécages désolés de ces pages sombres et pleines de poison ; car, à moins qu'il n'apporte dans sa lecture une logique rigoureuse et une tension d'esprit égale au moins à sa défiance, les émanations mortelles de ce livre imbiberont son âme comme l'eau le sucre. Il n'est pas bon que tout le monde lise les pages qui vont suivre ; quelques-uns seuls savoureront ce fruit amer sans danger. Par conséquent, âme timide, avant de pénétrer plus loin dans de pareilles landes inexplorées, dirige tes talons en arrière et non en avant. Écoute bien ce que je te dis : dirige tes talons en arrière et non en avant, comme les yeux d'un fils qui se détourne respectueusement de la contemplation auguste de la face maternelle ; ou, plutôt, comme un angle à perte de vue de grues frileuses méditant beaucoup, qui, pendant l'hiver, vole puissamment à travers le silence, toutes voiles tendues, vers un point déterminé de l'horizon, d'où tout à coup part un vent étrange et fort, précurseur de la tempête.

Isidore Ducasse

MANY-BODY PHYSICS WITH STRONGLY INTERACTING FERMIONS COUPLED TO LIGHT

Abstract

This thesis reports on the realization of the first experiments conducted with superfluid, strongly interacting Fermi gases of ^{6}Li coupled to the light field of an optical cavity. In the scope of existing ultracold atomic platforms, this is the first time that a system with strong ground state fermionic correlations is operated in the framework of cavity quantum electrodynamics (cQED). From a condensed matter perspective, the system features a fully controllable microscopic Hamiltonian with control over both the strength of the ground state and light-matter interactions and the geometry of the latter. This contrasts with usual solid-state systems, in which the properties of the ground states are hardly tunable. As such our experiment is the perfect platform to simulate the physics of strongly correlated matter coupled to light fields. The manuscript is divided in three parts.

The first part is dedicated to the presentation of technical details of the experiment and of measurement techniques we routinely employ to create and probe our strongly interacting gases coupled to light. We introduce the use of the cavity as a probing tool by presenting the achievement of strong light-matter coupling between the atomic ensemble and the cavity field. Similarly, we present a robust thermometry technique for the unitary Fermi gas, with which we measure temperature of the gases deep in the superfluid, quantum degenerate regime.

In a second part we focus on the measurements of the strong atom-atom correlations which emerge from the energy spectrum of the atoms-cavity system. We start by laying down the theoretical basis needed for the understanding of the origin of the strong atom-atom interaction, and present its consequence on the many-body wavefunction of the gas by introducing the two-body contact as a universal thermodynamic quantity. We then report on the observation of strong light-matter coupling between pairs of atoms and the cavity field via photoassociation transitions. We describe the resulting light-matter coupling strength in terms of the two-body contact, imprinting many-body correlations onto cavity spectra for the first time. In the following experiment we study the optomechanical response of the gas in the dispersive regime. We observe distorted cavity transmission profiles, signatures of the nonlinear Kerr effect. The strength of the nonlinearity is governed by the density response of the gas, which we express via an operator product expansion in terms of the contact.

In the last part, we investigate the effects of engineering long-range, photon-mediated interactions in the gas. We formally show how the system is expected, above a critical value for the strength of the long-range interaction, to undergo a phase transition to a density ordered state. The onset of density-ordering is observed by the superradiant properties of the ordered phase, and we show that it is also controlled by the density response of the unperturbed gas. In addition, we measure the divergence of the density wave susceptibility as the strength of the long-range interactions approaches the critical points: a striking feature of phase transitions. By measuring its temperature after the experiment, we prove that the gas remains superfluid.

Keywords: ultracold atoms, quantum gases, cavity qed, strongly interacting fermions, strongly correlated matter, photoassociation, optomechanics, quantum phase transitions, charge density waves, tan's contact

Laboratory for Quantum Gases

_ _ _ _ _

Résumé

Cette thèse présente les premières expériences effectuées avec des gaz de Fermi de ^{6}Li en interaction forte et couplés à la lumière par une cavité optique. Dans l'ensemble des expériences existantes d'atomes froids, c'est la première fois qu'un système de fermions fortement corrélés fait l'objet d'une étude d'un point de vue de l'électrodynamique quantique en cavité. D'autre part, d'un point de vue de la matière condensée l'Hamiltonien microscopique de notre système est contrôlable à souhait, de la force des interactions entre atomes dans l'état fondamental jusqu'à la force de celles induites par le couplage à la lumière. Ceci contraste avec les systèmes de matière condensée habituels, pour lesquels les propriétés de l'état fondamental ne sont pas modifiables à la volée. Notre expérience est donc la plateforme parfaite pour simuler la physique des matériaux fortement corrélés et couplés à la lumière. Le présent manuscrit, qui en témoigne, est divisé en trois parties.

La première partie est dédiée à la présentation des spécificités techniques de notre expérience ainsi qu'aux méthodes employées pour produire et sonder des gaz de fermions fortement corrélés. Nous introduisons la cavité optique comme outil pour sonder le système en présentant les résultats de nos premières expériences visant à établir le régime de couplage fort entre le gaz et le champ de cavité. De la même manière, nous présentons une méthode robuste de thermométrie du gaz de Fermi unitaire, que nous utilisons ensuite pour montrer que les gaz produits par l'expérience sont des superfluides fortement dégénérés.

Dans la seconde partie, nous nous focalisons sur des mesures des corrélations atomiques à travers des observations de spectres de cavité. Nous commençons par présenter la base théorique nécessaire à la compréhension de l'origine des interactions entre atomes, pour ensuite présenter son influence sur la physique à N corps du gaz. Ce faisant, nous introduisons une quantité thermodynamique universelle : le contact à deux corps. Nous présentons ensuite une série de mesures effectuées dans le régime de couplage fort entre paires d'atomes et la lumière, médié par des transitions de photoassociation. Les forces de couplage associées peuvent directement être liées au contact, ce qui prouve que notre expérience permet de mesurer les corrélations à N corps du gaz directement depuis les spectres d'énergie de la cavité. Dans le même esprit, nous étudions la réponse optomécanique du gaz dans le régime dispersif et observons des spectres de cavité distordus, signatures de l'effet Kerr non linéaire. La force de cette non linéarité optique est gouvernée par la fonction de réponse en densité du gaz, elle-même dépendante du contact.

Dans la dernière partie, nous introduisons un terme d'interaction à longue portée au sein du gaz, médiée par les photons de cavité. Ce système présente une transition de phase vers une onde de densité, pour une valeur de la force des interactions à longue portée plus grande qu'une valeur critique. Cette valeur critique est contrôlée par la fonction de réponse en densité du gaz, et la transition de phase est détectée grâce à la nature superradiante de la phase ordonnée. De plus, nous vérifions que la susceptibilité du système diverge lorsque la force des interactions approche le point critique. Nous mesurons la température du nuage après l'expérience et vérifions qu'il demeure superfluide.

Mots clés : atomes ultrafroids, gaz quantiques, electrodynamique quantique en cavité, fermions en interaction forte, matière fortement corrélée, photoassociation, optomécanique, transitions de phase quantique, ondes de densité de charge, contact de tan

Remerciements

En commençant un stage au sein du Laboratoire pour les Gaz Quantiques un matin d'hiver en 2017, pas un seul instant je ne me suis imaginé terminer la rédaction d'un manuscrit de thèse presque 6 ans plus tard. Chose faite, il est maintenant l'heure pour moi de *rendre des comptes* en remerciant aussi sincèrement et fidèlement que possible les personnes qui m'ont tour à tour aidé, accompagné, soutenu, fait rire, soûlé – au sens premier – ou tout simplement écouté ces quelques dernières années. C'est donc à l'aune de ma plume maladroite et de ma mémoire défaillante que ces mots leur sont dédiés.

En premier lieu, et comme le veut la tradition, je tiens à remercier chaleureusement Jean-Philippe qui m'a offert l'unique opportunité de travailler sur un tel projet. J'ai été extrêmement chanceux d'effectuer ma thèse sous sa supervision ; tant pour son impressionnante intuition physique et sa connaissance *quasi*-encyclopédique de la littérature scientifique que pour sa disponibilité pour répondre à mes questions, certaines plus urgentes que d'autres. Pour tout, merci. J'aimerais par la même occasion remercier les autres membres de mon jury de thèse qui ont aimablement accepté d'en faire partie : merci à Matthieu Wyart, Tilman Esslinger, Henning Moritz et Francesco Piazza.

Je remercie également les autres membres du labo, avec qui nous avons vécu, l'espace de plusieurs mois ou années, au gré de mers de Fermi capricieuses et autres nombreux écueils qui parsèment le quotidien de chercheurs en physique expérimentale. Ce quotidien fut quelque peu ingrat, souvent frustrant, mais, grâce à vous, jamais ennuyant. Merci donc à Kevin, Barbara, Hideki, Timo, Tabea et Giulia pour tous ces moments passés dans cette drôle de petite pièce du couloir C3. Le voyage fut houleux sous bien des aspects mais je peux m'estimer heureux d'avoir pu compter sur la présence de compagnons de fortune pour m'épauler.

Merci en particulier à Kevin avec qui j'ai tant appris, et ce malgré des goûts musicaux discutables et de terribles opinions en terme de pilosité faciale. Ta capacité à prendre à cœur chaque aspect de la manip – ou même de la vie – et ta détermination à toute épreuve sont les raisons pour lesquelles l'expérience fonctionne comme elle le fait aujourd'hui. En dépit de nombreux *I don't trust that* et autres *I don't see the two-photon picture*, une seule question demeure : *demande-moi plutôt ce que je n'ai pas ?* Je ne peux que souhaiter que les futures générations de thésards mettent autant de cœur à l'ouvrage que nous l'avons fait. Et à ce titre je sais que Timo et Tabea sont en train d'en assurer la relève. Pour ça, merci. Merci aussi à Giulia pour ton pragmatisme et ta bonne humeur, et je te souhaite de réussir à Florence.

Je voudrais également remercier Tigrane, qui vint compléter notre *oppressant* trio de pause café et dont le calme, la gentillesse et la chance au jeu n'ont eu de cesse de m'étonner. A toi et Kevin, merci pour tous ces moments passés à refaire le monde en dehors du labo, avec ou sans sushis, avec ou sans gin et avec ou sans chats. Votre présence lors de ma défense de thèse m'a beaucoup touché. Je souhaite aussi remercier les autres membres de l'équipe *downstairs* du labo : Nick avec qui j'ai exploré Hambourg, Toronto ou encore Obergurgl, et Francesca, Jonas et Rohit avec qui je l'espère j'ai partagé un peu plus qu'un canal de *wavemeter*.

Parmi le gens que j'ai pu côtoyer au quotidien, je remercie en particulier l'équipe technique et autres habitués de la *clean room* : Nicolas, Damien, Yoan, Jonathan, Adrien, Arnaud et Jean-Michel qui, non contents d'être d'agréables compagnons de pause café et de redoutables solveurs de mots croisés, ont été d'une aide cruciale lors du montage de l'expérience. Merci également aux membres de l'atelier de mécanique de l'institut : Gilles, Adrien, Olivier, Luc, Clément et les autres pour leurs contributions essentielles et leur patience à la vue de certains dessins techniques aux aspects hasardeux. Un tout grand merci à Claude pour son aide inestimable et sa gentillesse, le succès de nos expériences doit beaucoup à son savoir-faire. Enfin, merci à Karin, Gabriella et Anh pour leur assistance administrative tout au long de ces années.

Parce que la vie ne s'arrête pas en franchissant la porte du labo [*sic*], et même si j'ai été un peu lacunaire sur ce point, je tiens à remercier celles et ceux qui m'ont permis de prendre le large pendant ces années de thèse. Je pense en particulier à Quentin et Alexandre qui, malgré la distance nous séparant, ont été présents quotidiennement pour discuter, rire et débattre de tout – souvent – et de rien – parfois. Merci d'être là les gars. Merci aussi à mes potes de promo que je n'ai que trop peu vu ces derniers temps ; Ben, Eric, Stan, Carla, Oscar et tous les autres. Merci à Hugo pour ton soutien et ta présence ces derniers mois, et merci encore à Kevin, Tigrane, Chloé et Alex pour les moments passés ensemble, c'est toujours un plaisir de vous voir. Je remercie aussi mes potes du lycée et d'avant, en particulier Alexis, Florian et surtout David avec qui, dans ce qui semble maintenant être une autre vie, nous avons arpenté les gigantesques couloirs d'anciens couvents, maristes ou jésuites.

Pour de multiples raisons, certaines plus évidentes que d'autres, je ne serai pas arrivé où j'en suis sans eux ; merci à mes parents. Merci pour votre soutien indéfectible et votre abnégation sans limite quand il s'est agi de faire de notre confort et de notre réussite, à ma sœur, mon frère et moi, une priorité. Merci aussi de m'avoir hébergé pendant la rédaction de ma thèse, même si *on est pas à l'hôtel ici*. Merci à Zélie et Hippolyte pour leur soutien et leur accueil à Nantes, une ville qu'il m'est toujours agréable de visiter, grâce à vous. Evidemment, merci également à Corentin et Orlane pour les mêmes raisons. Merci à Philippe grâce à qui je me suis toujours senti à la maison dans un atelier de mécanique, et dont je n'ai jamais oublié les cours sur le fonctionnement d'un moteur à quatre temps. Merci à mes grands-parents qui, chacun à leur manière, ont fortement influencé la personne que je suis aujourd'hui. En particulier merci à Annette qui, malgré nos divergences sur certaines pratiques pseudoscientifiques, est probablement à l'origine de mon intérêt pour la science. Finalement, merci à ma famille de Belgique pour leur accueil chaleureux lors de mes – trop rares – visites à Bruxelles.

Enfin, je voudrais remercier Laurane qui a toujours su être là pour moi et dont l'amour et le soutien m'ont permis d'avancer jusqu'ici, sereinement. Merci évidemment à nos deux terreurs, Orion et Sirius, qui, sans trop en être conscients, ont avec toi grandement contribué à mon bonheur. Merci à tes ami.e.s : Camille, Sophie, Tania, Wendy, Robin, Robin, Martin, Martin, Yannick, Michael et les autres que je suis toujours ravi de retrouver le temps – souvent – d'une soirée. Pour finir, merci à ta famille, tes parents et tes sœurs, qui me fait me sentir un peu plus chez moi en Suisse.

Victor

Contents

Abstract vii

Remerciements ix

Contents xi

Introduction 1

I Production and Interrogation of Strongly Interacting Fermi Gases Coupled to Light 5

1 An experimental platform to study strongly interacting fermions coupled to light 7
- 1.1 A high finesse cavity inside a single-chamber experiment 8
  - 1.1.1 Overview of the ultra-high vacuum system 8
  - 1.1.2 Compact, bulk-machined electromagnets 10
  - 1.1.3 The high-finesse optical cavity 11
- 1.2 From hot vapor to quantum degenerate gas: production of a Fermi gas of ^{6}Li 13
  - 1.2.1 Laser cooling 14
  - 1.2.2 Evaporative cooling in cavity dipole traps 15
  - 1.2.3 Evaporative cooling in a running wave dipole trap 15

2 Probing strongly interacting Fermi gases strongly coupled to light 17
- 2.1 Probing the strong light-matter coupling 18
  - 2.1.1 Light-matter interaction and the strong coupling regime 18
  - 2.1.2 Strong light-matter coupling from near-resonance transmission spectroscopy 21
  - 2.1.3 Transmission spectroscopy in the dispersive limit 26
- 2.2 Absorption imaging for the thermometry of unitary Fermi gases 30
  - 2.2.1 High-intensity absorption imaging 31
  - 2.2.2 Temperature measurement using the equation of state 33

II Quantum Optical Signatures of the Short Range Two-Body Correlation Function 37

3 Two-body scattering for the many-body physics of interacting Fermi gases 39
- 3.1 Theoretical description of cold collisions 40
  - 3.1.1 Origin of the interaction 40

3.1.2 The two-body scattering problem . . . 41
3.1.3 Feshbach resonances . . . 47
3.2 Going from two- to many-body fermionic systems . . . 51
3.2.1 Energy spectrum of the interacting Fermi gas . . . 51
3.2.2 BEC–BCS crossover . . . 53
3.2.3 The two-body contact . . . 56

4 Fermionic pair-polaritons, magnifiers for two-body correlations 61
4.1 From two interacting dipoles to a photoassociated pair . . . 62
4.1.1 Interacting dipoles . . . 62
4.1.2 Molecular spectroscopy . . . 64
4.1.3 The case of $^6\text{Li}_2$ . . . 66
4.2 Observation of strong light-matter coupling on photoassociation transitions . . 67
4.2.1 Experimenta scheme . . . 67
4.2.2 Mapping out photoassociation transitions close to dissociation limits . . . 68
4.3 Many-body physics from vacuum Rabi splitting . . . 70
4.3.1 Rabi frequency of pairs coupled to light . . . 71
4.3.2 Many-body physics from the optical spectrum . . . 74
4.3.3 Continuous measurement of the two-body contact . . . 77

5 Optomechanical response of strongly interacting Fermi gases 81
5.1 Observation of a Kerr nonlinearity in a unitary Fermi gas coupled to light . . . 82
5.1.1 Kerr nonlinearities and optical bistability . . . 82
5.1.2 Response function from light-matter coupling . . . 83
5.1.3 Experimental realization . . . 86
5.2 The connection between light-matter coupling and the universal thermodynamics of strongly interacting fermions . . . 90
5.2.1 The Operator Product Expansion . . . 91
5.2.2 Density response in the BEC–BCS crossover . . . 94

III Cavity Mediated Long Range Interactions and Their Interplay with Short Range Physics 97

6 Density-wave ordering induced by photon-mediated long-range interactions 99
6.1 Engineering photon-mediated long-range interactions in a strongly correlated Fermi gas . . . 101
6.1.1 Effective photon-mediated atom-atom interactions from strong light-matter coupling . . . 101
6.1.2 Phase transition to a density ordered state . . . 105
6.1.3 Density response function . . . 108
6.2 Observation and characterization of density wave ordering . . . 111
6.2.1 Experimental procedure and observation of the phase transition . . . 111
6.2.2 Mapping the phase diagram . . . 113
6.2.3 Variation of the interaction parameter . . . 114
6.2.4 Experimental calibrations . . . 116
6.3 Measurement of the density wave susceptibility . . . 120
6.3.1 Implementation of fixed-**q** Bragg spectroscopy . . . 120
6.3.2 Measurement of the density response in the presence of long-range interactions . . . 122

6.4 Long-range interactions between pairs of atoms, an outlook 125
6.4.1 Dispersive regime for the pairs 125
6.4.2 Interpretation as an optical Feshbach resonance 127

Conclusion and outlooks **129**
Investigation of the density-wave ordered phase 130
Simulation of pair density waves 131
Cavity-enabled nondemolition transport measurements 131

Bibliography **133**

A Experiment control **149**

B Optical setups for the cavity probe and transverse pump beams **153**

C Properties of the density response function **155**
C.1 Definitions and spectral representation 155
C.2 Structure factor and sum rules 156

D Molecular term symbols **159**

Contents **161**
Curriculum Vitae 166

Introduction

> Et toute science, quand nous l'entendons non comme un instrument de pouvoir et de domination, mais comme aventure de connaissance de notre espèce à travers les âges, n'est autre chose que cette harmonie, plus ou moins vaste et plus ou moins riche d'une époque à l'autre, qui se déploie au cours des générations et des siècles, par le délicat contrepoint de tous les thèmes apparus tour à tour, comme appelés du néant.
>
> Alexander Grothendieck

The understanding of many-body phenomena in quantum systems lies at the heart of the most fascinating questions of contemporary physics. While the behavior of individual particles, be they electrons, atoms or molecules, is generally well predicted by sets of physical rules and principles, the description of ensembles of interacting particles is a formidable challenge. These many-body interacting systems are ubiquitous in nature, from solid-state materials and quantum fluids to biological and condensed matter systems. As such, understanding the phenomena resulting from the collective behavior of their constituents is essential to advance the comprehension of fundamental natural sciences.

In condensed matter systems, the role played by interparticle interactions has been identified in a number of emergent phenomena which cannot only be explained with elementary laws ruling the behavior of single electrons [1]. Conventional superconductivity for instance relies on a pairing mechanism for electrons which interact via the phonons of the underlying crystalline lattice [2]. In some materials however, Coulomb interaction itself leads to strong electronic correlations, which usually originate from a constrained spatial confinement of the electronic wavefunctions. The peculiar electronic behavior of these so-called *strongly correlated materials* gives rise to unusual properties [3], the modelling of which has to account for the strong correlations [4, 5]. High-temperature superconductors are paradigmatic examples of strongly correlated materials for which, since their discovery in 1986 [6], the exact mechanism behind their anomalously high critical temperatures remains an open question [7, 8]. Although there exist no unified theoretical framework describing the interactions which rule the properties of strongly correlated matter, these can still be employed in a number of applications ranging from the use of quantum Hall effect and its descendants for quantum computation [9, 10] to quantum magnets as memory devices [11].

One promising direction to further the understanding of strongly correlated matter is to resort to *quantum simulation*. The idea behind the quantum simulation approach is elegant, similarly to how aerodynamical properties of a plane can be inferred from models placed in a wind tunnel – a classical analogue simulator, quantum properties of a complex many-body system can be inferred from a simpler, controllable quantum model [12]. For such systems, classical computers become insufficient to calculate many-body properties for as low as a few tens of particles [13], due to the exponential growth of the underlying Hilbert spaces with number of interacting particles. Their quantum counterparts, which are promised to simulate the dynamics of arbitrary many-body Hamiltonians, are still in their infancy. Nevertheless, even if these so-called *noisy intermediate-scale quantum devices* have recently been proven to provide a quantum advantage in solving a very narrow class of problems [14, 15], bridging the technical and theoretical gaps to turn them into universal, fault-tolerant *digital* quantum simulators might take a few more years.[1] In the meantime, *analogue* quantum simulators have already granted insights into many classically untractable problems [16]. Instead of providing full control over arbitrary many-body Hamiltonians, these devices rather specialize in specific classes of problems by mimicking their dynamics in a controlled environment [17–21].

Ultracold atomic experiments probably represent the most versatile platforms for the analogue quantum simulation of a wide range of systems [22–29]. Since the initial achievements of Bose-Einstein condensation (BEC) [30, 31] and the production of superfluid Fermi gases [32] in the past decades, the field of quantum simulation with cold atoms has progressed to the point that several strongly correlated matter systems and phenomena can be accurately reproduced and studied in the labs, with unmatched controllability on the microscopic Hamiltonians [33]. In particular, the tunability of trapping potentials was harnessed to observe Anderson localization[34, 35], quantized conductance in neutral matter [36] or realize Josephson junctions [37, 38]. In addition and to the contrary of solid-state systems, interparticle interactions in atomic gases can be tuned with the use of Feshbach resonances [39] or optical lattices [26]. Ultracold atoms trapped in optical lattices have thus led to the realization of Mott insulators [40, 41], Tonks-Girardeau gases [42] or even of the topological Haldane model [43]. The additional use of quantum gas microscopes has yielded unprecedented insight into the physics of Hubbard models [44].

In two-component Fermi gases, the control over interparticle interactions offered by Feshbach resonances allows to push the simulation of strongly correlated matter even further. The interaction strength between particles can be tuned to arbitrarily high values – as high as allowed by quantum mechanics – where the system realizes the so-called unitary Fermi gas [45]. It is therefore a convenient model for the study of the most strongly interacting systems in nature such as neutron stars or nuclear matter [46]. As for BECs, strongly interacting Fermi gases are now routinely produced in experiments [47] and the tunability of their interparticle interactions has been employed to explore the physics of the BEC–BCS crossover [45, 48, 49], from the direct observation of Cooper pairs [50] to the measurement of the peculiar excitation spectra emerging from the strong interactions [51, 52].

On the other hand, the versatility offered by ultracold atomic experiments has allowed, via the use of high-finesse resonators – or cavities, to investigate light-matter interactions in the scope of cavity quantum electrodynamics (cQED) [53]. This framework made possible the control of interactions between atoms and photons down to single quanta level [54] which led to the realization of the strong coupling regime [55] between BECs and particular modes of the electromagnetic field, singled-out by the cavity [56, 57]. In this regime, a number of experiments have been carried out to explore the hazy border between cQED and condensed matter problems. In particular, the flexible means of engineering non-local, all-to-all interactions between the atoms provided by cQED [53, 58, 59] allowed to realize the self-organization of BECs during the past decade [60, 61], a phenomenon which has since been heavily studied in a number of configurations [62–68], simulating exotic phases of matter driven by strong light-matter interactions.

---

[1] Or decades.

In this work, we report on the realization of the first experiments conducted with superfluid, strongly interacting Fermi gases of ^{6}Li coupled to the light field of an optical cavity. The experimental setup therefore bridges the gap between the concepts introduced in the previous two paragraphs. From an ultracold atoms point of view, this is the first time that a system with strong ground state fermionic correlations is operated in the scope of cQED, a situation which is expected to give rise to exotic states of matter [69, 70] or even alter the intrinsic superfluid properties of the ground state gas [71, 72]. From a condensed matter perspective, the system features a fully controllable microscopic Hamiltonian with control over both the strength of the ground state and light-matter interactions and the geometry of the latter. This contrasts with usual solid-state systems, in which the properties of the ground states are hardly tunable yet for which the interactions with light fields offers fascinating perspectives [73].

The manuscript is organized in three parts as follows.

The first part is dedicated to technical details about the experimental setup.

- **In Chapter 1** we present the experimental platform used to produce strongly interacting gases of ^{6}Li within a high-finesse resonator. We give an overview of the main vacuum chamber, focusing on the design specificities compared to other cold atoms machines: the presence of a high-finesse cavity and the use of a single chamber for all the cooling trapping and probing procedures. We then detail the experimental sequence to produce the gases, which makes use of the cavity for efficient evaporative cooling.
- **In Chapter 2** we detail the tools at our disposal to characterize strongly interacting Fermi gases coupled to light. We start by highlighting the capabilities of the cavity as a probing tool by using it to measure the excitation spectrum of the atoms-cavity coupled system and prove that we work in the strong coupling regime using transmission spectroscopy. We then show how measurements of this excitation spectrum in the dispersive regime can be employed to infer the atom number in a weakly destructive way. Finally, we present an efficient thermometry method for the unitary Fermi gas, which we use to demonstrate that the unitary gases we routinely produce operate in the deeply quantum degenerate regime.

The second part focuses on the measurement of ground state correlations of strongly interacting Fermi gases using the cavity field.

- **In Chapter 3** we develop the formal tools which allow for the description of the strong ground state interactions in the so-called strongly interacting Fermi gases. Starting from two-body scattering, we move on to introduce its consequence on the many-body wavefunction of the gas and how it leads to the BEC–BCS crossover. In addition, we introduce the two-body contact as the key universal quantity formally linking the two- and many-body regimes.
- **In Chapter 4** we present the achievement of the strong coupling regime on photoassociation transitions. After introducing key molecular physics concepts necessary to the understanding of photoassociation, we show how cavity transmission spectroscopy can be employed to probe these transitions and measure the light-matter coupling strength. The strong coupling to these transitions creates new dressed states which hybridize pairs of atoms of opposite spins with photons: pair-polaritons. We then formally relate the measured coupling strength to the two-body contact, proving the influence of many-body physics in the optical spectra.

In Chapter 5 we report on the observation of an optomechanical Kerr nonlinearity in strongly interacting Fermi gases. We show that the strength of the nonlinearity, contained in the optical spectrum of the coupled system relates to a ground state property of the gas: its static density response function. With the use of an operator product expansion technique we formally link the density response function to universal quantities, including the two-body contact and internal energy of the gas. This gives another direct connection between a purely quantum optical observable and a ground-state property of strongly interacting Fermi gases.

The last part presents experiments involving the engineering of photon-mediated long-range interactions in the gas.

In Chapter 6 we present the realization of tunable long-range photon-mediated interactions by transversally pumping the system in the dispersive regime. We show how these long-range interactions lead to a phase transition of the gas to a density wave order state above a specific critical strength, the value of which is again controlled by the density response. We present measurements of the critical strengths for varying ground state interaction parameters. By introducing a variant of Bragg spectroscopy at fixed momentum, we measure the excitation spectrum of the gas in the presence of long range interactions and prove that the onset of the phase transition is accompanied by a divergence of the density response of the system. Finally, as an outlook we introduce the principle and first observations of the introduction of long-range interaction for pairs of atoms in the vicinity of a photoassociation transition, paving the way to the simulation of pair-density waves.

The work presented here has been carried out with Kevin Roux, Hideki Konishi, Barbara Cilenti, Timo Zwettler, Tabea Bühler, Giulia del Pace and Jean-Philippe Brantut over the course of five years.

Part I

Production and Interrogation of Strongly Interacting Fermi Gases Coupled to Light

Chapter 1

An experimental platform to study strongly interacting fermions coupled to light

> Machines are worshipped because they are beautiful and valued because they confer power; they are hated because they are hideous and loathed because they impose slavery.
>
> Bertrand Russell

Outline of the current chapter

1.1 A high finesse cavity inside a single-chamber experiment **8**
  1.1.1 Overview of the ultra-high vacuum system 8
  1.1.2 Compact, bulk-machined electromagnets 10
  1.1.3 The high-finesse optical cavity 11
1.2 From hot vapor to quantum degenerate gas: production of a Fermi gas of ^{6}Li **13**
  1.2.1 Laser cooling 14
  1.2.2 Evaporative cooling in cavity dipole traps 15
  1.2.3 Evaporative cooling in a running wave dipole trap 15

In this first chapter we introduce the apparatus with which the experiments presented in this manuscript were performed. The machine was designed and built to explore the physics of strongly interacting Fermi gases coupled to light within a high-finesse optical cavity. To that end, ^{6}Li was picked as the atomic species of choice and for good reasons: it is a fermion, its light mass allows for fast thermalization processes, the recipes to cool it down to quantum degeneracy are well known [47, 74–77], and it features an extraordinarily large Feshbach resonance [**zurnPreciseCharacterizationMathrmLi2013**, 78] which allows for a relatively easy control of two-body interactions – as described in details in chapter 3.

The chapter is organized as follows, in a first part we describe the experimental setup. It was designed to only feature a single vacuum chamber, within which all the trapping and cooling procedures would occur at the same point: the center of a high-finesse cavity sitting inside the chamber. This configuration removes the need to transport the atomic cloud between multiple chambers for different steps of the cooling and probing procedures, accelerating the experiment cycle. We then introduce the cavity, from its optical properties to its stabilization scheme, set up to control its resonance frequencies and tune them with respect to the ^{6}Li transition frequencies. Finally, we detail the general procedure employed to cool a hot atomic vapor of ^{6}Li down to the quantum degenerate regime, the starting point of all the subsequent experiments presented in this thesis. In addition, we present the experimental control software and hardware in appendix A.

As a thorough description of the experimental setup is contained in the PhD thesis of Kevin Roux [79], we will here simply focus on the main aspects of it. In addition, we detailed the design and production process of the electromagnets we use to address the Feshbach resonance in [80] and presented parts of the experimental sequence in [81].

1.1 A high finesse cavity inside a single-chamber experiment

1.1.1 Overview of the ultra-high vacuum system

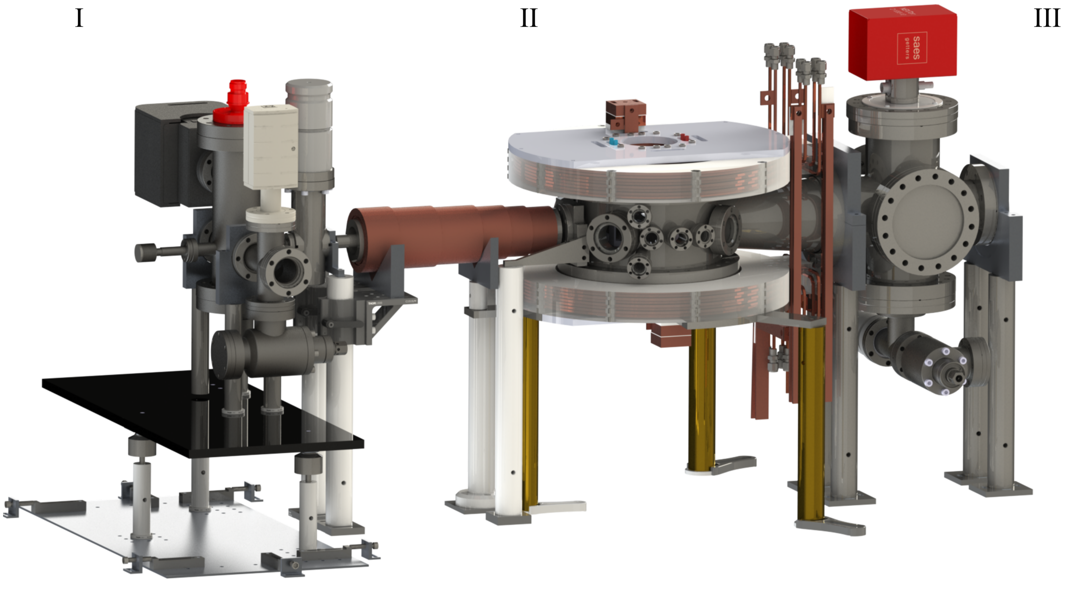

Figure 1.1: CAD view of the vacuum setup. I, oven chamber containing the lithium. II, Zeeman slower and main vacuum chamber where the atoms are trapped, cooled down and probed. III, pumping chamber. The length of the ensemble is approximately 2 m.

The vacuum system consists of a single enclosure, a CAD view of which is shown in figure 1.1. It is split in three chambers, connected by conical pipes which ensure differential pumping between the different regions of the apparatus. A set of vacuum pumps ensure that ultra-high vacuum (UHV) is reached within the whole enclosure, suppressing unwanted background collisions with thermal atoms.

The *oven chamber* is where pure liquid ^{6}Li is maintained at temperatures above its melting point in a small steel cylindrical enclosure, visible on the far left side of the figure: the oven. For the experiments presented here, it was operated at temperatures in the range of $320-400\,^\circ$C. While most of the lithium vapor exiting the oven ends up coating the inner parts of the oven chamber, a small fraction of atoms is allowed to travel to the next vacuum section through an aperture at the entrance of the Zeeman slower. This atomic flux can be blocked inside the chamber with the use of a metallic flag mounted on a remote-controlled stepper motor. Using both an ion pump (Agilent VacIon 20) and getter pump (SAES CapaciTorr D400), the pressure in this chamber is brought down to below 5×10^{-10} mbar, a value which measurement is limited by the reading of the pressure gauge (Pfeiffer PBR260). The chamber can be disconnected from the rest of the experiment by a manual gate valve (VAT CF16 all-metal), a feature which has proven to be convenient to refill the oven with lithium.

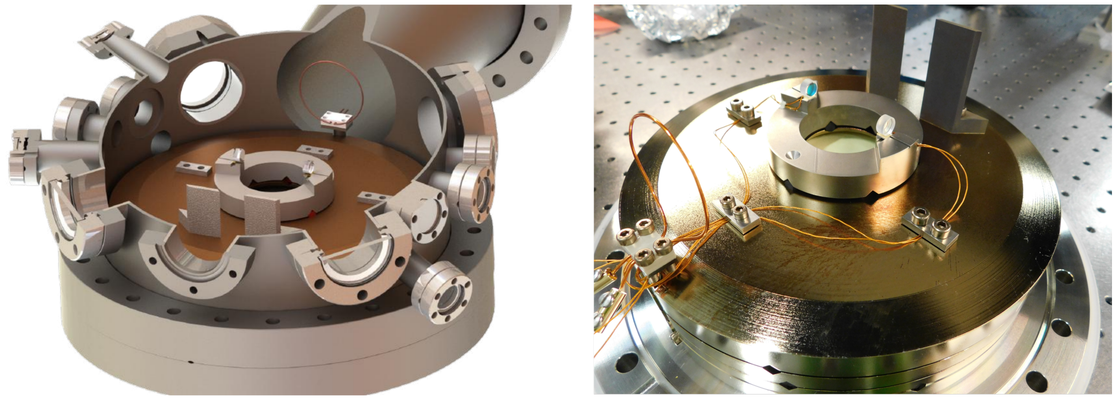

Figure 1.2: Pictures of the cavity sitting on top of its vibration dampening platform. Two vertical titanium pieces shield the mirrors from the atomic flux. The ensemble also features a single-loop antenna which can be used to address the radio-frequency transitions of ^{6}Li.

The *science chamber* is connected to the oven one via the Zeeman slower and hosts the *science cavity*, which rests on a stack of vibration-dampening stainless steel rings. A cut view of the chamber is depicted in figure 1.2, showing all the available optical accesses in the horizontal plane. It features re-entrant viewports on its top and bottom flanges to accommodate a set of compact electromagnets located as close as possible to the atoms, limiting the amount of current necessary to reach a given magnetic field. These electromagnets are presented in more details in the next paragraph. The re-entrant viewports might also be used in the future to set up a high numerical aperture imaging system, either to image the atomic density or to project potentials both with high-resolution.

The ultra-high vacuum in the science chamber is ensured by the *pumping chamber* which hosts an ion-getter pump (SAES NexTorr D1000-10). The pressure in this enclosure is read by a cold cathode pressure gauge (Pfeiffer IKR270). It routinely measures a pressure of 5×10^{-10} mbar, compatible with pressures in the science chamber of the order of 10^{-11} mbar, reduced because of the presence of a conical reduction and two angled elbows between the gauge and the science chamber.

1.1.2 Compact, bulk-machined electromagnets

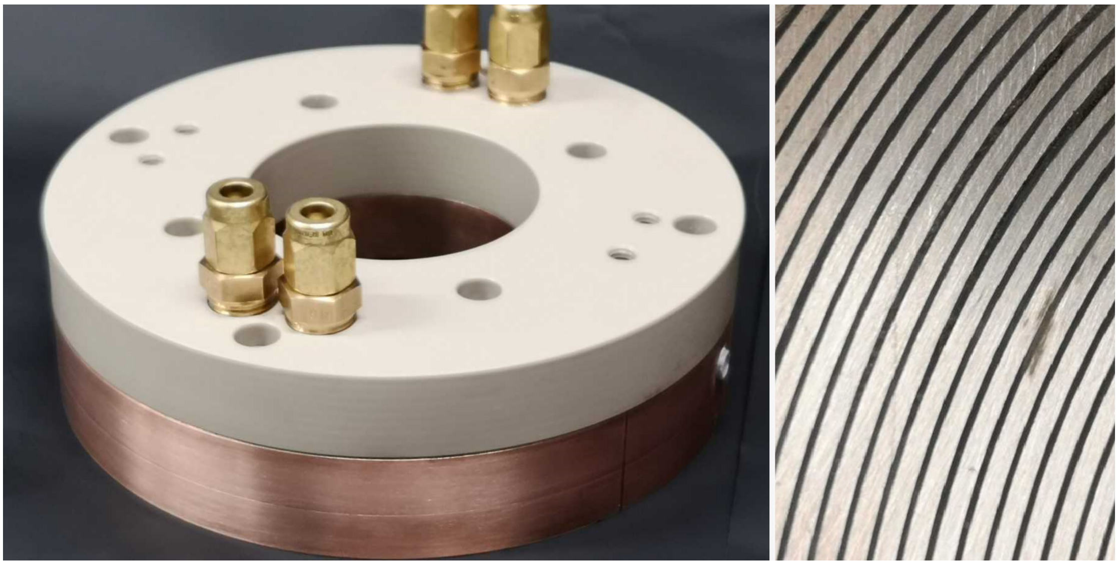

Figure 1.3: Picture of the electromagnet used in the experiment to address the broad Feshbach resonance of ^{6}Li. Left, picture of the assembled coil. It features the main copper body on top of which is attached a hollow PEEK cap. Serto connectors are used to connect the coil to the watercooling circuit. The cylindrical hole on the right side of the coil body hosts a ceramic tube through which the electrical connections pass. The assembly is attached to a support aluminum plate fixed atop the vacuum chamber as seen in figure 1.1, so that the coil body goes inside the re-entrant viewport. Right, a closeup view of the surface of the coil which shows a few turns separated by epoxy glue.

In order to reach the magnetic fields required to address the large Feshbach resonance of ^{6}Li located at 832 G and with the limited space at our disposal, we designed and built a pair of compacts, watercooled electromagnets. This section briefly summarizes their main features and more details are given in reference [80]. The design approach was heavily constrained by the limited space available within the re-entrant viewports, with a diameter of only 16 cm. Within such a limited volume, we optimized the watercooling efficiency in order to work with the highest possible volume of copper, thus requiring less current to reach a given magnetic field. Our watercooling strategy followed the reasoning presented in reference [82], where all the coil turns are cooled in parallel using a water duct that runs directly on top of them.

One assembled coil is presented in figure 1.3. The coil body consists of a single piece of copper machined into a spiral using an electroerosion procedure. The spiral is then vacuum-impregnated with epoxy glue to solidify it. In the end, we obtain a single solid cylindrical coil with inner and outer radii of 32 and 72 mm respectively, and a height of 22 mm. It comprises 31 turns which allows the pair of electromagnets to produce an offset field of $2.71\,\mathrm{G{\cdot}A^{-1}}$ oriented along the vertical direction at the location of the atoms in the chamber. Addressing the Feshbach resonance thus requires currents of the order of 300 A, which are provided by two power supplies (Delta Elektronika SM18-220) mounted in parallel. The coil configuration departs from Helmholtz, thereby creating a magnetic saddle point with a negative curvature along the horizontal direction, providing a confining potential for the high-field seeking atomic states we employ in the experiments.

Water is run directly on top of the coil, cooling down the 31 turns in parallel. It circulates in a duct created by a hollow PEEK cap placed on top of the coil body which presses against an o-ring to make the ensemble leak tight, and was tested up to 3.5 bar of overpressure with a water flow of $0.25\,\mathrm{l{\cdot}s^{-1}}$. During continuous operation the coil body never exceeds 30°C for an inlet water temperature of 17.5°C and a current of 300 A. As such its temperature is even lower during experimental cycles, since the high current is on for about 30% of the time. All in all this design proved to be extremely efficient in terms of water cooling. As a proof of its robustness, we have been operating the coils daily for the past 4 years without any incident.

1.1.3 The high-finesse optical cavity

The high-finesse optical cavity, or *science cavity*, is the central piece of the experiment. It is not only used to probe or drive the atomic ensemble but is also a core part of the gas preparation stage: we harness its power-enhancing properties to create deep optical dipole traps with limited input power [83]. We summarize here its properties and present the stabilization scheme with which we control its length and tune its resonance frequencies with respect to atomic transitions. A complete presentation of the theoretical basis required to understand the properties of optical cavities can be found *e.g.* in reference [84].

Properties of the cavity

A picture of the cavity taken right before closing the vacuum chamber is shown in figure 1.2 alongside a CAD view of its position within the science chamber. It is 4.131(1) cm long and formed by two 7.75 mm diameter mirrors with radii of curvature of 25 mm (from Advanced Thin Films). The distance between the mirrors was constrained by the choice of operating the MOT within the cavity: the large MOT beams required to capture a sizeable ^{6}Li cloud need to be accommodated in between the mirrors. Each mirror is glued on a shear piezoelectric actuator (Noliac CSAP02-C03) with a UHV compatible epoxy glue (Masterbond EP21TCHT-1). The cavity length is then controlled by applying a voltage bias across the electrodes of one of these piezos. Both of them are glued on a titanium ring, itself resting on top of a stack of non-magnetic stainless steel rings (of grade 1.4435 or 316LMo) with each stage separated by Viton rods. The ensemble forms a dampening platform which isolates the cavity from high-frequency vibrations and sits on the bottom flange of the science chamber.

On the optical side, the mirrors feature a trichroic coating, so that the cavity can be used with three different wavelengths

- at 671 nm, the wavelength which addresses the $2s \rightarrow 2p$ transitions of ^{6}Li
- at 1064 nm, to produce a deep, far off-resonant attractive dipole trap
- at 532 nm, to stabilize its length using the Pound-Drever-Hall technique [85, 86].

We summarize its optical properties in table 1.1. Its length and the mode waists are inferred from measurements of the transverse mode spacing and free spectral range, following definitions from [84], and the linewidths are obtained with ring-down measurements.

	671 nm	532 nm	1064 nm
Cavity length	4.131(1) cm		
Free spectral range (ν_{FSR})	3.6277(1) GHz		
Transverse mode spacing (ν_{TEM})	2.634(1) GHz		
Mirror diameter	7.75 mm		
Coating transmission	$T \simeq 50$ ppm	$T < 0.1$ %	
Finesse	$4.7(1) \cdot 10^4$	$2.4(1) \cdot 10^3$	$3.6(1) \cdot 10^3$
Linewidth $\kappa/2\pi$	0.077(1) MHz	1.5(1) MHz	1.0(1) MHz
TEM$_{00}$ mode waist	45.0(3) μm	40.1(3) μm	56.6(3) μm

Table 1.1: Summary of the cavity optical properties, reproduced from [79].

Active length stabilization

The length stabilization or *lock* of the science cavity is an essential step to perform the experiments. Undesired fluctuations of the cavity length induce shifts of its resonance frequencies and might cause the light fields used in the experiment to fall out of resonance. In addition to relative stabilization, the ability to tune the cavity resonance frequencies with respect to the atomic transitions is of tremendous importance as demonstrated in the rest of this manuscript.

The canonical method used to actively stabilize an optical cavity is called the Pound-Drever-Hall (PDH) technique and relies on the continuous measurement of the phase of a near-resonant light beam reflected off the cavity [85, 86]. The measurement of the frequency-dependent phase yields an error signal which is then used to feedback a control voltage to one of the piezos of the cavity to lock its length. Once locked, the light beam is resonant with the cavity and therefore creates a standing wave inside it. In order to mitigate the effect of this additional optical potential on the atomic dynamics we use a weak locking beam with a wavelength of 532 nm, far from any atomic resonance. In addition, the beam addresses a TEM$_{02}$ mode of the cavity, spreading the intracavity power over a large volume to minimize the residual potential depth. We estimate the associated peak dipole potential to be two orders of magnitude below the natural recoil energy of ^{6}Li, and never observed any unwanted consequences of the continuous presence of the locking light inside the cavity.

The beam at 532 nm is obtained from a frequency doubled 1064 nm fiber laser (NKT Adjustik amplified with an Azurlight ALS-IR), via second harmonic generation in a PPLN waveguide (NTT electronics). The stabilization of the cavity length on the 532 nm bean thus ensures the 1064 nm light to also be resonant with the cavity, bar a small constant chromatic shift coming from transmission through the mirrors substrates and compensated for by an acousto-optical modulator (AOM). We employ a 1064 nm beam to produce a deep dipole potential and capture the atoms after the MOT phase. This beam is made resonant with a TEM$_{01}$ mode of the cavity as to increase its trapping volume, which allows capturing more atoms.

Last, we require 671 nm light to be resonant with the cavity to probe the atomic transitions. The probing light is generated by frequency doubling the output of a 1342 nm narrow diode laser (Toptica TA Pro) with a PPLN waveguide. The corresponding laser setup is described in appendix B. In order to stabilize the probe frequency with respect to the cavity resonance frequency we employ a second optical cavity, the *transfer cavity* described in [79]. The resulting general stabilization scheme is depicted in figure 1.4, and it works the following way

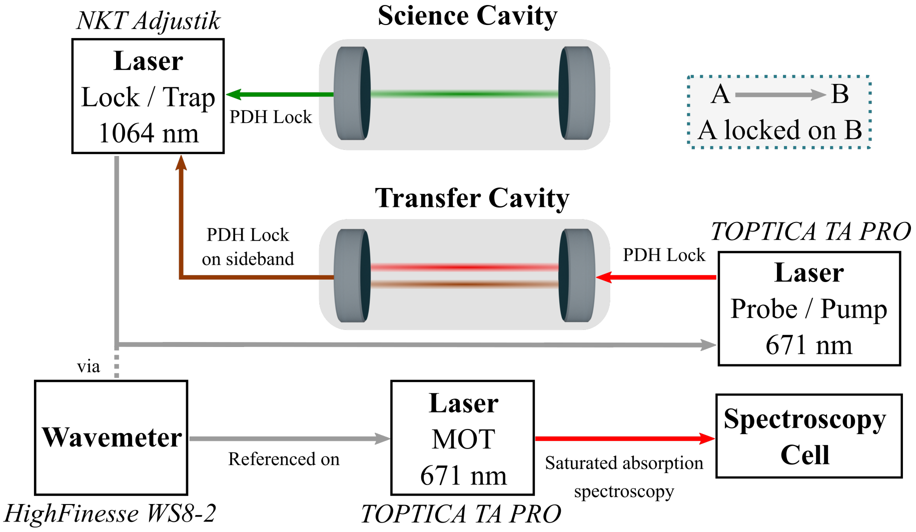
NKT Adjustik
Laser
Lock / Trap
1064 nm
Science Cavity
PDH Lock
A → B
A locked on B
Transfer Cavity
PDH Lock
on sideband
PDH Lock
TOPTICA TA PRO
Laser
Probe / Pump
671 nm
via
Wavemeter
Referenced on
Laser
MOT
671 nm
Saturated absorption
spectroscopy
Spectroscopy
Cell
HighFinesse WS8-2
TOPTICA TA PRO

Figure 1.4: Schematic of the frequency stabilization chain for the various laser frequencies and cavity lengths. We only display the beam lines directly involved in the PDH schemes.

- The length of the transfer cavity is stabilized with a PDH lock on a tunable sideband of the 1064 nm laser. With the science cavity lock, this ensures that both cavities length follow the variations of the 1064 nm laser frequency.

- The probe laser frequency is stabilized with a PDH lock of the 671 nm beam on the transfer cavity, such that a change of the 1064 nm laser frequency now also changes the probe frequency.

- Last, and since we ultimately care about the absolute frequency of the 671 nm beam, the 1064 nm laser frequency is set so that the reading of the absolute probe frequency on the wavemeter (HighFinesse WS8-2) has the wanted value. This is done by a digital PID loop with the wavemeter control software, which feeds back on the 1064 nm laser piezo.

- The wavemeter is calibrated by reading the frequency of the MOT laser, which is stabilized onto the ^{6}Li transitions via a saturated absorption spectroscopy cell.

All in all this robust lock scheme allows to tune the cavity length at will with respect to the atomic transitions. The lock of the transfer cavity onto a sideband of the 1064 nm laser adds a degree of freedom in the lockchain, granting full control over the relative detuning between the cavity resonance frequency and the probing beam frequencies. In addition, this scheme permits the concurrent use of a far off-resonant cavity dipole trap. All the relevant optical setups are presented in [79], except the recently modified probe laser path presented in appendix B.

1.2 From hot vapor to quantum degenerate gas: production of a Fermi gas of ^{6}Li

We now turn to the actual realization of a strongly interacting Fermi gas, starting from a hot vapor of ^{6}Li atoms inside the oven chamber. In this section, we sequentially describe the all-optical cooling procedure to reach quantum degeneracy, using standard laser and evaporative cooling techniques.

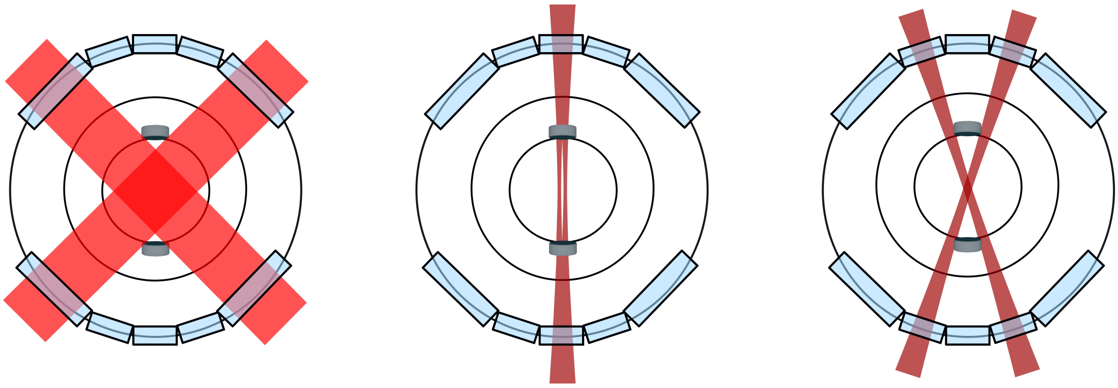

Figure 1.5: Sketches of the main cooling and trapping steps of the experimental cycle. Left, MOT stage. Center, cavity traps with a TEM_{01} mode structure. Right, crossed dipole trap. Each cycle lasts for approximately 4 s, mostly limited by the time spent loading atoms into the MOT.

As a guideline for the section, we summarize in figure 1.5 the main steps performed during an experiment cycle to prepare the Fermi gas, starting from a hot vapor in the oven chamber.

1.2.1 Laser cooling

Hot atoms leaving the oven chamber are continuously decelerated by the use of a Zeeman slower [87]. The Zeeman slower laser beam is produced by a dedicated 671 nm laser diode (Toptica TA Pro), which is offset locked to the MOT diode laser via the wavemeter. The beam has a total power of 155 mW and is focused down into the oven. As the atoms travel to the science chamber, the decreasing magnetic field generated by a dedicated pair of coils allows compensating for the velocity-dependent Doppler shift of their transition frequencies. They reach the center of the chamber with velocities of the order of tens of $\text{m}\cdot\text{s}^{-1}$, below the typical capture velocity of the MOT.

The MOT is obtained by a combination of a gradient of magnetic field, crossing zero at the center of the science chamber, and a set of 3 orthogonal and retro-reflected near-resonant beams [88]. Each of the circularly polarized beam has a total power of 50 mW spread over a 2.5 cm diameter, and is composed of two tones: the *cooler* and *repumper* respectively addressing the $|2s_{1/2}, F = 3/2\rangle \rightarrow |2p_{3/2}, F = 5/2\rangle$ and $|2s_{1/2}, F = 1/2\rangle \rightarrow |2p_{3/2}, F = 3/2\rangle$ transitions. The repumper light ensures that atoms populating the $|2s_{1/2}, F = 1/2\rangle$ state are optically pumped back in the $|2s_{1/2}, F = 3/2\rangle$ state in order to cycle the cooling transition. The atoms are loaded into the MOT from the Zeeman slower for a typical duration of 3 s and reach a temperature of a few hundreds of μK, higher than the Doppler temperature of 140 μK limited by the natural linewidth of the transitions $\Gamma = 2\pi \times 5.87\,\text{MHz}$ [74]. Before their transfer into an optical dipole trap, the atoms are optically pumped into the $|2s_{1/2}, F = 1/2\rangle$ by a cooling beam pulse and therefore end up populating the two lowest hyperfine states, $|2s_{1/2}, F = 1/2, m_F = 1/2\rangle$ and $|2s_{1/2}, F = 1/2, m_F = -1/2\rangle$ which we respectively label $|1\rangle$ and $|2\rangle$.

1.2.2 Evaporative cooling in cavity dipole traps

The atoms are loaded into a cavity dipole trap with a TEM_{01} mode structure as depicted in figure 1.5. The use of a TEM_{01} mode compared with a TEM_{00} was motivated by two points. First, its has a twice larger mode volume which increases its spatial overlap with the atomic cloud in the MOT. Second, while working with TEM_{00} modes we observed a strong bistable behavior of the cavity resonance frequency as a function of the cavity trap beam power [89], suggesting a heating effect of the mirrors surface which hindered the efficiency of the cavity lock and made the regulation of the intracavity power difficult. Using a higher-order mode thus reduces the peak intensity on the mirrors surface, and we found that using a TEM_{01} was sufficient to suppress the thermal bistable behavior, for a fixed incident power.

We inject 250 mW of laser power at 1064 nm in the cavity, which translates to a peak power of about 680 W at the center of the cavity mode with a beam waist of $56.6\,\mu$m. It corresponds to a peak trap depth of 8 mK, far above the temperature of the atoms in the MOT and comparable to the depths reached by experimental setups making use of high-power lasers. Once loaded in the cavity trap the atoms are held for 50 ms, the time it takes to ramp up the offset magnetic field to the location of the Feshbach resonance using the electromagnets described in the previous section. As we will discuss in chapter 3, near the resonance the s-wave scattering length for atoms in states $|1\rangle$ and $|2\rangle$ diverges and leads to a maximized value of the scattering cross-section, providing extremely beneficial conditions to perform forced evaporative cooling [90].

We perform forced evaporative cooling in three steps, in three different traps. Once the magnetic field is settled at $832\,G$, we linearly ramp down the power of the cavity trap to 10% of its initial value in 150 ms. We then transfer the atomic cloud in a second, lattice-free cavity trap with the same transverse intensity profile as the initial one. The inherent lattice structure of cavity modes makes evaporation processes inefficient since atomic ensembles cannot redistribute between sites and accumulate in the deepest regions of the trap. We circumvent the issue by using a lattice-free trap, created by injecting in the cavity a phase-modulated carrier beam with sidebands spaced by multiples of the cavity free spectral range. The sidebands thus drive neighboring longitudinal modes of the cavity so that the sum of their intensities is effectively homogenous inside the cavity [91]. In practice, we generate the sidebands with a free space phase modulator (Qubig PM9-NIR) driven at a frequency of 3.6277 GHz and a modulation depth of 1.27 rad. Both cavity traps, with and without lattice, are recombined on a polarized beamsplitter before their injection into the cavity. We perform the second linear evaporation ramp in this lattice-free trap, for a duration of 200 ms and down to an intracavity power of 70 mW.[1]

1.2.3 Evaporative cooling in a running wave dipole trap

At this stage, the gas typically comprises 1.5×10^6 atoms equally populating states $|1\rangle$ and $|2\rangle$, and the two arms of the TEM_{01} cavity trap. The last step of evaporation is performed in a crossed dipole trap made of two independent arms, shown in figure 1.5. We use AOMs to induce a frequency detuning between the two arms, suppressing interference effects. The transfer of the atoms in the crossed trap maximizes the overlap between the atomic density and the TEM_{00} mode of the cavity, which we address in the experiments with the probe. Each arm is focused on the cavity mode position with a waist of $33\,\mu$m and they intersect at angle of 36°. They both have an initial power of 1 W, ramped down to varying setpoints of the order of tens of mW in 450 ms. In the end we routinely prepare 6×10^5 atoms in states $|1\rangle$ and $|2\rangle$, strongly interacting via the Feshbach resonance in the unitary limit.

---

[1] As presented in the next chapter, we now have evidence that the gas held in this cavity trap is already deep in the degenerate regime, making the use of the next step of evaporative cooling redundant.

By performing thermometry on the gases with a technique presented in section 2.2, we verify that they are deeply degenerate with temperatures of the order of 10% of the Fermi temperature. These unitary Fermi gases serve as the basic bricks for all the experiments described in this manuscript. After the final evaporation ramp, we slightly increase the cross trap depth in order to stop the evaporation process. During this 50 ms recompression ramp, we have the possibility to vary the offset magnetic field around the Feshbach resonance in order to tune the interparticle interactions before probing the system.

Chapter 2

Probing strongly interacting Fermi gases strongly coupled to light

> I have come to believe that the whole world is an enigma, a harmless enigma that is made terrible by our own mad attempt to interpret it as though it had an underlying truth.
>
> Umberto Eco

Outline of the current chapter

2.1 Probing the strong light-matter coupling **18**
- 2.1.1 Light-matter interaction and the strong coupling regime 18
- 2.1.2 Strong light-matter coupling from near-resonance transmission spectroscopy 21
- 2.1.3 Transmission spectroscopy in the dispersive limit 26

2.2 Absorption imaging for the thermometry of unitary Fermi gases **30**
- 2.2.1 High-intensity absorption imaging 31
- 2.2.2 Temperature measurement using the equation of state 33

In this chapter, we present several measurement techniques used for all the experimental results contained in this manuscript. It serves as a direct follow-up of the previous one, where we introduced the experimental setup and the gas cooling and trapping procedures. In a fist section we introduce a theoretical description of the atomic ensemble coupled to the cavity field. Under this description, we present cavity transmission spectroscopy as a method to measure the energy spectrum of the coupled system and apply it in two different regimes. We distinguish between the *resonant* regime, where the system is probed in the vicinity of the atomic transitions, and the *dispersive* regime, where the probe is far-detuned. Our measurements represent the first realization of a strongly interacting fermionic system strongly coupled to light. In a second section we present a recently implemented thermometry technique, based on the usage of high-intensity imaging. Analysis of density profiles via absorption imaging complements the information granted by cavity signals and with it, we have the possibility to accurately measure the degeneracy parameter T/T_F of the unitary Fermi gases we routinely produce and study.

2.1 Probing the strong light-matter coupling

In this section we present the results leading to and following the realization of the strong coupling regime between our unitary Fermi gas and the cavity field for the first time. Along with presenting the achievement of the strong coupling regime, this section aims at introducing the experimental and formal tools used throughout the manuscript to probe the atomic ensemble with the cavity field.

We formally introduce a model for this coupled system, accounting for several ensembles of two-level systems and multiple cavity modes to better describe our experiment. We then introduce transmission spectroscopy as a measurement method of the energy spectrum of the coupled atoms-cavity system. Finally, we present measurements of the energy spectrum performed in two distinct regimes, with the probing light and cavity resonance either close to or far-detuned from the atomic resonances.

The results contained here were presented in journal articles for the resonant [92] and dispersive measurements [89], and discussed in more details in the PhD thesis of Kevin Roux [79].

2.1.1 Light-matter interaction and the strong coupling regime

The strong coupling regime

The coherent coupling of a two-level system to a single mode of the electromagnetic field is described by the Jaynes-Cummings model [93] which predicts in particular the celebrated splitting of the eigenenergies of the coupled system [94], provided that the strong coupling regime is reached.

This strong coupling regime corresponds to the situation where the fraction of photons coherently scattered by the two-level system in the considered mode of the electromagnetic field exceeds that of photons lost due to incoherent, dissipative processes. This regime is at the heart of emerging quantum technologies since it allows for the manipulation, observation and control of the quantum systems down to the single-photon level [94]. The use of high-finesse resonators allows for the drastic enhancement of coherent scattering of photons within a mode of the electromagnetic field, compared with the free-space situation [55]. The enhancement factor is directly proportional to the finesse $\mathcal{F}$ of the resonator and arises from the constructive interference of scattered photons between successive round-trips within it. The quantity measuring the ratio between coherent scattering of a single two-level system in a single resonator mode and the dissipative processes is called the cooperativity C_0 and is defined with

$$C_0 = \frac{4g_0^2}{\kappa\Gamma}. \tag{2.1}$$

The natural linewidth of the cavity κ and of the considered excited state Γ set the typical scales against which the coherent rate of exchange of excitations g_0 between the two-level system and the cavity mode has to be compared. If $C_0 > 1$, the system is said to be operating in the strong-coupling regime following our definition. The cooperativity can equivalently be expressed purely in terms of bare properties of the resonator, with

$$C_0 = \frac{24\mathcal{F}}{\pi k^2 \omega_0^2}, \tag{2.2}$$

where k is the magnitude of the wavevector of the cavity light field and ω_0 its waist. For the properties of our optical cavity described in section 1.1.3 we obtain $C_0 = 2.02$, meaning that our system already operates in the strong coupling regime for a single atom.

The generalization of the Jaynes-Cummings model for an ensemble of N two-level systems equally coupled to a single mode of the cavity field is called the Tavis-Cummings model [95] and is of particular interest for us since we deal with atomic ensembles. Its main prediction is the increase of the excitation exchange rate between the cavity field and the atomic ensemble by a factor $\sqrt{N}$, thus increasing the light-matter interaction strength. This is captured by the collective cooperativity defined by

$$C_N = NC_0 = \frac{4Ng_0^2}{\kappa\Gamma}. \tag{2.3}$$

For the typical atom numbers in the range of a few 10^5 presented in this thesis, C_N is of the same order of magnitude and therefore the incoherent dissipative processes are vastly suppressed with respect to the coherent exchange between atomic excitations and cavity photons.

General expression for the Hamiltonian

In order to formally describe the system, we consider two distinct[1] ensembles of two-level systems which represent the ground state of our degenerate, two-components Fermi gas after the preparation phase described in the previous chapter. The atoms thus populate the two lowest Zeeman sublevels $|1\rangle$ and $|2\rangle$ of the $F = 1/2$ hyperfine state [74] which ground state energies are shifted by $\hbar\omega_{12} = 76.3\,\mathrm{MHz}$ when working at $832\,\mathrm{G}$.

In the framework of second quantization, we label the matter-field operators corresponding to the ground state $|\sigma\rangle$ with $\hat{\psi}_\sigma(\mathbf{r})$, and to their corresponding excited state $\hat{\psi}_{\sigma\mathrm{e}}(\mathbf{r})$. They verify the fermionic anticommutation relation with $\left\{\hat{\psi}_\sigma(\mathbf{r}), \hat{\psi}^\dagger_{\sigma'}(\mathbf{r}')\right\} = \delta_{\sigma,\sigma'}\delta(\mathbf{r}-\mathbf{r}')$. We let the cavity be multimode and label its spatial mode functions with $u_\nu(\mathbf{r})$, which analytical expressions are obtained by the resolution of the Helmholtz equation within the resonator [84]. The fundamental transverse electromagnetic mode TEM$_{00}$ discussed later corresponds to $\nu = 0$ and has a Gaussian structure, while other indices correspond to higher order transverse modes. The cavity field is populated by the addition of an on-axis weak probe, with a frequency ω_p, shown in figure 2.1. Following the derivations presented in reference [96], we express the total Hamiltonian as

$$\hat{H} = \hat{H}_0 + \hat{H}_\mathrm{e} + \hat{H}_\mathrm{cav} + \hat{H}_\mathrm{lm} + \hat{H}_\mathrm{probe}. \tag{2.4}$$

---

[1] In the entirety of the manuscript we neglect Raman processes between the two distinct ground states.

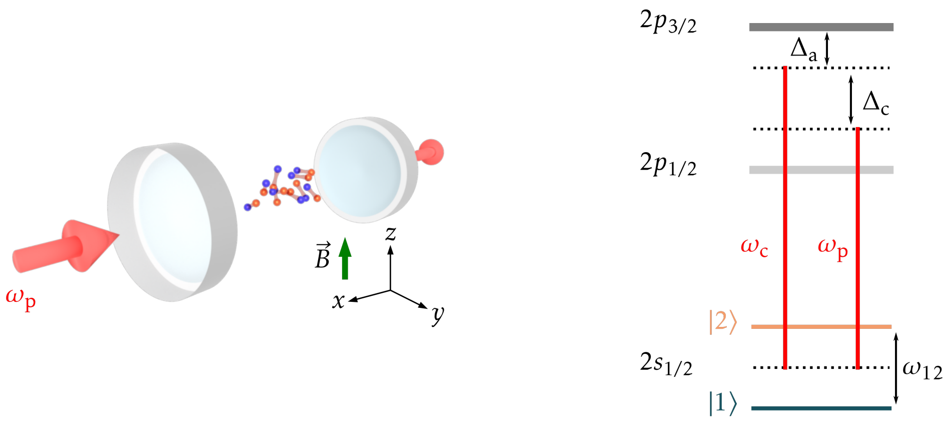

Figure 2.1: Probing setup and relevant atomic levels to describe the transmission spectroscopy experiment. Left, we probe the cavity on axis with a linearly polarized beam and record the photons leaking out of the cavity. Right, relevant energy levels of ^{6}Li at 832 G, including the probe laser frequency ω_p and an example cavity resonance frequency ω_c. In the experiment, as described in the text, the detunings Δ_a and Δ_a are varied independently. The thick gray lines depict the unresolved excited manifolds.

With

$$\begin{aligned}
\hat{H}_0 &= \sum_\sigma \int d\mathbf{r}\hat{\psi}^\dagger_\sigma(\mathbf{r})\left[-\frac{\nabla^2}{2m}+V_t(\mathbf{r})+\omega_\sigma\right]\hat{\psi}_\sigma(\mathbf{r}) \\
&\quad + \int d\mathbf{r}d\mathbf{r}'\hat{\psi}^\dagger_2(\mathbf{r}')\hat{\psi}^\dagger_1(\mathbf{r})V_p(|\mathbf{r}-\mathbf{r}'|)\hat{\psi}_1(\mathbf{r})\hat{\psi}_2(\mathbf{r}') && (2.5)\\
\hat{H}_e &= \sum_\sigma\sum_e \int d\mathbf{r}\hat{\psi}^\dagger_{\sigma e}(\mathbf{r})\left[-\frac{\nabla^2}{2m}+V_t(\mathbf{r})+\omega_{\sigma e}\right]\hat{\psi}_{\sigma e}(\mathbf{r}) && (2.6)\\
\hat{H}_{cav} &= \sum_\nu \omega_\nu \hat{a}^\dagger_\nu\hat{a}_\nu && (2.7)\\
\hat{H}_{lm} &= \sum_\nu\sum_\sigma\sum_e \int d\mathbf{r}g_{\nu,\sigma,e}\left(u_\nu(\mathbf{r})\hat{\psi}^\dagger_{\sigma e}(\mathbf{r})\hat{\psi}_\sigma(\mathbf{r})\hat{a}_\nu + \text{h.c.}\right) && (2.8)\\
\hat{H}_{probe} &= i\sum_\nu \beta_\nu(\hat{a}_\nu e^{-i\omega_p t} - \hat{a}^\dagger_\nu e^{i\omega_p t}), && (2.9)
\end{aligned}$$

where we have set $\hbar = 1$ and where the sums over indices σ and e represent the two considered atomic ground states, with their respective excited states $|\sigma e\rangle$. The sums over ν on the other hand relate to the cavity modes.

The first two terms $\hat{H}_0$ and $\hat{H}_e$ account for the ground and excited states energy contributions, respectively. V_t is the trapping potential, given here by the crossed optical dipole trap introduced in the previous chapter. The ground state contribution explicitly includes the effect of interatomic contact interactions via the pseudopotential V_p and is discussed in greater details in chapter 3. In addition, we disregard dipole-dipole interactions between atoms in the ground and excited states in the absence of photons for the time being, and will reintroduce them later in chapters 3 and 4.

The bare cavity energy is represented by $\hat{H}_{\mathrm{cav}}$, which sums contributions from all the populated cavity modes with $\hat{a}_\nu$ the bosonic photon annihiliation operator for the mode ν at energy ω_ν. The light-matter interaction term $\hat{H}_{\mathrm{lm}}$ describes the coherent exchange of excitations between the cavity field and the atomic ensemble. It explicitly includes the spatial dependency of the interaction via the shape of the cavity mode functions u_ν, while its strength is given by the maximal coupling strengths $g_{\nu,\sigma,\mathrm{e}}$ between a single atom in state σ and a single photon of the ν^{th} cavity mode. The coupling strengths depend explicitly on both the details of the underlying atomic transition and volume of the cavity mode V_ν with [94]

$$g_{\nu,\sigma,\mathrm{e}} = \langle \sigma \mathrm{e} | \hat{d} | \sigma \rangle \sqrt{\frac{\omega_\nu}{2\hbar \varepsilon_0 V_\nu}}, \tag{2.10}$$

where $\hat{d}$ is the atomic dipole operator. This expression involving dipole transition matrix elements leads to a strong dependence of the coupling strengths on the details of the polarization of the light field. Last, the contribution of the external probe is accounted for by $\hat{H}_{\mathrm{probe}}$, driving the cavity ν with a strength β_ν at a frequency ω_{p}.

This generic form of the total Hamiltonian $\hat{H}$ will serve a theoretical basis for the rest of the manuscript. Its exact diagonalization is challenging given the strongly interacting nature of its fermionic constituents which in particular makes it impossible to express the many-body wave function in a workable way, as it is for example done for condensate wavefunctions in the case of pure BECs. However, we shall see in the following sections how some approximations can lead to more convenient forms of the previous Hamiltonian.

2.1.2 Strong light-matter coupling from near-resonance transmission spectroscopy

We now turn to experimental observation of the strong coupling regime. In the above model, we tune the probe frequency ω_{p} to the vicinity of the D_2 σ_- transition $\left|2s_{1/2}, m_J = -1/2\right\rangle \to \left|2p_{3/2}, m_J = -3/2\right\rangle$. The probing setup is depicted by figure 2.1. In the Paschen-Bach regime, this allows us to only consider a single atomic excited state for each ground state, the other ones not being populated.

Ab-initio model for the coherent cavity field

In order to provide a qualitative understanding of the situation, we developed an ab-initio model describing the dynamics of the cavity field for the above Hamiltonian $\hat{H}$. The details of the calculations can be found in reference [79], and we simply sketch the main results here. The general procedure is to calculate the steady-state solutions of the master equations [97]

$$\frac{d\langle \hat{a}_\nu \rangle}{dt} = i\left\langle \left[\hat{H}, \hat{a}_\nu\right]\right\rangle - \frac{\kappa}{2}\langle \hat{a}_\nu \rangle. \tag{2.11}$$

We neglect quantum fluctuations and atom-field correlations, thus replacing the field operators by coherent amplitudes. For the case of the cavity field we have

$$\hat{a}_\nu \to \alpha_\nu. \tag{2.12}$$

We work in the rotating wave approximation, in a frame moving at the probe frequency ω_{p}. In the low saturation approximation for the atomic transitions, eliminating the internal and external atomic degrees of freedom, we obtain a set of equations of the field amplitude in mode ν

$$(i\Delta_\nu + \frac{\kappa}{2})\alpha_\nu = -\sum_\mu \sum_\sigma \frac{g_{\nu,\sigma} g_{\mu,\sigma}}{\frac{\Gamma}{2} + i\Delta_\sigma} \int d\mathbf{r} n_\sigma(\mathbf{r}) u_\nu(\mathbf{r}) u_\mu(\mathbf{r}) \alpha_\mu - \beta_\nu \tag{2.13}$$

where the sum over μ account for all the cavity modes, including ν. Γ is the linewidth of the excited atomic states and the considered detunings are defined with $\Delta_\nu = \omega_\nu - \omega_\mathrm{p}$ and $\Delta_\sigma = \omega_\sigma - \omega_\mathrm{p}$. n_σ is the local mean density of atoms in state $|\sigma\rangle$ and verifies $n_\sigma = \left\langle \hat{\psi}_\sigma^\dagger \hat{\psi}_\sigma \right\rangle$ and $\int d\mathbf{r} n_\sigma(\mathbf{r}) = N_\sigma$, the total number of atoms in that state.

The resolution of such a system of equation can be performed numerically and yields the total intensity in the cavity $\sum_\nu |\alpha_\nu^2|$, a quantity which can be experimentally measured as a function of the various detunings by means of transmission spectroscopy.

Transmission spectroscopy

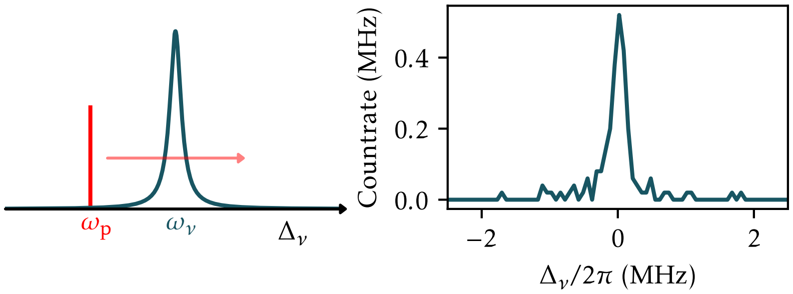

Figure 2.2: Example of transmission spectroscopy for an empty cavity. The probe frequency is swept across a resonance of the system, here corresponding to an empty cavity mode at frequency $\omega\nu$. The right panel depicts the corresponding experimental observation, with the transmitted countrate acquired on a single photon counter.

Transmission spectroscopy is performed by injecting a weak probe beam in the cavity and recording the transmitted photons on the single-photon counting module. We typically perform these measurements by dynamically sweeping the probe frequency while fixing the cavity length, which amounts to scanning Δ_ν with the previous notations. Figure 2.2 depicts the procedure and shows an empty cavity spectrum acquired with it. The linear sweep of the probe frequency is done with an acousto-optical modulator, and we map the measured photon arrival times to the frequency of the probe beam at the time of arrival, calibrated from the control signal sent to the AOM. If the frequency sweep rate is fast enough against the typical recoil frequencies associated with atomic dynamics, we can safely consider the atomic density to be frozen within the cavity mode and our method to effectively probe the energy spectrum of the coupled system.

We prepare a balanced gas at unitarity comprising 2×10^5 atoms and perform transmission spectroscopy by shining a probe beam mode matched to a TEM_{00} mode of the cavity of frequency $\omega_{\nu=0}$. This allows to set a frequency reference, where we define $\Delta_\mathrm{c} = \omega_0 - \omega_\mathrm{p}$ as the quantity we dynamically sweep during the experiment. Additionaly, we have $\beta_\nu = 0$ except for $\nu = 0$. In the same spirit, we define a single atom-cavity detuning Δ_a taken from the barycenter of the two ground states energies, and which is varied from one repetition of the experiment to the next by tuning the cavity length. The magnetic field allowing us to reach the unitary regime is oriented perpendicular to the cavity axis and the probe light is linearly polarized along the y axis defined in figure 2.1 so that it couples to both σ_+ and σ_- transitions. The probe sweep rate is set to $2\pi \times 100\,\mathrm{MHz/ms}$ and its power is set to keep the intracavity photon number below $\Gamma^2/8g_0^2 = 38$, the saturation threshold on resonance [79].

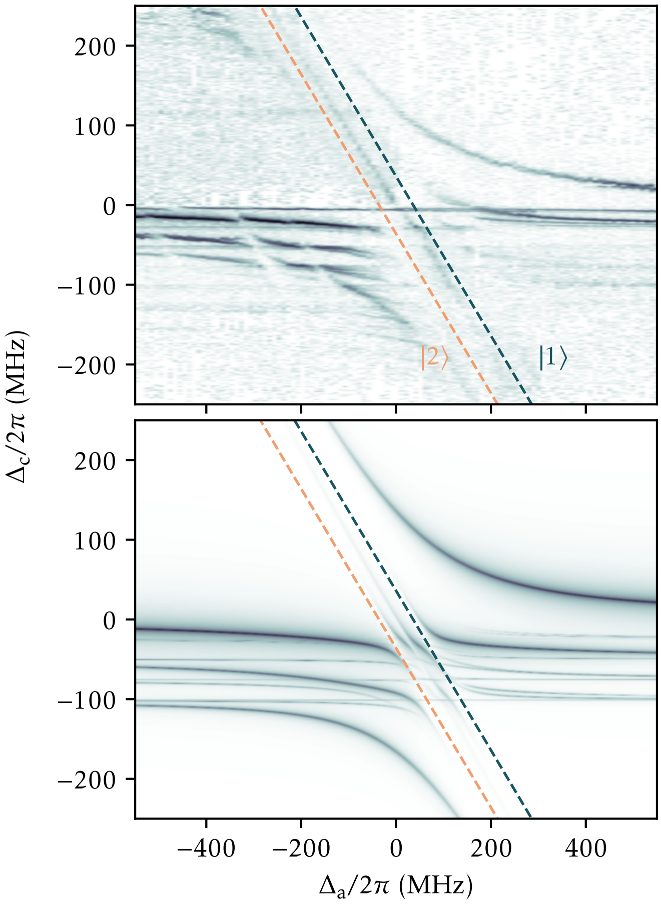

Figure 2.3: Transmission spectrum of the atoms-cavity coupled system. Top, actual data following the measurement procedure in the text. The color scale depicts the relative strength of the transmitted signal displayed in log scale. The bare atomic transitions for $|1\rangle$ and $|2\rangle$ are shown with blue and orange dashed lines, respectively. Bottom, transmission spectra obtained from the calculation accounting for the coupling to multiple cavity modes.

During a single experimental run we vary Δ_c by $2\pi\times100\,\mathrm{MHz}$, and then move the cavity length to increment Δ_a by steps of $2\pi \times 10\,\mathrm{MHz}$. We then repeat the measurements by adding a frequency offset within Δ_c using the locking scheme described in section 1.1.3, such that in total we explore $\Delta_c \in 2\pi\times[-250, 250]\,\mathrm{MHz}$ and $\Delta_a \in 2\pi\times[-550, 550]\,\mathrm{MHz}$. The results are presented in figure 2.3 together with the predictions from the model.

We observe two prominent avoided crossings as the bare cavity resonance approaches each atomic one, leading to three dressed state branches located above, below and between the two atomic resonances. The spectrum displays a richer structure for Δ_c, due to the presence of several families of high-order cavity modes, spaced by multiples of 25 MHz on the red side of the bare TEM$_{00}$ mode. These were mapped out in details in reference [79]. Each of these mode families couples to the atomic resonance, and are associated to dressed states mixing high-order and TEM$_{00}$ cavity modes with the atomic excitations. Even though the coupling efficiency of the probe beam with these high-order modes is less than 10^{-3}, the interaction with the finite size atomic cloud allows for scattering of the incident power into these modes, yielding large transmission for dressed states involving them as predicted by the overlap integral term in equation (2.13).

As depicted by the figure, the model well reproduces both the location and shape of the avoided crossings observed with the experiment. The structure of the dressed states also agree qualitatively for the high-order modes, but the precise location and strength of the various lines strongly depend on the exact position of the cloud, which is only known with limited accuracy. The evolution of the relative transmission along the dressed state branches also agrees qualitatively with the experimental spectrum.

The measured spectrum not only features strong coupling to the atomic resonances, but also weaker coupling to a set of matter-like excitations on the red side of the $\left|2s_{1/2}, m_J = -1/2\right\rangle \rightarrow \left|2p_{3/2}, m_J = -3/2\right\rangle$ transition. We attribute these excitations to photoassociation into weakly bound states of an asymptotic molecular potential. The detailed study of the coupling to these transitions is presented in chapter 4, where we show that the corresponding coupling strength is controlled by the short-range two-body correlation function.

Atom number scaling

To further verify the coherent nature of the light-matter coupling and quantify the coupling strength, we map our system to a generalization of the Tavis-Cummings model which accounts for the two independent ground states and a single TEM$_{00}$ cavity mode of frequency ω_c. In order to do so, we rewrite the Hamiltonian $\hat{H}$, disregarding the motional degrees of freedom and interactions in the ground state. For a single cavity mode and without the probe term, it reads

$$\hat{H} = \sum_{\sigma} \omega_{\sigma e} \int d\mathbf{r} \left(\hat{\psi}^{\dagger}_{\sigma e}(\mathbf{r}) \hat{\psi}_{\sigma e}(\mathbf{r}) - \hat{\psi}^{\dagger}_{\sigma}(\mathbf{r}) \hat{\psi}_{\sigma}(\mathbf{r}) \right) + \omega_c \hat{a}^{\dagger} \hat{a} + \sum_{\sigma} g \int d\mathbf{r} \left(\hat{\psi}^{\dagger}_{\sigma e}(\mathbf{r}) \hat{\psi}_{\sigma}(\mathbf{r}) \hat{a} + \text{h.c.} \right), \tag{2.14}$$

where we have dropped the spatial dependency of the cavity mode structure and considered that both dipole matrix elements coupling each ground state to their respective excited state were equal. In this description, the atomic ensemble is now homogeneously coupled to the cavity field, with only half of the density effectively contributing to the light-matter interaction.

This simplified form of the Hamiltonian allows for its expression as a collective spin 1/2 system and in this spirit we introduce the Dicke operators [98]

$$\hat{J}_{z,\sigma} = \int d\mathbf{r} \left(\hat{\psi}^{\dagger}_{\sigma e}(\mathbf{r}) \hat{\psi}_{\sigma e}(\mathbf{r}) - \hat{\psi}^{\dagger}_{\sigma}(\mathbf{r}) \hat{\psi}_{\sigma}(\mathbf{r}) \right) \tag{2.15}$$

$$\hat{J}_{\pm,\sigma} = \int d\mathbf{r} \hat{\psi}^{\dagger}_{\sigma e}(\mathbf{r}) \hat{\psi}_{\sigma}(\mathbf{r}). \tag{2.16}$$

such that

$$\hat{H} = \sum_{\sigma} \hat{J}_{z,\sigma} + \omega_{\mathrm{c}} \hat{a}^{\dagger} \hat{a} + g \sum_{\sigma} \left(\hat{J}_{\pm,\sigma} \hat{a} + \mathrm{h.c.} \right). \tag{2.17}$$

In the low saturation regime, the Holstein-Primakoff transformation allows to rewrite the Hamiltonian in terms of Bosonic operators $\hat{b}_{\sigma}$ describing individual, noninteracting collective optical excitations shared among atoms in state $|\sigma\rangle$ such that [99]

$$\hat{H} = \sum_{\sigma} \omega_{\sigma \mathrm{e}} \hat{b}_{\sigma}^{\dagger} \hat{b}_{\sigma} + \omega_{\mathrm{c}} \hat{a}^{\dagger} \hat{a} + g \sqrt{\frac{N}{4}} \sum_{\sigma} \left(\hat{b}_{\sigma}^{\dagger} \hat{a} + \mathrm{h.c.} \right) \tag{2.18}$$

with N the total atom number. This generalized model can be diagonalized in order to find its eigenenergies. For the cavity on resonance with the $|2\rangle$ transition so that $\Delta_{\mathrm{a}} = \omega_{\mathrm{c}} - \omega_{2\mathrm{e}} = \omega_{12}/2$, we expect one of the normal modes of the model at a frequency

$$E = \sqrt{g^2 \frac{N}{2} + \frac{\omega_{12}}{4}}, \tag{2.19}$$

which features the expected square root scaling in terms of atom number.

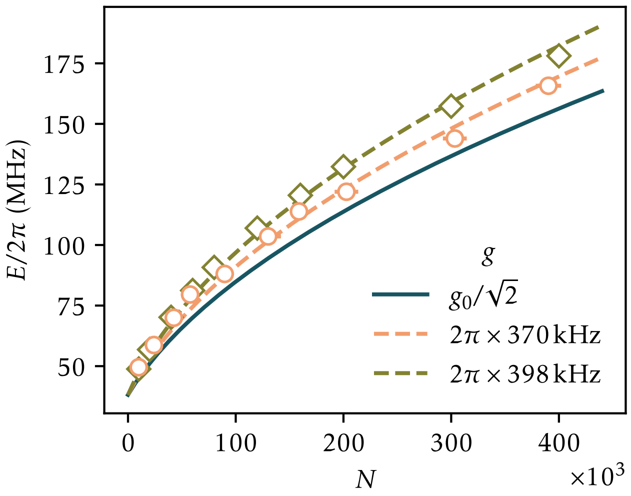

Figure 2.4: Position of the upper dressed state as a function of total atom number. Orange circles show experimental data and green diamonds are obtained from the ab initio theory calculation accounting for all the high-order cavity modes. The lines describe an analytical model with two atomic states and the TEM_{00} cavity mode only. The dashed lines are fits of both experimental data (orange) and theory calculation (green) with g as a free parameter. The blue solid line is the expected scaling for $g = g_0/\sqrt{2}$.

With the experiment, we tune the cavity frequency so that $\Delta_{\mathrm{a}} = \omega_{12}$ and measure the location of the upper polariton branch as a function of the prepared atom number. Using the upper polariton allows us to first approximation to discard the effects of coupling to higher-order modes and thus apply the present model. We acquire spectra by transmission spectroscopy and fit the location of the resonance with a Lorentzian profile. We present the results in figure 2.4, along with a fit of the data to equation (2.19). In addition, we also extract and fit the location of the upper dressed state predicted by the model of equation (2.13), computed for the same atom numbers.

Leaving g as an adjustable parameter, both the data and theory are well-fitted, confirming the coherent nature of light-matter coupling. We measure $g = 2\pi\times 0.370\,\mathrm{MHz}$ and $g = 2\pi\times 0.398\,\mathrm{MHz}$, respectively for the fit to the measurements and to the model. Both fitted values overestimate the expected $g = g_0/\sqrt{2} = 2\pi \times 339\,\mathrm{MHz}$, where the factor $\sqrt{2}$ comes from the linear polarization of the light which addresses the σ_- transition. We attribute the discrepancy to the neglected effect of the higher-order modes in the simpler model of this paragraph.

Nevertheless, the general agreement with a square-root dependency of the light-matter coupling strength with atom number confirms the coherent collective coupling of the atomic ensemble to the cavity light field, as described by the Tavis-Cummings model. The strong coupling between strongly interacting fermionic matter and optical fields is of tremendous interest for the creation, manipulation and interrogation of exotic quantum phases[69–72, 100] and as such, we have proved our experiment to be the perfect playground to explore these phenomena.

2.1.3 Transmission spectroscopy in the dispersive limit

In this section, we now move away from the resonant regime and describe the light-matter interactions in the dispersive limit. This limit corresponds to addressing the system with far detuned optical fields such that the atomic excited states are only virtually populated [55]. The excited states still influence the physics via their contribution to the polarizability [101] and the light-matter interactions can, to first order, simply be described in a two-photon picture where a ground state atom virtually absorbs and re-emits a photon. This process corresponds to an effective scattering event which, due to momentum conservation, can imprint a finite momentum to the atom. In the scope of cavity QED, the dispersive interaction can be used to mediate all-to-all, infinite range, interactions between an atomic ensemble and lead to interesting collective phenomena. While we present in chapter 6 the study of the effects of such long-range dispersive light-matter interactions, we focus in this section on the shift of the cavity resonance frequency induced by the dispersive interaction.

In what follows, we present a formal description of the dispersive regime which we then employ as a weakly-destructive measurement regime for the system. To do so, we use the same formalism as introduced in the previous section and start from the Hamiltonian of equation (2.4). We assume a single cavity mode, with a TEM_{00} structure, and consider the $2p_{1/2}$ and $2p_{3/2}$ excited manifolds, which correspond to D_1 and D_2 transitions respectively. We again work at $832\,\mathrm{G}$ so that the ground state energies are shifted by $\hbar\omega_{12}$ and take the energy of state $|1\rangle$ as a reference.

Adiabatic elimination and effective Hamiltonian

The total Hamiltonian reads, in second quantization formalism and in a frame rotating at the probe frequency ω_p

$$\begin{aligned}\hat{H} =& \Delta_\mathrm{c}\hat{a}^\dagger\hat{a}\\ &+\int d\mathbf{r}\hat{\psi}_1^\dagger(\mathbf{r})\left[-\frac{\nabla^2}{2m}+V_\mathrm{t}(\mathbf{r})\right]\hat{\psi}_1(\mathbf{r})\\ &+\int d\mathbf{r}\hat{\psi}_2^\dagger(\mathbf{r})\left[-\frac{\nabla^2}{2m}+V_\mathrm{t}(\mathbf{r})+\omega_{12}\right]\hat{\psi}_2(\mathbf{r})\\ &+\int d\mathbf{r}d\mathbf{r}'\hat{\psi}_2^\dagger(\mathbf{r}')\hat{\psi}_1^\dagger(\mathbf{r})V_\mathrm{p}(|\mathbf{r}-\mathbf{r}'|)\hat{\psi}_1(\mathbf{r})\hat{\psi}_2(\mathbf{r}')\\ &+\sum_\sigma\sum_\mathrm{e}\int d\mathbf{r}\hat{\psi}_{\sigma\mathrm{e}}^\dagger(\mathbf{r})\left[-\frac{\nabla^2}{2m}+V_\mathrm{t}(\mathbf{r})-\Delta_{\sigma\mathrm{e}}\right]\hat{\psi}_{\sigma\mathrm{e}}(\mathbf{r})\\ &+\sum_\sigma\sum_\mathrm{e}\int d\mathbf{r}g_{\sigma,\mathrm{e}}\left(u_0(\mathbf{r})\hat{\psi}_{\sigma\mathrm{e}}^\dagger(\mathbf{r})\hat{\psi}_\sigma(\mathbf{r})\hat{a}+\mathrm{h.c.}\right),\end{aligned}\tag{2.20}$$

with $\Delta_{\sigma\mathrm{e}}=\omega_\mathrm{p}-\omega_{\sigma\mathrm{e}}$ the detunings of the probe beam with respect to the frequencies of the transitions $|\sigma\rangle\to|\sigma\mathrm{e}\rangle$. We remind that the sums over σ refer to the ground states while those over indices e adress the excited ones.

Writing the Heisenberg equations for the excited fermionic fields, we obtain

$$\frac{d\hat{\psi}_{\sigma,\mathrm{e}}}{dt}=-i\left[-\frac{\nabla^2}{2m}+V_\mathrm{t}-\Delta_{\sigma,\mathrm{e}}\right]\hat{\psi}_{\sigma,\mathrm{e}}-ig_{\sigma,\mathrm{e}}u_0(\mathbf{r})\hat{a}\hat{\psi}_\sigma\tag{2.21}$$

which is a set of 4 independent equations – accounting for two excited states per ground state. The *adiabatic elimination* of these excited states then consists in considering the detunings $\Delta_{\sigma,\mathrm{e}}$ to be large against all the internal dynamics so that the kinetic and potential terms in the bracket above can be neglected [101]. This approximation is valid in the far-detuned regime, where we also have $d\hat{\psi}_{\sigma,\mathrm{e}}/dt=0$ since the excited states are not populated. We obtain

$$\hat{\psi}_{\sigma,\mathrm{e}}=\frac{g_{\sigma,\mathrm{e}}}{\Delta_{\sigma,\mathrm{e}}}u_0(\mathbf{r})\hat{a}\hat{\psi}_\sigma\tag{2.22}$$

which, after re-injection into equation (2.20) yields an effective Hamiltonian

$$\begin{aligned}\hat{H}_\mathrm{eff}=&\int d\mathbf{r}\hat{\psi}_1^\dagger(\mathbf{r})\left[-\frac{\nabla^2}{2m}+V_\mathrm{t}(\mathbf{r})\right]\hat{\psi}_1(\mathbf{r})+\int d\mathbf{r}\hat{\psi}_2^\dagger(\mathbf{r})\left[-\frac{\nabla^2}{2m}+V_\mathrm{t}(\mathbf{r})+\omega_{12}\right]\hat{\psi}_2(\mathbf{r})\\ &+\int d\mathbf{r}d\mathbf{r}'\hat{\psi}_2^\dagger(\mathbf{r}')\hat{\psi}_1^\dagger(\mathbf{r})V_\mathrm{p}(|\mathbf{r}-\mathbf{r}'|)\hat{\psi}_1(\mathbf{r})\hat{\psi}_2(\mathbf{r}')\\ &+\hat{a}^\dagger\hat{a}\left[\Delta_\mathrm{c}+\int d\mathbf{r}\sum_\sigma\sum_\mathrm{e}\frac{g_{\sigma,\mathrm{e}}^2}{\Delta_{\sigma,\mathrm{e}}}u_0^2(\mathbf{r})\hat{\psi}_\sigma^\dagger(\mathbf{r})\hat{\psi}_\sigma(\mathbf{r})\right].\end{aligned}\tag{2.23}$$

In addition, we slightly simplify the last term by considering that both ground states feature the same transition dipole matrix elements for the same transition [74]. For the D_1 transition we for example have $g_{1D_1}=g_{2D_1}=g_{D_1}$. In the same spirit, we have $\Delta_{1e}=\Delta_{2e}$ because of the relatively low Zeeman shift between the two considered ground states. In the end, the light-matter interaction part of the Hamiltonian now reads

$$\hat{H}_{\mathrm{lm}} = \hat{a}^\dagger \hat{a} \int d\mathbf{r} \left(\frac{g_{D_1}^2}{\Delta_{D_1}} + \frac{g_{D_2}^2}{\Delta_{D_2}} \right) u_0^2(\mathbf{r}) \hat{n}(\mathbf{r}) \tag{2.24}$$

with

$$\hat{n} = \sum_\sigma \hat{n}_\sigma = \sum_\sigma \hat{\psi}_\sigma^\dagger \hat{\psi}_\sigma \tag{2.25}$$

the total density operator.

The light matter interaction term results in a displacement of the cavity resonance frequency or *dispersive shift*, proportional to the spatial overlap between the atomic density and the cavity mode function. For a TEM_{00} with a cosine profile the integral can be evaluated and, equation (2.24) can equivalently be expressed with

$$\hat{H}_{\mathrm{lm}} = \Omega \hat{a}^\dagger \hat{a} \left(\frac{N}{2} + \hat{M} \right) \tag{2.26}$$

with $\Omega = \frac{g_{D_1}^2}{\Delta_{D_1}} + \frac{g_{D_2}^2}{\Delta_{D_2}}$ and $\hat{M}$ a collective displacement operator which originates from the lattice structure of the cavity field, imposing a modulation of the atomic density. In the case of a fast probe pulse, such as the ones we perform during transmission spectroscopy, the atomic density is considered to be frozen in time, and we take $\langle \hat{M} \rangle = 0$. However, for slower pulses the atoms may follow the imposed potential and thus lead to a displacement of the cavity resonance given by $\hat{M}$. This feedback mechanism between the atomic displacement and the shift of the cavity resonance relates to the field of optomechanics, and we dedicate the entirety of chapter 5 to the study of this effect.

For a frozen atomic density, we however get a simple expression of the dispersive shift with

$$\delta_{\mathrm{c}} = \Omega \frac{N}{2}. \tag{2.27}$$

Non-destructive dispersive shift measurement

The dispersive shift can be experimentally measured by transmission spectroscopy and comparing the location of the cavity resonance with the one without atoms. The difference between the two measurements is δ_{c}, relating the displaced cavity frequency to the total atom number. In the dispersive regime, such a measurement is weakly destructive in the narrow cavity limit [102], and we routinely use it to infer atom numbers before or after having performed other types of measurements. This contrasts with the usual, completely destructive, absorption imaging methods to measure atom numbers [103]. We present here some measurements performed on a unitary Fermi gas to assess their weakly destructive nature.

We study the destructivity of the cavity probe by performing transmission spectroscopy measurements multiple times on the same atomic cloud. We prepare atomic clouds comprising $N = 270 \times 10^3$ atoms and set the cavity length such that $\Delta_{D_2} = 2\pi \times 20\,\mathrm{GHz}$. We then probe the location of the dispersively shifted cavity resonance multiple times over 5 s on a single trapped cloud, and repeat the procedure for 10, 100, 250 and 500 probe pulses evenly spaced in time. The measured spectrum is presented in figure 2.5, with a fit of the position of each acquired

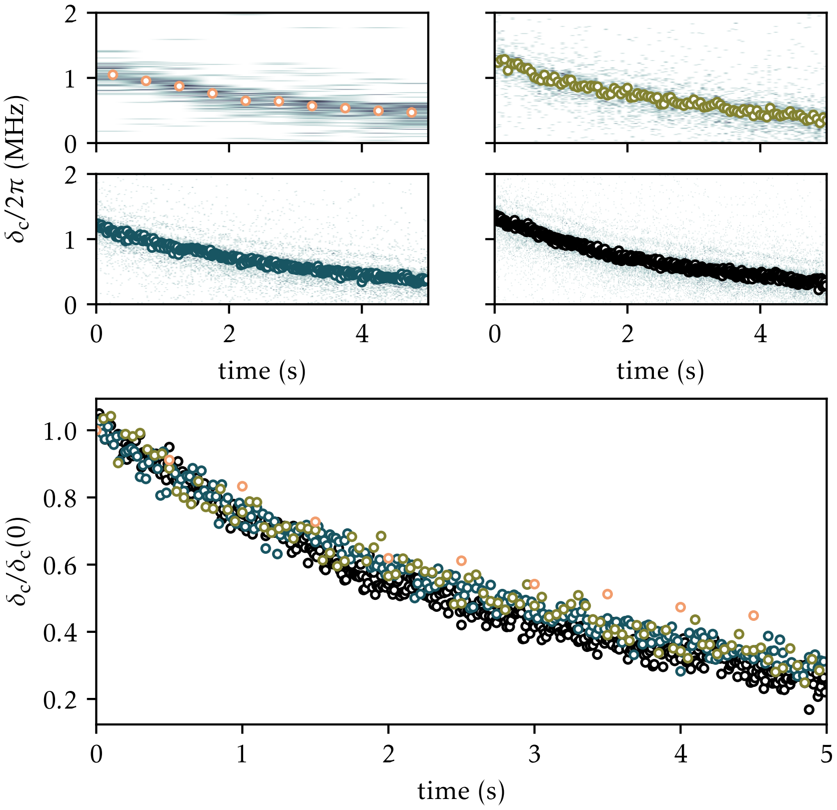

Figure 2.5: Measurement of the non destructivity of transmission spectroscopy in the dispersive regime. Top, each of the panel depicts a spectrum acquired over a single realization of the experiment. From top to bottom, left to right, we probed a single atomic cloud 10, 100, 250 and 500 times. The circles depict the extracted peak position of these spectra when fit with Lorentzian profiles.

spectrum. The presence of a clear resonance is obvious for each scan, with noise originating from the finite photon count. A weak ringing can be observed due to the sweep rate being comparable with the cavity linewidth.

By normalizing the location of the resonances with respect to the frequency of the first measurement of each series, to account for initial atom number variations between the different series, we observe a decrease of the dispersive shift by 7% for 500 pulses compared to 10. Translated into atom numbers, this amount to average losses of about 30 atoms per probing pulse, a good indication of a weakly destructive measurement. We note that the overall decaying trend is therefore due to the lifetime of the trapped unitary gas.

To further investigate the effects of transmission spectroscopy on the temperature of the cloud, we repeat the same measurement as above for 500 pulses, stopping after a variable number of probe pulses to evaluate the heating. We then transfer the cloud into a single-arm dipole trap

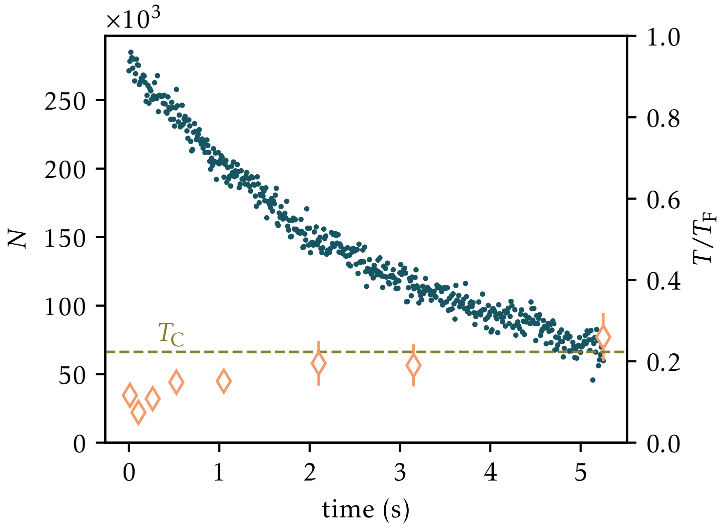

Figure 2.6: Heating and lifetime of the atomic ensemble with repeated probe pulses. We measure the heating of the atomic ensemble after 1, 10, 25, 50, 100, 200, 300 and 500 consecutive, evenly spaced, probe pulses (orange diamonds). The horizontal dashed line marks the location of the critical temperature for superfluidity at unitary for a trapped gas. The blue points depict the evolution of the atom number for a single cloud, probed 500 times over 5 s. A simple exponential decay fit to the data yields a time constant of 4.2 s, as a measure of the lifetime of the gas.

and measure its temperature.[2] The results are shown in figure 2.6 and even after 10 consecutive pulses we observe no detectable atom losses and measure $T/T_\mathrm{F} = 0.07(1)$, compatible with the temperature measured in the absence of probe. Remarkably, after 100 pulses we still measure a temperature of $T/T_\mathrm{F} = 0.15(1)$, still well below the superfluid critical temperature. This demonstrates that tens of repeated probes preserve the many-body physics of the Fermi gas for as long as 1 s, proving that the method is well suited to measure both fast and slow dynamical processes. In particular, it opens interesting applications to either probe non-equilibrium [104, 105] or transport [106] processes.

In the following chapters, we heavily employ these dispersive shift measurements to infer atom numbers on the very cloud we are working with, without disturbance.

2.2 Absorption imaging for the thermometry of unitary Fermi gases

While we have shown that the cavity grants a lot of information about the system, there still are a few observables to which cavity signals are almost completely insensitive to. Temperature is one of them.

In this section we now focus on the thermometry of the unitary Fermi to infer its degeneracy parameter T/T_F and prove that we work in the deeply degenerate regime $T \ll T_\mathrm{F}$, well below the critical temperature for superfluidity T_C [107, 108]. The problem of accurate thermometry for strongly interacting systems is notoriously difficult since exact descriptions only hold for ideal gases [47]. In the past several techniques have been employed, ranging from using another atomic species [109, 110] or internal state [111] to act as a thermometer, to fast, isentropic ramps of the interaction parameter to probe a non-interacting system [112]. Our first thermometry measurements and experimental observation of superfluidity were performed on spin-imblanced gases, fitting the wings of the majority component with a non-interacting profile [89, 92], and the method was described in details in reference [79]. It had the major drawback of relying on the usage of spin-imbalanced systems, thus requiring additional preparation steps and could not simply be performed after probing the balanced gases of interest, but rather on completely new atomic ensembles comprising fewer atoms.

---

[2] For this specific measurement, we used a thermometry technique explained in details in [79, 89].

Here we present a thermometry method which relies on fitting density profiles of in-situ, balanced unitary Fermi gases. As such, it is particularly convenient since it can for example be appended to any experimental sequence to measure the induced heating. Since the temperature of deeply degenerate unitary gases mainly affects the wings of the density profiles [47], the method relies on high signal-to-noise ratio of the measurements to infer the temperature. To increase the signal-to-noise ratio, we work with high-intensity absorption imaging, and we transfer the atomic cloud to a single arm of the crossed optical dipole trap prior to the measurement, in order to increase its apparent size for our resolution-limited imaging setup.

The section is organized as follows, we first introduce the working principles and calibrations for high-intensity imaging. In a second time we present the thermometry method, with which we use the measured equation of state of a unitary Fermi gas in order to infer the temperature. We apply the procedure to infer the temperature of the gas in the crossed optical dipole trap and in the cavity trap, showing that the first evaporative cooling stages already bring the system to the superfluid regime.

2.2.1 High-intensity absorption imaging

In-situ absorption imaging of dense clouds is often problematic due to low number of photons transmitted through the cloud, limiting the signal-to-noise ratio. We circumvent the issue by using high-intensity imaging pulses, with intensities comparable to the saturation intensity of D_2 transition of ^{6}Li, $I_{\text{sat}} = 2.54\,\text{mW.cm}^{-2}$. This implies that the intensity dependent term of the resonant cross-section σ cannot be neglected anymore and

$$\sigma = \frac{3\lambda^2}{2\pi}\frac{1}{1+I/I_{\text{sat}}} = \frac{\sigma_0}{1+I/I_{\text{sat}}}, \tag{2.28}$$

where I is the intensity of the imaging beam and lambda its wavelength. As a consequence, one cannot simply measure the relative variations of the beam intensity to infer the atomic optical density which follows from Beer-Lambert law $dI/dz = -n(x,y,z)\sigma I$, with n the atomic density and z the direction of propagation of the imaging pulse. Instead, the method relies on the absolute knowledge of the beam intensity, which has to be calibrated [103, 113, 114]. For high-intensity pulses, Beer-Lambert law yields [113]

$$\frac{\sigma}{\alpha}\int dz\, n(x,y,z) = -\ln\frac{I_{\text{t}}(x,y)}{I_{\text{i}}(x,y)} + \frac{I_{\text{i}}(x,y)-I_{\text{t}}(x,y)}{I_{\text{sat}}}, \tag{2.29}$$

with $\alpha > 1$ a calibration factor accounting for a reduction of the cross-section due to imperfect polarizations with respect to the quantization axis and the unresolved excited manifold. $n(x,y) = \int dz\, n(x,y,z)$ is the column density and $I_{\text{i}}(x,y)$ and $I_{\text{t}}(x,y)$ the incident and transmitted intensities respectively and are recorded by usual absorption imaging techniques. The computation of the integrated density therefore requires the knowledge of both α and $I_{\mathrm{i,t}}(x,y)/I_{\mathrm{sat}}$.

The approach we follow here is to calibrate I_{sat} in terms of detected counts per pixel on the imaging camera. Expressing the previous equation with counts per pixel on the sensor we have

$$\frac{\sigma}{\alpha}n(i,j) = -\ln\frac{C_{\mathrm{t}}(i,j)}{C_{\mathrm{i}}(i,j)} + \frac{C_{\mathrm{i}}(i,j) - C_{\mathrm{t}}(i,j)}{C_{\mathrm{sat}}}, \tag{2.30}$$

where the total counts measured by the pixel (i,j), $C(i,j)$, linearly depend on the intensity. To calibrate C_{sat}, we require the previous expression to yield values of $\mathrm{OD}(i,j) = \sigma n(i,j)/\alpha$ independent of the incident intensity, since the actual number of atoms should not depend on the imaging intensity.

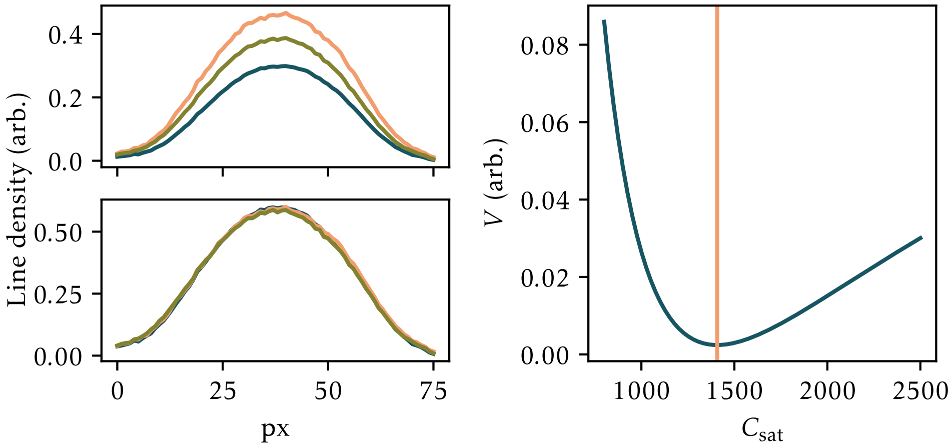

Figure 2.7: Calibration of the photon counts on the camera which correspond to the saturation intensity. Left, doubly integrated optical densities obtained by absorption imaging for three different imaging beam intensities. The top panel depicts the optical densities as we would compute them without the high-intensity correction in equation (2.30). The bottom one show the same data but with the correction term and C_{sat} extracted from the minimization of V, as shown by the right panel. For this specific dataset, we obtain $C_{\mathrm{sat}} = 1407$, with an imaging pulse duration of $4\,\mu$s.

The idea is to acquire absorption images of the cloud for imaging beam intensities spanning a significant range around I_{sat} and impose all the measured optical densities, for a fixed arbitrary value of α, to be equal. The problem thus amounts to minimizing the quantity [115]

$$V(C_{\mathrm{sat}}) = \sum_{i,j}\sum_{n}\left(\mathrm{OD}_n(i,j,C_{\mathrm{sat}}) - \langle \mathrm{OD}(i,j,C_{\mathrm{sat}})\rangle\right)^2 \tag{2.31}$$

where the average is taken over the entire dataset. We take care of performing the calibration on data taken for the same atom number, within a 2% range, so that we should actually expect the same OD. Having access to dispersive shift measurements prior to taking absorption images, we can assign a known atom number for each of the measured densities. Figure 2.7 summarizes the measurement. We note that we measure exactly the same density profiles even though the imaging beam intensity is varied from 0.5 to 2 I_{sat}.

The calibration of α follows directly. We simply fix it so that the atom numbers computed from $N = \int dxdydz\, n(x,y,z)$ matches the ones measured from the dispersive shifts, including the high-intensity correction to the optical density. For this dataset, we get $\alpha = 1.05$. This value is close to one, indicating that optical depumping is efficiently suppressed by using a closed transition at high magnetic fields.

2.2.2 Temperature measurement using the equation of state

The temperature measurement technique we use follows from the method presented in reference [116] and further detailed in the supplementary materials of [117]. It relies on the argument, that under the universal hypothesis, the density of the unitary gas n can be expressed as a universal function of $q = \mu\beta$ with μ the chemical potential and β the inverse temperature, uniquely determined by the degeneracy parameter T/T_{F}. The homogeneous density is given by

$$n = \frac{1}{\lambda_T^3} f_n(q) \tag{2.32}$$

where λ_T is the thermal de Broglie wavelength and $f_n(q)$ the universal phase-space density which has been accurately determined from the measurement of the equation of state of unitary Fermi gases with ^{6}Li [110, 118–120]. Given the knowledge of the equation of state one can then assign a temperature to a given homogeneous density. However, for a harmonically trapped system such as ours the density is spatially varying, and we have to resort to the local density approximation (LDA) and perform a spatial average of the atomic density over the trap. In the LDA, the space-dependent chemical potential is expressed with

$$\mu(x,y,z) = \mu_0 - V_{\mathrm{t}}(x,y,z), \tag{2.33}$$

μ_0 being its value at the center of the trap. The double integration, along y and z, of the space-dependent density in equation (2.32) then gives the line density

$$n(x) = A\left(\frac{T}{T_{\mathrm{F}}}\right)^{5/2} f_p\left(\left(\sqrt{\xi} - x^2/R_x^2\right)\frac{T_{\mathrm{F}}}{T}\right) \tag{2.34}$$

with

$$A = \frac{m}{2\pi\omega_y\omega_z\hbar^3} E_{\mathrm{F}}^{5/2} \tag{2.35}$$

$$f_p(q) = \int_{-\infty}^{q} du\, f_n(u). \tag{2.36}$$

ξ is the Bertsch parameter, E_{F} the Fermi energy and ω_i the trapping frequency of the harmonic dipole trap along the integrated direction $i = y,z$. R_x characterizes the typical extent of the cloud along the remaining direction. Equation (2.34) thus readily yields a fit function for measured in-situ line densities of unitary Fermi gases, where A, R_x and the degeneracy parameter T/T_{F} are left as fit parameters.

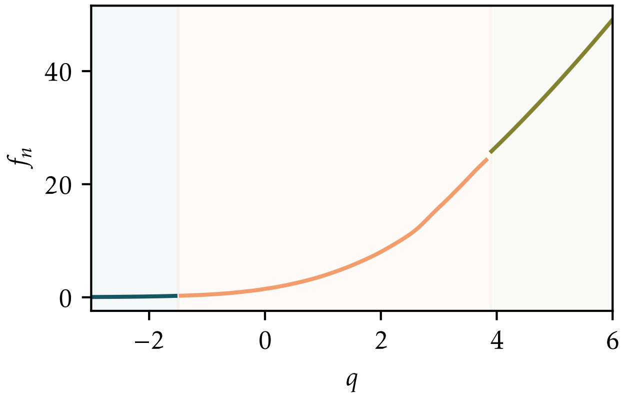

Figure 2.8: Evaluation of $f_n(q)$ in the three different regimes presented in the text and depicted by the three different colors. The blue region corresponds to where we apply the virial theorem. The orange one where use the measurements from [121] and the green one to where we use the large-q expansion of f_n.

Its evaluation however requires the knowledge of $f_p(q)$, which follows from $f_n(q)$ given equation (2.36). Reference [121] gives measurements of n/n_0 as a function of $q \in [-1.5, 3.9]$, with n_0 the density of a non-interacting Fermi gas. It is expressed with [47]

$$n_0(q) = -\frac{1}{\lambda_T^3}\mathrm{Li}_{3/2}(-e^q) \tag{2.37}$$

with Li_m the polylogarithm of order m, such that

$$f_n(q) = -\mathrm{Li}_{3/2}(-e^q)\frac{n}{n_0}(q) \tag{2.38}$$

can be directly evaluated for $q \in [-1.5, 3.9]$ using experimental data. Outside this range, we resort to convenient approximations to evaluate the function. For $q < -1.5$ we can apply a virial expansion of the equation of state which coefficients b_k are known up to fourth order with [110, 122]

$$f_n(q) = \sum_k k b_k e^{kq}. \tag{2.39}$$

For colder temperatures and $q > 3.9$ we have access to a large-q expansion of f_n with [123]

$$f_n(q) = \frac{(4\pi)^{3/2}}{3\pi^2}\left[\left(\frac{q}{\xi}\right)^{3/2} - \frac{\pi^4}{480}\left(\frac{3}{q}\right)^{5/2}\right], \tag{2.40}$$

which includes contributions due to thermal excitations of phonons. All in all, we show the general dependency of f_n on q in figure 2.8. We now turn to the examination of the density profiles acquired with high signal-to-noise ratio and yielding a correct atom number.

Temperature in the crossed dipole trap

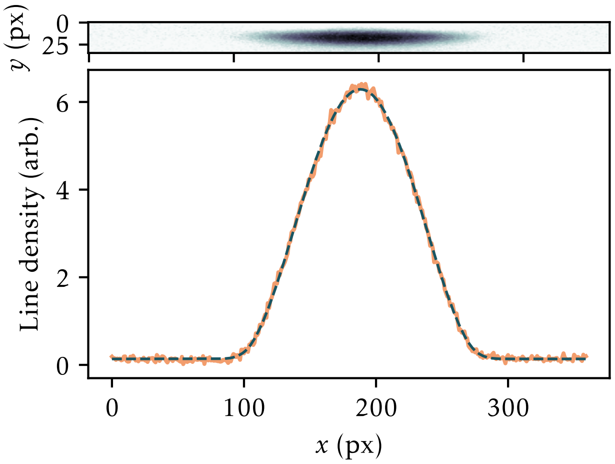

Figure 2.9: Temperature fitting from absorption imaging. Top, the measured optical density of a gas transferred in one arm of the crossed dipole trap. Bottom, the line density obtained by integrating the column density along the y direction (orange line), along with its fit to the density profile derived in the text (dashed blue line). The agreement is excellent and we get $T/T_\mathrm{F} = 0.071$.

We apply the technique on some example data, obtained for a gas at unitarity and after evaporation in the crossed optical dipole trap presented in section 1.2.3. We then ramp down the power of one of the arm to zero in 50 ms while increasing the power of the second one in order to stop the evaporation process. We then acquire absorption images of the cloud, taken after a time-of-flight of 200 μs, short against the typical trapping periods, and fit the measured line densities using equation (2.34). Figure 2.9 displays the result of the fit on a single atomic ensemble. We obtain excellent agreement with the model for all the data and measure $T/T_\mathrm{F} = 0.067 \pm 0.012$.

This result confirms that we work in the deeply degenerate regime, well below the superfluid phase transition temperature [45]. It also yields results very similar to what we obtained with our previous fitting method [79]. Throughout the manuscript, we infer the temperatures of strongly interacting gases prepared away from the unitary regime by relying on the measured temperature at unitarity.

Temperature in the cavity trap

In addition, we recently measured the temperature of the cloud held in the cavity dipole trap with a TEM_{01} mode structure. There, the cloud is actually split in two, with equal atomic population in each lobe of the trap. The right panel of figure 2.10 shows an in-situ absorption image of the cloud, which was off-centered on purpose on the imaging sensor in order to fully image the wings of the density profile. We apply the previous temperature measurement procedure after the second evaporation ramp in the cavity and before the usual transfer of the cloud into the crossed dipole trap. We fit the temperature of the clouds in each independent arm of the trap and average the results together for a single experimental run. The left panel of figure 2.10 shows the results, for varying setpoints of the final trap power and subsequent hold time in the trap.

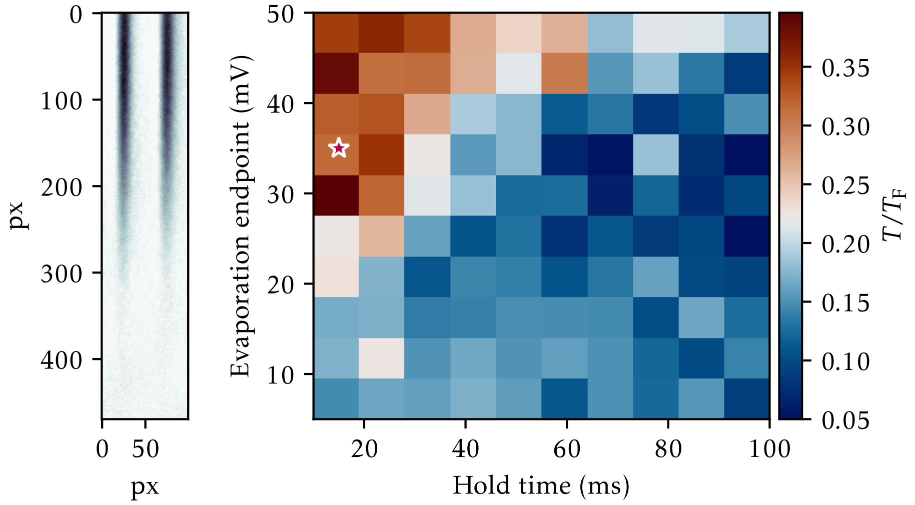

Figure 2.10: Temperature fitting in the TEM_{01} mode of the cavity trap. Left, example of an absorption image in the trap. The cloud is voluntarily off-centered on the camera sensor as to fully image its wings, essential for the fitting procedure. To fit the temperature we assume the cloud is symmetrical in the long direction. Right, temperature map of the gas in the cavity trap. The color scale is centered on $T/T_F = 0.223$, the critical temperature for a harmonically trapped unitary gas. The star shows the experimental parameters used in the rest of the manuscript, before transferring the cloud in the crossed trap. The final trap power is proportional to the evaporation setpoint in mV.

We observe that for either a deep evaporation or with sufficiently long hold time the gas becomes superfluid, with a temperature below the critical one. This feature is really promising as it suggests that one could get rid of the crossed dipole trap for future experiments, while still operating in the deeply degenerate regime. Using a TEM_{00} mode of the cavity instead would yield a single arm trap, inside which the atomic density would by construction maximally overlap with the cavity mode. This configuration would also free some optical accesses and reduce the total duration of the experimental runs by removing one evaporation ramp.

Part II

Quantum Optical Signatures of the Short Range Two-Body Correlation Function

Chapter 3

Two-body scattering for the many-body physics of interacting Fermi gases

> Nothing dramatic happens right on the Feshbach resonance.
>
> Ludovic Pricoupenko & Yvan Castin

Outline of the current chapter

3.1 Theoretical description of cold collisions **40**
- 3.1.1 Origin of the interaction 40
- 3.1.2 The two-body scattering problem 41
- 3.1.3 Feshbach resonances 47

3.2 Going from two- to many-body fermionic systems **51**
- 3.2.1 Energy spectrum of the interacting Fermi gas 51
- 3.2.2 BEC–BCS crossover 53
- 3.2.3 The two-body contact 56

In this chapter, we introduce and discuss key concepts and consequences of scattering theory, applied to the case of two colliding ^{6}Li atoms. Our goal here is twofold, we first want to develop a solid basis for the understanding of some phenomena ruling the collective behavior of our ultracold gases, stemming from purely two-body interactions. On the other hand, we also want to derive specific expressions which will prove to be useful for the intepretation of experimental results in the following chapters. To these ends, in a first part we focus on two-body scattering and introduce the concepts of scattering length and amplitude, Feshbach resonances and pseudopotential, starting from the description of the origin of the van der Waals interaction potential between two atoms. In a second part we show how these two-body concepts play a role in the many-body behavior of the strongly interacting gas, with the introduction of a simple model to derive its ground state energy. We then discuss the BEC–BCS crossover and unitary Fermi gas and their experimental realization, and conclude with the presentation of the two-body *s*-wave contact as a key universal quantity which formally links the two- and many-body regimes.

3.1 Theoretical description of cold collisions

3.1.1 Origin of the interaction

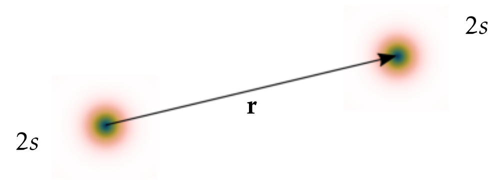

Figure 3.1: Two interacting ^{6}Li atoms in their electronic ground state $2s$, at a relative distance $\mathbf{r}$.

As a starting point for the upcoming discussion on the consequences of ultracold scattering, we begin with a brief presentation of the origin and physical description of interaction potentials between cold atoms. In this paragraph, and for the rest of this manuscript, we only consider two-body interactions between ^{6}Li atoms occupying two different pseudospin states, as described in section 1.2. Given the fermionic nature of ^{6}Li atoms, three- – or few- – body interactions are strongly suppressed by Pauli exclusion principle and therefore not taken into account here. We thus consider two atoms in the situation depicted in figure 3.1. Seen as ensembles of point charges, the Coulomb interaction energy between them reads

$$V_{int} = \sum_i \sum_j \frac{q_i q_j}{4\pi\epsilon_0 r_{ij}} \tag{3.1}$$

where each sum is taken over the charged components of one atom, with electric charge $q_{i,j}$. To simplify the description and considering that the two charge ensembles do not overlap, one can apply a multipole expansion of the previous expression and obtain a power series in $r = |\mathbf{r}|$ instead. The atoms being neutral, the monopole – or charge-charge – term of the interaction is simply zero and therefore one must consider the dipole-dipole interaction as the first non-trivial term of the expansion. The associated operator reads

$$\hat{V}_d = \frac{1}{4\pi\epsilon_0} \frac{\hat{\mathbf{d}}_a \cdot \hat{\mathbf{d}}_b - 3(\mathbf{e}_z \cdot \hat{\mathbf{d}}_a)(\mathbf{e}_z \cdot \hat{\mathbf{d}}_b)}{r^3} \tag{3.2}$$

where the a and b subscripts refer to the two atoms, with dipole moments $\hat{\mathbf{d}}_a = \sum_{i\in a} q_i(\hat{\mathbf{r}}_i - \hat{\mathbf{r}}_b)$ and $\hat{\mathbf{d}}_b$, where $\hat{\mathbf{r}}_{a,b}$ is the position of the nuclei of atom a, b and the sum is taken over the electrons.

In a perturbative treatment of the problem, the first order contribution of the dipole-dipole interaction potential to the total energy is zero due to the spherical symmetry of the electronic wavefunctions of atoms in the ground $2s$ states. However, at second order in $\hat{V}_d$, where one considers virtual excitations of the atoms, the contribution is in general nonzero and therefore the unperturbed energy is displaced by a quantity $\propto V_d^2$. The resulting long-range potential is usually represented by a van der Waals potential of the form

$$V_d(r) = -\frac{C_6}{r^6}, \tag{3.3}$$

where the C_6 coefficient can be computed from the estimation of matrix elements of $\hat{V}_d$ taken between the ground and excited electronic states. In the particular case of ^{6}Li, this calculation gives $C_6 \approx 1393$ atomic units [124][1]. This description only holds in the long-range limit, where the overlap of the two electronic clouds yields a negligible contribution. At shorter ranges, where the overlap is sizeable, the clouds repel each other and this effect is modeled by the addition of a soft core repulsive term $\propto 1/r^{12}$ to the interaction potential to yield the so-called Lennard-Jones potential.

In addition, one can define a specific length scale of the two-body problem: the range of the potential r_0, above which the effect of the potential might be neglected. The existence of a finite range for a potential is a consequence of the kinetic energy cost needed to localize a particle within one of its bound states, following the uncertainty principle. For a pair of atoms of reduced mass $\mu = m_1 m_2/(m_1 + m_2) = m/2$ interacting via the van der Waals potential described above, the range r_0 of the potential thus verifies

$$C_6/r_0^6 \leq \hbar^2/2\mu r_0^2. \tag{3.4}$$

This condition naturally leads to the definition of the range of the interaction potential, called in this case the van der Waals range

$$R_{\text{vdW}} = \frac{1}{2}\left(\frac{2\mu C_6}{\hbar^2}\right)^{1/4} \tag{3.5}$$

where the prefactor 1/2 comes from a more careful derivation of the range of the potential, for example done in paragraph 3.7.1 of reference [125]. For ^{6}Li, $R_{\text{vdW}} \approx 31\, a_0$ which is orders of magnitude smaller than the mean interparticle distance associated with the typical values of the ultracold gases densities $n^{-1/3} \approx 2000\, a_0$.

3.1.2 The two-body scattering problem

We now focus on the scattering properties of their collision under the effect of the potential. The main goal of this section is to derive the concept of *scattering length* which we will in the following part prove to be controllable via *Feshbach resonances*. We will also introduce a simpler version of the interaction potential for cold collisions also known as the *pseudopotential*, which faithfully reproduces the scattering properties of the two colliding atoms.

---

[1] For the reader unaccustomed with Hartree atomic units, this amounts to $C_6 \approx 1.33 \cdot 10^{-76}\,\text{J}{\cdot}\text{m}^6$.

Scattering amplitude from an operatorial approach

We start by considering two identical particles interacting via the previously defined long-range potential V_d. In the center of mass frame, their relative motion is described by the Hamiltonian

$$\hat{H} = \hat{K} + \hat{V}_d \tag{3.6}$$

with $\hat{K} = \hat{\mathbf{p}}^2/2\mu$ and $\mathbf{p}$ their relative momentum. In the case of an elastic collision with energy $E = \hbar^2 k^2/2\mu > V_d(\infty) = 0$, we seek to obtain an expression for the stationary scattering state ψ solution of

$$\hat{H}\psi = E\psi. \tag{3.7}$$

In operator notation, this amounts to solving

$$(E - \hat{K})\left|\psi\right\rangle = \hat{V}_d\left|\psi\right\rangle \tag{3.8}$$

which yields, for an incoming wavevector $\mathbf{k}$, the following Lippmann-Schwinger equation

$$\left|\psi_{\mathbf{k}}\right\rangle = |\mathbf{k}\rangle + \hat{G}_0^+\hat{V}_d\left|\psi_{\mathbf{k}}\right\rangle \tag{3.9}$$

where the first term corresponds to the free particle solution with $\langle\mathbf{r}|\mathbf{k}\rangle = e^{i\mathbf{k}\mathbf{r}}$ in position representation. The second term involves the Green operator $\hat{G}_0^+$ solution of equation (3.8) for an impulse source term, such that

$$(E - \hat{K})\hat{G}_0^+(E) = \mathbb{1}. \tag{3.10}$$

The chosen Green operator corresponds to an outgoing wave denoted by the superscript +, with

$$\hat{G}_0^+(E) = \frac{1}{E - \hat{K} + i\varepsilon}, \tag{3.11}$$

and

$$\langle\mathbf{r}'|\hat{G}_0^+(E)|\mathbf{r}\rangle = -\frac{\mu}{2\pi\hbar^2}\frac{e^{ik|\mathbf{r}'-\mathbf{r}|}}{|\mathbf{r}'-\mathbf{r}|}. \tag{3.12}$$

We can now turn to the implicit form of $\left|\psi_{\mathbf{k}}\right\rangle$ defined by equation (3.9) and show that it can be explicitly developed with

$$\begin{aligned}
\left|\psi_{\mathbf{k}}\right\rangle &= |\mathbf{k}\rangle + \hat{G}_0^+\hat{V}_d\left|\psi_{\mathbf{k}}\right\rangle \\
&= |\mathbf{k}\rangle + \hat{G}_0^+\hat{V}_d\left(|\mathbf{k}\rangle + \hat{G}_0^+\hat{V}_d\left|\psi_{\mathbf{k}}\right\rangle\right) \\
&= |\mathbf{k}\rangle + \hat{G}_0^+\hat{V}_d\left(|\mathbf{k}\rangle + \hat{G}_0^+\hat{V}_d\left(|\mathbf{k}\rangle + \ldots\right)\right) \\
&= |\mathbf{k}\rangle + \hat{G}_0^+\hat{T}(E)|\mathbf{k}\rangle
\end{aligned} \tag{3.13}$$

where we have introduced the transition operator $\hat{T}(E)$, which is from what precedes also a solution of a Lippmann-Schwinger equation

$$\hat{T} = \hat{V}_d + \hat{V}_d\hat{G}_0^+\hat{T}. \tag{3.14}$$

The matrix elements $\langle \mathbf{k}'|\hat{T}|\mathbf{k}\rangle$ therefore account for all the possible paths to couple states $|\mathbf{k}'\rangle$ and $|\mathbf{k}\rangle$ together under the effect of $\hat{V}_d$. In position space, with $\psi(r) = \langle \mathbf{r}|\psi_{\mathbf{k}}\rangle$, we write

$$\begin{aligned}\psi(r) &= e^{i\mathbf{kr}} + \langle \mathbf{r}|\hat{G}_0^+\hat{T}(E)|\mathbf{k}\rangle \\ &= e^{i\mathbf{kr}} + \int d\mathbf{r}' \frac{-\mu}{2\pi\hbar^2}\frac{e^{ik|\mathbf{r}'-\mathbf{r}|}}{|\mathbf{r}'-\mathbf{r}|}\langle \mathbf{r}'|\hat{T}(E)|\mathbf{k}\rangle\end{aligned} \tag{3.15}$$

where we have used the closure relation $\int d\mathbf{r}'|\mathbf{r}'\rangle\langle\mathbf{r}'| = \mathbb{1}$. In the limit $|\mathbf{r}| \to \infty$ and looking at the scattering center from the direction $\mathbf{n}$, we can expand the spherical wave contribution $|\mathbf{r}'-\mathbf{r}|^{-1}e^{ik|\mathbf{r}'-\mathbf{r}|} \sim r^{-1}e^{ikr}e^{-ik\mathbf{nr}'}$ so that

$$\begin{aligned}\psi(r) &= e^{i\mathbf{kr}} + \frac{-\mu}{2\pi\hbar^2}\frac{e^{ikr}}{r}\int d\mathbf{r}' e^{-ik\mathbf{nr}'}\langle \mathbf{r}'|\hat{T}(E)|\mathbf{k}\rangle \\ &= e^{i\mathbf{kr}} + \frac{-\mu}{2\pi\hbar^2}\langle k\mathbf{n}|\hat{T}(E)|\mathbf{k}\rangle\frac{e^{ikr}}{r} \\ &= e^{i\mathbf{kr}} + f(k,\theta)\frac{e^{ikr}}{r}\end{aligned} \tag{3.16}$$

where we have introduced the scattering amplitude $f(k,\theta)$ with θ the angle between $\mathbf{n}$ and the direction of the incoming wave along $\mathbf{k}$, under the assumption that the interaction potential is symmetrical. This last form of the scattering state ψ is quite powerful; a scattering state in the limit $|\mathbf{r}| \to \infty$ can be seen as the superposition of an incoming plane wave and a scattered spherical wave with an amplitude $f(k,\theta)$, a situation depicted by figure 3.2.

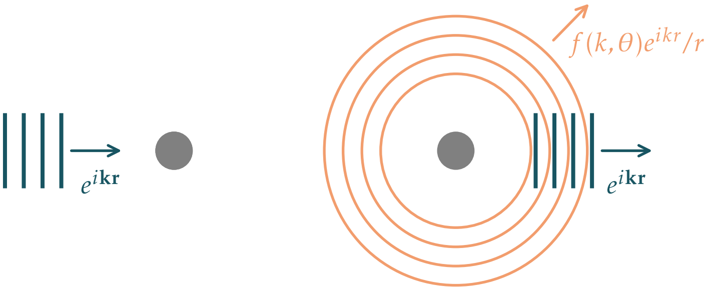

Figure 3.2: Modelization of two-body scattering. An incoming particle scatters off a scattering center and the resulting outgoing wavefunction is taken to be the sum of the transmitted and scattered ones.

Phase shifts from partial wave analysis

We will now focus on the calculation of the scattering amplitude in order to put it in a more convenient form to represent the low energy collisions typically occurring in our gases. To this end, we adopt an approach based on partial waves decomposition which closely follows the derivations found *e.g.* in chapter XVII of reference [126].

We consider a scattering state ψ solution of equation (3.7) which can be decomposed in the basis of spherical harmonics

$$\psi(r) = \sum_l A_l X_l(r) Y_{l,m}(\theta, \phi) \tag{3.17}$$

where the summation is taken over the possible scattering channels, or quantized values of the angular momentum l with projection m on the quantification axis, chosen to be aligned with the interatomic axis here. The radial functions X_l are solutions of

$$\frac{1}{r^2}\frac{d}{dr}\left(r^2\frac{dX_l}{dr}\right) + \left(k^2 - \frac{l(l+1)}{r^2} - \frac{2\mu}{\hbar^2}V_d(r)\right)X_l = 0 \tag{3.18}$$

which is obtained with the substitution $\hat{\mathbf{p}}^2 = -\hbar^2\nabla^2$ with spherical coordinates in equations (3.6) and (3.7), and for a given value of l. This spherical form of Schrödinger's equation leads to the definition of an effective interaction potential which now embeds the angular momentum of the scattering pair; we can write $V_{\text{eff}}(r) = V_d(r) + \hbar^2 l(l+1)/(2\mu r^2)$. The additional term leads to the existence of a repulsive "centrifugal" barrier going as $1/r^2$ for $l > 0$, which height has to be overcome in order for the scattering pair of atoms to feel the effect of V_d. For ^{6}Li and $l = 1$, this amounts to a potential step $V_0 \approx 8\,\text{mK}$, a temperature much larger than the typical ones featured in experiments. This is the reason why only $l = 0$ or s-wave scattering processes are considered in practice.

It can be shown, by neglecting the potential and centrifugal energies, that the functions X_l take the following asymptotic form

$$X_l \underset{r\to\infty}{\sim} \frac{1}{r}\left[(-1)^{l+1}e^{-ikr} + e^{2i\delta_l}e^{ikr}\right] \tag{3.19}$$

with the phases $\delta_l(k)$ obtained from the resolution of equation (3.18). From this asymptotic form one can already picture the motivation behind the current calculation; X_l represents the superposition of an incoming plane wave and an outgoing one, dephased by a quantity δ_l. Taking into account the contributions for each partial wave, we will in the end obtain an expression for ψ which only depends on the phases δ_l. Thus, these contain all the information about the scattering process under the potential V_d and therefore their calculation fully characterizes the interaction.

To obtain the expression for the scattering amplitude as a function of the phases δ_l, we compare the last line of equation (3.16) to equation (3.17) in which we inject the asymptotic form of the X_l functions. Doing so, we also take into account the symmetry of the problem about the interatomic axis and therefore drop the contribution of the azimuthal angle ϕ and impose $m = 0$. On one hand, equation (3.17) yields

$$\begin{aligned}\psi(r) \underset{r\to\infty}{\sim} &\frac{e^{-ikr}}{r}\sum_l (-1)^{l+1}A_l\sqrt{\frac{2l+1}{4\pi}}P_l(\cos\theta)\\ &+\frac{e^{ikr}}{r}\sum_l e^{i\delta_l}A_l\sqrt{\frac{2l+1}{4\pi}}P_l(\cos\theta)\end{aligned} \tag{3.20}$$

where we expressed the spherical harmonics $Y_{l,0}$ as functions of the Legendre polynomials P_l of order l. On the other hand, using the expansion of the plane wave $e^{i\mathbf{kr}}$ term of equation (3.16) in spherical harmonics, the equation now reads

$$\begin{aligned}\psi(r) \underset{r\to\infty}{\sim} & \frac{e^{-ikr}}{r}\frac{1}{2ik}\sum_l (-1)^{l+1}(2l+1)P_l(\cos\theta) \\ & + \frac{e^{ikr}}{r}\left(f(k,\theta) + \frac{1}{2ik}\sum_l (2l+1)P_l(\cos\theta)\right)\end{aligned} \tag{3.21}$$

and leads, with the identification of the e^{-ikr} and e^{ikr} terms, to

$$f(k,\theta) = \sum_l (2l+1)P_l(\cos\theta)f_l(k) \tag{3.22}$$

where the scattering amplitude for the scattering channel l verifies

$$\frac{1}{f_l(k)} = \frac{k}{\tan\delta_l(k)} - ik. \tag{3.23}$$

Scattering length and pseudo-potential

We now turn to scattering processes occurring in the $l = 0$ channel only, or s-wave scattering, with $k \to 0$. The scattering amplitude then only depends on the s-wave phase shift $\delta_0(k)$ which verifies[2]

$$\tan\delta_0(k) \underset{k\to 0}{=} ak \tag{3.24}$$

The proportionality coefficient a of the previous expression is called the s-wave scattering length defined as

$$a = -\lim_{k\to 0}\frac{\tan\delta_0(k)}{k} \tag{3.25}$$

and leads to an expansion of $f(k)$ in powers of k, usually written as

$$\frac{1}{f(k)} = -\frac{1}{a} - ik + \mathcal{O}(k^2). \tag{3.26}$$

From this last expression and the previous paragraph, we see the physical significance of the scattering length; it is the phase shift experienced by a scattered wave for $r \to \infty$ and $k \to 0$ and as such describes all the relevant aspects of the interaction. To convey a clearer picture of its effect, let's examine the asymptotic behavior of ψ. From what precedes, in the long-range region where $k^2 \gg V_d$, the scattering wavefunction takes the form

$$\begin{aligned}\psi(r) & \underset{r\to\infty}{\propto} \frac{1}{r}\left[-e^{-ikr} + e^{-2ika}e^{ikr}\right] \\ & \propto \frac{\sin(kr - ka)}{r}\end{aligned} \tag{3.27}$$

and thus features a node at $r = a$, for $a > 0$ and for all values of k in the limit $k \to 0$. This means that the potential can effectively be replaced by a hard-core sphere of radius a, which also forces

---

[2] The following result comes from the comparison of the asymptotic – taking $r \to 0$ and $r \to \infty$ – solutions of equation (3.18) for $l = 0$. The analytic connection of these solutions for small k yields the proportional scaling of $\tan\delta_0(k)$ with k.

$\psi(a,k) = 0$, and lead to the same physical behavior of the scattered wavefunctions for $r > a$.[3]

Since the scattering length fully describes the interaction process in the regime where we work, it is quite natural to build on the idea of substituting the "real" interaction potential with a simpler model, which yet still yields the same scattering properties. In fact, from what precedes, a given interaction potential might be replaced by another one provided that the model potential leads to the same scattering amplitude as defined by equation (3.26). We will take advantage of this to introduce a potential which indeed leads to the same value of the scattering length as V_d but also provides a very convenient short range form of the two-body scattering wavefunctions, useful for the rest of this chapter; the pseudo-potential.

Following the developments presented in reference [127], the pseudo-potential V_{p} is defined by its action on the two-body scattering state such that

$$V_{\mathrm{p}}\left[\psi(r)\right] = g\delta(r)\frac{\partial}{\partial r}\left[r\psi(r)\right]\Big|_{r=0} \tag{3.28}$$

with g a coupling constant which value is set to recover the same value of a as defined above. Under the effect of this potential one needs to re-evaluate the matrix elements $\langle k\mathbf{n}|\hat{T}_{\mathrm{p}}|\mathbf{k}\rangle$ of equation (3.16) in order to obtain the scattering amplitude, with $\hat{T}_{\mathrm{p}}$ the modified transition matrix accounting for the new pseudo-potential. It turns out – by construction – that the calculation leads to an exact and convenient expression for the scattering amplitude in the pseudo-potential

$$f(k) = -\frac{a}{1+ika} \tag{3.29}$$

where g was chosen so that $a = g\mu/2\pi\hbar^2$, so that the scattering amplitude corresponds exactly to the development of equation (3.26) to the first order in k. Moreover, the short range part of the two-body scattering state can be expressed as

$$\psi(r) \underset{r\to 0}{=} -\frac{a}{1+ika}\left[\frac{1}{r} - \frac{1}{a} + \mathcal{O}(r)\right], \tag{3.30}$$

sometimes put in a more compact form

$$\frac{d}{dr}\left[r\psi(r)\right]\Big|_{r=0} = -\frac{1}{a}\left[r\psi(r)\right]\Big|_{r=0} \tag{3.31}$$

where we have injected $f(k)$ in equation (3.16) and used $e^{ikr}/r \underset{r\to 0}{\sim} 1/r + ik + \mathcal{O}(r)$. These expressions of the two-body wavefunction realize the Bethe-Peierls boundary condition [128] and, as we will see in the next sections, will be central to address the *many-body* problem.

Scattering length and bound states of the interaction potential

In this paragraph, we very briefly present one important consequence of the definition of the scattering length in terms of the phase shift of the scattered wavefunction. According to Levinson's theorem [129] the s–wave, zero-energy, phase shift $\delta(0)_0$ features a direct dependence on the number of bound states n_{b} of the interaction potential with

$$\delta(0)_0 - \delta(\infty)_0 = (n_{\mathrm{b}} + \frac{1}{2})\pi. \tag{3.32}$$

---

[3] For $a < 0$ the situation is slightly different, the wavefunctions now feature a "virtual" node at a non-physical $r = a$, and the direct analogy with a different type of potential cannot be made anymore.

While $\delta(k)_0 - \delta(\infty)_0$ is in general complicated to explicitly evaluate, Levinson's theorem imposes that it must increase by a multiple of π when a new bound state "enters" the potential. Since the scattering length depends on $\tan(\delta(0)_0)$, one therefore expects it to diverge for every bound state entering the potential.[4] This explains the anomalously large value of the s−wave scattering length of ^{6}Li: there exists an almost-bound virtual state of interaction potential.

Its sign on the other hand comes from the relative location of the bound state with respect to the dissociation threshold. For a bound state of energy $E = \frac{\hbar^2 k^2}{2\mu}$, close to the dissociation threshold, equation (3.26) states that the scattering amplitude $f_0(k)$ features a pole at $k = i/a$. If the bound state is real, we obtain $E = -\frac{\hbar^2}{2\mu a} < 0$ which links its energy with the scattering length. The corresponding wavefunction $\psi(r) \sim e^{-r/a}/r$ must be normalizable which imposes $a > 0$. On the other hand if the bound state instead is virtual and lies on the other side of the dissociation threshold, the scattering length becomes negative.

3.1.3 Feshbach resonances

We present here a key tool of the study and manipulation of quantum gases; the Feshbach resonance. As a type of scattering resonance, Feshbach resonances correspond to a drastic modification of the scattering length a via the introduction of an important collisional phase shift δ during s-wave scattering events. In the case of Feshbach resonances, the mechanism which modifies the collisional phase shift relies on the near-resonant coupling of the initial scattering state with some other bound state. More so, they do not only modify the scattering length but, for reasons we will detail in what follows, also allow for its continuous tuning even to diverging values thus realizing different interaction regimes of the quantum gases.

We refer the reader interested to more in-depth derivations and discussions to one of the many great overviews of Feshbach resonances [39].

Two channels model

As briefly mentioned above, Feshbach resonances involve two collisions channel; an energetically accessible scattering *open* channel and a second, energetically forbidden, *closed* channel. In the presence of an external magnetic field, the two collision channels are realized by considering the different spin polarized configurations of the scattering pair, as depicted in figure 3.3. Ultracold ^{6}Li atoms typically collide in a spin triplet configuration so that the open channel corresponds to the associated interaction potential. The closed channel on the other hand corresponds to the van der Walls interaction potential for a spin singlet configuration, which is shifted towards higher energies compared to the open channel and therefore not accessible for the initial scattering pair.

Since pairs in different spin configurations feature different magnetic moments, a variation of the magnetic field induces a relative change of the energy of the two channels and doing so, bound states within the closed channel can be brought into resonance with scattering states of the open channel[5]. With the addition of a coupling mechanism between the two channels – which here takes the form of the hyperfine interaction, this description realizes a magnetic Feshbach resonance.

---

[4] This result is intimately linked to the fact that the transition matrix shares its poles with the scattering amplitude and that these poles correspond to bound states of the interaction potential – see *e.g.* chapter 12-d of reference [130] for a complete derivation.

[5] As we will see, the actual resonance condition differs slightly from this statement. The correction comes from the fact that the coupling between the two channels also displaces the bound state energies of the closed channel.

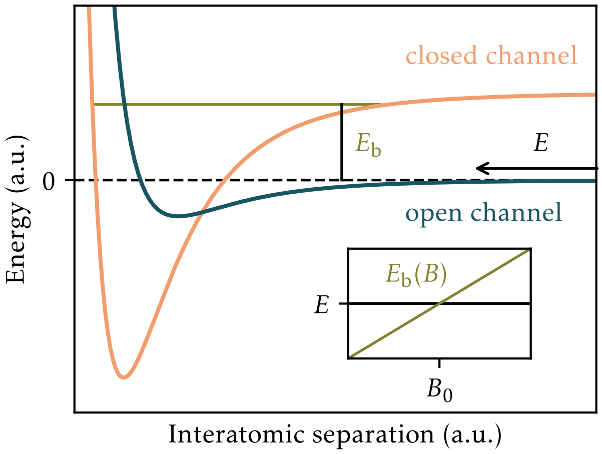

Figure 3.3: Two channel model for the Feshbach resonance. A pair of atoms with kinetic energy E scatters under the effect of a van der Waals interaction potential with a dissociation threshold lower than E; the open channel (solid blue curve). The closed channel (solid orange curve) features an inaccessible threshold and hosts a bound state of energy E_b, defined from the threshold of the open channel. This bound state can be brought in an out of resonance with the initial scattering state by tuning the external magnetic field B (inset). The resonance occurs at a magnetic field B_0, when the bound state energy matches E.

Our goal for this paragraph is to show how the coupling of a scattering state of the open channel to a bound state of the close channel induces a drastic modification of the scattering length. To this end, we consider the situation depicted in figure 3.3. More formally, we will follow the approach presented in [131] and only consider a single bound state contribution to the problem in what is known as the isolated resonance approximation.[6]

In the most general way, we write $\left|\psi_{\mathrm{o,c}}\right\rangle$ the components of the scattering pair wavefunction respectively projected in the open and closed channels. We include an operator $\hat{W}$ which couples the two channels so that the system satisfies the following coupled Schrödinger equations

$$(\hat{K} + \hat{V}_{\mathrm{o}})\left|\psi_{\mathrm{o}}\right\rangle + \hat{W}\left|\psi_{\mathrm{c}}\right\rangle = E\left|\psi_{\mathrm{o}}\right\rangle \tag{3.33}$$

$$(\hat{K} + \hat{V}_{\mathrm{c}})\left|\psi_{\mathrm{c}}\right\rangle + \hat{W}\left|\psi_{\mathrm{o}}\right\rangle = E\left|\psi_{\mathrm{c}}\right\rangle \tag{3.34}$$

where $\hat{V}_{\mathrm{o,c}}$ are the interaction potentials for the open and closed channels. In the absence of coupling, with $\hat{W} = 0$, the situation is exactly the one described by equation (3.8) for the open channel and $\left|\psi_{\mathrm{o}}\right\rangle = \left|\psi\right\rangle$ with the previous notations. In that case, since $\hat{V}_{\mathrm{c}}(\infty) > E$, the closed channel is not populated and $\left|\psi_{\mathrm{c}}\right\rangle = 0$. Therefore, using the same operatorial approach as earlier in the section, we can write

$$\left|\psi_{\mathrm{o}}\right\rangle = \left|\psi\right\rangle + \hat{G}_{\mathrm{o}}^{+}\hat{W}\left|\psi_{\mathrm{c}}\right\rangle \tag{3.35}$$

$$\left|\psi_{\mathrm{c}}\right\rangle = \hat{G}_{\mathrm{c}}^{+}\hat{W}\left|\psi_{\mathrm{o}}\right\rangle \tag{3.36}$$

---

[6] Accounting for the contribution of multiple other bound states is a tougher task which will not be dealt with here. In practice, the additional contributions are accounted for using multichannel quantum defect theory [132].

with the Green operators $\hat{G}^+_{\mathrm{o,c}}(E) = (E - \hat{K} - \hat{V}_{\mathrm{o,c}} + i\varepsilon)^{-1}$. The isolated resonance approximation consists in singling out the closed channel bound state of interest $\left|\psi_{\mathrm{b}}\right\rangle$ with energy E_{b} and disregarding all other bound state contributions to $\hat{G}^+_{\mathrm{c}}$ so that it can be put under the form of a single projector

$$\hat{G}^+_{\mathrm{c}}(E) = \frac{\left|\psi_{\mathrm{b}}\right\rangle\!\left\langle\psi_{\mathrm{b}}\right|}{E - E_{\mathrm{b}}}. \tag{3.37}$$

Its substitution into the previous system of equations yields

$$\left|\psi_{\mathrm{o}}\right\rangle = \left|\psi\right\rangle + \hat{G}^+_{\mathrm{o}}\hat{T}_{\mathrm{o}}\left|\psi\right\rangle \tag{3.38}$$

$$\left|\psi_{\mathrm{c}}\right\rangle = z\left|\psi_{\mathrm{b}}\right\rangle \tag{3.39}$$

where we have introduced

$$\hat{T}_{\mathrm{o}} = \frac{\hat{W}\left|\psi_{\mathrm{b}}\right\rangle\!\left\langle\psi_{\mathrm{b}}\right|\hat{W}}{E - E_{\mathrm{b}} - \left\langle\psi_{\mathrm{b}}\middle|\hat{W}\hat{G}^+_{\mathrm{o}}\hat{W}\middle|\psi_{\mathrm{b}}\right\rangle} \tag{3.40}$$

$$z = \frac{\left\langle\psi_{\mathrm{b}}\middle|\hat{W}\middle|\psi\right\rangle}{E - E_{\mathrm{b}} - \left\langle\psi_{\mathrm{b}}\middle|\hat{W}\hat{G}^+_{\mathrm{o}}\hat{W}\middle|\psi_{\mathrm{b}}\right\rangle}. \tag{3.41}$$

We see from equation (3.39) that we indeed find an expression for the closed channel wavefunction where only one bound state $\left|\psi_{\mathrm{b}}\right\rangle$ is populated. The problem is thus now reduced to scattering in a single channel, with the previously derived $\left|\psi\right\rangle$ acting as the incident state and a new transition operator $\hat{T}_{\mathrm{o}}$, as described by equation (3.38). The scattering amplitude is then proportional to the matrix element $\left\langle\psi_{\mathrm{b}}\middle|\hat{T}_{\mathrm{o}}\middle|\psi_{\mathrm{b}}\right\rangle$ which features a pole at $E = E_{\mathrm{b}} + \Delta$ with $\Delta = \left\langle\psi_{\mathrm{b}}\middle|\hat{W}\hat{G}^+_{\mathrm{o}}\hat{W}\middle|\psi_{\mathrm{b}}\right\rangle$.[7]

In the low energy and asymptotic limits, the first term of equation (3.38) will yield a phase shift of the scattered wavefunction leading to a "background" scattering length exactly given by equation (3.25), which we note a_{bg}. The "resonant" s-wave shift δ_{res} induced by the coupling between both channels can be put under the form [131]

$$\delta_{\mathrm{res}} = \arctan\left(-\frac{\Gamma/2}{E - E_{\mathrm{b}} - \Delta}\right) \tag{3.42}$$

with $\Gamma = 2\pi|\left\langle\psi_{\mathrm{b}}\middle|\hat{W}\middle|\psi\right\rangle|^2$. The associated resonant scattering length $a_{\mathrm{res}} = -\lim_{k\to 0}\frac{\tan\delta_{\mathrm{res}}(k)}{k}$ contributes to the total scattering length

$$\begin{aligned} a &= a_{\mathrm{bg}} + a_{\mathrm{res}} \\ &= a_{\mathrm{bg}} - \frac{\lim_{k\to 0}\Gamma/2k}{E_{\mathrm{b}} + \Delta}. \end{aligned} \tag{3.43}$$

Using the fact that in practice E_{b} can be tuned by a variation of an external magnetic field, the previous equation is often expressed as

$$a = a_{\mathrm{bg}}\left(1 - \frac{\Delta B}{B - B_0}\right) \tag{3.44}$$

---

[7] We see here that this resonance condition differs from the naive $E = E_{\mathrm{b}}$ guess by a quantity Δ which results from the coupling between the two channels.

with ΔB the magnetic width of the resonance and B_0 its position. Under this form, it appears clearly that the scattering length diverges at the position of the resonance, and changes sign when the resonance is crossed. In practice, provided that ΔB is large enough, Feshbach resonances thus offer a very convenient way of tuning the scattering length to almost arbitrary values. In the following paragraph, we will specialize in ^{6}Li and present the resonance we use in the experiment.

Feshbach resonances of ^{6}Li

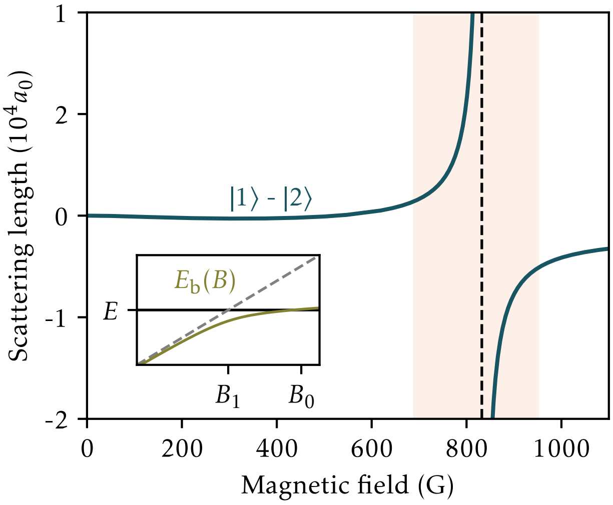

Figure 3.4: Broad Feshbach resonance of ^{6}Li (solid blue curve). The position B_0 of the resonance is depicted by the vertical dashed line. The shaded area shows the strong interaction region typically explored throughout this thesis. In inset, we show an updated and more precise version of the inset of figure 3.3. Because of its hyperfine coupling with the initial scattering state (horizontal solid line), the energy of the bound state[a] (solid green line) gets strongly displaced and *avoids* crossing the scattering state energy up until B_0. The point B_1 where it would have crossed in the absence of coupling is the location of another, way more narrow, Feshbach resonance [133]. It originates from the component of the singlet interaction potential with a zero nuclear spin projection, which thus do not couple to the scattering state via hyperfine interaction. Its energy is depicted by the oblique dashed line.

---

[a] The bound state in question is the last bound state $v = 38$ of the singlet interaction potential $^1\Sigma_g^+$ – with molecular notations defined in appendix D.

In the case of ^{6}Li, we present in figure 3.4 the Feshbach resonance for a pair of atoms populating the two lowest hyperfine ground states $|1\rangle$ and $|2\rangle$. The resonance condition occurs at $B_0 = 832.18(8)\,\mathrm{G}$ with a background scattering length $a_{\mathrm{bg}} = -1582(1)\,a_0$ and width $\Delta B = -262.3(3)\,\mathrm{G}$ [134]. These values are large with respect to other alkali atoms, for which a_{bg} is of the order of the range of the van der Walls interaction potential of $\sim 100\,a_0$ and with ΔB usually being several orders of magnitude lower.

The unusual case of Lithium is well explained by taking into consideration an almost bound state of its triplet potential, lying only at an energy of 300 kHz above the dissociation threshold of the potential, which is orders of magnitude lower than the typical binding energies in such potentials. From what we have seen with the discussion on bound states, the presence of this virtual state therefore produces an anomalously large and negative background scattering length. Had the triplet potential been just a fraction of a percent deeper, the virtual bound state would have entered the potential and yielded a positive background scattering length.

3.2 Going from two- to many-body fermionic systems

Having presented some properties of two-body ultracold scattering, we now show how one can put this knowledge to use in order to bridge the gap from *two* to *many* fermions systems. For a Fermi gas of density n, the typical length scale associated with interactions away from a Feshbach resonance is of the order of $a_{\mathrm{bg}} \sim R_{\mathrm{vdW}}$, much smaller than the average interparticle spacing $k_{\mathrm{F}}^{-1} \sim n^{-1/3}$ with k_{F} the Fermi wavevector: the gas is only weakly interacting. However, the situation drastically changes in the vicinity of a Feshbach resonance, by letting a diverge we can realize situations where $|a| \gg k_{\mathrm{F}}^{-1}$ thus entering the *strongly interacting* regime, where the consequences of two-body scattering lead to strong modifications of the many-body behavior. The strength of the interactions are usually characterized by the dimensionless parameter $(k_{\mathrm{F}}a)^{-1}$, and we accordingly label the strongly interacting regime the region where $(k_{\mathrm{F}}|a|)^{-1} < 1$.

One point of this strongly interacting regime is of particular interest; when $a \to \pm\infty$, $(k_{\mathrm{F}}|a|)^{-1} = 0$ and k_{F}^{-1} becomes the only relevant length scale as a drops out of the problem, making this limit universal. It realizes what is known as a *unitary* Fermi gas, a name which comes from the unitary properties of the two-body scattering matrix associated with a diverging scattering length. Such a gas features the strongest known interpaticle interactions and therefore is a perfect toy model for the study of strongly correlated systems [23, 24]. While the limit $a \to \pm\infty$ may seem problematic, we will see in the following paragraphs that all physical quantities behave smoothly when $(k_{\mathrm{F}}|a|)^{-1}$ explores the strongly interacting region.

We will first present a simple model based on two-body scattering to derive the energy spectrum of the (strongly) interacting Fermi gas, even in the presence of a diverging scattering length. In a second part, we will look in more details into what is known as the *BEC–BCS crossover* [45, 135] and how it is realized in practice by tuning the scattering length across the strongly interacting regime. Finally, we will introduce a quantity know as the *contact* which bridges the conceptual gap between two- and many-body systems, and defines universal thermodynamical relations.

3.2.1 Energy spectrum of the interacting Fermi gas

We will start our discussion on the energy spectrum of an interacting Fermi gas by reigniting the previous concern about the limit $a \to \pm\infty$. In a mean field approach, the contribution to the internal energy of the interparticle interactions is usually expressed as

$$\Delta E \propto g n_1 n_2 \tag{3.45}$$

with $n_{1,2}$ the number densities of each fermionic component. The sign of a directly rules the sign of the coupling $g = 4\pi\hbar^2 a/m$ and therefore controls the nature of the interactions. A positive scattering length leads to $\Delta E > 0$ and the interactions are labeled as repulsive since they tend to increase the gas internal energy, and correspondingly they are attractive for $a < 0$. This description obviously raises a question about the above mentioned unitary regime: what happens for $a = \pm\infty$? The issue lies in the expression of g which contradicts the universal hypothesis, the gas properties should only depend on k_F. Indeed, g diverges with diverging a and changes sign around the resonance which leads to a ill-defined nature of the interactions on the Feshbach resonance. Even though a more careful calculation of the second virial coefficient – intimately linked to the internal energy of the system – prevents the divergence of the internal energy when the Feshbach resonance is approached [136], the nature of the interactions on the resonance is still paradoxical.

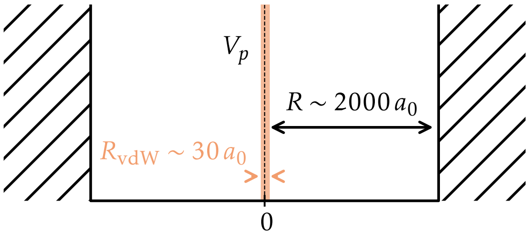

Figure 3.5: Two fermions scattering in a box. The horizontal axis represents the relative coordinate. The vertical dashed line represents the 0–range pseudopotential and the orange shaded area depicts the effective range of the van der Waals potential which leads to the same value of a as V_p. The hatched region corresponds to the boundary condition imposed by the $N-2$ remaining fermions.

We develop here a simple argument to tackle the above paradox. It is based on a description of a strongly interacting two-components Fermi gas which involves the scattering concepts presented in the last section. Doing so, we will also very conveniently derive the typical shapes of the two-body scattering wavefunctions in the strongly interacting regime $1 > (k_\mathrm{F}|a|)^{-1}$, which will prove useful in the next chapter. Our approach follows the arguments presented in [137]: out of a strongly interacting homogeneous Fermi gas comprising N particles, we isolate two fermions of opposite spins scattering under the influence of the pseudo-potential V_p described in section 3.1.2. The effect of the interaction of the scattering pair with the $N-2$ other particles of the gas is modeled by a spherical box of radius $R \approx n^{-1}$ with absorbing boundary conditions such that the two-body wavefunction ψ vanishes for $r = R$. A one dimensional sketch of the situation is depicted by figure 3.5.

As we have shown in the last section, the usage of the pseudopotential is equivalent to imposing the contact condition described by equation (3.31) at the origin and then solving the free Schrödinger equation everywhere else in the box. We consider the gas to have a total energy E and two particles to be scattering with energy $\epsilon = \hbar^2k^2/\mu > 0$ which verifies $E = N\epsilon/2$. By solving Schrödinger's equation, the reduced radial wavefunction $u(r) = r\psi(r)$ can be expressed as

$$u(r) \propto \sin(k(r-R)) \tag{3.46}$$

where we have imposed the boundary condition $u(R) = 0$. Applying the contact condition to $u(r)$ yields $\tan(kR) = ka$, which we can solve to obtain the energy spectrum of the gas as a function

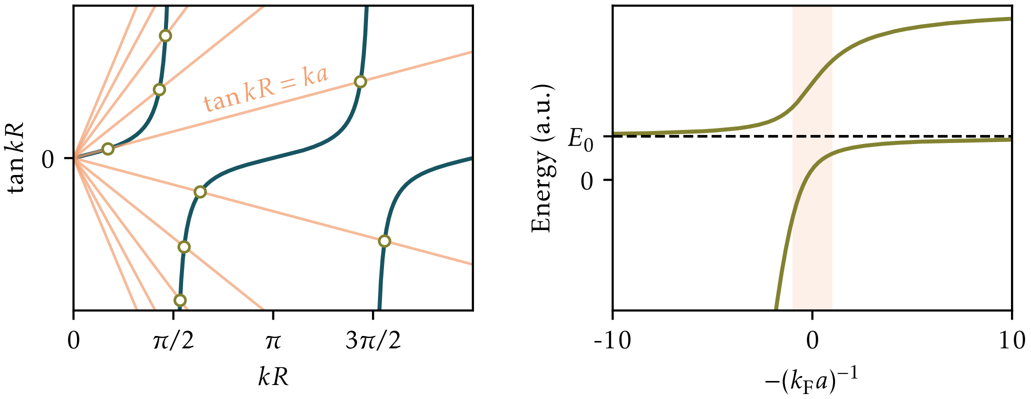

Figure 3.6: Energy spectrum of the interacting Fermi gas and its graphical derivation. Left panel, we show some the solutions of $\tan(kR) = ka$, for different values of a (orange lines). For a given value of a the curves intersect multiple times (circles) and result in the existence of multiple energy branches. Right panel, the energy branches predicted by the model. As a main result, the ground branch energy lies below the energy of a non-interacting Fermi gas E_0 (horizontal dashed line) for all values of a. The shaded area represents the values of $(k_\mathrm{F} a)^{-1}$ typically explored in this thesis.

of a. The graphical resolution of such an equation is depicted by the left panel of figure 3.6, where we see that there exists multiple solutions for a given a: the gas features multiple energy branches. To get a complete picture, one must also consider negative energies $E = -\hbar^2\kappa^2/\mu < 0$, for which we have $u(r) \propto \sinh(\kappa(r-R))$ and $\tanh(\kappa R) = \kappa a$ and which lead to the $E < 0$ branch of the right panel, connecting smoothly to the $E > 0$ part of the ground branch.

First and foremost, we notice that the energy of the ground branch lies below the energy of a non-interacting Fermi gas E_0, only crossing it when a changes sign around 0. This ensures that the interacting Fermi gas prepared in the ground branch is *always attractive*, no matter the sign of the scattering length. In addition, the smooth variations of the energies of the branches at the location of the Feshbach resonance indeed confirm that nothing dramatic happens, a fact which is also verified by looking at other thermodynamical quantities [137]. From the expressions for the wavefunctions obtained above, we calculate their shape for energies corresponding to the ground branch and scattering lengths spanning the strongly interacting regime, shown in figure 3.7.

3.2.2 BEC–BCS crossover

From the discussion on Feshbach resonances, the $a > 0$ region of the strongly interacting regime corresponds to a bound state of the closed channel becoming energetically accessible for a scattering pair, and therefore allows for atoms to bind in real space with binding energy $E = -\frac{\hbar^2}{2\mu a}$. The bosonic character of these fermion pairs and their ability to condense has imposed the name *BEC regime* for this interaction region.

When crossing over to the other side of the resonance, with $a < 0$, one can wonder what happens to the pairs since two-body scattering theory doesn't ensure the existence of bound

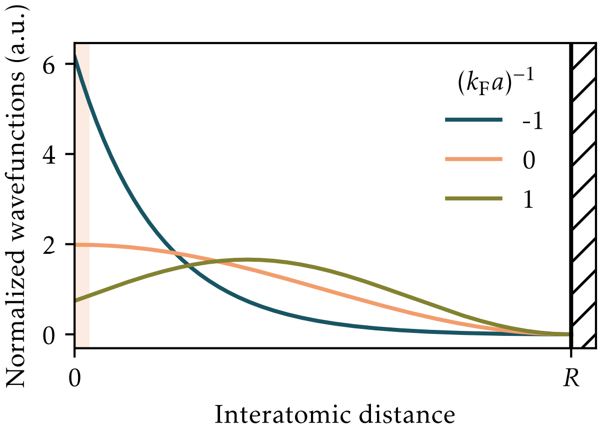

Figure 3.7: Two-body reduced wavefunctions for strongly interacting Fermi gases, for different values of the interaction parameter and corresponding energies in the ground branch of figure 3.6. Their short range behavior shows the expected $\propto r/a$ trend from the Bethe-Peierls boundary conditions. The shaded area corresponds again to the range of the van der Waals interaction potential, while the hatched area depicts the boundary conditions imposed by the many-body problem.

states in 3D for arbitrarily weak interactions. The solution lies in Cooper pairing as described by BCS theory [2, 138, 139]; in the presence of a Fermi sea, pairs of atoms with opposite momenta can form atop the Fermi sphere. Since the accessible density of state is effectively constant on the surface of the sphere, pairing is allowed to occur for arbitrarily low interaction strengths. In other words, pairing becomes a many-body effect stabilized by Pauli blocking, which was modelized by the box boundary conditions presented above. The ground state of the gas in this *BCS regime* is then a condensate of Cooper pairs.

By continuously tuning the interaction parameter thanks to a Feshbach resonance, we can smoothly follow the ground branch of figure 3.6. Doing so, we explore the so-called *BEC–BCS crossover* when the ground state of the system smoothly evolves from a condensate of weakly bound Cooper pairs on the BCS side of the resonance, to a condensate of tightly bound molecules on the BEC side. This smooth crossover regime was predicted by Eagles [141] and Leggett [142] and Nozières and Schmitt-Rink [143] for finite temperatures, and is now routinely explored in ultracold atoms experiments [144, 145]. One of the greatest success of the BEC–BCS crossover theory is the prediction of a superfluid phase of pairs, which persists for all values of the interaction parameter. We show the corresponding phase diagram in figure 3.8. In the following paragraphs, we will detail some interesting properties of the unitary Fermi gas, and we refer the reader to more complete articles for further details [45, 48, 49].

The unitary Fermi gas

As mentioned above, the inverse Fermi momentum being the only relevant length scale at unitarity, the properties of the unitary Fermi gas are independent of the nature of its constituents and become scale-invariant. As such, the current description can be applied to any fermionic

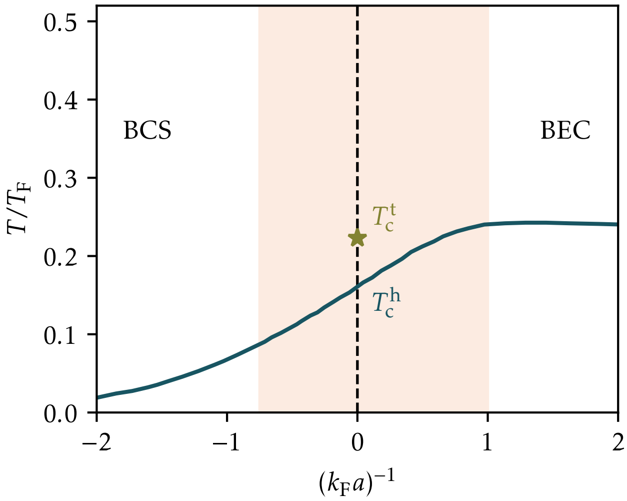

Figure 3.8: Critical temperatures for the superfluid phase transition in the BEC–BCS crossover. The solid blue curve represents the critical temperature for an homogeneous gas T_c^h [140] and the green star the measured critical temperature for a trapped gas at unitarity T_c^t [121]. Below these limits, the gas is in a superfluid state. The shaded area depicts the strongly interacting regime explored in this work.

systems featuring diverging scattering lengths; the most commonly cited examples apart from quantum gases being neutron stars and quark-gluon plasmas [46]. The only relevant associated energy scale in that regime is the Fermi energy

$$E_F = \frac{\hbar^2 k_F^2}{2m} \tag{3.47}$$

on which all thermodynamical quantities depend. For instance, the chemical potential μ_∞ at unitarity is directly proportional to E_F with

$$\mu_\infty = \xi^q E_F \tag{3.48}$$

where $q = 1$ for a homogeneous gas and $\frac{1}{2}$ for an harmonically trapped one[8]. The ratio between the chemical potential and the Fermi energy at unitarity $\xi = 0.370$ [134] is called the Bertsch parameter and is a universal function of the reduced temperature T/T_F, with $k_B T_F = E_F$.

In this regime, the size of the pairs is again of the order of the k_F^{-1}, and they condense to a superfluid state below a critical temperature

$$T_c = \alpha T_F \tag{3.49}$$

where $\alpha = 0.157(15)$ for a homogeneous system [110]. According to figure 3.8, this superfluid state persists for all interaction parameters below the critical temperature. Since the superfluid character of strongly interacting Fermi gases below T_c has been experimentally observed in various configurations all over the BEC–BCS crossover [146], we will in this thesis simply rely on temperature measurements as proofs of superfluidity. To access the gas temperature, we measure its equation of state through measurements of in-situ density profiles, as reported in section 2.2.

---

[8] The need to disambiguate between homogeneous and non-homogeneous gases – such as gases trapped in a harmonic potential – comes from the dependence on the position of all the relevant physical quantities for non-homogeneous gases. In practice, we work under the local density approximation and assume that these gases are still locally homogeneous in order to then average the relevant quantities over the trap volume. In this approximation, we usually write the position dependent chemical $\mu(r) = \mu_0 - V(r)$, with μ_0 the chemical potential taken at an arbitrary point and $V(r)$ the trapping potential.

3.2.3 The two-body contact

Here we define the concept of two-body *contact* $\mathcal{I}$, also sometimes referred to as *Tan's contact*. The concept originates from the seminal work done by Tan, who introduced the contact as a link between two- and many-body physics with a series of universal relations [147–149]. Its name stems from its definition as the universal short-range limit of the two-body correlation function; it effectively gives a measure of the likelihood of finding two particles "in contact".

We start by giving a definition of the contact which involves the two-body correlation function and therefore the results of section 3.1.2. In a second part, we then show how this previous microscopic definition can actually be linked to macroscopic thermodynamical quantities such as the internal energy of the gas. Finally, we will give a brief overview of the various experimental evidences, proving the universal relations.

Definition from two-body correlations

Following the approach presented in reference [150], we start with the generic form of the two-body density matrix found *e.g.* in chapter 2 of [151] for a generic many-fermions system at equilibrium

$$\rho(\mathbf{r}_{1,\alpha},\mathbf{r}_{2,\beta},\mathbf{r}_{3,\alpha},\mathbf{r}_{4,\beta}) = \left\langle \psi_\alpha^\dagger(\mathbf{r}_1)\psi_\beta^\dagger(\mathbf{r}_2)\psi_\beta(\mathbf{r}_4)\psi_\alpha(\mathbf{r}_3)\right\rangle \tag{3.50}$$

where $\psi_\sigma^\dagger(\mathbf{r})$ is the fermionic field operator in a second quantization form, creating a particle of spin σ at position $\mathbf{r}$. It can be equivalently expressed in terms of the many-body wave function $\Psi(\mathbf{r}_1,\ldots,\mathbf{r}_N)$ with

$$\rho(\mathbf{r}_{1,\alpha},\mathbf{r}_{2,\beta},\mathbf{r}_{3,\alpha},\mathbf{r}_{4,\beta}) = \frac{N^2}{4}\int d\mathbf{r}_5,\ldots,d\mathbf{r}_N \Psi^\dagger(\mathbf{r}_1,\ldots,\mathbf{r}_N)\Psi(\mathbf{r}_1,\ldots,\mathbf{r}_N). \tag{3.51}$$

In the following, we set $\mathbf{r}_2 = \mathbf{r}_4 = 0$ to recover the general structure of the two-body correlation function and our goal is to find a convenient form of the previous integral in the limit $\mathbf{r}_1, \mathbf{r}_3 \ll k_\mathrm{F}^{-1}$, effectively singling out a pair of atoms a short distance and integrating over the rest of the many-body coordinates. For more convenient notations, we replace the spin indices α, β by the hyperfine state labelling $1, 2$ and define $\mathbf{r} = \mathbf{r}_3$ and $\mathbf{r}' = \mathbf{r}_1$. Using the hermiticity of the density matrix, we decompose it on the basis of two-body wavefunctions [152]

$$\left\langle \psi_2^\dagger(\mathbf{r}')\psi_1^\dagger(0)\psi_1(0)\psi_2(\mathbf{r})\right\rangle = \sum_i n_i \phi_{12}^{i\dagger}(\mathbf{r}')\phi_{12}^i(\mathbf{r}). \tag{3.52}$$

The main assumption of the contact theory is then to state that in the limit $\mathbf{r} \to 0$ the relative parts of the two-body wavefunctions $\phi_{12}^i(\mathbf{r})$ are solely determined by short-range two-body physics and, under the influence of the pseudopotential, can be put under the form of equation (3.30) for $k \to 0$. We then have

$$\phi_{12}^i(\mathbf{r}) = B_i \psi(|\mathbf{r}|) \tag{3.53}$$

with ψ given by equation (3.30). We can therefore reformulate equation (3.52) in the limit $\mathbf{r}, \mathbf{r}' \ll k_\mathrm{F}^{-1}$ such that

$$\left\langle \psi_2^\dagger(\mathbf{r}')\psi_1^\dagger(0)\psi_1(0)\psi_2(\mathbf{r})\right\rangle = \sum_i A_i\left(\frac{1}{k_\mathrm{F}a}, \frac{T}{T_\mathrm{F}}\right)\left[\frac{1}{|\mathbf{r}'|} - \frac{1}{a}\right]\left[\frac{1}{|\mathbf{r}|} - \frac{1}{a}\right] \tag{3.54}$$

where the coefficients A_i contain the many-body contributions coming from the n_i eigenvalues and center-of-mass factors B_i of the ϕ_{12}^i functions. We explicitly let them depend on the interaction parameter and reduced temperature to highlight their many-body origin. By defining the average contact $\mathcal{C}$ with

$$\mathcal{C} = 16\pi^2 \sum_i A_i > 0 \tag{3.55}$$

we obtain the sought-after form of equation (3.50)

$$\left\langle \psi_2^\dagger(\mathbf{r}')\psi_1^\dagger(0)\psi_1(0)\psi_2(\mathbf{r})\right\rangle = \frac{1}{16\pi^2}\mathcal{C}\left[\frac{1}{|\mathbf{r}'|} - \frac{1}{a}\right]\left[\frac{1}{|\mathbf{r}|} - \frac{1}{a}\right], \tag{3.56}$$

which, with equation (3.51) in mind, confirms the role played by the contact; it is the proportionality factor which appears from the integration of $\Psi^\dagger\Psi$ after having let

$$\Psi(\mathbf{r}_1, \ldots, \mathbf{r}_N) \underset{r'=|\mathbf{r}_1-\mathbf{r}_2|\ll k_\mathrm{F}^{-1}}{\longrightarrow} \psi(r')\bar{\Psi}(\mathbf{R}, \mathbf{r}_3, \ldots, \mathbf{r}_N) \tag{3.57}$$

and integrating over all the remaining many-body coordinates. This leaves the short-range part of the two-body wavefunction $\psi(r')$ as the sole quantity controlling the behavior of ρ, which *a priori* was a purely many-body quantity.

To be consistent with the literature, we also introduce the integrated contact – or simply contact – $\mathcal{I}$ and $\mathcal{C}(\mathbf{R})$ the contact density as

$$\mathcal{I} = \int d\mathbf{R}\,\mathcal{C}(\mathbf{R}) = \Omega\mathcal{C}, \tag{3.58}$$

with Ω the total volume. The contact is an extensive quantity with a dimension corresponding to the inverse of a distance. We have shown its role as the parameter controlling the short-range behavior of the many-body physics, but it is also involved in other meaningful physical quantities. For instance, it gives the number of pairs[9] in a given volume of the gas: the left-hand side of equation 3.56 is nothing less, for $\mathbf{r} = \mathbf{r}'$, than the local density-density correlator $\left\langle n_1(\mathbf{R} + \frac{\mathbf{r}}{2})n_2(\mathbf{R} - \frac{\mathbf{r}}{2})\right\rangle$ with n_i the local density of spin i. In the limit $|\mathbf{r}| \ll a$, its integration over a sphere of radius s then yields the pair density

$$n_p(\mathbf{R}, s) = \frac{s}{4\pi}\mathcal{C}(\mathbf{R}). \tag{3.59}$$

Link to thermodynamics

In this paragraph, we want to show that the contact is involved in the thermodynamical properties of the system via a series of universal relations proved by Tan [148, 149]. These relations confirm that the contact is not only defined in some peculiar limits of density or momentum distributions but rather consists in a true thermodynamical quantity, conjugate to the inverse scattering length a^{-1}. This is expressed by the *adiabatic sweep theorem* which states

---

[9] Here, the term "pairs" relates to two atoms of opposite spins located at a relative distance $r \ll k_\mathrm{F}^{-1}$ and does *not* refer to Cooper pairs, which relative size can very well overcome the mean interparticle distance.

$$\frac{\partial E}{\partial(1/a)} = -\frac{\hbar^2 \mathcal{I}}{4\pi m} \tag{3.60}$$

with E the energy of the system. The theorem holds true as long as the interparticle distance remains larger than the range of the interaction potential and does so for any state at equilibrium, hence its universal label. Its derivation involves the Hellmann-Feynman theorem which links the variation of energy with the Hamiltonian of the system

$$\frac{\partial E}{\partial a} = \left\langle \frac{\partial \hat{H}}{\partial a} \right\rangle, \tag{3.61}$$

where the right-hand side can be evaluated in several ways [150, 152, 153] which all involve the calculation of terms of the form $\int d\mathbf{r}_1, \ldots, d\mathbf{r}_N V(|\mathbf{r}' - \mathbf{r}|)\Psi^\dagger\Psi$, making a direct connection with the previous paragraph.

Experimental measurements

We now turn to actual experimental verifications of the contact theory and present here some of the measurements performed in the past years which verified the universal relations presented above.

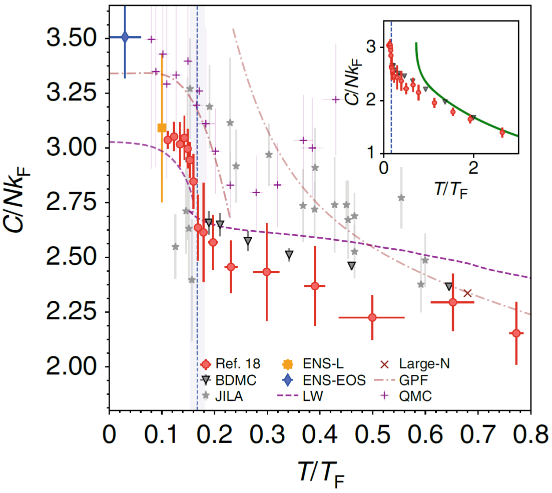

Figure 3.9: Variation of the contact of unitary Fermi gases with the temperature. The figure is reproduced from [154] and the datasets correspond to references therein.

The universality of the contact was experimentally demonstrated by the Jin group with a degenerate gas of ^{40}K [155]. They did so by comparing three different types of measurements as a function of the interaction parameter $(k_F a)^{-1}$ close to a Feshbach resonance. Two of the methods relied on measuring the tail of the momentum distributions which depends on the contact via [147]

$$n_\sigma(\mathbf{k}) \to \frac{\mathcal{I}}{k^4}, \tag{3.62}$$

while the third one was performed by means of radiofrequency spectroscopy, where the transfer rate of atoms between hyperfine spin states is directly linked to the contact [156]. In addition, and in the same article, they demonstrated the adiabatic sweep theorem given by equation (3.60). Radiofrequency spectroscopy was more recently employed by the Sagi group to measure the contact in strongly interacting Fermi gases, this time delving deeper on the BEC side of a Feshbach resonance [157]. Similar results obtained with a completely different technique relying on the measurement of the dynamic structure factor of an interacting gas of ^{6}Li by the Vale group [158] have shown the same scaling of the contact against interaction parameter, with the universality of the contact appearing in the high-energy tail of the structure factor [159, 160].

In figure 3.9 we show measurements of the variations of the contact for unitary Fermi gases with temperature, as presented by the Zwierlein group with their own work performed with radiofrequency spectroscopy [154]. It should be noted that the same year, the Vale group published a similar figure in which their data show an almost identical trend [161], again highlighting the variety of physical quantities depending on the contact. In chapter 5 we present yet another object which explicitly depends on the contact: the static density response of our strongly interacting gas.

As an outlook for the upcoming chapter, we briefly mention the indirect work performed by the Hulet group to measure the contact. Using bound-to-bound spectroscopy they measured the closed channel population of a gas of ^{6}Li when crossing over a Feshbach resonance [162], and in a later analysis of their data Werner, Tarruell and Castin could extract the contact from that measured population [163]. Our experiment operates in a very similar regime, with one major difference. The Hulet group measured the population of the closed channel by driving a transition from a bound state of the interaction potential to an excited molecular state. Our work on photoassocaition spectroscopy on the other hand addressed a free-to-bound transition, between scattering pairs of atoms and excited molecular state. Similarly, this allowed us to measure the contact.

Chapter 4

Fermionic pair-polaritons, magnifiers for two-body correlations

> A diatomic molecule is a molecule with one atom too many.
>
> Arthur Schawlow

Outline of the current chapter

4.1 From two interacting dipoles to a photoassociated pair **62**
4.1.1 Interacting dipoles 62
4.1.2 Molecular spectroscopy 64
4.1.3 The case of $^6\mathrm{Li}_2$ 66
4.2 Observation of strong light-matter coupling on photoassociation transitions **67**
4.2.1 Experimenta scheme 67
4.2.2 Mapping out photoassociation transitions close to dissociation limits 68
4.3 Many-body physics from vacuum Rabi splitting **70**
4.3.1 Rabi frequency of pairs coupled to light 71
4.3.2 Many-body physics from the optical spectrum 74
4.3.3 Continuous measurement of the two-body contact 77

In this chapter, we present our study of fermionic pairs of atoms coupled to light in a high-finesse cavity. The chapter closely follows the results reported in [164].

The starting point for the project was the observation of a set of matter-like excitations strongly coupled to the cavity field as introduced in section 2.1.2 and which correspond to none of the well-known ^{6}Li transitions. Instead, these extra lines correspond to photoassication transitions, for which a pair of atoms collectively absorbs a photon to form an excited molecule [165, 166]. Two-body transitions to excited molecular states were studied in details in cold atomic gases, employed as a purely spectroscopic tool to accurately determine the shape of molecular potentials and wavefunctions [167, 168], or as we discussed in the last part of the previous chapter to measure the closed channel fraction of Feshbach molecules of ^{6}Li in the BEC-BCS crossover [162], which has been linked to the contact [163]. Photoassociation also offers interesting perspectives for the field of ultracold chemistry, allowing for the direct creation of ground state molecules by robust control of the decay channels of excited photoassociated pairs [169, 170]. While coherent Rabi oscillations on ultra-narrow photoassociation transitions have been observed in weakly interacting gases of two-electron atoms [171, 172], our experiment brings photoassociation in the strong coupling regime, where the interaction between photons and pairs overcomes all dissipative processes. In this regime, the universal properties of the short-distance pair correlations of the quantum gas get imprinted onto the optical spectrum.

The chapter is organized as follows. In a first part, we explain the mechanisms behind photoassociation, from its origin with dipole-dipole interactions to its use as a spectroscopic tool by introducing some molecular spectroscopy concepts. We then present the performed experiments with a strongly interacting Fermi gas in as high-finesse cavity and interpret our measurements in terms of the two-body contact, which proves the influence of many-body physics in the measured optical spectra. Finally, we show how the coupling to photoassociation transitions, combined with the weakly destructive nature of cavity transmission spectroscopy as presented in chapter 2, might be harnessed to perform dynamical measurements of pair correlations.

4.1 From two interacting dipoles to a photoassociated pair

In this section, we aim at conveying an intuitive picture for two-body photoassociation, taking the example of two colliding ^{6}Li atoms. Starting from the dipole term of the multipole expansion of the interaction potential for two colliding atoms presented in section 3.1.1, we derive the characteristic $-C_3/r^3$ long-range shape of the interaction potential for a pair of atoms sharing one excitation. We then introduce some molecular spectroscopy concepts such as the Franck-Condon principle, which determines the probability for a pair of atoms to undergo a photoassociation transition and which will be a central point to the physical interpretations made later in this chapter. Finally, we turn to the case of ^{6}Li and detail the interaction potentials addressed by our experiment.

4.1.1 Interacting dipoles

We consider a pair of ^{6}Li atoms in the situation depicted by figure 4.1. We recall the dipole interaction introduced in chapter 3 under the Born-Oppenheimer approximation and in the limit where the distance r between the two dipoles is much larger than their respective size: $r \gg r_{a,b}$

$$\hat{V}_d = \frac{1}{4\pi\epsilon_0} \frac{\hat{\mathbf{d}}_a \cdot \hat{\mathbf{d}}_b - 3(\mathbf{e}_z \cdot \hat{\mathbf{d}}_a)(\mathbf{e}_z \cdot \hat{\mathbf{d}}_b)}{r^3} \tag{4.1}$$

with the same notations. The difference with the previous chapter now consists in the state basis the $\hat{V}_d$ operator acts on, where one of the two atoms is electronically excited to a $2p$ state *i.e.* with orbital angular momentum $|\mathbf{l}_\alpha| = l_\alpha = 1$, the subscript α denoting either atom a or b. Taking the atom b to be initially excited, we note $|l_a\lambda_a\rangle \otimes |l_b\lambda_b\rangle = |l_a\lambda_a, l_b\lambda_b\rangle = |00, 1\lambda_b\rangle$ the initial wavefunction. Here λ_α is the projection of $\mathbf{l}_\alpha$ on the molecular axis. In this configuration one can show at the first order of the perturbation, *e.g.* following the complement $\mathrm{C_{XI}}$ of reference [173],

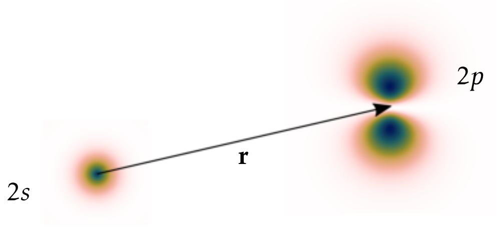

Figure 4.1: Representation of a ^{6}Li atom in its electronic ground state $1s^2 2s^1$ (here $2s$) interacting with another which valence electron is excited to a $2p$ orbital, similarly to what is realized in our experiments. They are separated by a distance r.

that

$$\langle 1\lambda_a, 00|\, \hat{V}_d \,|00, 1\lambda_b\rangle \propto \frac{1}{r^3} \tag{4.2}$$

are the only non-zero matrix elements of $\hat{V}_d$ for $\lambda_a = \lambda_b$. The invariance by rotation around $\mathbf{e}_z$ of the dipole-dipole interaction potential ensures that the projection of the total orbital angular momentum on the molecular axis $\Lambda = \lambda_a + \lambda_b$ is conserved[1] or equivalently that $[\hat{V}_d, \hat{\Lambda}] = 0$. This last observation leads to the expression of $\hat{V}_d$ with a block diagonal structure composed by three 2×2 matrices, one for each possible value of Λ

$$\hat{V}_{d,\Lambda} = C_3 k_\Lambda \begin{pmatrix} 0 & \frac{1}{r^3} \\ \frac{1}{r^3} & 0 \end{pmatrix} \tag{4.3}$$

with $k_\Lambda = 1$ for $|\Lambda| = 1$ or -2 for $\Lambda = 0$. The C_3 coefficient is directly proportional to the $2p$ state radiative linewidth Γ,[2] and emerges from the evaluation of single atom matrix elements of the form $\langle 10|\mathbf{e}_z \cdot \hat{\mathbf{d}}|00\rangle$ in equation (4.2).

The diagonalization of the $\hat{V}_{d,\Lambda}$ matrices yields a set of eigenenergies with typical C_3/r^3 scaling, the sign of which determines if the resulting potential is attractive or repulsive. For the process of photoassociation, we are only interested in the attractive ones and will therefore disregard repulsive molecular potentials for what follows.[3]

The previous calculation only considered a simple version of the interaction Hamiltonian – limited to the electrostatic interactions – to derive the typical shape of the molecular interaction potential. In practice, to obtain the exact shape of the interaction potential, one would need to account for all the possible degrees of freedom of the complex molecular system in the Hamiltonian $\hat{H}_m$. For example, following reference [174], this results in the addition of extra terms

$$\hat{H}_m = \hat{H}_{SL} + \hat{H}_R + \hat{H}_C + \hat{H}_{SR} + \hat{H}_{CR} + \hat{H}_{SS} + \ldots \tag{4.4}$$

which here describe spin-orbit coupling, rotational energy, centrifugal distortion, spin-rotation coupling, orbit-rotation coupling and spin-spin coupling respectively. In reality however, one can take advantage of fact that the energy scales associated with each of these terms remain small with respect to the electrostatic potential at short distances to neglect them to derive the general shape of the potential. One must nevertheless keep in mind that they can lead to coupling and mixing between different potentials, and thus to drastic changes in the computed distribution of bound states within a given potential.

---

[1] This assertion only holds true in the absence of other interaction terms of the molecular Hamiltonian, for instance taking spin-orbit coupling into account leads to a ill-defined value of Λ. This relates to the choice of the proper Hund's case to describe the interaction, which will not be discussed here but which is extensively discussed in textbooks [174].

[2] This direct connection of the strength of the molecular interaction potential with the atomic radiative linewidth has been used, *e.g.* for ^{6}Li in [175], to accurately measure linewidths from measurements of the molecular spectra.

[3] One should note, however, that repulsive potentials can be of interest for some applications. For example, they are used in the scope of optical shielding to control the spontaneous decay of molecules [176].

We can take the example of the next leading order term, the spin-orbit coupling interaction, which takes the form $\hat{H}_{SL} \propto \mathbf{L} \cdot \mathbf{S}$ with $\mathbf{S} = \mathbf{s}_a + \mathbf{s}_b$ the total spin vector and $\mathbf{L} = \mathbf{l}_a + \mathbf{l}_b$. For ^{6}Li, this term leads to an energy contribution of the order of 10 GHz, which can be neglected compared with the ~ 100 THz electrostatic interaction at short ranges. However, in the long range limit, where the dipole-dipole interaction becomes increasingly small, the spin-orbit coupling interaction dominates and leads to the fine splitting of the asymptotic branch of the interaction potential. This behavior is well reproduced by the Movre-Pichler model [166] which explicitly includes molecular spin-orbit coupling on top of the dipole-dipole interaction.

4.1.2 Molecular spectroscopy

In cold atoms experiments, photoassociation involves the transition of a pair of atoms to a bound state of an excited molecular potential. Experimentally, this is done shining a laser beam frequency detuned from the dissociation limit of the molecular potentials. When the process is resonant with a bound molecular state molecular formation may occur, and is typically accompanied by consequent observed trap losses: either the molecule decays to a bound state of its ground state potential or the pair dissociates with enough kinetic energy for the two free atoms to leave the trap. In this section, we present key concepts for the understanding of the photoassociation in the scope of molecular spectroscopy. In appendix D we give the definitions of the molecular term symbols used to label adiabatic in the rest of the chapter.

Franck-Condon principle

The transition dipole moments ruling photoassociation transitions are directly proportional to a quantity called the Franck-Condon factor $|\langle e|g\rangle|^2$ [166] which quantifies the overlap of the molecular ground and excited state radial wavefunctions, $|g\rangle$ and $|e\rangle$ respectively. This principle is illustrated by figure 4.2 where we clearly see that the role played by the oscillatory nature of bound and excited state wavefunctions in the determination of transition probabilities.[4]

At short distances, rapidly oscillating bound state wavefunctions lead to a vanishingly small transition matrix element and therefore the Franck-Condon factor is mainly determined by the contribution near the last lobe of excited wavefunctions, where they can be very accurately modeled by Airy functions [166]. For long range bound states lying close to the dissociation limit, the typical radius where the last lobe of the wavefunctions is located is similar to the classical outer turning point of the potential, and therefore the Condon radius – at which the photoassociation laser photons are resonant with the $|g\rangle \rightarrow |e\rangle$ transition – is also close to the classical outer turning point.

These considerations make photoassociation a prime candidate to investigate pair correlations in the ground state: due to the small relative values of R_C compared with typical interparticle distances in cold gases, systems exhibiting strong short-range correlations feature a higher coupling to photoassociation transitions as seen in studies of pair correlations [162, 178–181].

---

[4] In addition, a more precise evaluation of the Franck-Condon factor with the so-called reflection approximation [177] shows a systematic decreasing trend with decreasing values of R_C, as a consequence of the shape of the potentials. This decrease is responsible for the observed weakening of photoassociation signals in spectroscopic studies with increasing binding energies.

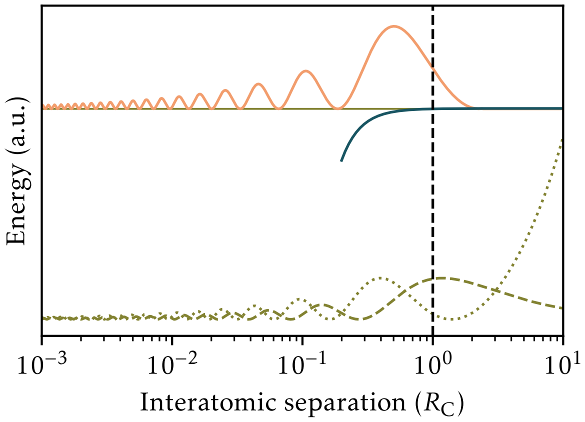

Figure 4.2: Illustration of the Franck-Condon principle. The probability of driving a transition between a ground scattering state (not shown here) and a bound excited molecular state (olive horizontal line) is proportional to the integral overlap of the corresponding wavefunctions. Here, since the excited state wavefunction goes to zero away from the potential and oscillates quickly at short distances, the only relevant point to consider is the so-called Condon point R_C (black dashed line) where it features a prominent lobe. Two possible scattering wavefunctions in the ground state are represented, one maximizes the transition probability due to having a maximum close to R_C (olive dashed line) while the other results in a vanishing transition matrix element due to the presence of a node close to R_C (olive dotted line). The solid blue line depicts a $1/r^3$ potential around R_C.

However, without strong light-matter coupling, performing these measurements has been limited to the investigation of incoherent processes.

Bound states spectroscopy close to the dissociation limit

Close to the dissociation limit where the interaction potentials can be approximated with $D - C_n/r^n$ with D the dissociation limit and n the order of the long range scaling of the potential, LeRoy and Bernstein have famously demonstrated [182] that the energy $E(v)$ of a bound state with integer label v taken from the dissociation limit can be expressed

$$E(v) = D - \left[(v_D - v)\frac{\hbar}{2}\left(\frac{2\pi}{\mu}\right)^{1/2} \frac{\Gamma(1+1/n)}{\Gamma(1/2+1/n)} \frac{n-2}{C_n^{1/n}} \right]^{2n/(n-2)} \tag{4.5}$$

with μ the reduced mass of the molecule and v_D a non-integer index representing the position of a bound state which would be located exactly at the dissociation limit. With the spectroscopic measurement of a set of binding energies, this formula can be used to infer the corresponding C_n coefficients with a few percent uncertainty.[5] A more precise version [183] takes into account higher order dispersion terms of the long range potential and was in particular applied for the case of ^{6}Li to infer C_3 coefficients [167].

---

[5] Under the condition that all the measured binding energies effectively belong to the same potential, a statement which is not so obvious to make for experiments operating close to the dissociation limits of several potentials.

4.1.3 The case of ^{6}Li$_2$

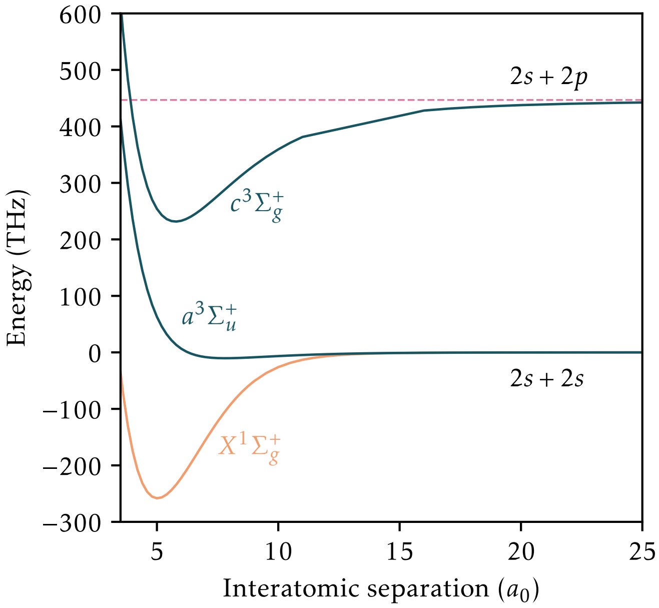

Figure 4.3: Ground and excited molecular potentials for ^{6}Li$_2$ obtained from theory calculations [184]. The blue curves represent triplet potentials with $|\mathbf{S}| = 1$ and the orange one the ground state single potential with $|\mathbf{S}| = 0$. The excited potential dissociates in the $2s+2p$ limit (red dashed line) where its fine splitting, of the order of 10 GHz, is not resolved at this scale and thus not displayed. It features the expected $-C_3/r^3$ behavior at long range with a classical turning point lying around $200\,a_0$, while the ground state potentials show a characteristic $-C_6/r^6$ scaling. Molecular term notations are explained in appendix D.

Photoassociation spectroscopy has been used for over two decades for the specific case of ^{6}Li and therefore the spectroscopic properties of the ground and excited molecular potentials are well studied. We present in figure 4.3 the potentials used in the scope of this manuscript; the two ground potentials represent the two scattering channels introduced in the scope of our discussion on Feshbach resonances while the excited $c^3\Sigma_g^+$ potential is the one addressed with our experiments. It was almost entirely characterized, using photoassociation to measure its most weakly bound $\nu = 56-84$ [167] and more tightly bound $\nu = 20-26$ [185] vibrational levels,[6] while the most deeply bound levels $\nu = 1-7$ were measured using Fourier transform infrared spectroscopy [186].

In addition to pure spectroscopic concerns, photoassociation was also employed with ^{6}Li in the vicinity of the broad s-wave Feshbach resonance. There, as seen in chapter 3, the $\nu = 38$ bound state of the singlet ground state potential $X^1\Sigma_g^+$ is brought into resonance with the zero energy scattering state of the ground triplet potential $a^3\Sigma_u^+$. This coupling between the open channel triplet scattering state and closed channel bound singlet molecular state realizes what is commonly referred to as a Feshbach molecule and previous works have used photoassocitation to probe the closed channel fraction of these Feshbach molecules by engineering couplings between pairs populating the $\nu = 38$ bound state of $X^1\Sigma_g^+$ and other accessible states using excited molecular potentials, with interaction strengths spanning the whole BEC–BCS crossover [162, 179].

---

[6] Here, in order to be consistent with the literature, the labelling convention for vibrational levels is taken to be the opposite of what was defined for the LeRoy Bernstein formula (4.5); the lowest integer number now corresponds to the most deeply bound state.

4.2 Observation of strong light-matter coupling on photoassociation transitions

In the previous section we have laid down the principles needed to understand the origin and some applications of photoassociation. In this section, we will put this knowledge to use by showing how we achieved the strong coupling of photoassociated pairs of atoms to light via our high-finesse optical cavity.

4.2.1 Experimenta scheme

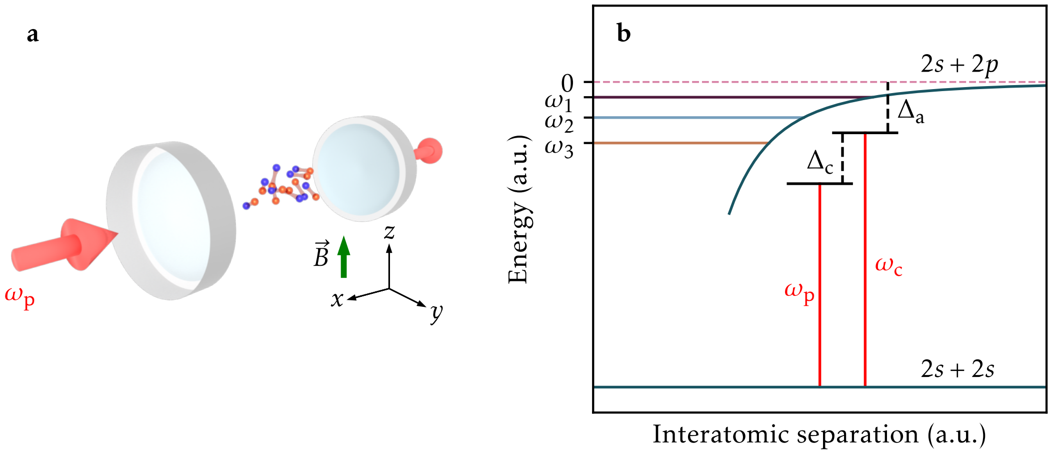

Figure 4.4: Experimental scheme to probe photoassociation transitions with a high-finesse cavity. **a** During the experiment, we send a weak probe laser beam at a frequency ω_p through a high-finesse cavity and acquire the photons leaking out of the cavity on the single photon counter. **b** The cavity resonance frequency ω_c is detuned by an amount Δ_a from the $2s + 2p$ dissociation limit (red dashed line) of the addressed excited molecular potential (dark blue line) which, as an example here, supports three bound states (the three solid horizontal lines with binding energies $\omega_{1,2,3}$). During one realization of the experiment, we dynamically sweep the detuning Δ_c between the probe laser and the cavity.

The measurements described throughout this section and the next are performed similarly as those presented in section 2.1.2. Instead of focusing on the bare atomic resonances, we now detune our cavity resonance frequency to the location of photoassociation transitions with the goal of observing signatures of strong coupling to these transitions by looking at the energy spectrum of the coupled system using cavity transmission spectroscopy.

The experiments are schematically described by figure 4.4**a**. We prepare superfluid gases comprising around $4 \cdot 10^5$ atoms equally populating the two lowest hyperfine spin states – denoted $|1\rangle$ and $|2\rangle$ –, with a temperature $T = 0.08T_\mathrm{F}$ in the crossed optical dipole trap presented in section 1.2.3. Before probing the system we can tune the value of the magnetic field offset B from 832 G – where evaporative cooling is performed – to another point around the Feshbach resonance to change the interaction strength. The magnetic field ramp is performed in 50 ms and is accompanied by an increase of the crossed trap depth to reach trapping frequencies of $2\pi \times 188(9)$, $579(28)$ and $608(30)$ Hz in the x, y, z directions respectively. This compression ramp halts the evaporation process and maximizes the geometrical overlap between the atomic cloud and the TEM_{00} mode of the cavity – to which the probe beam is mode-matched – to ensure maximal light-matter coupling. The transmission spectroscopy technique used to probe the system is then completely analogous to what was presented in section 2.1.2.

We present the general detuning scheme in figure 4.4**b**. The zero of energy from which we quantify our cavity detuning Δ_a corresponds to the $\left|2s_{1/2}, m_J = -1/2\right\rangle \rightarrow \left|2p_{3/2}, m_J = -1/2\right\rangle$ single atom transition, at a magnetic field of 832 G. The zero of energy for the detuning of the probe beam with respect to the cavity resonance frequency Δ_c is taken to be the energy of the fundamental TEM_{00} mode of the cavity. We display the example of three bound states of an excited molecular potential dissociating in the $2s + 2p$ limit denoted by their binding energy $\omega_{1,2,3}$, which can be resonantly probed by setting $\Delta_a = \omega_{1,2,3}$, as we will see in the next paragraph.

4.2.2 Mapping out photoassociation transitions close to dissociation limits

Energy spectrum

We performed the experiment for $\Delta_\mathrm{a} \in 2\pi \times [-16.5, +4]$ GHz by steps of $2\pi \times 10$ MHz, and sweeping the value of Δ_c either from $-2\pi \times 50$ MHz to 0 or from 0 to $2\pi \times 50$ MHz. Due to the large amount of measurements needed, the full dataset acquisition took several days over which the experimental conditions usually slightly vary, ultimately leading to the "patchwork" features of the full energy spectrum presented by figure 4.5**a**.

We observe three major avoided crossings corresponding to the bare atomic transitions to the D_1 and D_2 lines. We attribute them respectively, ordered by increasing resonance frequency, to the $\left|2s_{1/2}, m_J = -1/2\right\rangle \rightarrow \left|2p_{1/2}, m_J = 1/2\right\rangle$, $\left|2s_{1/2}, m_J = -1/2\right\rangle \rightarrow \left|2p_{3/2}, m_J = -3/2\right\rangle$ and $\left|2s_{1/2}, m_J = -1/2\right\rangle \rightarrow \left|2p_{3/2}, m_J = 1/2\right\rangle$ transitions, or respectively D_1 σ_+, D_2 σ_- and D_2 σ_+ in short. The D_2 σ_- avoided crossing was the one studied in more detail in section 2.1.2. These transitions are the most prominent because of the choice of the linear probe polarization which is almost horizontal, only making a small angle with the y axis of figure 4.4**a**. With the vertical direction of the quantization axis z imposed by the magnetic field, the probe beam thus mainly drives $\Delta m_J \pm 1$ or $\sigma_\pm$ transitions. Since the probe polarization also features a small non-zero component along z, $\Delta m_J = 0$ or π transitions are also addressed and result in the weaker lines with avoided crossings observed around $\Delta_\mathrm{a} = -2\pi \times 9$ GHz and $\Delta_\mathrm{a} = 0$ GHz. The weaker branches around $\Delta_\mathrm{c} = -2\pi \times 25$ MHz come from the presence of higher-order transverse cavity modes to which the probe beam weakly couples.

The remaining features of the spectrum which take the form of a multitude of smaller avoided crossings located on the main atomic branches correspond to photoassociation transitions to

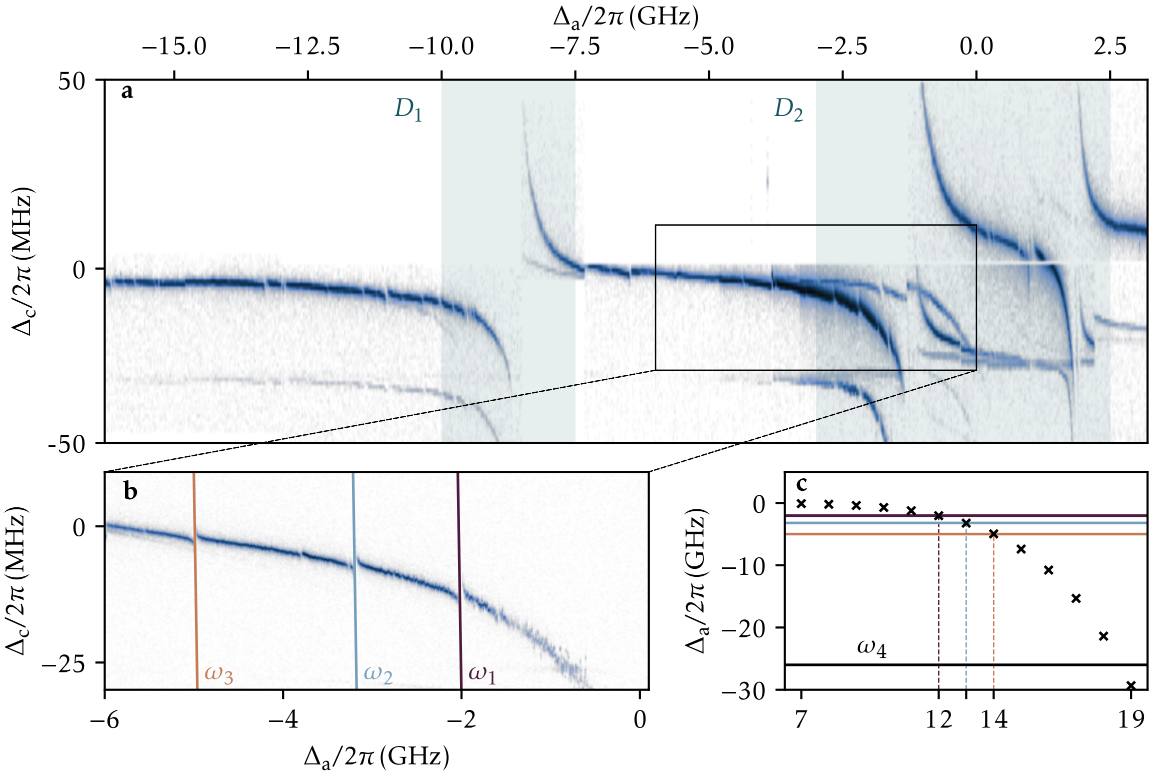

Figure 4.5: Strong coupling on photoassocation transitions near the dissociation limits. **a** Broad energy spectrum map of the system acquired via cavity transmission spectroscopy. The three prominent avoided crossings correspond to strong coupling of single atoms to light while the many smaller ones correspond to coupling to photoassociation transitions. The spectrum is displayed in log scale. **b** Zoom on a region of the upper panel, taken with a different polarization of the probe beam. On this part of the atomic branch we observe three strongly coupled photoassociation transitions to bound vibrational levels with binding energies $\omega_{1,2,3}$, highlighted by the oblique solid lines. **c** Vibrational levels of a same potential and their binding energies resulting from a fit of equation (4.5) to $\omega_{1,2,3}$. We also depicted the energy of another bound state considered in this study, ω_4, which belong to another potential.

excited molecular states.[7] The observation of clear avoided crossings is the signature of the strong coupling of pairs of atoms to light, with the coherent excitation exchange rate dominating both the natural cavity decay rate and the decay rate of the excited molecular states.

---

[7] The attribution each of these transitions to a given bound state of a well-defined interaction potential represents a challenge which would surely deserve a detailed study on its own. The complexity is hinted at in the last paragraph of section 4.1.1. In the dissociation limit, the electrostatic interaction energy becomes comparable with many other possible energy scales of the molecular problem and one has to take into account the corresponding coupling elements. The inclusion of the high magnetic field and its coupling to every degree of freedom of a molecule adds another layer of complexity to the task.

Selection of specific transitions

To study this coupling in detail, we decided for the rest of the chapter to focus on four specific transitions. We label each of such transition according to the frequency detuning[8] at which we observed the corresponding resonance on the above spectrum: $\omega_{1,2,3,4}$. These transitions were probed using a purely vertically polarized probe beam, therefore only coupling to π transitions to obtain cleaner spectra. The first three resonances are depicted in the spectrum shown in figure 4.4**b**, which is taken for detunings depicted by the black box of panel **a**, but with a different probe polarization. On this branch, we observe three clear avoided crossings at respective detunings $\omega_{1,2,3} = -2\pi \times 2.03, 3.21, 4.99\,\mathrm{GHz}$. The fourth transition is not depicted here but corresponds to $\omega_4 = -2\pi \times 25.99\,\mathrm{GHz}$.

This last ω_4 transition was picked because we could attribute it to a specific documented bound state of the $c(1^3\Sigma_g^+)$ potential described in the previous section. We probed the resonance in a spectroscopic effort to reproduce the results from [167][9] and found that we were able to resolve the $\nu = 65 - 84$ documented vibrational levels of the $c(1^3\Sigma_g^+)$ potential with our setup. The ω_4 transition thus corresponds to the $\nu = 81$ bound state of the molecular potential and was chosen in particular because there was no other photoassociation transition in its vicinity.

For $\omega_{1,2,3}$ the story is slightly different and we could not attribute them to known bound states. However, by fitting the measured binding energies to equation (4.5) we observe that they would correspond to consecutive $\nu = 12 - 14$ bound states of the same potential – with the convention used for the LeRoy Bernstein equation. The bound state distribution of that potential inferred from the fit is displayed in figure 4.4**c**, where we see that the dissociation limit of the potential is exactly at the location of the D_2 π transition. We also verify that ω_4 belongs to another potential as the fit predicts no bound state for this binding energy. The inclusion of ω_4 in the initial fit never lead to a meaningful result for all the other transitions.

4.3 Many-body physics from vacuum Rabi splitting

Having shown that we observe strong light-matter coupling on multiple photoassociation transitions, we now present how the measurement of the strength of this coupling relates to the contact defined in chapter 3. This measurement demonstrates for the first time a direct connection between a typical observable of quantum optics experiments, the Rabi frequency, and the universal thermodynamics ruling the many-body ground state of strongly interacting Fermi gases.

We start with a formal introduction of pairs of atoms coupled to light, by giving an explicit expression for the light-matter interaction. We show how the corresponding Hamiltonian for the system can be mapped to a generalization of the Tavis-Cummings model, describing an ensemble of two-level systems coupled to light. As shown in chapter 2 this model predicts a prominent Rabi splitting of the eigenenergies of the light-matter coupled system in the strong coupling regime, which translates into large avoided crossings in the optical spectra. We employ the model to measure Rabi frequencies for the $\omega_{1,2,3,4}$ lines by directly fitting the observed avoided crossings. We repeat the measurement by tuning the interaction strength between the ground state atoms using the Feshbach resonance introduced in chapter 3. We observe clear variations of the Rabi frequencies as the interaction parameter is varied with magnetic field, with a similar trend for all the transitions.

---

[8] As a reminder, the detunings are taken from the D_2 π transition at 832G. From what precedes, this does not necessarily mean that the corresponding bound states all belong to potentials dissociating in the $\left|2s_{1/2}, m_J = -1/2\right\rangle \to \left|2p_{3/2}, m_J = -1/2\right\rangle$ limit.

[9] In that reference, the zero detuning frequency corresponds to the transition frequency between the hyperfine barycenter of the $2s$ ground state and the $2p_{1/2}$ manifold with unresolved hyperfine structure, at zero magnetic field.

To explain these variations, we formally show that the strength of the light-matter coupling between the pairs and the cavity field is expected to connect to the many-body physics of the gas by an explicit dependency on the contact. We experimentally prove this fact by comparing our data to theoretical predictions for the scaling of the contact with interaction strength. For all transitions, the data fit the model remarkably well, proving the deep connection between the measured optical spectra and the many-body universal physics ruling the ground-state of the gas. In addition, we introduce an experimental probing scheme to continuously measure the value of the contact, on a single run of the experiment.

4.3.1 Rabi frequency of pairs coupled to light

Expression for the Rabi frequency

We consider the Hamiltonian for the system

$$\hat{H} = \hat{H}_0 + \hat{H}_\mathrm{e} + \hat{H}_\mathrm{m} + \hat{H}_\mathrm{cav} + \hat{H}_\mathrm{int} \tag{4.6}$$

where $\hat{H}_0$ encompasses the kinetic energy and external trap terms for both the ground state atoms and excited molecules. Since the time scales associated with the mechanical motion of the components of the system contained in the previous terms are small against the ones associated with optical processes, we disregard this part of the total Hamiltonian in what follows. $\hat{H}_\mathrm{e}$ and $\hat{H}_\mathrm{m}$ respectively describe the atomic and molecular excited states. $\hat{H}_\mathrm{cav}$ represents the energy of a single mode cavity light field and $\hat{H}_\mathrm{int}$ contains the details of the interactions between ground state atoms, excited molecules and photons.

We assume to be working in the dispersive regime for the atoms, as introduced in section 2.1.3, so that the atoms-cavity interaction term simply leads to a dispersive shift of the bare cavity resonance. In the framework of second quantization and in a frame rotating at the frequency of a photoassocation transition associated with a bound state with binding energy ω_i, the two remaining terms of $\hat{H}$ can then be expressed as

$$\hat{H}_\mathrm{light} = -\Delta_{\omega_i} \hat{a}^\dagger \hat{a} \tag{4.7}$$

$$\hat{H}_\mathrm{int} = \frac{i\Omega_0}{2} \left(\int d\mathbf{R} d\mathbf{r} g(\mathbf{R}) f(\mathbf{r}) \hat{\psi}_i^\dagger(\mathbf{R}) \hat{\psi}_1(\mathbf{R} - \frac{\mathbf{r}}{2}) \hat{\psi}_2(\mathbf{R} + \frac{\mathbf{r}}{2}) \hat{a} - \mathrm{h.c.} \right) \tag{4.8}$$

where $\hat{a}^\dagger$ and $\hat{a}$ respectively create and annihilate a photon in the cavity mode. $\hat{H}_\mathrm{int}$ describes the interaction of colliding pairs of atoms with center of mass at position $\mathbf{R}$ and spaced by $\mathbf{r}$. We note $\hat{\psi}_{1,2}$ the fermionic field operators associated with atoms respectively in state $|1\rangle$ and $|2\rangle$ and similarly $\hat{\psi}_i$ the bosonic field operator for the excited molecule. Through the absorption of a photon from the cavity field, the atoms form an excited molecule in the considered molecular state. This process is captured by the term $\hat{\psi}_i^\dagger(\mathbf{R}) \hat{\psi}_1(\mathbf{R} - \frac{\mathbf{r}}{2}) \hat{\psi}_2(\mathbf{R} + \frac{\mathbf{r}}{2}) \hat{a}$ which is integrated over the relative coordinate $\mathbf{r}$ to account for the radial structure of the molecular state wavefunction $f(\mathbf{r})$. The second integration is performed over the center of mass coordinate to account for the mode structure $g(\mathbf{R})$ of the cavity field. Last, Ω_0 corresponds to the Rabi frequency for a single pair and a single photon.

From there, $\hat{H}$ can be expressed with as a standard single mode light-matter coupling

Hamiltonian in the rotating wave approximation

$$\hat{H} = -\Delta_{\omega_i}\hat{a}^\dagger\hat{a} + \frac{i\Omega_0}{2}\left(\hat{F}^\dagger\hat{a} - \hat{F}\hat{a}^\dagger\right) \tag{4.9}$$

where $\hat{F}^\dagger = \int d\mathbf{R}d\mathbf{r}g(\mathbf{R})f(\mathbf{r})\hat{\psi}_i^\dagger(\mathbf{R})\hat{\psi}_1(\mathbf{R}-\frac{\mathbf{r}}{2})\hat{\psi}_2(\mathbf{R}+\frac{\mathbf{r}}{2})$ encompasses the details of the pairs-light interaction and can be seen as a collective spin 1/2 operator, as introduced when discussed the generalized Tavis-Cummings model in section 2.1.2. This form of the Hamiltonian therefore predicts a vacuum Rabi splitting of the eigenenergies of the pairs-light coupled system, in complete analogy to what we have already discussed for the case of atoms coupled to light. To make the connection with the Rabi frequency explicit, we employ a mapping of $\hat{F}$ to a bosonic pair annihilation operator $\hat{b}$ via the Holsetein-Primakoff transformation [99]. It yields

$$\hat{b} = \frac{\hat{F}}{\sqrt{\left\langle\left[\hat{F},\hat{F}^\dagger\right]\right\rangle}} \tag{4.10}$$

which is an operator describing collective optical excitations shared among pairs of atoms coupled to light. With this definition, the Hamiltonian can then be rewritten with

$$\hat{H} = -\Delta_{\omega_i}\hat{a}^\dagger\hat{a} + \frac{i\Omega}{2}\left(\hat{b}^\dagger\hat{a} - \hat{b}\hat{a}^\dagger\right) \tag{4.11}$$

and $\Omega = \Omega_0\sqrt{\left\langle\left[\hat{F},\hat{F}^\dagger\right]\right\rangle}$ is now the Rabi frequency of the system which quantifies the excitation exchange rate between pairs and the cavity field. We call *pair-polariton* the atomic pair thus dressed by the cavity field, similarly as for single atoms coupled to light.

The prominent Rabi splitings expected in the strong coupling regime for such a model were presented in figure 4.5 for $\omega_{1,2,3}$. In addition, we show in figure 4.6**a** a close-up view of optical spectra acquired in the vicinity of the ω_4 line. We observe a prominent avoided crossing, which with the model above, confirms that we achieve the strong coupling regime for pairs coupled to light.

Measurement and magnetic field dependence

In order to extract Rabi frequencies Ω from the observed avoided crossings in the measured spectra, we fit the latter with an expression for the cavity transmission T obtained from purely classical considerations [55], incorporating the cavity and atomic decay rates κ and Γ

$$T = \frac{A}{\left[1 + \frac{\Omega^2}{2\kappa\Gamma_\mathrm{m}}L_\mathrm{a}(\Delta_{\omega_i} + \tilde{\Delta}_\mathrm{c})\right]^2 + \left[\frac{2(\tilde{\Delta}_\mathrm{c} - \alpha\Delta_{\omega_i})}{\kappa} + \frac{\Omega^2}{2\kappa\Gamma_\mathrm{m}}L_\mathrm{d}(\Delta_{\omega_i} + \tilde{\Delta}_\mathrm{c})\right]} \tag{4.12}$$

with κ the natural linewidth of the cavity, $\Delta_{\omega_i} = \Delta_\mathrm{a} - \omega_i$ and $\tilde{\Delta}_\mathrm{c} = \Delta_\mathrm{c} - \delta_\mathrm{c}$ the probe-cavity detuning taken from the dispersively shifted cavity resonance δ_c defined in section 2.1.3. The parameters $A, \alpha, \Gamma_m, \delta_\mathrm{c}, \Omega$ and ω_i are determined from the fit. A is an overall normalization parameter, α accounts for a linear slope of the background branch on which we observe the avoided crossing[10], Γ_m is the linewidth of the excited molecular state, Ω the Rabi frequency

---

[10] The slope comes from the background atomic polariton, which "bends" in energy as a resonance is approached, *e.g.* as seen in figure 4.4**b**.

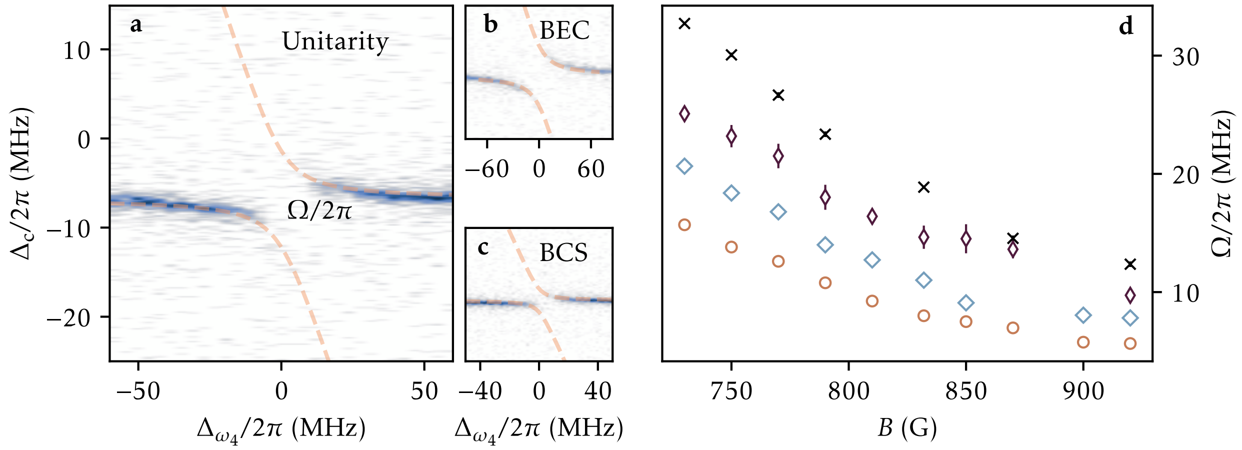

Figure 4.6: Variation of the coupling strength with magnetic field. **a** Energy spectrum of the system measured around ω_4 at unitarity on which is overlapped the result of the fit to eqaution (4.12) (dashed orange line) to extract the coupling strength Ω. **b**-**c** Energy spectrum of the same transition taken at different points of the BEC–BCS crossover. The origin of the Δ_ω axis takes into account the Zeeman shift induced by the change of the magnetic field. **d** Scaling of the coupling strength Ω for magnetic fields which correspond to interaction parameters spanning the strongly interaction regime of the BEC–BCS crossover, for the four considered transitions with binding energies $\omega_{1,2,3,4}$ (respectively depicted by diamonds, squares, circles and crosses).

and ω_i the location of the resonances defined above. The functions $L_a(\Delta)$ and $L_d(\Delta)$ respectively correspond to the absorptive and dispersive Lorentzian lineshapes with

$$L_a(\Delta) = \frac{\Gamma_m^2}{\Gamma_m^2 + 4\Delta^2} \qquad L_d(\Delta) = \frac{-2\Delta\Gamma_m}{\Gamma_m^2 + 4\Delta^2}. \tag{4.13}$$

We show an example of the fit of the ω_4 resonance at unitarity in figure 4.6**a** and on the BEC and BCS side of the resonance in panels **b** and **c** respectively. The fit results are displayed with a model which doesn't take linewidths into account, for clarity. We measure $\Omega = 2\pi \times (12.7(1), 18.9(1), 32.7(3))\,\mathrm{MHz}$ for values of the magnetic field $B = (730, 832, 920)\,\mathrm{G}$ which respectively correspond to the BEC, unitarity and BCS regimes. While these measured Rabi frequencies demonstrate that the strong coupling regime persists for values of the interaction strength spanning the strongly interacting regime of the BEC–BCS crossover, we also observe a sizeable variation of Ω, of a factor larger than two, going from the BCS to the BEC side of the resonance.

To further quantify this large variation of the Rabi frequency, we measure Ω for more values of the magnetic field around the Feshbach resonance, which controls the ground state interparticle interactions, and for all four $\omega_{1,2,3,4}$ transitions. We show the results in figure 4.6**d**, where we observe a clear trend with the Rabi frequency for a given transition being the largest on the BEC side and decreasing smoothly towards the BCS side. The quantitatively similar trend for all the different transitions suggests that the variation of Rabi frequency does not depend on the details of the molecular transitions – since we address bound molecular states with different binding energies and electronic configurations – but rather on the nature of the two-body scattering ground state which is contained in the $\left\langle \left[\hat{F}, \hat{F}^\dagger\right] \right\rangle$ term obtained above.

4.3.2 Many-body physics from the optical spectrum

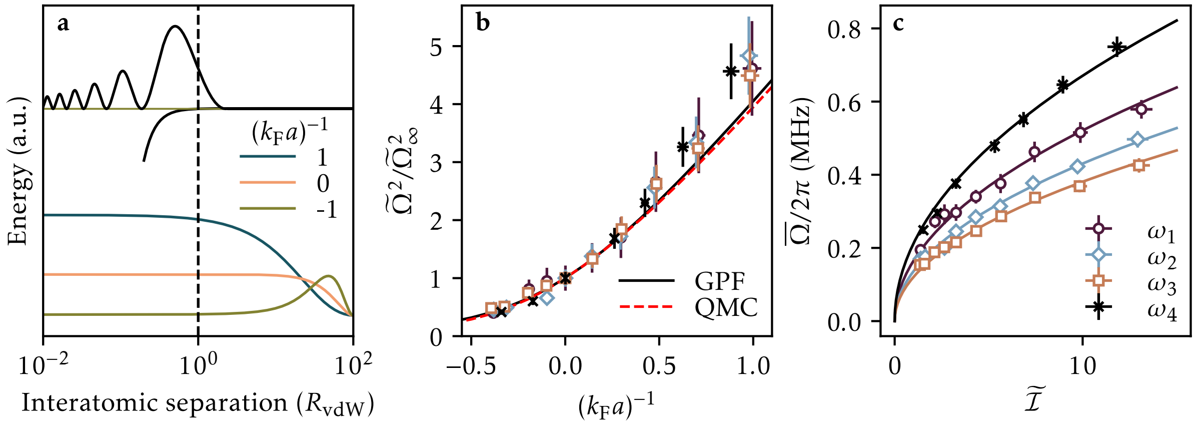

Figure 4.7: Measurement of the contact from quantum optics observables. **a** Franck-Condon principle applied to our strongly interacting Fermi gas, with three ground state two-body wavefunctions depicted for different values of the the interaction parameter (bottom solid lines) and were computed in section 3.2.1. Their overlap with a typical excited wavefunction (top black solid line) at the Condon point (vertical dashed line) thus exhibits a sizeable variation with interaction parameter. **b** Rescaled Rabi frequency (see text) for the four photoassocation transitions as a function of interaction parameter compared to theoretical values of the contact obtained from Gaussian Pair Fluctuation and Quantum Monte-Carlo [187]. The theory predictions have already been experimentally confirmed [158]. **c** Scaling of the measured Rabi frequencies as a function of the total contact (markers) per particule and their fit with a square root model (solid line) to extract the single-pair single-photon Rabi frequency.

A simple picture of the influence of the ground state wavefunctions of strongly interacting Fermi gases on photoassociation transitions can be obtained given the shape of the two-body scattering wavefunctions derived in section 3.2.1 and is shown in figure 4.7**a**. We see that the transition dipole moments – directly proportional to the Franck-Condon factor – show a significant dependence on the interaction parameter because of the variation of the amplitude of the ground state wavefunctions around the Condon point[11] when interactions are varied. In what follows, we present a more formal approach to the previous description, with an explicit calculation of the Rabi frequency to highlight its dependence on the initial two-body ground state wavefunction and on its short-range part; the contact.

---

[11] In our case, the Condon points are located at typical values of the order of $100\,a_0$ which are small against the mean interparticle distance $k_{\mathrm{F}}^{-1} \sim n^{-1/3} \approx 0.1 - 1\,\mu$m with n the density. This means the photoassication process effectively probes the short range part of the two-body ground state wavefunctions.

Rabi frequency as a function of the contact

We start by computing the commutator contained in the Rabi frequency of equation (4.11)

$$\begin{aligned}\left[\hat{F},\hat{F}^\dagger\right] = \int & d\mathbf{R}d\mathbf{r}d\mathbf{R}'d\mathbf{r}' g(\mathbf{R})f(\mathbf{r})g^*(\mathbf{R}')f^*(\mathbf{r}') \\ & \times\Big[(\delta(\mathbf{R}-\mathbf{R}')+\hat{\psi}_i^\dagger(\mathbf{R})\hat{\psi}_i(\mathbf{R}'))\hat{\psi}_2^\dagger(\mathbf{R}'+\frac{\mathbf{r}'}{2})\hat{\psi}_1^\dagger(\mathbf{R}'-\frac{\mathbf{r}'}{2})\hat{\psi}_1(\mathbf{R}-\frac{\mathbf{r}}{2})\hat{\psi}_2(\mathbf{R}+\frac{\mathbf{r}}{2}) \\ & -\hat{\psi}_i^\dagger(\mathbf{R})\hat{\psi}_i(\mathbf{R}')\hat{\psi}_1(\mathbf{R}-\frac{\mathbf{r}}{2})\hat{\psi}_2(\mathbf{R}+\frac{\mathbf{r}}{2})\hat{\psi}_2^\dagger(\mathbf{R}'+\frac{\mathbf{r}'}{2})\hat{\psi}_1^\dagger(\mathbf{R}'-\frac{\mathbf{r}'}{2})\Big]\end{aligned} \tag{4.14}$$

where we have used the bosonic field commutation relation $\left[\hat{\psi}_i(\mathbf{x}),\hat{\psi}_i^\dagger(\mathbf{x}')\right]=\delta(\mathbf{x}-\mathbf{x}')$. Assuming that we work in the low saturation regime for the photoassociation transition with $\langle\hat{\psi}_i^\dagger\hat{\psi}_i\rangle\sim 0$, the expectation value of the above expression reads

$$\left\langle\left[\hat{F},\hat{F}^\dagger\right]\right\rangle = \int d\mathbf{R}|g(\mathbf{R})|^2\int d\mathbf{r}d\mathbf{r}' f(\mathbf{r})f^*(\mathbf{r}')\left\langle\hat{\psi}_2^\dagger(\mathbf{R}+\frac{\mathbf{r}'}{2})\hat{\psi}_1^\dagger(\mathbf{R}-\frac{\mathbf{r}'}{2})\hat{\psi}_1(\mathbf{R}-\frac{\mathbf{r}}{2})\hat{\psi}_2(\mathbf{R}+\frac{\mathbf{r}}{2})\right\rangle \tag{4.15}$$

where the four-point correlator on the right-hand side corresponds to the one used in equation 3.50 to introduce the two-body contact, up to a shift of the translation-invariant coordinate system. Following the reasoning presented in section 3.2.3 at short distance, with $a, k_\mathrm{F}^{-1}\gg|\mathbf{r}|\sim R_\mathrm{C}$, we write

$$\left\langle\hat{\psi}_2^\dagger(\mathbf{R}+\frac{\mathbf{r}'}{2})\hat{\psi}_1^\dagger(\mathbf{R}-\frac{\mathbf{r}'}{2})\hat{\psi}_1(\mathbf{R}-\frac{\mathbf{r}}{2})\hat{\psi}_2(\mathbf{R}+\frac{\mathbf{r}}{2})\right\rangle = \frac{\mathcal{C}(\mathbf{R},a)}{16\pi^2}\left(\frac{1}{|\mathbf{r}'|}-\frac{1}{a}\right)\left(\frac{1}{|\mathbf{r}|}-\frac{1}{a}\right) \tag{4.16}$$

with a the scattering length and where we let the contact density $\mathcal{C}$ explicitly depend on spatial coordinates, so that

$$\left\langle\left[\hat{F},\hat{F}^\dagger\right]\right\rangle = \int d\mathbf{R}|g(\mathbf{R})|^2\mathcal{C}(\mathbf{R},a)\left|\int drf(r)\left(\frac{1}{|r|}-\frac{1}{a}\right)\right|^2 \tag{4.17}$$

where the integral on relative radial coordinates can be approximated using a simple expression for the excited wavefunction. Considering only the last lobe of this wavefunction as yielding a sizeable contribution due to the Franck-Condon principle, we model the reduced radial wave function $u(r)=f(r)/r$ by a square function centered around the Condon point, with width L and amplitude A.[12] We then have

$$\int drf(r)\left(\frac{1}{|r|}-\frac{1}{a}\right) = A\int_{R_\mathrm{C}-L/2}^{R_\mathrm{C}+L/2} dr\left(1-\frac{r}{a}\right) = AL\left(1-\frac{R_\mathrm{C}}{a}\right) \tag{4.18}$$

and finally

$$\Omega^2 = \Omega_0 A^2L^2\left|\left(1-\frac{R_\mathrm{C}}{a}\right)\right|^2\int d\mathbf{R}|g(\mathbf{R})|^2\mathcal{C}(\mathbf{R},a) \tag{4.19}$$

To quantify the relative variations of Ω when we vary the interaction parameter $1/k_\mathrm{F}a$, we define $\widetilde{\Omega}^2=\Omega^2/(Nk_\mathrm{F})\left|\left(1-\frac{R_\mathrm{C}}{a}\right)\right|^{-2}$ which effectively accounts for the variations of prepared atom numbers across repetitions of the experiment, and for the variations of the density and $\frac{R_C}{a}$ with $1/k_F a$. Using $\widetilde{\Omega}_\infty^2 = \widetilde{\Omega}^2(1/k_F a = 0)$, we show the rescaled measurements of $\widetilde{\Omega}^2/\widetilde{\Omega}_\infty^2$ in figure 4.7**b**, which correspond to the same data as presented in figure 4.6**d**. We observe a collapse of all the relative scalings of the rescaled Rabi frequency for the different photoassociation transitions on theory curves obtained from trap-averaged interaction dependence of the contact $\mathcal{I}$ [158, 187]. We attribute the deviation of our data from theory on the BEC side of the resonance by $\sim 15\%$ to finite temperature and the simplicity of the molecular model employed to rescale Ω.

---

[12] As we will see below, A and L can be further estimated using the shape of the Airy function solution of Schrödinger's equation for a linearized potential around the Condon point, with binding energy ω_i.

This collapse of the data confirms the universal role played by the two-body ground state wavefunction in the photoassociation signal. Once the molecular details factored out in equation (4.19), the relative scaling of the Rabi frequency with interaction strength only depends on the contact. It also demonstrates the direct correspondence between the optical spectrum of the cavity represented by the measured Rabi frequency and the many-body physics of the quantum gas contained in the contact. The observed relative variation of the Rabi frequency with interaction strength, spanning tens of MHz, remains surprisingly large before the Fermi energy of the gas, being two orders of magnitude lower. Through photoassociation, our system therefore acts as a magnifier for two-body correlations by mapping them onto an amplified optical spectrum. The magnification factor directly depends on the $\Omega_0 \int d\mathbf{R}|g(\mathbf{R})|^2$ factor, which translates small changes on the energy of the gas into large changes in the optical signal.

Number of pairs coupled to light

In order to further build on the pair-polariton approach to describe our system and in analogy with the Tavis-Cummings model, we write

$$\Omega = \Omega_0 \sqrt{\frac{N_p}{2}} \tag{4.20}$$

where N_p is the number of pairs coupled to light and the factor 1/2 accounts for the mode structure of the cavity field. Integrating equation (3.59) to count the number of pairs in a sphere of radius L, which again approximates the width of the last lobe of the excited molecular wavefunction, we get

$$\Omega = \Omega_0 \sqrt{\widetilde{\mathcal{I}} \frac{N k_F L}{4\pi}} \tag{4.21}$$

where the integrated contact per particle $\widetilde{\mathcal{I}}$ is defined as a function of the total contact with $\mathcal{I} = \widetilde{\mathcal{I}} N k_F$ and N the total atom number. The radius L is estimated to be the width of the Airy function solution of the Schrödinger equation for a linearized excited molecular potential around the Condon point. In this case

$$V(r) = -\frac{C_3}{r^3} \approx -\omega_i \left(1 - \frac{3r}{R_C}\right) \tag{4.22}$$

and the Schrödinger equation for the reduced radial wavefunction $u(r)$ reads

$$\frac{\hbar^2}{\mu} \frac{d^2}{dr^2} u(r) - 3\frac{\omega_i}{R_C} r u(r) = 0 \tag{4.23}$$

which solution is the Airy function

$$u(r) = Ai\,(r/r_0) \tag{4.24}$$

with $r_0 = \left(\frac{\hbar^2 R_C}{3\mu\omega_i}\right)^{1/3}$ the spatial extent of the last lobe of $u(r)$. Therefore, by setting $L = r_0$, we respectively obtain $L = (28.9, 23.6, 19.4, 12.6)\,a_0$ for $\omega_{1,2,3,4}$.

We show the variations of $\bar{\Omega} = \Omega/\sqrt{N k_F L}$ in figure 4.7**c** as a function of $\widetilde{\mathcal{I}}$ which we assume to know from the previous mapping of Ω to the contact. We observe the square root scaling expected from equation (4.21) for all considered photoassociation transitions, which confirms the analogy with the Tavis-Cummings model for pairs coupled to light. Fitting the curves with a square root model, we obtain $\Omega_0 = 2\pi \times (595(11), 492(5), 435(7), 765(5))\,\mathrm{kHz}$ for the four photoassociation transitions respectively. These values of the single-pair single-photon Rabi frequencies are of the same order of magnitude as the single-atom single-photon one of $2\pi \times 780\,\mathrm{kHz}$ for the $D2$ π transition, such that, in analogy with single atoms, our cavity has a cooperativity for single pairs close to unity.[13] Our system thus allows in principle for the application of well established single-atom quantum optical protocols using pairs in a strongly interacting Fermi gas.

4.3.3 Continuous measurement of the two-body contact

So far, our measurement technique of the contact relied on the realization of several experimental runs, a common limitation of cold atoms platform. However, as already proven in chapter 2 the use of a cQED methods allows to perform weakly destructive transmission spectroscopy measurements. In this section, we present a weakly destructive method to infer the contact from single run measurements of the Rabi frequency.

In what we presented above, measurements were repeated for various values of Δ_a in order to reconstruct and fit the avoided crossings of the energy spectra. The need for several points to reconstruct the avoided crossings stems from the fact that we can not disambiguate changes of the polariton energy originating from the contributions of atoms and pairs. Indeed, in a single run we record a Lorentzian profile given by equation (4.12) which location depends both on Δ_a and δ_c.

To circumvent this limitation and be able to measure Ω from a single experimental run, we apply a slightly modified probing scheme presented by figure 4.8**a**. Instead of using a purely vertical polarization for the probe, addressing only π transitions, we rotate it by an angle of 26° so that it acquires a horizontal component now addressing $\sigma_\pm$ transitions. The practical consequence in the scope of photoassociation is that we now address simultaneously another set of excited molecular potentials when performing the above described experiments, similarly to the early explorations presented in figure 4.5**a**. The idea behind this modified scheme is to use one polarization component of the photons to extract the overall dispersive shift δ_c and the second one to measure the Rabi frequency, with the independent knowledge of δ_c.

This probing change is reflected in the measured optical spectra, an example of which is shown in figure 4.8**b** for ω_4. We now observe two overlapping avoided crossings, corresponding to two different bound states, each being addressed by one polarization component of the probe and separated by $\omega_{4\pi} - \omega_{4\sigma}$. The central, most prominent, avoided crossing corresponds to the previously defined ω_4 bound state, now labelled $\omega_{4\pi}$, while the second one corresponds to the newly addressed $\omega_{4\sigma}$ bound state.

In addition, we demonstrate the weakly destructive capabilities of the experiment by probing the system 50 times during a single run, each probe pulse being separated by 10 ms to let the

---

[13] Even though the "single pair" concept is ill-defined since pairs cannot be isolated individually because their existence in the first place is many-body effect.

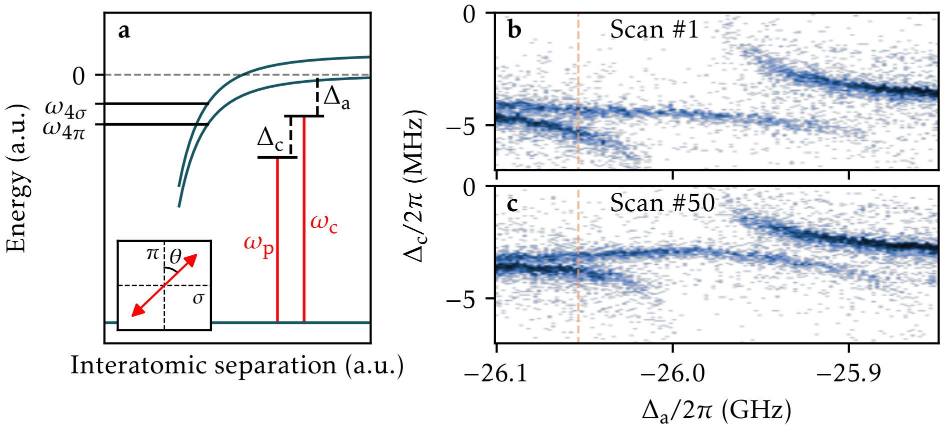

Figure 4.8: Modified version of the probe scheme. **a** By rotating the linear probe polarization by an angle θ from the original vertical orientation, we address a new set of excited molecular potentials. The bound states addressed by photoassociation in these potentials are labelled with respect to the polarization component of the photon addressing them, here we show $\omega_{4\pi}$ and $\omega_{4\sigma}$ as examples. **b-c** Energy spectra obtained with the modified probe polarization which feature two distinct avoided crossings corresponding to strong coupling to both $\omega_{4\pi}$ and $\omega_{4\sigma}$ transitions. For each value of Δ_a, the system is probed 50 times and panels **b** and **c** respectively show the reconstructed spectra corresponding to all the first and 50^{th} probe pulses.

gas thermally equilibrate. For each value of Δ_a, we therefore acquire 50 spectra and can then reconstruct 50 avoided crossings as displayed by figures 4.8**b-c**. The unusual bending of the polariton branches of panel **c** and general smaller avoided crossings come from losses induced by the repeated measurements, which are more prominent at the location of photoassociation transitions, and from the finite lifetime of the unitary gas in a trap.

From these 50 repetitions, we now measure the evolution of the Rabi frequency. In figure 4.9**a** we show the observed signal during the first probe pulse at a detuning $\Delta_a = -2\pi \times 26.06\,\text{GHz}$, depicted by a vertical dashed line in figure 4.8**b**. We fit this double Lorentzian signal with a modified of equation (4.12) accounting for the presence of a second resonance and with the knowledge of $\omega_{4\pi}$ and $\omega_{4\sigma}$. The fit result, shown as a solid orange line, models well the system and allows us to extract simultaneously the values of Ω and δ_c. For a single run of the experiment, we show these measured Ω and δ_c in figure 4.9**b** for each of the 50 scans. We observe a continuous decrease of the Rabi frequency along with a continuous decrease of the dispersive shift, which we both attribute to a decrease of atom number over the duration of a single run. These losses originate both from the finite lifetime of the gas in the trap and from the photoassociation process itself.

Even in the presence of significant losses, we show that the many-body physics interpretation of the Rabi frequency is preserved by evaluating $\widetilde{\Omega} = \Omega/\sqrt{Nk_F}$ for each of the scans, where Nk_F is directly inferred from δ_c. We present the results normalized by the value of the Rabi frequency obtained for the first scan $\widetilde{\Omega}_0$ in figure 4.9**c**, with a solid orange line. We repeat the procedure for 20 different choices of Δ_a around $\omega_{4\pi}$ and average the measured $\widetilde{\Omega}$ shown as the solid black line in the same panel, which features a constant value across the 50 pulses. As the measured

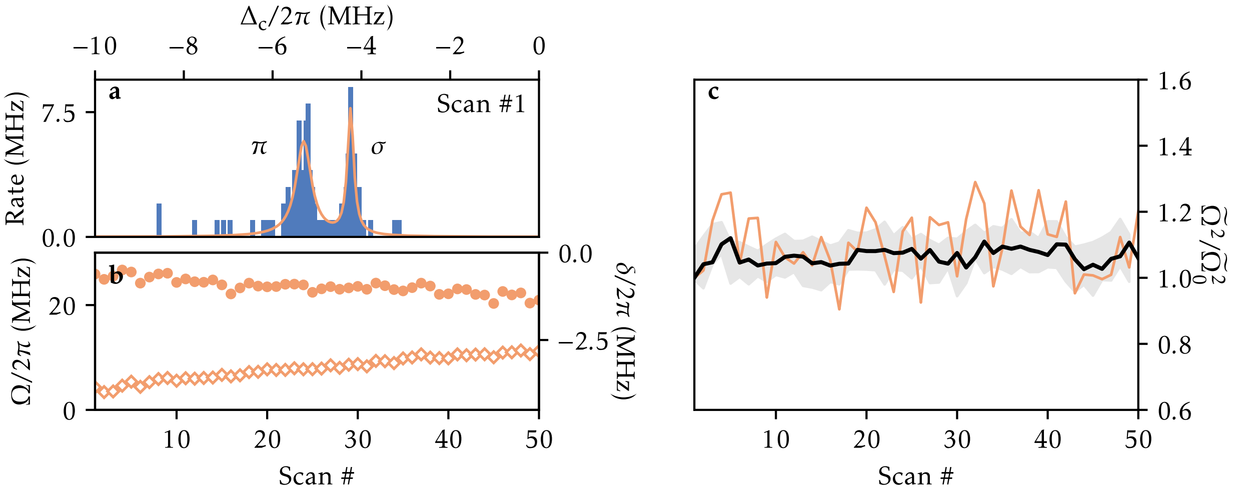

Figure 4.9: Continuous measurement of the contact over a single experimental run. **a** The measured transmission spectrum for a single probe pulse around $\omega_{4\pi}$ and its fit (solid line) on a model accounting for a double resonance. The obsrved peaks are attributed to different components of the probe polarization (see text). **b** Dispersive shift δ_c (empty diamonds) and Rabi frequency Ω (full circles) extracted from the previous fits on single-pulse spectra and shown for each of the 50 pulses performed during one experimental run. **c** Rescaled Rabi frequency measured computed for each of the 50 probe pulses of panel **b** (solid orange line) and rescaled by the Rabi frequency of the first pulse $\widetilde{\Omega}_0$. The black solid line is an average of 20 of such measurements taken at different values of Δ_a, with a standard deviation depicted by the shaded area.

quantity $\widetilde{\Omega}$ is directly proportional to the total contact per particle from equation (4.21), we have therefore shown that the contact remains constant over a single experimental run, or equivalently, our ability to continuously probe the many-body character of the strongly interacting Fermi gas without disturbing it.

Conclusion

The proven ability of the cavity field to couple directly to the pair correlation function in the dispersive regime suggests the possibility to engineer pair–pair interactions mediated by cavity photon exchanges [188], opening an uncharted territory to quantum simulation as presented in the outlook of chapter 6. Beyond these fundamental questions, the weakly destructive and time-resolved character of the cavity-assisted measurement will be of immediate, practical interest in the study of correlations after quenches, such as spin diffusion [189], repulsively interacting Fermi gases where pairing competes with ferromagnetism [190], or during slow transport processes [105, 191], complementing other high-efficiency methods [192]. Last, our work adds the exquisite control over photons of a high finesse cavity to the existing cold molecules toolbox [170], opening the way to dissipation engineering of cold chemistry [193–195].

Chapter 5

Optomechanical response of strongly interacting Fermi gases

> Those who do not move, do not notice their chains.
>
> Rosa Luxemburg

Outline of the current chapter

5.1 Observation of a Kerr nonlinearity in a unitary Fermi gas coupled to light 82
- 5.1.1 Kerr nonlinearities and optical bistability 82
- 5.1.2 Response function from light-matter coupling 83
- 5.1.3 Experimental realization 86

5.2 The connection between light-matter coupling and the universal thermodynamics of strongly interacting fermions 90
- 5.2.1 The Operator Product Expansion 91
- 5.2.2 Density response in the BEC–BCS crossover 94

In this chapter, we report on the observation of an optomechanical Kerr nonlinearity in our degenerate, strongly interacting Fermi gas and on its connection with the underlying many-body physics. It closely follows our results reported in [196]. Along with our work on photoassociation, this project brings another physical quantity to be measured from cavity spectra: the density response function which depends on the ground-state properties of the gas. It thus provides another direct connection between the many-body physics of strongly interacting Fermi gases and quantum optics.

The framework of cavity optomechanics naturally describes collective displacements of atoms within a cloud dispersively coupled to light in a high finesse cavity [197]. When injecting light into the cavity, the photons induce a collective displacement of the atomic density which feeds back on the effective length of the cavity and therefore on its resonance frequency. This results in a well-known Kerr nonlinearity, visible in the experiments as distorted, bistable cavity transmission profiles. Such nonlinearities have been observed in the context of cold atoms for tightly confined, thermal clouds [198, 199] and homogeneous Bose-Einstein condensates [57, 200, 201]. For ideal Fermi gases, the effect has been predicted [202] but was not observed before our work. In addition to its observation, we harness the dependency of the Kerr nonlinearity on the many-body ground state properties of the gas to measure those from optical spectra, bringing a new application to the cavity optomechanics toolbox.

In a first section, we derive the origin of the optomechanical nonlinearity stemming from the form of the light-matter coupling Hamiltonian in the dispersive regime. We show that the strength of the nonlinearity depends on the density response function of the gas and demonstrate our ability to measure it via cavity transmission spectroscopy. In a second section, we prove that the density response function is deeply connected to many-body physics with the use of an operator product expansion (OPE) to relate it to two universal thermodynamic properties of the gas, the contact and the internal energy. In a comparison with measurements in the BEC–BCS crossover, we find that the response quantitatively describes the scaling of the nonlinearity with interaction strength. The OPE approach is motivated by the cavity photons wavevector $2k_c$ exceeding the Fermi wavevector k_F, so that the response function has a universal character inherited from the short range physics of the Fermi gas. Our experiment therefore provides a method to measure universal response functions of strongly correlated systems by the direct observation of optical spectra.

5.1 Observation of a Kerr nonlinearity in a unitary Fermi gas coupled to light

In this section, we show how the collective displacement of the atoms originating from a weak cavity field is connected to the density response of the gas, making the connection between Kerr nonlinearities and intrinsic many-body properties. We first briefly present Kerr nonlinearities and their consequences in cavity systems in terms of optical bistability, a phenomenon which can be observed in the experiment. In a second part, we formally connect the strength of such observed nonlinearities to the density response function and present their measurement technique. We report on the observation of a Kerr nonlinearity in a unitary Fermi gas.

5.1.1 Kerr nonlinearities and optical bistability

Optical bistability refers to the situation where an optical system features two possible output transmission intensities for the same given input intensity. The Fabry-Pérot resonator is a canonical example of system featuring such a behavior, if a medium with certain absorption and dispersion coefficients α and k is placed inside the resonator, itself illuminated with a field of amplitude E_0, the circulating field in the resonator can generally be expressed with [203]

$$E = \frac{tE_0}{1 - r^2 e^{2ikl - \alpha l}} \tag{5.1}$$

with r and t the reflection and transmission coefficients of the symmetric resonator and l its length. Bistability emerges in this system when the coefficients α and k are allowed to depend on E, a situation in which the previous equation now admits multiple nontrivial solutions. From this description, we see that bistability can emerge from either a saturation of optical transitions and therefore consists in *absorptive bistability* or rather, when k depends on E, show *refractive*

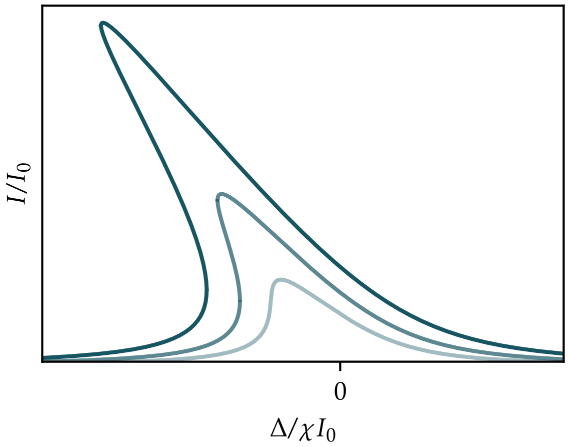

Figure 5.1: Depiction of optical bistability in a resonator. Darker shades of blue depict increasing input intensity. As the input intensity increases, the Lorentzian profiles get more and more distorted as a result of a Kerr nonlinearity. The axis labels are defined from equation (5.2).

bistability. In any case, we also note from the above equation that a change of these parameters can be interpreted as an effective modification of the resonator length.

Refractive bistability is obtained in the case of a Kerr medium, which index of refraction kc/ω features a linear dependency on the field E. This is the typical situation realized for cold atomic gases in optical cavities; in the dispersive regime the intracavity light field acts as an optical potential for the atoms, modifying their density overlap with the cavity mode and thus their coupling to light. In turn, this modified coupling impacts the effective length of the cavity and the atoms effectively act as a Kerr medium in the dispersive regime, making the coupled atoms-cavity system feature optical bistability.

In the absence of absorption, the intracavity intensity can generally be put under the form

$$I = \frac{I_0}{1 + (\Delta + \chi I)^2} \tag{5.2}$$

where Δ represents the detuning between the empty cavity resonance frequency and the frequency of the light field, and χ is the Kerr parameter quantifying the strength of the optical bistability. If $\chi = 0$ we recover the usual Lorentzian lineshape for the cavity output intensity. We display some spectra $I(\Delta)$ computed from the above equation for increasing values of I_0 in figure 5.1. All spectra feature optical bistability which emerges as a strong distortion of the originally Lorentzian profile towards negative detunings. The bistable branches appear in the distorted region, where $I(\Delta)$ features multiple solutions.

5.1.2 Response function from light-matter coupling

We now show how our atoms-cavity coupled system exhibits an optical bistability, its link to density response and our measurement methods to extract its value from cavity transmission spectra.

Hamiltonian of the system

We start from the expression of the Hamiltonian describing a two-component interacting Fermi gas coupled to light. Expressed in the dispersive coupling regime, as introduced in section 2.1.3, and in the presence of an external coherent on-axis driving field it reads

$$\hat{H} = \hat{H}_0 + \hat{H}_{\text{light}} + \hat{H}_{\text{d}} + \hat{H}_{\text{lm}}, \tag{5.3}$$

and we recall in what follows the expression for each of its terms, in a frame rotating at the driving field frequency and setting $\hbar = 1$ for now. The Hamiltonian $\hat{H}_0$ encompasses the contributions from the external trapping potential V_{t}, the kinetic energy and the two-body contact interactions with

$$\hat{H}_0 = \sum_{\sigma} \int d\mathbf{r} \hat{\psi}^{\dagger}_{\sigma}(\mathbf{r}) \left[-\frac{\nabla^2}{2m} + V_{\text{t}}(\mathbf{r}) \right] \hat{\psi}_{\sigma}(\mathbf{r}) + \int d\mathbf{r} d\mathbf{r}' \hat{\psi}^{\dagger}_{2}(\mathbf{r}') \hat{\psi}^{\dagger}_{1}(\mathbf{r}) V_{\text{p}}(|\mathbf{r} - \mathbf{r}'|) \hat{\psi}_{1}(\mathbf{r}) \hat{\psi}_{2}(\mathbf{r}') \tag{5.4}$$

where V_{p} is the pseudopotential described in section 3.1.2, and $\hat{\psi}^{\dagger}_{\sigma}(\mathbf{r})$ the fermionic field operator creating a particle of spin σ at a position $\mathbf{r}$. The bare cavity energy is represented by

$$\hat{H}_{\text{light}} = -\Delta_{\text{c}} \hat{a}^{\dagger} \hat{a} \tag{5.5}$$

where $\Delta_{\text{c}} = \omega_{\text{p}} - \omega_{\text{c}}$ is the detuning between the frequency of the fundamental TEM$_{00}$ mode of the cavity ω_{c} and the frequency of the driving probe ω_{p}. We explicitly include the contribution of the probe as a coherent driving field expressed with

$$\hat{H}_{\text{d}} = i\beta(\hat{a}^{\dagger} - \hat{a}) \tag{5.6}$$

with amplitude β. The remaining term of $\hat{H}$ describes the dispersive light-matter interaction via

$$\hat{H}_{\text{lm}} = \frac{g_0^2}{\Delta_a} \hat{a}^{\dagger} \hat{a} \int d\mathbf{r} \hat{n}(\mathbf{r}) \cos^2 \mathbf{k}_{\text{c}} \mathbf{r} \tag{5.7}$$

with $\hat{n} = \sum_{\sigma} \hat{n}_{\sigma} = \sum_{\sigma} \hat{\psi}^{\dagger}_{\sigma} \hat{\psi}_{\sigma}$ the total density operator and where the $\cos^2$ term comes from the spatial dependency of the single atom single photon coupling strength $g(\mathbf{r}) = g_0 \cos \mathbf{k}_{\text{c}} \mathbf{r}$, with $\mathbf{k}_{\text{c}}$ the cavity mode wavevector. We define $\Omega = g_0^2/\Delta_a$ the dispersive shift per particle of the cavity resonance frequency, with the frequency detuning between the cavity resonance frequency and the excited atomic manifold Δ_a being the largest energy scale of the problem.

Turning our attention to this dispersive interaction term, we put it in a more suitable form

$$\begin{aligned} \hat{H}_{\text{lm}} &= \Omega \hat{a}^{\dagger} \hat{a} \int d\mathbf{r} \hat{n}(\mathbf{r}) \frac{1}{2} \left(1 + \frac{e^{2i\mathbf{k}_{\text{c}}\mathbf{r}} + e^{-2i\mathbf{k}_{\text{c}}\mathbf{r}}}{2} \right) \\ &= \Omega \hat{a}^{\dagger} \hat{a} \left(\frac{N}{2} + \frac{1}{4} (\hat{n}_{2\mathbf{k}_{\text{c}}} + \hat{n}_{-2\mathbf{k}_{\text{c}}}) \right) \\ &= \Omega \hat{a}^{\dagger} \hat{a} \left(\frac{N}{2} + \hat{M} \right) \end{aligned} \tag{5.8}$$

where we have introduced the $\mathbf{q}$ Fourier component $\hat{n}_{\mathbf{q}}$ of the density operator. This interaction term can therefore be interpreted in a more intuitive picture: from the atoms point of view it imposes a lattice potential with a depth $\Omega \hat{a}^{\dagger} \hat{a}$ depending on the number of intracavity photons $\bar{n} = \left\langle \hat{a}^{\dagger} \hat{a} \right\rangle$, with a $\pi/|\mathbf{k}_{\text{c}}|$ spacing. On the other hand, this interaction term also describes a shift of the cavity resonance frequency added on top of the dispersive shift $\delta_\mathrm{c} = \Omega N/2$, which originates from a collective displacement of the atoms $\hat{M}$. Since this collective displacement is induced by the presence of the lattice potential which depends on $\bar{n}$, the total shift of the cavity resonance effectively depends on the intracavity intensity. The system therefore acts as a Kerr medium.

Optical bistability and linear response

Following the previous comment, we now seek to express the intracavity photon number in a form which makes the bistable behavior explicit. To this end, we write down the equation of motion for the cavity field using the Heisenberg-Langevin equation[1] [59, 204, 205] for $\hat{a}$, disregarding its fluctuations

$$\begin{aligned}\dot{\hat{a}} &= -i\left[\hat{H},\hat{a}\right] - \frac{\kappa}{2}\hat{a} \qquad (5.9)\\ &= -\left(i\Delta_\mathrm{c} + \frac{\kappa}{2}\right)\hat{a} - i\Omega\left(\frac{N}{2} + \hat{M}\right)\hat{a} - \beta, \qquad (5.10)\end{aligned}$$

with κ the natural linewidth of the cavity. In a mean-field description for the photons, we now look at the expectation value of the above expression in the steady-state limit $\dot{\hat{a}} = 0$,[2] and describe it as a complex number α so that $\left\langle \hat{a}^\dagger \hat{a}\right\rangle = |\alpha|^2 = \bar{n}$. Equation (5.10) then yields

$$\beta = -\left(i(\Delta_\mathrm{c} + \frac{N}{2}\Omega) + \frac{\kappa}{2}\right)\alpha - i\Omega\left\langle \hat{M}\hat{a}\right\rangle, \qquad (5.11)$$

with the value of $\left\langle \hat{M}\hat{a}\right\rangle$ left to evaluate. To do so, we employ linear response theory for a small perturbation of the system $\Omega\hat{M}\hat{a}^\dagger\hat{a}$ and write down the corresponding Kubo formula [206]

$$\left\langle \hat{M}\hat{a}\right\rangle = \left\langle \hat{M}\hat{a}\right\rangle_0 - i\int_{-\infty}^{0} dt \left\langle\left[\hat{M}(0)\hat{a}(0), \Omega\hat{M}(t)\hat{a}^\dagger(t)\hat{a}(t)\right]\right\rangle_0, \qquad (5.12)$$

where the expectation values $\langle\cdot\rangle_0$ are taken with respect to the undisturbed Hamiltonian, so that $\left\langle \hat{M}\hat{a}\right\rangle_0 = 0$ since the $\pm 2\mathbf{k}_\mathrm{c}$ Fourier components of the density are not populated. Imposing again the coherent, steady-state cavity field condition we obtain

$$\left\langle \hat{M}\right\rangle\alpha = -i\Omega\alpha|\alpha|^2 \int_{-\infty}^{0} dt \left\langle\left[\hat{M}(0), \hat{M}(t)\right]\right\rangle_0, \qquad (5.13)$$

or explicitly

$$\left\langle \hat{M}\right\rangle = -i\Omega|\alpha|^2 \int_{-\infty}^{0} dt \frac{1}{16}\left(\left\langle\left[\hat{n}_{2\mathbf{k}_\mathrm{c}}(0), \hat{n}_{-2\mathbf{k}_\mathrm{c}}(t)\right]\right\rangle_0 + \left\langle\left[\hat{n}_{-2\mathbf{k}_\mathrm{c}}(0), \hat{n}_{2\mathbf{k}_\mathrm{c}}(t)\right]\right\rangle_0\right), \qquad (5.14)$$

where we have used the condition $\left\langle \hat{n}_\mathbf{q}\hat{n}_{\mathbf{q}'}\right\rangle_0 = \delta_{\mathbf{q},-\mathbf{q}'}$ and the Heisenberg equation of motion to define the time evolution of the operators $\hat{O}(t) = e^{i\hat{H}t}\hat{O}e^{-i\hat{H}t}$.

To make sense of the previous equation, we conveniently introduce the retarded density-

---

[1] See also *e.g.* chapter 9.4 of [97] for a complete formal picture and application to a similar case.

[2] The steady-state condition ensures that at all time, the atomic density has adapted to the external perturbation.

density response function – or susceptibility – per atom [207]

$$\chi^{\mathrm{R}}(\mathbf{q},\omega) = -\frac{i}{N}\int_{-\infty}^{+\infty} dt\theta(t)e^{i\omega t}\left\langle\left[\hat{n}_{\mathbf{q}}(t),\hat{n}_{-\mathbf{q}}(0)\right]\right\rangle_0 \tag{5.15}$$

which characterizes the linear response of the density under a perturbation at wavevector **q** and frequency ω. We detail some of its properties and useful relations in appendix C. Its substitution in equation (5.14) under time-translation invariance yields

$$\left\langle\hat{M}\right\rangle = \frac{N\Omega}{8}\bar{n}\chi^{\mathrm{R}}(2\mathbf{k}_{\mathrm{c}},\omega=0) \tag{5.16}$$

where we used $\chi^{\mathrm{R}}(\mathbf{q},0)=\chi^{\mathrm{R}}(-\mathbf{q},0)$. Finally, we can rewrite equation (5.11) as

$$\alpha = -\frac{\beta}{\frac{\kappa}{2}+i\left(\Delta_{\mathrm{c}}+\delta_{\mathrm{c}}+\frac{N\Omega^2}{8}\bar{n}\chi^{\mathrm{R}}(2\mathbf{k}_{\mathrm{c}},0)\right)}, \tag{5.17}$$

or more conveniently in terms of intracavity photons

$$\bar{n} = \frac{\bar{n}_0}{1+\frac{4}{\kappa^2}\left(\delta+\eta\bar{n}\right)^2}, \tag{5.18}$$

with the maximal photon number $\bar{n}_0 = 4|\beta|^2/\kappa^2$, $\delta = \Delta_{\mathrm{c}}+\Omega N/2$ the detuning with respect to the dispersively shifted cavity resonance δ_{c} and $\eta = N\Omega^2\chi^{\mathrm{R}}(2\mathbf{k}_{\mathrm{c}},0)/8$. Put under this form, equation (5.18) features two important consequences for the system

- First, the optical nonlinearity is now made explicit via the $\delta+\eta\bar{n}$ term of the denominator which acts as the total refractive shift of the cavity with a linear dependency on the intracavity photon number and thus indeed describes a nonlinear Kerr medium [203], in a form similar to that of equation (5.2).
- Second, the strength of this nonlinearity given by η is directly proportional to the density response of the gas which then can be read out from optical spectra since in the experiment the detected photon number is proportional to $\bar{n}$.

The imaginary part of the density response function is connected to the dynamical structure factor via detailed balancing, and has been measured with high precision [52, 158, 161] using the dependency of the energy absorption rate of the gas on the structure factor [208]. However, the purely real zero-frequency – or static – response, which our system is sensitive to according to equation (5.16), has never been measured due to the impossibility to directly observe weak, short wavelength density perturbations in a strongly interacting system.

5.1.3 Experimental realization

Experimental parameters

To observe the onset of bistability in the experiment, we slightly modify the cavity transmission probing procedure described in section 2.1.3 in order to realize the steady-state criterion for the cavity field imposed in the previous paragraph. When acquiring optical spectra, we therefore set the probing beam frequency sweep rate to be slow against the typical timescales associated with

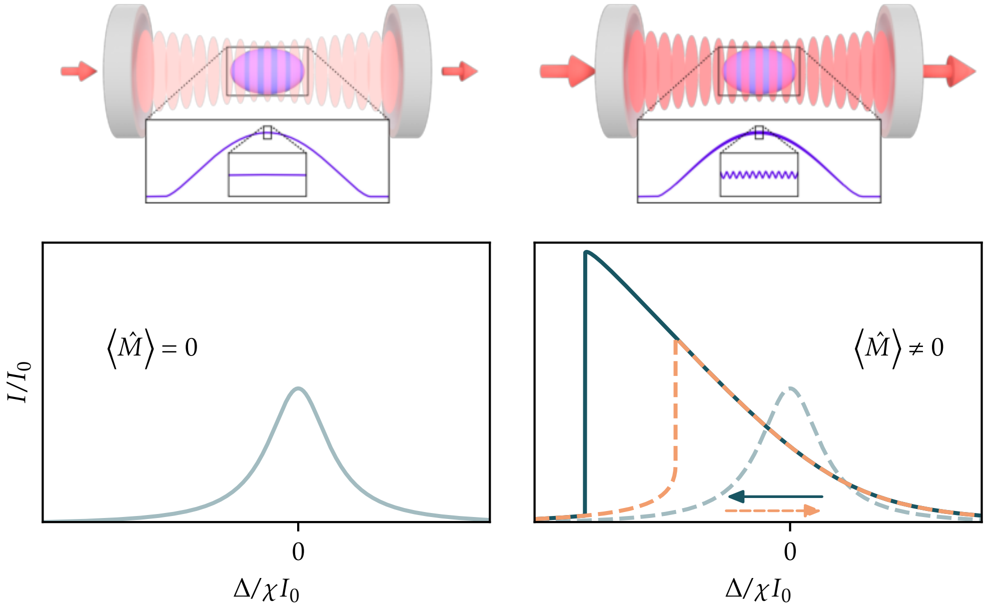
$\langle \hat{M} \rangle = 0$
I/I_0
0
$\Delta/\chi I_0$
$\langle \hat{M} \rangle \neq 0$
0
$\Delta/\chi I_0$

Figure 5.2: A strongly interacting Fermi gas trapped within the mode of the high-finesse cavity is probed by a weak laser on-axis laser beam. Left, for a low enough probe intensity the dipole force exerted by the resulting intracavity lattice does not perturb the atomic density and $\langle \hat{M} \rangle = 0$. With equation (5.18) one therefore recovers the usual symmetric Lorentzian cavity spectrum. Right, for large probe intensities the lattice imposes a weak density modulation with $\langle \hat{M} \rangle \neq 0$. The observed lineshapes $\bar{n}(\delta)$ then feature a significant asymmetry as a consequence of bistability (blue curve). When varying the detuning δ from positive to negative values, we continuously follow the highest stable branch for the photons (blue arrow). For the opposite detuning sweep direction, we would instead follow the lowest stable branch (orange dashed curve).

atomic motion which are of the order of $E_R^{-1} = 13.57\,\mu$s, so that from the field point of view the atomic density has instantaneously adapted to the imposed density modulation. In addition, we set the frequency sweep direction to go from positive (blue) to negative (red) detunings as to adiabatically follow the upper branch of the expected bistable spectra.[3] The probing procedure and effect on the atomic density is summarized in figure 5.2.

We prepare degenerate, balanced two-component Fermi gases with the procedure described in section 1.2. For the present experiments, the gases typically comprise $6 \cdot 10^5$ atoms in total, at a temperature of $T = 0.08\,T_F$ held in the crossed dipole trap with trapping frequencies $(\omega_x, \omega_y, \omega_z) = 2\pi \times (187, 565, 594)\,$Hz. Before probing the atoms-cavity energy spectrum, we set the offset magnetic field to 832 G, thus only considering unitary Fermi gases.

We tune the cavity length to detune its resonance frequency by $\Delta_a = -2\pi \times 13.9\,$GHz from the $\left|2s_{1/2}, m_J = -1/2\right\rangle \to \left|2p_{3/2}, m_J = -1/2\right\rangle$ – or $D_1\ \pi$ transition – where we work in the dispersive coupling regime.[4] The probe beam polarization is linearly oriented along the magnetic field direction to only couple to π transitions and during a single experimental run we dynamically sweep its frequency from the blue to the red side of the dispersively shifted cavity position δ_c, by $-2\pi \times 3\,\mathrm{MHz}$ in $3\,\mathrm{ms}$. This particular probe sweep time was also chosen to mitigate the effect of atomic loss during the measurement, and we give more detail on the procedure below. While the probe frequency is being swept, we record the arrival times of the photons leaking out of the cavity on the single-photon counter.

---

[3] In early explorations, we also swept the probe from the red to the blue side of the cavity to follow the lower bistable branch but found out that the instantaneous jump of the intracavity photon number towards maximal values would lead to more drastic heating and losses, making the signal harder to interpret.

[4] We also make sure to carefully avoid any photoassociation transition in the vicinity of the probing region.

Observation and measurement of the optical nonlinearity

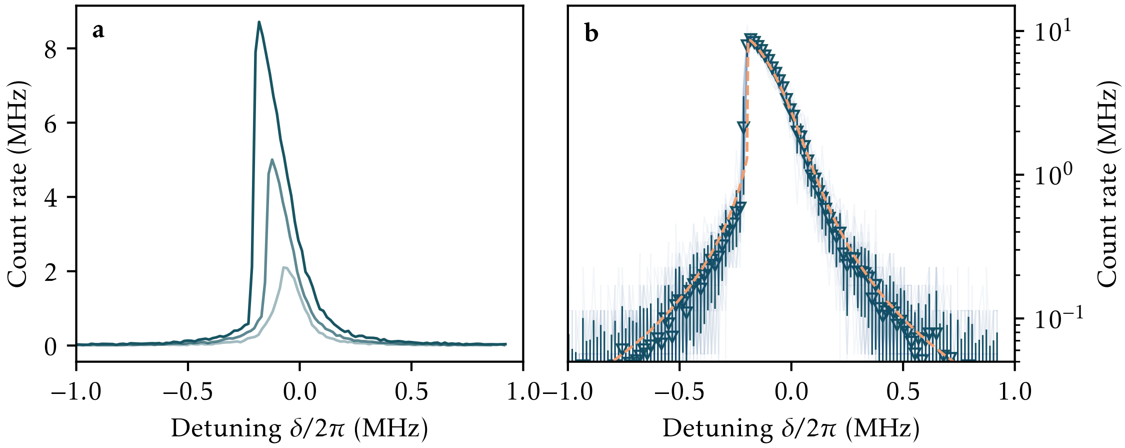

Figure 5.3: Onset of optical bistability in a strongly interacting Fermi gas coupled to light. **a** Averaged transmission spectra over 20 runs of the experiment for three different probe beam intensities. As the probe power increases so does the distortion of the measured profiles, from symmetrical Lorentzian (light blue) to a strongly modified one featuring a sharp edge on the red side, characteristic of the bistable behavior (dark blue). **b** Log-scale plot of 30 aggregated and averaged transmission spectra taken for the highest probe intensity (blue triangles) and of the fit of the averaged spectrum to equation (5.19) (orange dashed line).

We observe the onset of bistability originating from the Kerr nonlinearity of the system when increasing the intensity of the probing beam, as shown in figure 5.3**a**. The distortion of the transmitted Lorentzian profile and the emergence of the sharp edge towards the red side of the cavity resonance for higher intensities qualitatively match the predictions of equation (5.18). To quantify the strength of the nonlinearity, we infer η from a fit of the measured lineshapes $\bar{n}(\delta)$ to a modified version of the same equation

$$\frac{16\eta'^2}{\kappa^4}\bar{n}_{\mathrm{det}}^3 + \frac{16\delta\eta'}{\kappa^3}\bar{n}_{\mathrm{det}}^2 + \left(1 + \frac{4\delta^2}{\kappa^2}\right)\bar{n}_{\mathrm{det}} - \bar{n}_{0,\mathrm{det}} = 0 \tag{5.19}$$

where $\eta' = \eta/\epsilon$ with ϵ the quantum efficiency of the detection chain. The fit parameters are η', the dispersive shift δ_c contained in δ and $\bar{n}_{0,\mathrm{det}}$. The detected photon number $\bar{n}_{\mathrm{det}}$ is defined with respect to the intracavity photon number with

$$\bar{n}_{\mathrm{det}} = \epsilon \frac{\kappa}{2} \bar{n}. \tag{5.20}$$

The roots of equation (5.19) yield the solutions $\bar{n}_{\mathrm{det}}(\delta)$ for each value of δ. The maximal values of the real roots represent the upper branch of the bistable profile and therefore are chosen to fit the data and extract η', as shown in figure 5.3**b**. We explicitly fit the logarithm of the measured transmission spectrum to equally weight all data points, as we found that the value of the measured nonlinear parameter η' was extremely sensitive to the shape of the tails of the signals. To obtain good signal-to-noise ratios in the tails, we average 30 transmission spectra together, making sure to align them on their characteristic sharp edge to account for shot-to-shot experimental fluctuations. All in all, the fitting results show excellent agreement with equation (5.18) over two orders of magnitude and therefore allow us to confidently extract the values of η' as fitting parameters.

Losses and probe sweep rate determination

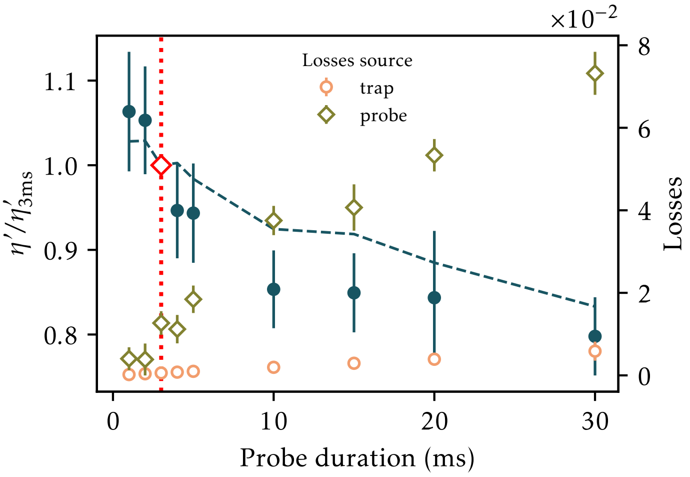

Figure 5.4: Effect of atomic losses on the measured optical nonlinearity strength η'. The red vertical dashed line and square mark the chosen probe duration, at which both the trap and probe induced losses are below the percent level (see text). We observe a clear decrease of η' for increasing probe durations (blue circles), a trend which is well explained by adapting our model to account for a linear loss rate as depicted by the dashed blue curve.

In order to select the optimal probe frequency sweep rate, we vary the probe duration for a fixed length of the frequency sweep interval and measure the relative variations of η' using the procedure described above. The results are shown in figure 5.4 and are normalized with respect to the value measured for a probe duration of 3 ms. We attribute the observed relative decrease of η' with increasing probe duration to atomic losses occurring during the measurement.

To confirm this hypothesis, we measure the atomic losses during the slow sweep of the probe frequency by measuring the relative change of dispersive shift δ_c before and after the sweep. In addition, we measure the losses purely due to the finite lifetime of the trapped Unitary Fermi gas by repeating the same procedure but sending no light on the atoms during the main sweep. Both of these measurements are also reported in figure 5.4. We then simulate the effect of a linear atomic loss rate L on the measured value of η' by adapting equation (5.18) with

$$\eta \longleftrightarrow \eta_{\mathrm{L}}(t) = \eta\left[1 - \frac{Lt}{N}\right] \tag{5.21}$$

$$\delta \longleftrightarrow \delta_{\mathrm{L}}(t) = \frac{d\Delta_{\mathrm{c}}}{dt}t + \frac{\Omega}{2}(N - Lt) \tag{5.22}$$

where $\frac{d\Delta_{\mathrm{c}}}{dt}$ is the probe frequency sweep rate. Using this model we simulate photon traces which take into account with the measured values of loss rates as a function of the probe duration. We then fit these simulated data to extract the corresponding nonlinearity strength η' and obtain the dashed blue curve of figure 5.4. Since the simulated data accounting for the measured loss rates feature the same relative trend as the real data, we conclude that atomic losses are indeed responsible for the decrease of η' for longer probe durations.

In the end we settle for a probing duration of 3 ms, at which the total losses are still around the percent level at unitarity and, as we will see later, under a few percents in the BEC–BCS crossover.

5.2 The connection between light-matter coupling and the universal thermodynamics of strongly interacting fermions

In the previous section, the connection between many-body physics and the optomechanical nonlinearity was shown to originate from the structure of the dispersive light-matter coupling Hamiltonian. We have in addition proved our ability to measure the strength of this nonlinearity by accurately modelling the observed optical transmission profiles acquired in the unitary regime.

In this section, we make the connection between the strength of the nonlinearity with the many-body physics of the system explicit by a calculation of the density response function $\chi^{\mathrm{R}}(\mathbf{q},\omega)$ in the strongly interacting and short-range regime. Taking the short-range limit is motivated by the spacing of the intracavity lattice probing the system compared to the mean interparticle distance with $2k_{\mathrm{c}} \approx 2.5k_{\mathrm{F}}$. In this limit, the density response can be asymptotically expanded using an operator product expansion (OPE) approach. The OPE is a standard approach of quantum field theory which states that the product of local operators at different points in space and time can be expanded in terms of local operators. It was originally introduced by Wilson [209] and was in particular used by Braaten and Platter [153, 210] to derive Tan's relations presented in chapter 3. In terms of density operators, the OPE can be generally expressed with

$$\hat{n}(\mathbf{R} + \mathbf{r}/2, t)\hat{n}(\mathbf{R} - \mathbf{r}/2, 0) = \sum_m c_m(\mathbf{r}, t)\hat{O}^m(\mathbf{R}, 0), \tag{5.23}$$

where $\hat{O}^m$ is a local operator and the Wilson coefficients $c_m(\mathbf{r}, t)$ are functions of the relative coordinates. We note that this form is reminiscent to that of equation (3.52) an as such one can expect the local operators $\hat{O}^m$ to depend on the universal thermodynamics of the gas. In the short-range limit, the OPE becomes a powerful tool as the first few terms with low scaling dimensions in the operator sum dominate the identity [45] and can therefore be applied to our system.

In a second part, we present the measurements of the optical nonlinearity strength in the BEC–BCS crossover and compare them to the OPE calculation.

5.2.1 The Operator Product Expansion

The detailed analysis and derivations of the OPE on the density response function have been presented in references [159, 211–213], so that we only focus here on the essential ideas and results. We also derive limit cases for the OPE results, providing independent boundaries in the far BEC and BCS regimes.

Derivation of the asymptotic expansion of χ^{R}

As the OPE involves products of local operators, we shall first express the susceptibility in terms of the local density. Taking the inverse Fourier transform of the density components in equation (5.15) we obtain

$$\chi^{\mathrm{R}}(\mathbf{q},\omega) = -\frac{i}{N}\int d\mathbf{R}\int d\mathbf{r}\int_{-\infty}^{+\infty} dt\theta(t)e^{i\omega t-2i\mathbf{k}\mathbf{r}}\langle[\hat{n}(\mathbf{R}+\mathbf{r}/2,t),\hat{n}(\mathbf{R}-\mathbf{r}/2,0)]\rangle_0 \tag{5.24}$$

where the correlator now explicitly involves products of local density operators. While we would like to apply the OPE to this retarded response function as it is directly accessible in the experiment, the diagrammatic nature of the calculations underlying the OPE makes preferable the use of time-ordered operators [211, 212]. We therefore introduce the time-ordered susceptibility

$$\chi^{\mathrm{T}}(\mathbf{q},\omega) = -\frac{i}{N}\int_{-\infty}^{+\infty} dte^{i\omega t}\left\langle T\left[\hat{n}_{\mathbf{q}}(t),\hat{n}_{-\mathbf{q}}(0)\right]\right\rangle_0 \tag{5.25}$$

where T denotes time-ordering and which features the same local development as in equation (5.24). Its connection with the retarded susceptibility is simple; following appendix C we have $\mathrm{Re}\left[\chi^{\mathrm{T}}(\mathbf{q},\omega)\right] = \mathrm{Re}\left[\chi^{\mathrm{R}}(\mathbf{q},\omega)\right]$. Since we only consider static perturbations with $\omega = 0$, detailed balancing ensures $\mathrm{Re}\left[\chi^{\mathrm{R}}(\mathbf{q},0)\right] = \chi^{\mathrm{R}}(\mathbf{q},0)$ so that $\chi^{\mathrm{R}}(\mathbf{q},0)$ can be retrieved from the calculation of $\chi^{\mathrm{T}}(\mathbf{q},0)$. Using equation (5.23) we get in a generic way

$$\chi^{T}(\mathbf{q},\omega) = \sum_m c_m(\mathbf{q},\omega)\int d^3R\frac{\langle\hat{O}^m(\mathbf{R})\rangle_0}{N}, \tag{5.26}$$

for which the Wilson coefficients c_m have been explicitly evaluated in the asymptotic limit of large q and up to order $(k_{\mathrm{F}}/q)^2$ in references [211, 212] and by our theory collaborator, Shun Uchino. The density response per atom can then be written

$$\chi^{\mathrm{T}}(\mathbf{q},\omega) \approx c_n(\mathbf{q},\omega) + c_{\mathcal{I}}(\mathbf{q},\omega)\tilde{\mathcal{I}} + c_{\mathcal{H}}(\mathbf{q},\omega)\tilde{\mathcal{H}} \tag{5.27}$$

with $\tilde{\mathcal{I}}$ and $\tilde{\mathcal{H}}$ respectively the total contact and internal energy per particle. The Wilson coefficients $c_{n,\mathcal{I},\mathcal{H}}(\mathbf{q},\omega)$ can be directly calculated in the limit $\omega = 0$ such that the OPE for $\chi^{\mathrm{R}}(\mathbf{q},0)$ reads

$$\chi^{\mathrm{R}}(\mathbf{q},0) = -\frac{2}{\epsilon_q} - \frac{8\tilde{\mathcal{H}}}{3\epsilon_q^2} - \frac{\pi\tilde{\mathcal{I}}}{2\epsilon_q q}\left[\frac{1}{1-\frac{2}{qa}} - \frac{8}{\pi qa(1-\frac{2}{qa})} + \frac{16}{\pi^2(qa)^2(1-\frac{2}{qa})} - \frac{8}{3\pi^2 qa}\right], \tag{5.28}$$

with a the scattering length, $q = |\mathbf{q}|$ and $\epsilon_q = \hbar^2 q^2/2m$. This expression features a singularity for $qa = 2$ and thus becomes diverging in the BEC regime, an unphysical situation since the density response and structure factor for an interacting Fermi gas in the BEC regime are known to be dominated by the excitation of free pairs and take a finite value [214, 215]. This feature originating from the uncontrolled nature of the asymptotic OPE is mitigated by considering the strongly interacting limit with $qa \gg 1$ so that

$$\chi^{\mathrm{R}}(\mathbf{q},0) = -\frac{2}{\epsilon_q} - \frac{8\tilde{\mathcal{H}}}{3\epsilon_q^2} - \frac{\pi\tilde{\mathcal{I}}}{2\epsilon_q q}\left[1 - \frac{8+24\pi-6\pi^2}{3\pi^2 qa}\right], \tag{5.29}$$

which do not feature a divergence anymore.[5] This result, via the explicit introduction of the contact, the internal energy and the scattering length, links the strength of the optical nonlinearity in our system $\eta \propto \chi^{\mathrm{R}}(\mathbf{q},0)$ with the universal thermodynamics of its many-body ground state via equation (5.18). Again, its interpretation is twofold; we can either control the strength of an optical nonlinearity by tuning the strength of the two-body interactions in the BEC–BCS crossover, or we can directly measure the universal many-body quantities by quantifying the strength of the measure nonlinearity, as shown in the previous section.

Limit cases

We can evaluate equation (5.29) in limits cases of the BEC–BCS crossover for $|(k_{\mathrm{F}}a)^{-1}| \gg 1$ to derive boundaries for our measurement of the density response as a function of the interaction parameter.

In the BEC limit, we already motivated the existence of a finite value for the density response of a gas of molecules. We calculate its value following the arguments presented in reference [214], without taking interactions effects into account, the dynamic structure factor $S_{\mathrm{BEC}}(\mathbf{q},\omega)$ for a non-interacting BEC is simply peaked at the recoil frequency of a molecule of mass $2m$ with

$$S_{\mathrm{BEC}}(\mathbf{q},\omega) = 2N\delta\left(\hbar\omega - \frac{\epsilon_q}{2}\right) \tag{5.30}$$

where the pre-factor $2N$ comes from the f–sum rule, see appendix C

$$N\epsilon_q = \hbar^2 \int_{-\infty}^{+\infty} d\omega\omega S_{\mathrm{BEC}}(\mathbf{q},\omega). \tag{5.31}$$

The density response per atom then follows from the structure factor[6]

$$\begin{aligned}\chi^{\mathrm{R}}_{\mathrm{BEC}}(\mathbf{q},0) &= -\frac{1}{N}\int_{-\infty}^{+\infty} d\omega\left[\frac{S_{\mathrm{BEC}}(\mathbf{q},\omega) + S_{\mathrm{BEC}}(-\mathbf{q},\omega)}{\omega}\right]\\ &= -\frac{8}{\epsilon_q}.\end{aligned} \tag{5.32}$$

On the other hand on the BCS side, we start from the expression of the total density response per atom $\chi(q,\omega)$ of a noninteracting Fermi gas in three dimensions [216]. At zero frequency where it is purely real, it reads

---

[5] As detailed below, we confirm with the experiment the validity of taking this $qa \gg 1$ limit by showing a good agreement of equation (5.29) with our measurements.

[6] We note that the following expression is the reason why this problem is trivial for bosonic systems; the density response per particle is simply constant and follows from textbook definitions [208].

$$\chi(q,0) = -\frac{3}{4E_\mathrm{F}}\left(1+\frac{4-q^2}{4q}\log\left|\frac{1+q/2}{1-q/2}\right|\right) \tag{5.33}$$

with E_F the Fermi energy and where $q = k/k_\mathrm{F}$ is a reduced wavevector, in units of the Fermi wavevector. In the limit of high q the previous expression can be expanded in powers of $1/q$, yielding

$$\chi(q,0) = -\frac{3}{4E_\mathrm{F}}\left(\frac{3}{8q^2}+\frac{32}{15q^2}+o\left(\frac{1}{q^4}\right)\right). \tag{5.34}$$

Introducing the internal energy per particle of the non-interacting gas $\tilde{\mathcal{H}}_\mathrm{BCS} = 3E_\mathrm{F}/4$ and the definition of q, we get

$$\chi(k,0) = -\frac{2}{\epsilon_k} - \frac{8\tilde{\mathcal{H}}_\mathrm{BCS}}{3\epsilon_k^2}. \tag{5.35}$$

We notice that this expression exactly matches equation (5.29) without the contact term, meaning that the OPE prediction faithfully reproduces the expected behavior of the density response of a non-interacting Fermi gas far on the BCS side of the Feshbach resonance. By making the substitution $k \leftrightarrow q$ we define the density response per atom in the BCS regime with

$$\chi^\mathrm{R}_\mathrm{BCS}(\mathbf{q},0) = -\frac{2}{\epsilon_q} - \frac{8\tilde{\mathcal{H}}_\mathrm{BCS}}{3\epsilon_q^2}. \tag{5.36}$$

Internal energy evaluation

To calculate the internal energy of the gas in the strongly interacting regime, we make use of the adiabatic sweep theorem defined by equation (3.60) of section 3.2.3. It relates the variation of internal energy of the system with scattering length to the contact, and we remind its formulation under the present chapter's notations

$$\frac{\partial\tilde{\mathcal{H}}}{\partial(1/a)} = -\frac{\hbar^2\tilde{\mathcal{I}}}{4\pi m}. \tag{5.37}$$

We obtain the internal energy per particle by integrating the above expression from unitarity to a^{-1}

$$\tilde{\mathcal{H}}(a^{-1}) = \tilde{\mathcal{H}}(0) - \frac{\hbar^2}{4\pi m}\int_0^{a^{-1}}\tilde{\mathcal{I}}(x)dx \tag{5.38}$$

where the energy per particle at unitarity is defined as a function of the Bertsch parameter $\sqrt{\xi}$ and the energy of the non-interacting gas with $\tilde{\mathcal{H}}(0) = \sqrt{\xi}\tilde{\mathcal{H}}_\mathrm{BCS}$ [47].

Even though the internal energy has already been evaluated in the BEC–BCS crossover [217, 218], equation (5.38) allows for the calculation of $\chi^\mathrm{R}(\mathbf{q},0)$ with the sole knowledge of the contact $\mathcal{I}$ as a function of the interaction parameter which, as presented in section 3.2.3, has been measured accurately in the crossover in the past decade [219–222]. We therefore rewrite the density response

$$\chi^\mathrm{R}(\mathbf{q},0) = -\frac{2}{\epsilon_q} - \frac{8}{3}\frac{1}{\epsilon_q^2}\left[\tilde{\mathcal{H}}(0) - \frac{\hbar^2}{4\pi m}\int_0^{a^{-1}}\tilde{\mathcal{I}}(x)d(x)\right] - \frac{\pi\tilde{\mathcal{I}}}{2q\epsilon_q}\left[1-\frac{8+24\pi-6\pi^2}{3\pi^2 qa}\right] \tag{5.39}$$

where it now only depends on scattering length and the contact. For the sake of completeness and to the detriment of simplicity, we reformulate the above expression in terms of the adimensionnal contact $\tilde{\mathcal{I}}/k_\mathrm{F}$ which is the quantity calculated and measured in the above-mentioned studies. Doing so, we also explicitly make the contact depend on the interaction parameter. In the end we obtain

$$\begin{aligned}\chi^\mathrm{R}(\mathbf{q},0) = -\frac{2}{\epsilon_q}\Bigg[1 + \left[\frac{k_\mathrm{F}}{q}\right]^2 \Bigg[&\sqrt{\xi} - \frac{2}{3\pi}\int_0^{\frac{1}{k_\mathrm{F}a}} \frac{\tilde{\mathcal{I}}}{k_\mathrm{F}}(x)dx\Bigg] \\ &+ \frac{\pi k_\mathrm{F}}{4q}\frac{\tilde{\mathcal{I}}}{k_\mathrm{F}}\left(\frac{1}{k_\mathrm{F}a}\right)\left[1 - \frac{8+24\pi-6\pi^2}{3\pi^2 k_\mathrm{F}a}\frac{k_\mathrm{F}}{q}\right]\Bigg]\end{aligned} \tag{5.40}$$

which now allows us to explicitly compute this response function in the BEC–BCS crossover, and compare it with measurements with $\mathbf{q} = 2\mathbf{k}_\mathrm{c}$.

5.2.2 Density response in the BEC–BCS crossover

Having established the formal link between the retarded density response $\chi^\mathrm{R}(\mathbf{q},0)$ controlling the strength of the optical nonlinearity and the two-body contact, we now focus on measuring the variations of η as a function of the interaction parameter $(k_\mathrm{F}a)^{-1}$ in the BEC–BCS crossover.

Experiment and comparison with theory

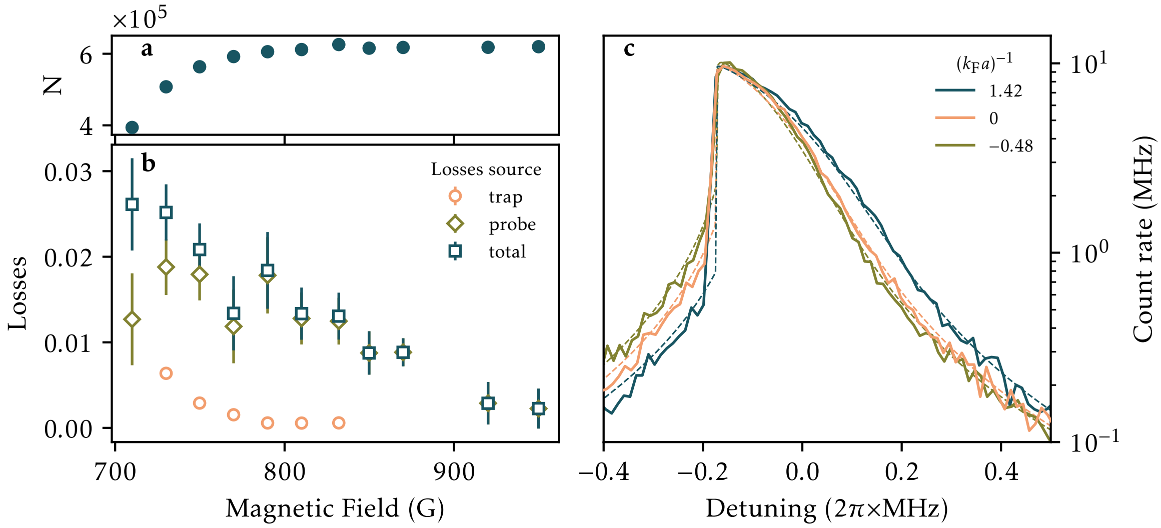

Figure 5.5: Observation of the Kerr nonlinearity in the BEC–BCS crossover. **a** Measured atom number via dispersive shift before the main probing pulse for magnetic field spanning the crossover. **b** Corresponding losses measured from the comparison of dispersive shifts before and after the main experiment (green diamonds) and before an after simply holding the atoms in the trap for the same total duration (orange circles). **c** Log-scale averages of 30 bistable profiles measured for three different values of the interaction parameter (solid lines) and their fit (dashed lines). As $(k_\mathrm{F}a)^{-1}$ increases the profiles become wider and sharper, but still require log-scale to be accurately fit.

We repeat the experiments presented in the previous section and vary the offset magnetic field at which the system is probed from 710 to 950 G. Doing so, we use the same probe frequency sweep rate of $-2\pi \times 3\,\mathrm{MHz}$ over 3 ms. In figure 5.5**a** we display the mean total atom number N measured for each of the magnetic fields, which shows a decreasing trend towards the BEC side of the Feshbach resonance because of an increased three-body loss rate. From the knowledge of atom numbers we compute the associated Fermi wavevector using $\hbar^2 k_\mathrm{F}^2/2m = \hbar(3\omega_x\omega_y\omega_z N)^{1/3}$ in the harmonic trap convention. We verify that even with different trap loss rates over the crossover, the total atomic losses occurring during the measurement for the considered probing duration are still well mitigated and below the few percents level, as shown by panel **b**. Finally, we present in panel **c** examples of fits of equation (5.19) to measured bistable profiles for notable points in the BEC–BCS crossover. In addition, we observe the consequence of a varying interaction strength: it controls both the width of the profiles and the sharpness of the jump from the upper to lower branch at fixed maximal intracavity photon number.

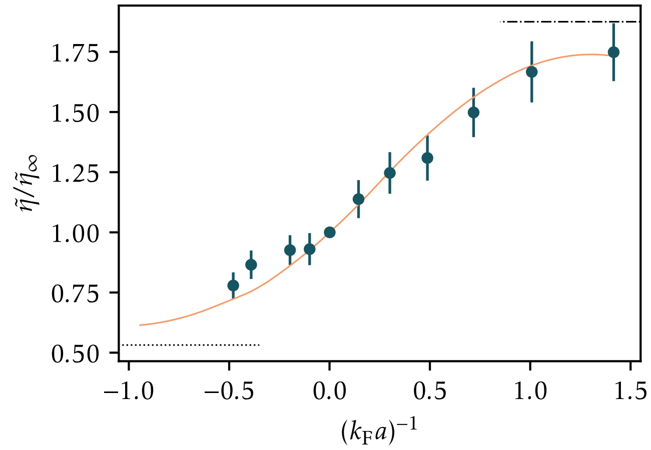

Figure 5.6: Variation of the short-range density response in the BEC–BCS crossover. The measurements of the density response are normalized by the value measured at unitarity (blue circles) and compared to the rescaled prediction of equation (5.40) (orange line), showing excellent relative agreement in the crossover. The dotted line corresponds to the prediction of equation (5.36) on the BCS side and the dash-dotted one is calculated with equation (5.32) on the BEC side, providing independent boundaries for our model.

Since our procedure measures the nonlinear strength rescaled by the quantum efficiency of the detection chain, which calibration is not known *a priori*, we rescale the values of $\eta' = \eta/\epsilon$ with respect to η'_∞ measured at unitarity for $1/a = 0$. Considering that the light shift per atom Ω does not vary in the dispersive regime with a change of the interaction parameter, the rescaled nonlinear strength reads

$$\begin{aligned} \frac{\eta'}{\eta'_\infty} &= \frac{\eta}{\eta_\infty} \\ &= \frac{N\chi^\mathrm{R}(2\mathbf{k}_\mathrm{c},0)}{N_\infty\chi^\mathrm{R}_\infty(2\mathbf{k}_\mathrm{c},0)}, \end{aligned} \tag{5.41}$$

effectively cancelling the dependency on the quantum efficiency. We apply the same rescaling to the theoretical predictions given by equation (5.40) in order to compare with the measurements.

The results are presented in figure 5.6 where $\tilde{\eta} = \eta'/N$ to account for atom number preparation variations in the crossover in accordance with panel **a** of figure 5.5. The excellent agreement of our data with the theory predictions confirm the deep connection between the optical nonlinearity and the universal, many-body physics of the Fermi gas and adds the static density response to the set of response functions experimentally accessible following Tan's relations. The agreement with equation (5.40) indicates that the increase of nonlinearity towards the BEC regime originates predominantly from the increase of the contact. On the BEC side, the agreement validates our extrapolation of expression (5.28) in the strongly interacting $qa \gg 1$ limit, and calls for a deeper understanding of the singularities of the OPE.

Detection efficiency calibration

From the strong relative agreement between the data and theory, we can turn to absolute comparisons in order to estimate the quantum efficiency of the detection chain ϵ which appears in the measured density response but of course not in the theory predictions. Indeed, using values at unitarity

$$\frac{\eta'_{\infty,\text{meas}}}{\eta_{\infty,\text{theo}}} = \frac{1}{\epsilon} \tag{5.42}$$

we obtain

$$\epsilon \approx 3\%, \tag{5.43}$$

including a reflective optical density filter with an attenuation factor of ~ 10 placed in front of the detector in order to desaturate it. This calibration of the detection efficiency can now be employed to infer the actual intracavity photon number at the peak of transmission profiles using equation (5.20). This gives $\bar{n}_0 \approx 1350$ which corresponds to a circulating power of $\approx 1.45\,\mu\text{W}$ inside the cavity, and thus to an intracavity lattice depth $\approx 0.2\,E_\text{R}$ with $E_\text{R}/h = 73.7\,\text{kHz}$ the single-photon recoil energy of ^6Li. The shallow lattice results in an actual density modulation of the atomic density of the order of a few percent therefore only weakly disturbing the system yet strikingly yielding an order-of-magnitude amplification of the cavity signals as seen in figure 5.3**a**.

Conclusion

Compared with spectroscopic probes also sensitive to the contact, the optomechanical coupling operates in the static limit where driving the cavity changes the properties of the steady-state of the system. In fact, the correspondence established by equation (5.16) also translates the optical nonlinearity into an interaction between the density fluctuations mediated by light, repulsive on the blue side of the cavity resonance and attractive on the other, similar to cavity-induced squeezing in spin ensembles [223]. Our experiment shows that this effect is controlled by the contact, which we have now proven to be directly accessible from optical spectra albeit differently as it was with the light-matter coupling to pairs presented in the previous chapter.

Following this remark, we could extend our optomechanical response measurement to the vicinity of a photo-association transition, where the dispersive shift acquires directly a contribution proportional to the contact. Correspondingly we could measure the optomechanical response functions such as the contact-density and contact-contact responses, describing three and four-body effects, which to our knowledge have never been observed experimentally.

Part III

Cavity Mediated Long Range Interactions and Their Interplay with Short Range Physics

Chapter 6

Density-wave ordering induced by photon-mediated long-range interactions

> On a level plain, simple mounds look like hills; and the insipid flatness of our present bourgeoisie is to be measured by the altitude of its great intellects.
>
> Karl Marx

Outline of the current chapter

6.1 Engineering photon-mediated long-range interactions in a strongly correlated Fermi gas 101
  6.1.1 Effective photon-mediated atom-atom interactions from strong light-matter coupling 101
  6.1.2 Phase transition to a density ordered state 105
  6.1.3 Density response function 108
6.2 Observation and characterization of density wave ordering 111
  6.2.1 Experimental procedure and observation of the phase transition . . 111
  6.2.2 Mapping the phase diagram 113
  6.2.3 Variation of the interaction parameter 114
  6.2.4 Experimental calibrations 116
6.3 Measurement of the density wave susceptibility 120
  6.3.1 Implementation of fixed-**q** Bragg spectroscopy 120
  6.3.2 Measurement of the density response in the presence of long-range interactions 122
6.4 Long-range interactions between pairs of atoms, an outlook 125
  6.4.1 Dispersive regime for the pairs 125

6.4.2 Interpretation as an optical Feshbach resonance 127

With this chapter we present a series of experiments conducted with our strongly interacting atomic ensemble dispersively coupled to light. In addition to the strong short-range interactions presented in details in chapter 3 we implement density-density long-range interactions, local in momentum, mediated by a transverse pump beam. For a sufficiently large strength of the long-range interactions, the atomic density spontaneously acquires a density modulation with a spatial structure matching that of the long-range interactions. This phase transition is accompanied by superradiant light scattering into the cavity mode.

This *self-organization* process to a density ordered phase was observed in wide range of atomic systems, from thermal gases [224] to BECs [60, 61] and lattice Bose gases [62, 225], and more recently in non-interacting Fermi gases [226]. In weakly interacting BECs this self-organization phase transition is a manifestation of the Dicke-superradiant phase transition and has allowed for the quantum simulation of supersolidity [227]. By exploiting more atomic internal levels and many cavity modes, a variety of rich phenomena ranging from magnetic ordering [228, 229] to dynamic gauge fields [230] and self-ordering in elastic optical lattices [231] were observed in bosonic systems. Even more intriguing phenomena ranging from threshold-less self-organization in low dimensions to cavity-induced superconducting paring and topological states have been predicted for fermions [69–71, 232–237]. We observed this phenomenon for the first time with strongly-interacting fermions and as such, the results and discussions of the present chapter closely follow our corresponding article [238].

The chapter is organized as follows: we start by presenting the theoretical framework to describe a strongly interacting Fermi gas coupled to a high-finesse cavity and pumped from the side by a far-detuned lattice beam. We show that this system features tunable long-range density-density interactions with a spatial structure inherited from the interference of the pump and cavity fields. By the examination of the density instabilities in such a system, we prove that it is prone to acquire a density order above a critical strength of the long-range interactions. We show that this critical point directly depends on the density susceptibility of the atoms at the wavevectors corresponding to the imposed density modulation. In a second part, we present our measurements and experimental realization of the phase transition to a density wave for a strongly interacting Fermi gas. We explore the regime where both interactions are strong: the contact interaction allows for the realization of the BEC–BCS crossover across which we systematically observe density wave ordering due to the long-range interactions. In a third part, we present a measurement scheme of the density response of the system in the presence of the long-range interactions, showing that it features a divergence at the location of the critical point as expected from a second order phase transition. We find that even in the presence of strong contact interactions, photon-mediated interactions modify the zero-frequency particle-hole susceptibility, and lead to the spontaneous formation of a density wave order above a critical strength in the attractive case. Finally, as an outlook, we apply the formalism and experimental techniques presented in the rest of the chapter to induce long-range interactions between pairs of atoms, in the vicinity of a photoassociation transition. We report on preliminary observations of a modified critical strength for the phase transition near the transition. We then introduce an interesting interpretation of the situation: the realization of an optical Feshbach resonance.

6.1 Engineering photon-mediated long-range interactions in a strongly correlated Fermi gas

Recent years have seen tremendous efforts to engineer more complex many-body systems using tailored longer-range interactions [239]. As a first key extension in this direction, dipolar interactions between atoms with large permanent magnetic moment were successfully used to create supersolid phases of bosons [240], marked by the onset of quantum droplets formation. In such systems however the long-range magnetic dipole-dipole interactions are not tunable, their strength and anisotropic spatial structure being set by the magnetic moments of the atomic species used.

Rydberg atoms provide another road to the realization of long-range interacting system, this time with anisotropic interactions tunable by the choice of Rydberg states [241, 242]. Rydberg dressing of interacting ^{6}Li atoms on a lattice has recently been used to realize quenches of strong long-range interactions [243], opening the way for simulation of the dynamics of the extended Fermi-Hubbard model. Fermionic polar molecules interacting with strong electric dipole moments are also expected to simulate exotic phases of matter, but have yet to be produced in the deeply degenerate quantum regime [244].

Cavity quantum electrodynamics on the other hand provides a tunable platform for engineering non-local, all-to-all interactions among polarizable particles mediated by cavity photons [58, 188, 245]. In a single-mode cavity this interaction has a spatially periodic, infinite-range structure which arises from the interference of a pump beam and the cavity mode [246], with a tunable strength given by the intensity of the pump beam. Since the spatial structure of the interaction is set by the interference pattern, it can be modified by the use of higher-order cavity modes and lead to rich phases [67].

In this section, we explicitly derive the structure of the long-range interactions stemming from the peculiar geometry of our system presented in figure B.2 of appendix B. We show that scattering of photons off single atoms lead to correlated recoils between the atom ensemble, delocalized over the cavity mode and which magnitude depends on the wavevectors of interference pattern between the pump and cavity fields. We then show how the existence of this long-range interaction can lead to density instabilities in the system and therefore to density ordering. Finally, we show how the density response of the system controls the phase transition and emphasize on how the small angle between the pump and cavity fields, as described in appendix B, allows us to address the fermionic nature of our system.

6.1.1 Effective photon-mediated atom-atom interactions from strong light-matter coupling

Hamiltonian of the system

The many-body Hamiltonian describing the atomic ensemble coupled to the cavity field in the dispersive regime was introduced in section 2.1.3 and reads

$$\hat{H} = \hat{H}_0 + \hat{H}_{\mathrm{light}} + \hat{H}_{\mathrm{lm}}. \tag{6.1}$$

The first two terms respectively correspond to the atomic and bare cavity energy contributions, given in the framework of second quantization and in a frame rotating at the pump beam frequency by

$$\begin{aligned}\hat{H}_0 =& \sum_\sigma \int d\mathbf{r}\hat{\psi}^\dagger_\sigma(\mathbf{r})\left[-\frac{\nabla^2}{2m} + V_\mathrm{t}(\mathbf{r})\right]\hat{\psi}_\sigma(\mathbf{r}) \\ &+ \int d\mathbf{r}d\mathbf{r}'\hat{\psi}^\dagger_2(\mathbf{r}')\hat{\psi}^\dagger_1(\mathbf{r})V_\mathrm{p}(|\mathbf{r}-\mathbf{r}'|)\hat{\psi}_1(\mathbf{r})\hat{\psi}_2(\mathbf{r}')\end{aligned} \tag{6.2}$$

$$\hat{H}_\mathrm{light} = -\Delta_\mathrm{c}\hat{a}^\dagger\hat{a} \tag{6.3}$$

where V_t is the external trapping potential, V_p the pseudopotential described in section 3.1.2, and $\hat{\psi}^\dagger_\sigma(\mathbf{r})$ the fermionic field operator creating a particle of spin σ at a position $\mathbf{r}$, expressed with $\hbar = 1$. Since the cavity gets populated with photons scattered from the transverse pump, the detuning $\Delta_\mathrm{c} = \omega_\mathrm{p} - \omega_\mathrm{c}$ is defined as the difference between the frequency of the fundamental TEM_{00} mode of the cavity ω_c and the frequency of the driving pump beam ω_p. Finally, $\hat{a}$ is the cavity photon annihilation operator so that the total intracavity photon number is $\hat{a}^\dagger\hat{a}$.

Compared with the previous chapters, we account for the presence of the off-resonant pump beam, which makes a 18° angle with the cavity mode as depicted in appendix B, in the light-matter interaction term $\hat{H}_\mathrm{lm}$ by expressing

$$\hat{H}_\mathrm{lm} = \sum_i \frac{1}{\Delta_{\mathrm{a},i}} \int d\mathbf{r}\hat{n}(\mathbf{r})\hat{\phi}^\dagger_i(\mathbf{r})\hat{\phi}_i(\mathbf{r}) \tag{6.4}$$

where $\hat{n} = \sum_\sigma \hat{n}_\sigma = \sum_\sigma \hat{\psi}^\dagger_\sigma\hat{\psi}_\sigma$ is the total density operator. This Hamiltonian contains the ground state energy shift contributions from the dispersive coupling of the light field to both the D_1 and D_2 π transitions, represented by the indices $i = 1, 2$. We define the detunings again with respect to the pump beam frequency such that $\Delta_{\mathrm{a},i} = \omega_\mathrm{p} - \omega_{\mathrm{a},i}$ and with $\omega_{\mathrm{a},i}$ the frequency of the D_i π transition of ^{6}Li. The total fields $\hat{\phi}_i(\mathbf{r})$ are defined as the sum of the cavity and coherent pump fields [246], taking their standing wave nature into account with

$$\hat{\phi}_i(\mathbf{r}) = g_i\hat{a}\cos\mathbf{k}_\mathrm{c}\mathbf{r} + \Omega_i\cos\mathbf{k}_\mathrm{p}\mathbf{r}, \tag{6.5}$$

g_i being the single atom single cavity photon coupling strength to the D_i π transition and Ω_i the pump Rabi frequency for the same transition. Equation (6.4) can therefore be explicitly put under the form

$$\hat{H}_\mathrm{lm} = \int d\mathbf{r}\hat{n}(\mathbf{r})\left[U_0\hat{a}^\dagger\hat{a}\cos^2\mathbf{k}_\mathrm{c}\mathbf{r} + V_0\cos^2\mathbf{k}_\mathrm{p}\mathbf{r} + \eta_0(\hat{a}+\hat{a}^\dagger)\cos\mathbf{k}_\mathrm{c}\mathbf{r}\cos\mathbf{k}_\mathrm{p}\mathbf{r}\right], \tag{6.6}$$

which is the total effective lattice potential experienced by the atoms in the dispersive regime [205], with

$$U_0 = \frac{g_1^2}{\Delta_{\mathrm{a},1}} + \frac{g_2^2}{\Delta_{\mathrm{a},2}}, \tag{6.7}$$

$$V_0 = \frac{\Omega_1^2}{\Delta_{\mathrm{a},1}} + \frac{\Omega_2^2}{\Delta_{\mathrm{a},2}}, \tag{6.8}$$

$$\eta_0 = \frac{g_1\Omega_2}{\Delta_{\mathrm{a},1}} + \frac{g_2\Omega_1}{\Delta_{\mathrm{a},2}}, \tag{6.9}$$

the two-photon Rabi frequencies associated with each of the terms of equation (6.6) which respectively depict

- An optical lattice of depth $U_0\hat{a}^\dagger\hat{a}$ associated with the TEM$_{00}$ mode of the cavity field, dispersively shifting the cavity resonance frequency as described in the previous chapters. We define the resulting dispersive shift with $\hat{\delta}_\mathrm{c} = U_0\hat{a}^\dagger\hat{a}\int d\mathbf{r}\hat{n}(\mathbf{r})\cos^2\mathbf{k}_\mathrm{c}\mathbf{r}$, and the corresponding shifted pump-cavity detuning $\hat{\tilde{\Delta}}_\mathrm{c} = \Delta_\mathrm{c} - \hat{\delta}_\mathrm{c}$.
- A second, 1D optical lattice associated with the pump. Its depth V_0 is directly proportional to the power of the beam. In what follows, we include the contribution from this term in the atomic Hamiltonian $\hat{H}_0$.
- A third, 2D optical lattice resulting from the interference between the coherent pump and the vacuum cavity field. Its depth is given by the photon scattering rate η_0 between the pump and cavity fields, a process analogous to Rayleigh scattering which originates from the dispersive interaction with the atomic density.

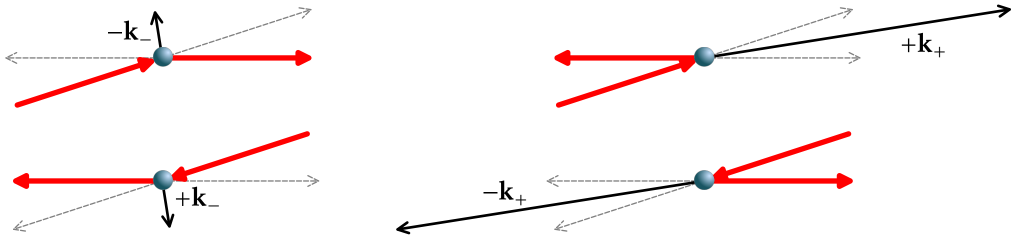

Figure 6.1: Two-photons single-atom scattering processes depicting the total momenta imparted on single atoms by the dispersive interaction term. The red arrows depict the momentum of the photons while the gray dashed ones correspond to atomic recoils which sum up to $\pm\mathbf{k}_\pm$. We only show the processes where a photon is first absorbed from the pump and scattered back into the cavity mode, but the reverse process is as likely to happen.

The crucial part of the light-matter interaction for the present chapter lies in this interference term. Simply put, in the dispersive regime, it describes the ability of the pump and cavity fields to coherently exchange photons via atomic absorption and emission processes. We depict these two-photons, single-atom scattering processes in figure 6.1 where each scattering event is accompanied by a momentum kick of the atom. For clarity, we only show processes starting from the virtual absorption of a pump photon followed by its emission into the cavity mode but the reverse situation where a cavity photon is first absorbed is equally likely. We note $\pm\mathbf{k}_\pm$ the total momentum kicks imparted on the atoms by the two-photon scattering processes, defined as

$$\begin{aligned}\cos\mathbf{k}_\mathrm{c}\mathbf{r}\cos\mathbf{k}_\mathrm{p}\mathbf{r} &= \frac{1}{2}\left[\cos\left(\mathbf{k}_\mathrm{c}\mathbf{r}+\mathbf{k}_\mathrm{p}\mathbf{r}\right)+\cos\left(\mathbf{k}_\mathrm{c}\mathbf{r}-\mathbf{k}_\mathrm{p}\mathbf{r}\right)\right]\\ &= \frac{1}{2}\left[\cos\mathbf{k}_+\mathbf{r}+\cos\mathbf{k}_-\mathbf{r}\right]\end{aligned} \tag{6.10}$$

from an expansion of the spatial structure of the last term of equation (6.6).

We define the *order parameter* $\hat{\Theta} = \int d\mathbf{r}\hat{n}(\mathbf{r})\cos\mathbf{k}_\mathrm{c}\mathbf{r}\cos\mathbf{k}_\mathrm{p}\mathbf{r}$, which quantifies the spatial overlap between the atomic density and the interference lattice. From equation (6.6), this term directly controls the photon scattering rate between the pump and cavity fields. It can be expressed in terms of the Fourier components of the density operator as introduced in section 5.1.2 with

$$\hat{\Theta} = \frac{1}{4}(\hat{n}_{\mathbf{k}_+} + \hat{n}_{-\mathbf{k}_+} + \hat{n}_{\mathbf{k}_-} + \hat{n}_{-\mathbf{k}_-}), \tag{6.11}$$

so that the total Hamiltonian for the system can be expressed as

$$\hat{H} = \hat{H}_0 - \hat{\tilde{\Delta}}_{\mathrm{c}}\hat{a}^\dagger\hat{a} + \eta_0(\hat{a} + \hat{a}^\dagger)\hat{\Theta}. \tag{6.12}$$

For an unperturbed system with η_0, with either a homogeneous or slowly varying density, $\left\langle\hat{\Theta}\right\rangle = 0$ and scattering events from the pump photons into the cavity mode are suppressed. In the absence of an external on-axis drive and up to fluctuations, the cavity mode is thus not populated.

In the following paragraph we show that despite a suppressed scattering rate of pump photons into the cavity mode, virtual photons can still be exchanged between atoms and mediate long-range interactions between them, with a range extending over the whole cavity mode volume [58, 204, 247].

Photon-mediated long-range interactions

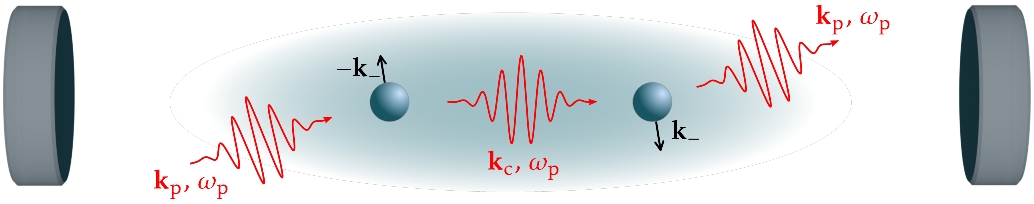

$\mathbf{k}_\mathrm{p}$, ω_p
$-\mathbf{k}_-$
$\mathbf{k}_-$
$\mathbf{k}_\mathrm{c}$, ω_p
$\mathbf{k}_\mathrm{p}$, ω_p

Figure 6.2: Long-range interaction processes between atoms stemming from single-atom scattering processes. This specific example pictures how correlated recoils between atoms at $\pm\mathbf{k}_\pm$ emerge from successive scattering events.

In the limit where the energy scale associated with the cavity photons given by $\hat{\tilde{\Delta}}_{\mathrm{c}}$ is large against the one associated to atomic displacements – of the order of the recoil energy E_R – we assume that the cavity field instantaneously adapts to and adiabatically follows any atomic dynamics. Writing down the Heisenberg-Langevin equation of motion for the cavity field,

$$\begin{aligned} \frac{d}{dt}\langle\hat{a}\rangle &= -i\left\langle\left[\hat{H},\hat{a}\right]\right\rangle - \frac{\kappa}{2}\langle\hat{a}\rangle \\ &= i\left[\tilde{\Delta}_{\mathrm{c}}\langle\hat{a}\rangle - \eta_0\left\langle\hat{\Theta}\right\rangle\right] - \frac{\kappa}{2}\langle\hat{a}\rangle \end{aligned} \tag{6.13}$$

where we have included the natural cavity linewidth κ, the adiabatic condition for the cavity field means that we can set

$$\frac{d}{dt}\hat{a} = 0 \tag{6.14}$$

by considering its steady state. We obtain

$$\langle \hat{a} \rangle = \frac{\eta_0 \left\langle \hat{\Theta} \right\rangle}{\tilde{\Delta}_c + i\frac{\kappa}{2}}, \tag{6.15}$$

which emphasizes the point raised in the previous paragraphs, in the steady state limit the cavity field serves as a measure of the overlap between the atomic density and the pump-cavity interference lattice quantified by $\left\langle \hat{\Theta} \right\rangle$. As a crucial consequence, because of the one-to-one correspondence given by the above equations between $\hat{\Theta}$ and $\hat{a}$, a measurement of a finite cavity field implies the existence of a modulation of the atomic density by the 2D optical lattice.

We then perform the adiabatic elimination of the cavity field in equation (6.12) with the use of a high-frequency expansion of equation (6.15) in the interaction picture for the photon [248]. To first order in $1/\tilde{\Delta}_c$ we obtain

$$\hat{H}_{\text{eff}} = \hat{H}_0 + \mathcal{D}_0 \hat{\Theta}^2, \tag{6.16}$$

with

$$\mathcal{D}_0 = \tilde{\Delta}_c \eta_0^2 / (\tilde{\Delta}_c^2 + \kappa^2) \tag{6.17}$$

the strength of the long-range interactions. Because its signs follows that of $\tilde{\Delta}_c$, it either corresponds to attractive or repulsive interactions, depending on the sign of $\tilde{\Delta}_c$. Equation (6.16) now effectively describes the interaction processes in an *atom only* picture, the effect of the scattered virtual photons being contained in the $\hat{\Theta}^2$ term with

$$\hat{\Theta}^2 = \int d\mathbf{r} d\mathbf{r}' \hat{n}(\mathbf{r}) \hat{n}(\mathbf{r}') \cos \mathbf{k}_c \mathbf{r} \cos \mathbf{k}_p \mathbf{r} \cos \mathbf{k}_c \mathbf{r}' \cos \mathbf{k}_p \mathbf{r}', \tag{6.18}$$

which represents an effective density-density interaction. An example of such an interaction process for two atoms is shown in figure 6.2. Its range is only limited by the mode volume of the cavity mode and therefore, under the assumption that the typical atomic clouds are fully contained within the mode of the cavity, is of infinite nature. The strength of this cavity-mediated *long-range* density-density interaction is given by $\mathcal{D}_0$. From equation (6.9), we directly see that $\mathcal{D}_0$ is in particular controlled by the power of the pump beam, which tunability then allows for the variation of the infinite-range interaction strength in the experiment.

6.1.2 Phase transition to a density ordered state

Having motivated the existence of an effective density-density long-range interaction for our fermionic system coupled to light, we show in this section how this interaction term may lead to a structural phase transition of the atomic ensemble. We start by proving that there exists a critical value for the long-range interaction strength $\mathcal{D}_{0C}$ above which $\left\langle \hat{\Theta} \right\rangle$ acquires a finite value. We show in a second time that this critical value is in particular determined by the density-density response of the unperturbed system, the same function we introduced in chapter 5.

The general idea developed in the literature for bosonic self-organization [249] and in theory proposals for non-interacting fermions [233, 234, 250] to infer the critical point for the phase transition is based on a calculation of $\left\langle \hat{\Theta} \right\rangle = \bar{\Theta}$ at equilibrium, determined by the global minima of the free energy $\mathcal{F}$. In such systems, the location of the minima of free energy and therefore the possible values for $\bar{\Theta}$ follow a threshold behavior. This is usually derived by expressing $\mathcal{F}$ in even powers of the order parameter, following Landau theory for thermal phase transitions [251].

Generally one can write

$$\mathcal{F} = \mathcal{F}_0 + \alpha\bar{\Theta}^2 + \beta\bar{\Theta}^4 + \mathcal{O}\left(\bar{\Theta}^6\right) \tag{6.19}$$

with equilibrium points given by $\partial\mathcal{F}/\partial\bar{\Theta} = 0$. The solutions of this equation depend on the sign of α/β, which in turn depends on the strength of the long-range interactions so that above a certain critical strength, the ratio flips sign. This change of sign therefore corresponds to the emergence of different equilibrium points for the free energy and thus of different values of $\bar{\Theta}$. Below the critical point, we see from equation (6.19) that the trivial minimal free energy is given for $\bar{\Theta} = 0$, a situation for which the atomic density is unperturbed or equivalently, as we have shown, the cavity field is not populated. On the other hand, above the critical point we have $\bar{\Theta} \neq 0$ and the system features a modulation of its density, accompanied by scattering of light inside the cavity mode.

Free energy and density functional

In order to apply a similar reasoning to our strongly-interacting system we resort to a general density functional theory approach to construct a thermodynamical functional which, as the Legendre transform of the free energy, carries the same amount of information about the system. In particular, it will be defined to only depend on the value of the control variable $\bar{\Theta}$. This approach is motivated by the fact that a direct analytic calculation of the free energy for a strongly correlated system is extremely challenging. We proceed by following a method presented by Antoine Georges to derive instabilities of the Ising magnet [252–254] and adapt it to our system.

We start from the Hamiltonian given by equation (6.16), and constrain the expectation value of $\hat{\Theta}$ to take a given value $\bar{\Theta}$ via the introduction of a Lagrange multiplier λ, thermodynamical conjugate to $\hat{\Theta}$ such that

$$\hat{H} \rightarrow \hat{H}(\lambda) = \hat{H}_0 + \mathcal{D}_0\hat{\Theta}^2 - \lambda\hat{\Theta}. \tag{6.20}$$

We note that this step is completely analogous to introducing a given value of the chemical potential μ in order to enforce a given value for the particle number N which then verifies $\left\langle\hat{N}\right\rangle = N$. In our case, the value of λ is then fixed as for the system to verify $\left\langle\hat{\Theta}\right\rangle = \bar{\Theta}$. We also note that by design, the minimization of the energy associated with the unconstrained Hamiltionian of equation (6.20) will yield the same equilibrium points as the minimization of energy associated with the Hamiltionian of equation (6.16) under the constraint $\left\langle\hat{\Theta}\right\rangle = \bar{\Theta}$.

We then introduce the density functional $\Omega(\bar{\Theta}, \lambda)$ as

$$\Omega(\bar{\Theta}, \lambda) = \mathcal{F} + \lambda\bar{\Theta}, \tag{6.21}$$

which is nothing else than the Legendre transform of the free energy $\mathcal{F}$ – often called *effective action* in the condensed matter literature – in terms of the parameters $\bar{\Theta}$ and λ. As such, Ω carries the same information about the system as any other thermodynamical potential, but is expressed in a more convenient way to be manipulated in terms of $\bar{\Theta}$ and λ. By design, we also now have an equivalence between imposing $\left\langle\hat{\Theta}\right\rangle = \bar{\Theta}$ and the equilibrium condition $\partial\Omega/\partial\lambda = 0$. In principle, this differential equation can be employed to infer the value of $\lambda(\bar{\Theta})$ which forces the system to fulfill $\left\langle\hat{\Theta}\right\rangle = \bar{\Theta}$, but in practice we are again limited by our ability to express $\mathcal{F}$ in a convenient way to write down any analytical formula for $\lambda(\bar{\Theta})$. We can however consider its value to be known and simply define a new functional $\Gamma\left[\bar{\Theta}\right]$ such that

$$\Gamma\left[\bar{\Theta}\right] = \Omega(\bar{\Theta}, \lambda(\bar{\Theta})). \tag{6.22}$$

In the following step, we make explicit the dependency of Γ on the long-range interaction strength by expanding it with

$$\Gamma\left[\bar{\Theta}\right] = \Gamma_0\left[\bar{\Theta}\right] + \int_0^{\mathcal{D}_0} d\mathcal{D}_0 \frac{\partial \Gamma}{\partial \mathcal{D}_0}[\Theta], \tag{6.23}$$

where the term $\Gamma_0\left[\bar{\Theta}\right]$ is the non-interacting functional, taken for a system with $\mathcal{D}_0 = 0$ and with a different Lagrange multiplier λ_0 which still ensures $\left\langle\hat{\Theta}\right\rangle_0 = \bar{\Theta}$. The derivative under the integral of the above equation can be computed directly from an application of the Hellmann-Feynmann theorem such that

$$\frac{\partial \Gamma}{\partial \mathcal{D}_0} = \frac{\partial \mathcal{F}}{\partial \mathcal{D}_0} \underset{\text{H.F.}}{=} \left\langle \frac{\partial \hat{H}}{\partial \mathcal{D}_0} \right\rangle = \left\langle \hat{\Theta}^2 \right\rangle \tag{6.24}$$

where the derivatives are evaluated at constant $\bar{\Theta}$ and $\lambda(\bar{\Theta})$. We then obtain an exact form of the functional

$$\Gamma\left[\bar{\Theta}\right] = \Gamma_0\left[\bar{\Theta}\right] + \int_0^{\mathcal{D}_0} d\mathcal{D}_0 \left\langle \hat{\Theta}^2 \right\rangle\Big|_{\bar{\Theta},\lambda(\bar{\Theta})}. \tag{6.25}$$

Mean-field approximation and density instabilities

Effectively, the Legendre transform switched the representation of the system where λ was a control variable of the free energy $\mathcal{F}$ to a more convenient situation, where the order parameter is now the control variable of a new potential. In the end, $\mathcal{F}(\lambda)$ and $\Gamma\left[\bar{\Theta}\right]$ carry the same information about the system but with a switch of the control and response parameters. This statement is better understood by writing down the following direct consequences of taking the Legendre transform [255]

$$\frac{\partial \mathcal{F}}{\partial \lambda} = -\bar{\Theta} \tag{6.26}$$

$$\frac{\partial \Gamma}{\partial \Theta} = \lambda, \tag{6.27}$$

and as a result, studying the instabilities of the free energy in terms of λ becomes equivalent to studying those of $\Gamma\left[\bar{\Theta}\right]$.

Its introduction as a new thermodynamic potential therefore allows us to study the stability of the system in terms of $\bar{\Theta}$ as the control variable. Our problem then now amounts to computing $\partial^2\Gamma/\partial\bar{\Theta}^2$ to look for instabilities. In order to do so, we first make an important simplification to the problem and perform a *mean-field approximation* by setting $\left\langle\hat{\Theta}^2\right\rangle = \bar{\Theta}^2$ and thus completely disregarding the correlations $\left\langle\hat{\Theta}^2\right\rangle - \left\langle\hat{\Theta}\right\rangle^2$. Equation (6.25) then reduces to

$$\Gamma\left[\bar{\Theta}\right] = \Gamma_0\left[\bar{\Theta}\right] + \mathcal{D}_0\bar{\Theta}^2, \tag{6.28}$$

which is a development of the free energy in even powers of $\bar{\Theta}$ as in Landau's theory, truncated at second order because of the mean-field approximation. It is likely that in order to capture the complete physical picture of the phase transition, one has to perform the full calculation including the neglected quantum correlations of equation (6.25). By defining the susceptibility of the system as [1]

$$\chi = \frac{\partial \bar{\Theta}}{\partial \lambda}, \tag{6.29}$$

equation (6.27) leads to

$$\frac{\partial^2 \Gamma}{\partial \bar{\Theta}^2} = \frac{\partial \lambda}{\partial \bar{\Theta}} = \chi^{-1}, \tag{6.30}$$

which, with equation (6.28), yields

$$\chi^{-1} = \chi_0^{-1} + 2\mathcal{D}_0 \tag{6.31}$$

or

$$\chi = \frac{\chi_0}{1 + 2\chi_0 \mathcal{D}_0} \tag{6.32}$$

with χ_0 the susceptibility of the system in the absence of long-range interactions. This last relation for the susceptibility is a well-known result for response functions computed in the mean-field approximation, often labelled as *Random Phase Approximation*. It features a divergence for a critical value of the interaction strength

$$\mathcal{D}_{0C} = -\frac{1}{2\chi_0}, \tag{6.33}$$

uniquely determined by the value of χ_0. The diverging susceptibility marks the onset of a second order phase transition[2], and for values of the interaction parameter $|\mathcal{D}_0| > |\mathcal{D}_{0C}|$ the susceptibility changes sign and the system becomes unstable towards acquiring a finite value of $\langle \hat{\Theta} \rangle$: towards *density wave ordering*.

Experimentally we can therefore access the phase transition using the dependency of $\mathcal{D}_0$ on the pump beam parameters given by equation (6.17). Increasing its absolute value amounts to either increasing the pump power or decreasing its detuning with respect to the dispersively shifted cavity resonance, in order to reach the required critical strength $\mathcal{D}_{0C}$. Above the critical point the system is expected to acquire a modulation of its density, with a spatial structure given by the geometry of the interference lattice described in equation 6.6 and this process is accompanied by scattering of light into the cavity mode. To convey a clear picture of the situation, we sketch the total light field when the system enters the ordered phase in figure 6.3.

6.1.3 Density response function

Before carrying on with the experimental observations of the phase transition, we first present in this section the physical meaning of the susceptibility χ and introduce a way to compute χ_0, allowing us to compare experimental measurements of $\mathcal{D}_{0C}$ with predictions coming from the equations obtained at the end of the previous section.

To unveil the role of χ as the density response function we again apply the idea of considering a small perturbation of the system in the form $-\lambda\hat{\Theta}$ so that the formalism developed in the previous section applies. In particular the definition for the susceptibility holds, and it verifies $\chi = \partial\bar{\Theta}/\partial\lambda$. Our goal is now to show that this quantity is indeed the static density response

---

[1] We show in the following paragraph that this seemingly arbitrary definition actually directly connects to the density response function or density susceptibility already discussed in chapter 5.

[2] Performing the mean-field approximation for the order parameter and neglecting its correlations has forced us to consider the phase transition to be of second order.

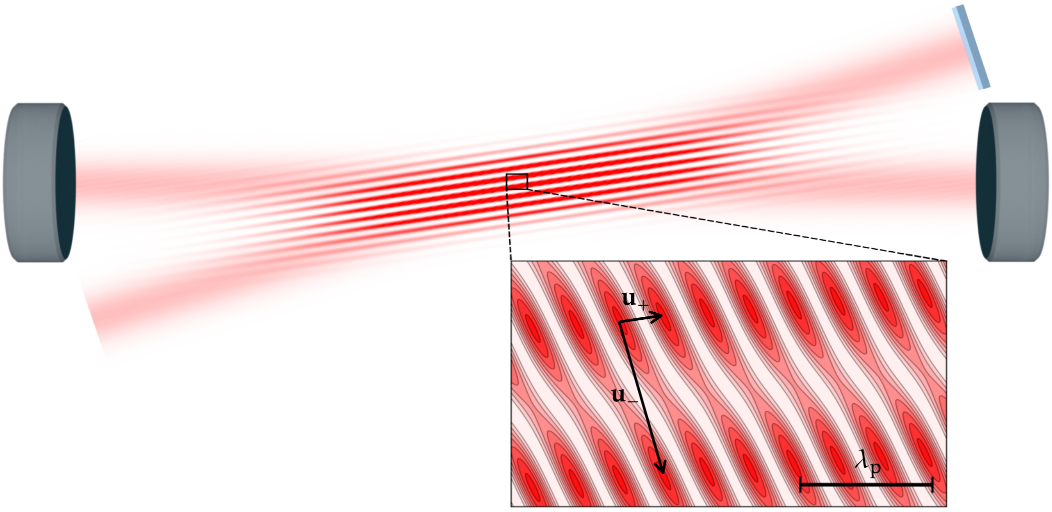

Figure 6.3: Geometry of the light fields above the critical point. We clearly observe the role played by the small angle between the pump and cavity fields. Their interference in the ordered phase yields a 2D lattice with wavevectors $\mathbf{k}_\pm$, imposing a density modulation with the same geometry on the atomic density (not displayed here). Below, we show a close-up view of the direct lattice with associated real space vectors $\mathbf{u}_\pm$ to further emphasize the large imbalance between $|\mathbf{k}_-|$ and $|\mathbf{k}_+|$. λ_p is the wavelength of the pump and cavity photons.

function of the gas, as introduced in chapter 5. We consider the system without long-range interactions such that $\chi = \chi_0$ and the first order response of the expectation value of $\hat{\Theta}$ to the perturbation is given by Kubo formula [206], such that

$$\left\langle \hat{\Theta} \right\rangle = \bar{\Theta} = \bar{\Theta}_0 + i\lambda \int_{-\infty}^{0} dt' \left\langle [\hat{\Theta}(0), \hat{\Theta}(t')] \right\rangle_0 \tag{6.34}$$

where the index 0 now refers to the absence of long-range interaction and of density perturbation, so that with the definition of χ

$$\chi_0 = \frac{\partial \bar{\Theta}}{\partial \lambda} = i \int_0^{\infty} dt \left\langle [\hat{\Theta}(t), \hat{\Theta}(0)] \right\rangle_0 . \tag{6.35}$$

The commutator is easily developed in terms of the time-dependent Fourier components of the density distribution $\hat{n}_\mathbf{q}(t)$ coming from the definition of the order parameter $\hat{\Theta}$ defined by equation (6.11). We recall the definition of the total time-retarded density-density response function

$$\chi^\mathrm{R}(\mathbf{q}, \omega) = -i \int_{-\infty}^{+\infty} dt \theta(t) e^{i\omega t} \left\langle \left[\hat{n}_\mathbf{q}(t), \hat{n}_{-\mathbf{q}}(0) \right] \right\rangle_0 , \tag{6.36}$$

such that equation (6.35) leads to

$$\chi_0 = -\frac{1}{16} \left[\chi^\mathrm{R}(\mathbf{k}_-, 0) + \chi^\mathrm{R}(-\mathbf{k}_-, 0) + \chi^\mathrm{R}(\mathbf{k}_+, 0) + \chi^\mathrm{R}(-\mathbf{k}_+, 0) \right], \tag{6.37}$$

which indeed is the sum of the density response functions of the atomic ensemble, evaluated at all the possible interference lattice wavevectors. We note that we again obtain a purely static response function, this is due to χ being defined in the thermodynamic ground state of the system, and as such χ_0 is a purely real-valued function. In addition, we have now made clear the existence of two different length scales for our system, associated with the density responses at $|\mathbf{k}_+|$ and $|\mathbf{k}_-|$. In the following we focus on deriving approximations to evaluate the density response contributions to χ_0 in these two regimes in order to obtain an estimation for $\mathcal{D}_{0\mathrm{C}}$.

Evaluation of the susceptibility

Defining the Fermi energy E_{F} with its value taken at the center of our trap, where the density is maximal, we have that for the typical gases we prepare at unitarity

$$|\mathbf{k}_-| = 0.54\, k_{\mathrm{F}} \tag{6.38}$$

$$|\mathbf{k}_+| = 3.39\, k_{\mathrm{F}} \tag{6.39}$$

or in terms of the recoil energy associated with scattering processes of total momenta $\pm\mathbf{k}_-$ and $\pm\mathbf{k}_+$

$$\epsilon_{\mathbf{k}_-} = 0.29\, E_{\mathrm{F}} \tag{6.40}$$

$$\epsilon_{\mathbf{k}_+} = 11.51\, E_{\mathrm{F}}, \tag{6.41}$$

defined with $\epsilon_q = \hbar^2|\mathbf{q}|^2/2m$.

In the regime $|\mathbf{k}_+| \gg k_{\mathrm{F}}$, which corresponds to the short wavelength contributions to χ_0, the density response can be evaluated in the BCS-BEC crossover using the product operator expansion technique presented in chapter 5. As shown there, the leading order contribution to the response function reads

$$\chi^R(\mathbf{k}_+, 0) \sim -2N/\epsilon_{\mathbf{k}_+}. \tag{6.42}$$

On the other hand, the long-wavelength contributions $\chi^R(\mathbf{q} = \pm\mathbf{k}_-, 0)$ are evaluated by considering the $\mathbf{q} \to 0$ limit. As presented in appendix C, the value of the local response function $\chi^R(0,0)$ is given by the compressibility sum rule

$$\chi^R(0,0) = -\int d\mathbf{r}\frac{\partial n}{\partial \mu} = -\int d\mathbf{r} n^2 \kappa, \tag{6.43}$$

where κ is the isothermal compressibility of the gas and can be inferred from the thermodynamic equation of state for the strongly interacting Fermi gas, which has been accurately measured in the BEC–BCS crossover as a function of the contact interaction strength [256, 257]. We use the interpolation formula for the universal thermodynamic functions provided in reference [256] to deduce the compressibility of the homogeneous Fermi gas, the quantity involved in equation (6.43). We then use the local density approximation to perform trap-averaging and to relate it to the Fermi energy E_{F} at the center of the trap.

All in all, we notice that throughout the BCS–BEC crossover, the ratio $\chi^R(\mathbf{k}_-)/\chi^R(\mathbf{k}_+)$ is the smallest in the far BCS regime and bounded from below by $3\epsilon_{\mathbf{k}_+}/4E_{\mathrm{F}}$, which is ~ 12 for our parameters. We therefore neglect the short wavelength contributions to the total response and simply consider

$$\chi_0 = \frac{1}{8}\int d\mathbf{r}\frac{\partial n}{\partial \mu}. \tag{6.44}$$

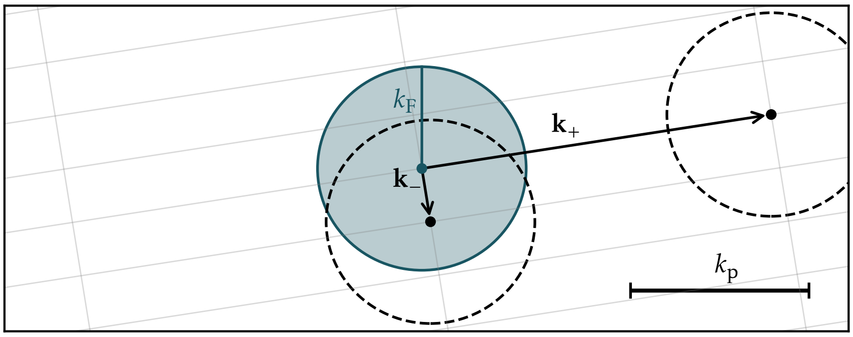

Figure 6.4: Momentum-space picture of the long-range interactions. Photon scattering from the pump into the cavity and vice versa via the atoms imparts momentum kicks $\pm\mathbf{k}_\pm$ onto the latter, displacing the Fermi surface (blue disc). Since $|\mathbf{k}_-| < k_F$, the photon-mediated interactions induce particle-hole excitations at the Fermi surface, which cost little energy to drive. k_p is the magnitude of the wavevector associated with the pump beam.

This hierarchy $|\mathbf{k}_+| \gg |\mathbf{k}_-|$ and its consequence in terms of the relative magnitudes of the associated density responses is made clear by figure 6.4, which represents the system in momentum space. The coupling between momentum modes coming from the large wavevector contributions is not restricted by Pauli principle, at least not without external distortion of the Fermi surface such as in reference [226]. However, the small wavevector contributions associated with $\pm\mathbf{k}_-$ directly address particle-hole excitations atop the Fermi surface at zero-frequency, as demonstrated by a largely increased density response. Equivalently, we see that it is much more energetically favorable for the system to self-modulate its density at $\pm\mathbf{k}_-$ than for the short-wavelength case. The general momentum dependency of the response function is well reproduced by Lindhard function [258], which only quantitatively holds for a noninteracting system.

6.2 Observation and characterization of density wave ordering

In this section, we now turn to the experimental observation of the phase transition to the density ordered state and relate it to the concepts developed above. In a first part we present the general measurement procedure and results, obtained for a unitary Fermi gas. In a second time, we extend our measurements to the BEC–BCS crossover and compare the measured critical values of $\mathcal{D}_0$ at which the phase transition sets with the theoretical predictions derived from the previous section, and do it as a function of the interaction parameter. Finally, and for completeness, we present some useful calibrations of the system.

6.2.1 Experimental procedure and observation of the phase transition

In the experiment, we prepare a degenerate Fermi gas of $N = 3.5\times 10^5$ ^{6}Li atoms equally populating the two lowest hyperfine states, trapped within a mode of our high-finesse optical cavity and in the vicinity of a broad Feshbach resonance at 832 G. The photon-mediated interactions

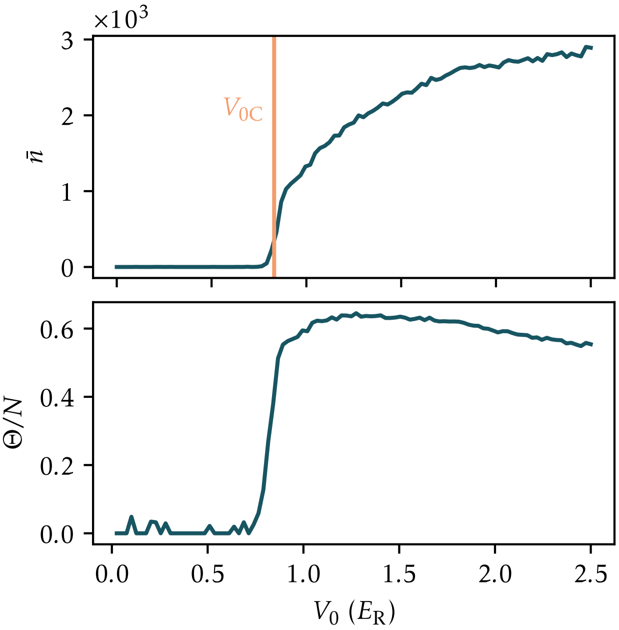

Figure 6.5: Evolution of the intracavity photon number and order parameter as the phase transition is crossed. We observe a clear threshold behavior for the intracavity photon number $\bar{n} = \left\langle \hat{a}^\dagger \hat{a} \right\rangle$, which we translate in terms of order parameter following the derivations presented in the text. We measure the critical value of the pump power $V_{0\mathrm{C}}$ by finding the maximal slope of the signals. This example data set comes from a single repetition of the experiment and was measured at $\Delta_\mathrm{c} = -2\pi \times 2.6\,\mathrm{MHz}$. The intracavity photon number is obtained by converting the measured photon count rate using the quantum efficiency calibration of the detection chain presented in section 5.2.2. $\bar{\Theta}$ being an extensive quantity, we rescale its value by the number of atoms to obtain a dimensionless parameter.

are turned on by illuminating the cloud from the side using a retro-reflected pump beam, polarized along the quantification axis given by the direction of the magnetic field. The pump and the neighboring cavity TEM_{00} resonance are detuned with respect to the atomic D_2 transition by $-2\pi \times 138.0\,\mathrm{GHz}$. There, the atoms induce a dispersive shift of the cavity resonance by $\delta_\mathrm{c} = U_0 N/2 = -2\pi \times 280$ kHz, exceeding the cavity linewidth $\kappa = 2\pi \times 77(1)$ kHz. The pump beam intersects the cavity at an angle of 18° as shown in appendix B, such that two discrete, density-fluctuation modes at momenta $\mathbf{k}_\pm$ are coupled to light, as discussed in the previous section. We use pump-cavity detunings $|\Delta_\mathrm{c}|/2\pi$ between 1 and 10 MHz for which $|\Delta_\mathrm{c}| \gg |\delta_\mathrm{c}|, \kappa$ and the cavity field adiabatically follows the atomic dynamics, ensuring that the system is accurately described by the Hamiltonian (6.12).

We observe density wave ordering upon increasing the strength of the photon-mediated interaction above a critical threshold. Experimentally, we linearly ramp up the pump power, and therefore the pump lattice depth V_0, and monitor the intracavity photon number by recording the photon flux leaking through one of the cavity mirrors, while keeping all other parameters fixed. In figure 6.5 we show a typical photon trace and the corresponding values of the order parameter, linked by equation (6.15), as V_0 is linearly increased up to $2.5\,E_\mathrm{R}$ over 5 ms, with $E_\mathrm{R} = \hbar^2 k_\mathrm{p}^2/2m = h \times 73.67$ kHz the recoil energy for ^{6}Li. The built-up in the cavity field above a critical pump strength $V_{0\mathrm{C}}$ corresponding to a critical long-range interaction strength $\mathcal{D}_{0\mathrm{C}}$ marks the onset of density wave ordering as discussed earlier in the chapter. The choice of ramp time for the pump power and the calibration of the pump lattice depth in terms of E_R are both described later in section 6.2.4.

6.2.2 Mapping the phase diagram

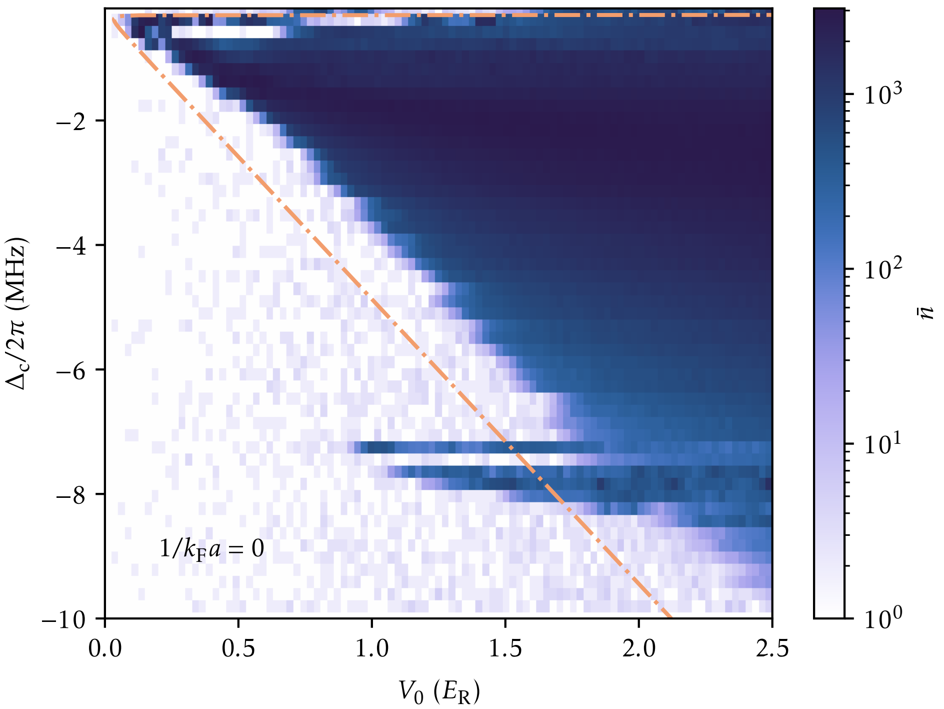

Figure 6.6: Phase diagram of the unitary Fermi gas in the V_0–Δ_c plane, exhibiting density wave ordering. The dash-dotted line depicts the location of the theory predictions for the critical interaction pump depth as described in the text. Each line is an average of three photon traces taken with a vertical binning of $2\pi \times 200\,\mathrm{kHz}$ and horizontal binning of $50\mu\mathrm{s}$, corresponding to $2.5 \times 10^{-2}\,E_\mathrm{R}$.

Repeating this measurement as a function of Δ_c, we construct the phase diagram of the system in the V_0–Δ_c plane, presented in figure 6.6. For small $|\Delta_\mathrm{c}|$, the phase boundary is a straight line, corresponding to a constant ratio V_0/Δ_c, showing that the boundary is determined only by $\mathcal{D}_0$. For $|\Delta_\mathrm{c}| \lesssim |\delta_\mathrm{c}|$, we observe instabilities likely due to optomechanical effects. For $|\Delta_\mathrm{c}| > 2\pi \times 3$ MHz, we observe a systematic deviation from the linearity, likely due to the lattice formed by the pump, changing the gas properties [259]. This single-particle effect is not captured by our treatment of the effective interaction Hamiltonian (6.12). The structures arising for $\Delta_\mathrm{c} \sim -2\pi \times 7$ and $-2\pi \times 8\,\mathrm{MHz}$ originate from the presence of high-order transverse modes of the cavity, with mode functions overlapping with the atomic density as already discussed in chapter 2. The fact that we observe such structures in terms of density ordering and not when directly probing the system on axis as in section 2.1.2 showcases the sensitivity of the present method. We also note that when detuning the pump frequency to $-2\pi\times 25$ and $-2\pi\times 50$ we observe density ordering in all of the higher-order cavity modes observed in the same section.

The prediction for the phase boundary is presented as the dash dotted line in figure 6.6. It comes from an evaluation of equation (6.17) at the critical point, where we have $\mathcal{D}_{0\mathrm{C}} = -1/2\chi_0$ such that

$$\eta_{0\mathrm{C}}^2 = -\frac{\tilde{\Delta}_\mathrm{c}^2+\kappa^2}{2\chi_0\tilde{\Delta}_\mathrm{c}}. \tag{6.45}$$

By noticing that $g_1\Omega_2 = g_2\Omega_1$ in equations (6.7) through (6.9), we also have $\eta_0^2 = U_0V_0$ and therefore

$$V_{0\mathrm{C}} = -\frac{\tilde{\Delta}_\mathrm{c}^2+\kappa^2}{2U_0\chi_0\tilde{\Delta}_\mathrm{c}}, \tag{6.46}$$

which can be solved for all values of Δ_c spanned by the measurement, with the knowledge of χ_0 computed from equation (6.44). In the regime $|\Delta_\mathrm{c}| < 2\pi\times 3\,\mathrm{MHz}$, where the effect of the pump lattice are negligible, we observe a discrepancy of a factor of 2 with respect to the prediction.

6.2.3 Variation of the interaction parameter

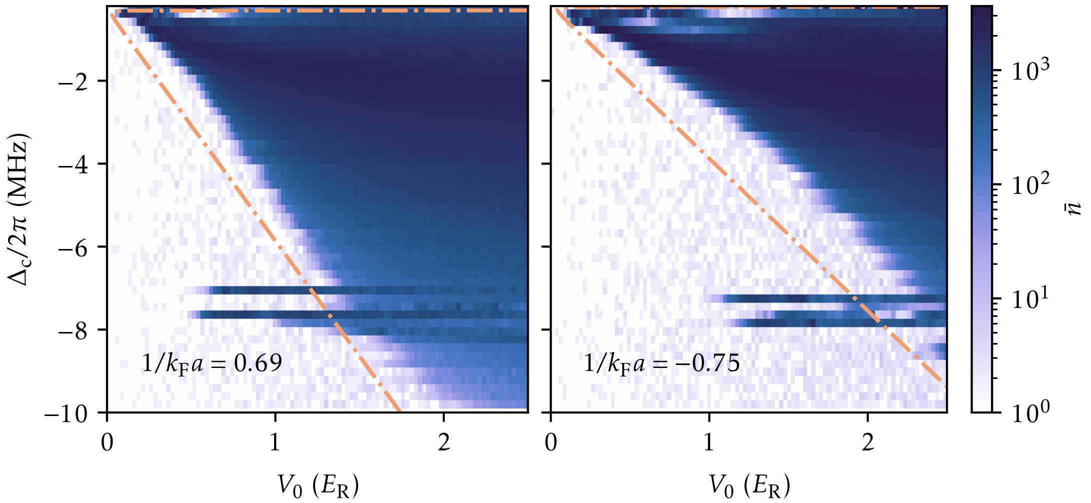

Figure 6.7: Phase diagrams for strongly interacting Fermi gases prepared in the BEC (left) and BCS (right) regimes. The diagrams show similar features across the BEC–BCS crossover, with a displaced phase boundary. All other experimental conditions are similar to the ones used to acquire the phase diagram of figure 6.6.

Having access to calculations of χ_0 and thus predictions for the phase boundary spanning the whole BEC–BCS crossover, we repeat the measurements presented in the above paragraph for different values of the scattering length. We first note that for all the explored values of the interaction parameter, we systematically observe density wave ordering for a sufficiently strong pump. We therefore acquire similar phase diagrams throughout the BEC–BCS crossover and present two of them in figure 6.7, which correspond to interaction parameters $(k_{\mathrm{F}}a)^{-1} = -0.75$ and 0.69 for the BCS and BEC side of the resonance respectively.[3] While these phase diagrams are qualitatively similar to the one measured at unitarity, with a linear phase boundary at small Δ_{c}, we observe a systematic shift of the density wave phase boundary towards larger pump strengths as the system crosses over from the BEC to the BCS regimes. In the regime $-0.7\,\mathrm{MHz} < \Delta_{\mathrm{c}}/2\pi < -3\,\mathrm{MHz}$, the linear phase boundary observed at unitarity persists for all scattering lengths.

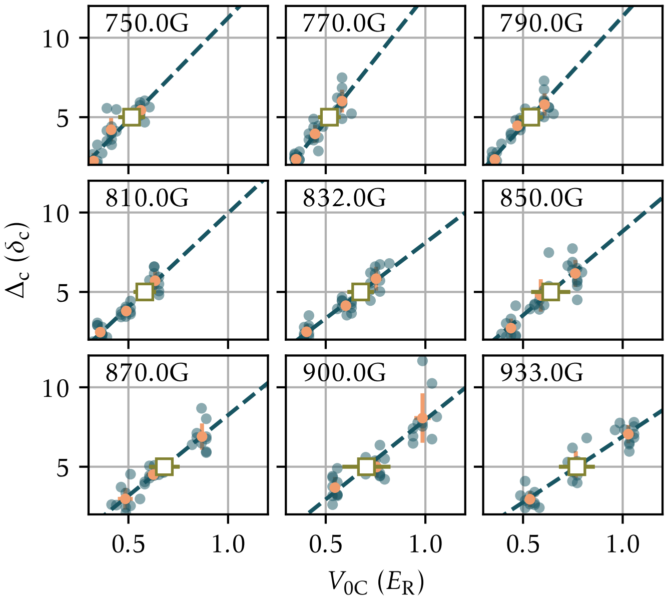

Figure 6.8: Systematic measurement of the critical pump depth as a function of the contact interaction parameter. Each panel represents a different set of measurement, acquired for magnetic fields across the Feshbach resonance. The light blue points correspond to single-shot measurements of $V_{0\mathrm{C}}$ and the orange points are their averaged value with a binning of $2\pi \times 500\,\mathrm{kHz}$. We retrieve $V_{0\mathrm{C}}$ by looking at the point with the highest slope in the photon traces, as showcased by figure 6.5. The dashed blue line is a linear fit to all the data, and we infer the value of $V_{0\mathrm{C}}$ at exactly $\tilde{\Delta}_{\mathrm{c}} = 5\delta_{\mathrm{c}}$ from it (white square).

In order to systematically study the dependency of the phase boundary on the interaction parameter, we extract the value of the critical pump lattice depth inferred at a fixed relative value of the pump frequency with respect to the dispersively shifted cavity. This allows to discard the trivial effect of a systematically varying atom number as we change the interaction parameter in the gas preparation stage of the experiment. The procedure to determine the critical pump depth is summarized in figure 6.8. Even by taking the atom number dependency of the dispersive shift out of the equation, we still observe a clear variation of V_0 with $(k_{\mathrm{F}}a)^{-1}$.

---

[3] In this chapter we define the Fermi energy by its value at the center of our trap, which systematically overestimates the trap averaged value used in the previous chapters and therefore leads to lower values of the interaction parameter for similar magnetic fields.

To make a qualitative comparison between the critical points which accounts for a varying Fermi energy in the crossover, we compute the dimensionless long-range interaction parameter $N\mathcal{D}_0/E_\mathrm{F}$. Figure 6.9 presents the phase diagram in the parameter plane of the short- and long-range interaction strengths. We observe a smooth dependence of the phase boundary on the short-range interaction, with a systematically lower critical long-range interaction strength in the BEC side. It, however, underestimates the absolute threshold by about a factor of two for all short-range interaction strengths, indicating that our approach which consists in only considering the zero-temperature compressibility overestimates the actual susceptibility. We for example expect that finite wavevector and finite temperature should generally decrease the susceptibility. More so, the discrepancy could also come from the neglected contribution to the susceptibility which we discarded when making the mean-field approximation back when we derived equation (6.28).

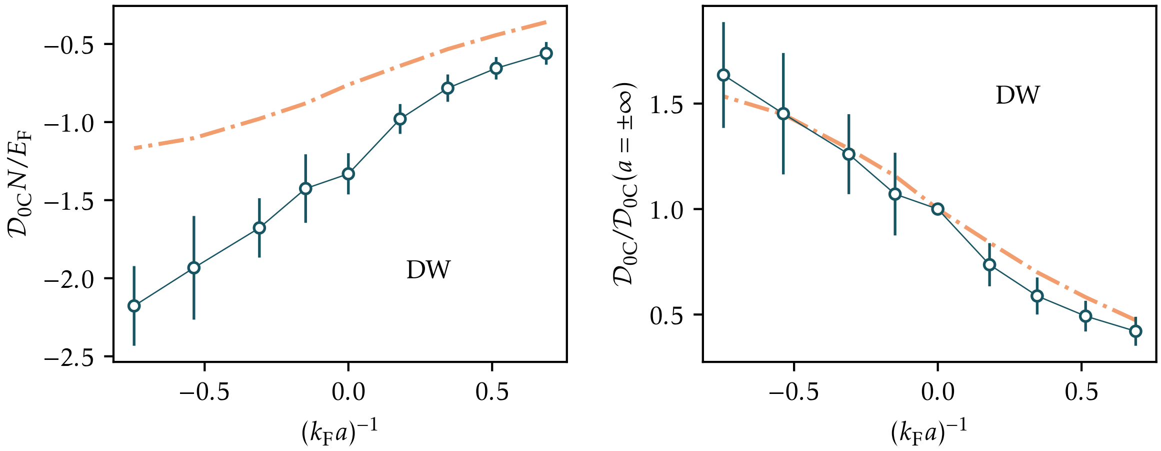

Figure 6.9: Phase diagram for the short- versus long-range interaction strengths, measured at a constant relative detuning $\tilde{\Delta}_\mathrm{c} = 5\delta_\mathrm{c}$ (blue circles). Above a critical value, the system systematically exhibits a modulated density, denoted by the 'DW' label. The orange dash-dotted line is the critical interaction strength calculated from theory. The left panel pictures the absolute measured and computed values which features a discrepancy of a factor of 2 over all the BEC–BCS crossover. Nevertheless, the relative scaling of the critical interaction strength is still well captured by our model as shown by the right panel where all the data are rescaled with respect to the value at unitarity.

6.2.4 Experimental calibrations

Pump ramp time and lifetime in the ordered phase

In order to set the pump ramp time used in the measurements presented above, we systematically varied the duration of its linear power ramp while keeping the endpoints constant and measured the variation of the critical point as a function of this ramp time. An example of such a

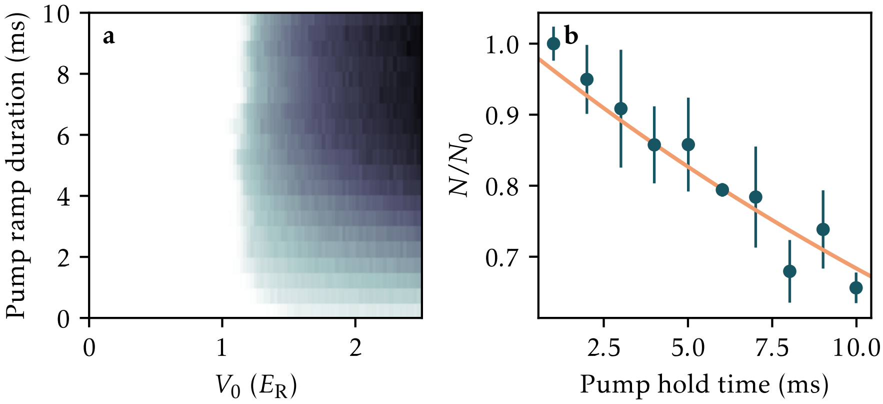

Figure 6.10: Pump ramp time and lifetime calibration. **a** Evolution of the critical and photon number as a function of the pump ramp duration. Each line is a photon trace acquired for a unitary gas at a detuning of $\Delta_c = -2\pi \times 3\,\mathrm{MHz}$ and displayed in log scale. **b** Lifetime measurement of the unitary Fermi gas in the density ordered phase.

measurement is presented by the panel **a** of figure 6.10, acquired for a unitary Fermi gas and with $\Delta_c = -2\pi \times 3\,\mathrm{MHz}$. We observe that above 2 ms, the critical point V_{0C} doesn't vary with increasing ramp duration but that the number of photon scattered in the cavity still does. However, above 5 ms the number of photons in the ordered phase stays constant, and therefore we settled for that particular value of the ramp duration, thus fixing the rate to be $0.5\,E_R$/ms. We observed similar trends for all the explored interaction parameters and detunings.

With similar experimental parameters, we additionally measure the lifetime of the gas in the ordered phase by first ramping up the pump power recoil at a rate of $0.5\,E_R$/ms to $V_{0C} = 1.3\,E_R$, slightly above the critical point, and then holding the gas in the trap with the pump at constant power for varying durations. We measure the atom number after the procedure and plot its relative variation against the hold time, as shown in the panel **b** of figure 6.10. Out of and exponential decay fit we extract a value of $\tau = 26 \pm 4\,\mathrm{ms}$ for the time constant. We note that this value is much lower than any of the natural trap lifetimes measured across de BEC–BCS crossover, suggesting that scattering losses dominate over any other decay process.

Lattice depth calibration

We calibrate the depth of the pump lattice using Kapitza-Dirac diffraction, one of the many existing techniques to calibrate depths of optical lattices with cold atomic ensembles [260].

The idea is to pulse the pump lattice onto the atomic density for a short time τ and measure the fraction of atoms diffracted in a number of momentum states $|n\rangle$, which we label in multiples of the momentum transfer $n \times \hbar\mathbf{k}$, with $\mathbf{k} = 2\mathbf{k}_p$. Usually this calibration is done in the Raman-Nath regime, for which the light-matter interaction time τ is much smaller than the recoil time of the atoms which sets the typical lattice dynamics time. However, in our case the lowest experimentally achievable pulse duration is 2.5μs, which is of the order of the recoil time of ^{6}Li with $E_R^{-1} = 13.57\mu$s, so that the kinetic energy of the atoms during the pulse cannot be neglected. To account for this kinetic energy contribution, we apply the method described in details in

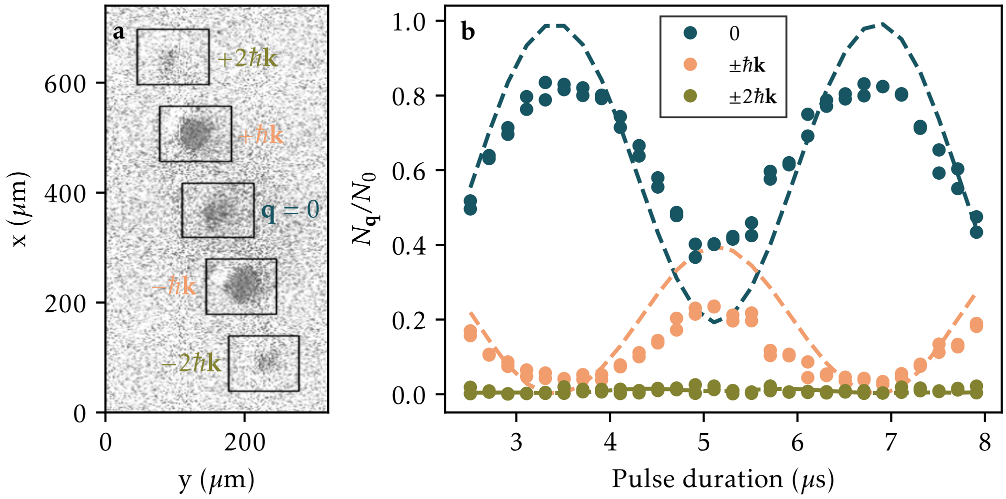

Figure 6.11: Pump lattice depth calibration. **a** Absorption picture of a molecular cloud after diffraction on the pump lattice. We systematically measure the population in each momentum mode highlighted by the black squares and labelled with the total corresponding two-photon momentum transfer. **b** Evolution of the population in the observed momenta modes as a function of the lattice pulse duration. The dashed lines are fit of our data to equation (6.47), from which we infer $V_0 = 2.5\,E_\mathrm{R}$ for a pump power of 3.1 mW and a detuning with respect to the atomic resonances $\Delta_\mathrm{a} = -2\pi \times 138.0\,\mathrm{GHz}$.

reference [261] and express the relative population of atoms diffracted in state $|n\rangle$ with

$$P_n = J_n^2\left(\frac{\beta}{2} + \mathrm{sinc}\frac{\alpha}{2}\right) \tag{6.47}$$

with $\beta = V_0/(\hbar\tau)$, α the pulse duration in units of the two-photon recoil time and J_n the n^{th} Bessel function of the first kind.

Experimentally, we measure the relative populations P_n with a gas produced on the far BEC side of the Feshbach resonance at 695 G in order to obtain a real condensate of molecules, with the weakest possible interparticle interactions. We pulse the pump lattice for a varying duration after having released the molecular BEC from the dipole trap and take an absorption image of the cloud after an additional 1.5 ms of time-of-flight. A typical absorption picture is shown in the panel **a** of figure 6.11. We extract the relative populations by fitting Gaussian profiles to cropped regions of the image, as shown in the figure. Repeating the measurement for varying pulse durations, we obtain the typical curves of panel **b** on which we fit equation (6.47) to extract a single value of β in units of E_R and therefore of $s_\mathrm{mol} = V_0/E_{\mathrm{R,mol}}$. In addition, we have to account for a reduction of a factor 4 for the measured s_mol with respect to s_atom. Indeed, we perform the measurements on a gas of molecules with $E_{\mathrm{R,mol}} = E_\mathrm{R}/2$ and with twice the polarizability of single atoms, thus experiencing a lattice potential four times as deep.

Calibration of pump-induced heating

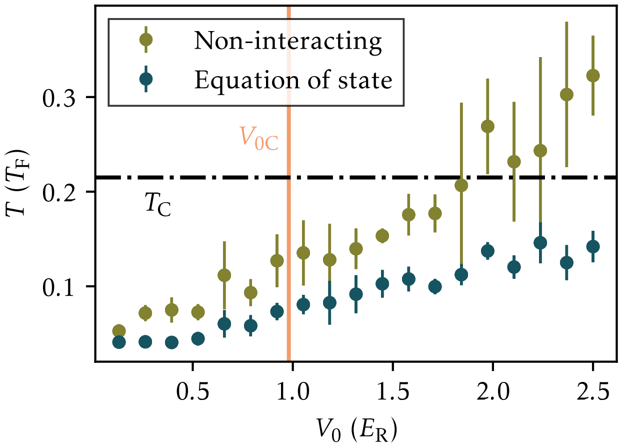

Figure 6.12: Measurement of the heating due to the pump lattice. We apply the processing technique presented in section 2.2 to extract the temperature out of an absorption image of the cloud with the unitary Fermi gas equation of state. In addition, we present measurements using a second technique which rely on comparing the shape of the cloud with that of a non-interacting gas [47]. While the temperature fit to the profile of a non-interacting gas yields higher temperatures than a direct fit to the equation of state both of the inferred temperatures are still around the same order of magnitude. In addition, they both confirm that the cloud remains in a superfluid state even after having entered the ordered phase. The experimental procedure is detailed in the text and the critical pump depth for the phase transition is denoted by the vertical orange line, while the critical temperature for a unitary gas trapped under the harmonic approximation is denoted by the horizontal dash-dotted line.

One major concern when performing the above experiments is the pump-induced heating and atomic losses. Here we perform thermometry of the unitary gas to verify that it remains in a superfluid state even after ramping up the pump power and crossed the density wave order transition.

As discussed in section 2.2, thermometry is performed by transferring the cloud into one of the arm of the crossed dipole trap and measuring the doubly integrated density profile thanks to the high-intensity imaging setup. The reduced temperature in this trap is deduced from a fit of the measured density profiles to the 1D equation of state of a unitary Fermi. This method yields a reduced temperature T/T_{Fh} defined with respect to the Fermi temperature of the gas in a harmonic trap with

$$T_{\mathrm{Fh}} = \hbar\bar{\omega}(3N)^{1/3}, \tag{6.48}$$

where N is the total number of atoms and $\bar{\omega} = (\omega_x\omega_y\omega_z)^{1/3} = 2\pi \times 106\,\mathrm{Hz}$ is the geometric mean of the oscillation frequencies in the single-arm trap.

We estimate the heating due to the pump by measuring the temperature of the cloud after a linear ramp of the pump lattice depth to varying end values at a constant rate, and then ramping it back to zero with the same rate. This measurement thus provides an upper bound for the pump-induced heating since in the above experiments we only ramp up the probe power. The measurement is performed for a unitary gas with a pump-cavity detuning of $\Delta_c = -2\pi \times 2.5\,\mathrm{MHz}$. The cloud is transferred in the single-arm dipole trap between the pump lattice ramp and the actual temperature measurement. With increasing pump power we observe a monotonically increasing temperature of the cloud shown in figure 6.12. Interestingly, temperature shows no particular feature when the pump power reaches and exceeds the density wave ordering critical point. At the critical point, we measure a temperature of $T = 0.12(2)T_{\mathrm{Fh}}$, an increase by a factor of 50% compared with the initial one. Heating is sufficient to heat the cloud above the superfluid critical temperature of $0.21T_{\mathrm{Fh}}$ [120] for a strength of the long-range interactions exceeding $2\mathcal{D}_{0C}$, deep in the ordered phase. Even though we do not have access to measurements of the temperature directly in the ordered phase, we have still shown that the cloud remains superfluid after the phase transition and going back to the unperturbed one.

6.3 Measurement of the density wave susceptibility

While the measurement of the cavity field allows for the identification of the onset of DW order, it does not yield information on the photon-mediated interactions below the transition. Nevertheless, the long-range interactions strongly modify properties of the gas even far below the ordering transition, via virtual cavity photons as shown in section 6.1. In this section, we now explore this by directly measuring the susceptibility of the system χ as a function of the long and short-range interaction strengths. Indeed, with equation (6.32) in mind, we expect a divergence of χ as $\mathcal{D}_0$ is increased to approach the critical point.

6.3.1 Implementation of fixed-q Bragg spectroscopy

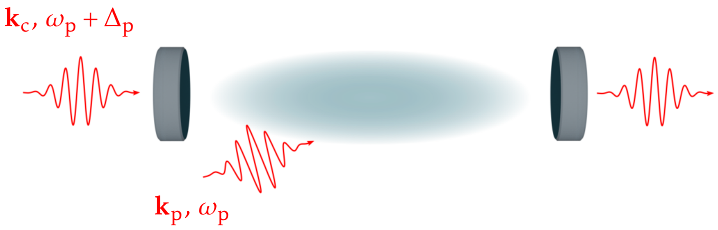
$\mathbf{k}_{\mathrm{c}}, \omega_{\mathrm{p}} + \Delta_{\mathrm{p}}$
$\mathbf{k}_{\mathrm{p}}, \omega_{\mathrm{p}}$

Figure 6.13: Experimental setup to measure the density wave susceptibility. In the presence of a given pump field, which sets the strength of the long-range interactions, we shine an on-axis beam with a finite frequency detuning Δ_{p} from the pump beam. The resulting total light field features a 2D lattice structure given by the interference of the two beams, with an amplitude oscillating at a frequency set by their detuning. This effectively excites the system at wavevectors $\pm\mathbf{k}_{\pm}$ and its corresponding density response gets mapped onto the cavity field.

In order to directly measure the susceptibility, we slightly modify the experimental procedure and implement a variant of Bragg spectroscopy by driving the cavity on-axis with a very weak probe laser in addition to the transverse pump as sketched in figure 6.13. This scheme was first presented in reference [262] where it was implemented for a similar use for the case of bosons. It amounts to imposing a density wave pattern at $\mathbf{k}_{\pm}$ for values of $\mathcal{D}_0$ below the critical point. In this paragraph, we show that the value of $\chi(\mathcal{D}_0)$ is directly linked to the resulting photon leakage rate.

The Hamiltonian of the system given by equation (6.12) is modified to accommodate the additional weak probe at frequency ω_{drive} by adding an on-axis drive term

$$\hat{H}_{\text{drive}} = \beta\left[\hat{a}e^{i(\Delta_{\text{p}}t-\phi_0)} + \text{h.c.}\right], \tag{6.49}$$

with strength β. We note ϕ_0 the initial, uncontrolled, phase between the pump beam and on-axis probe. In the experiment, we impose a small detuning Δ_{p} between the pump frequency ω_{p} and the drive frequency ω_{drive}, imposing a slow winding of the phase during the probing time. This winding leads to a slowly oscillating intracavity photon number as we show below.

The adiabatic elimination of the cavity field in the presence of the drive leads to a modified expression for the effective Hamiltonian

$$\hat{H}_{\text{eff}} = \hat{H}_0 + \mathcal{D}_0\hat{\Theta}^2 + \frac{2\beta}{\eta_0}\mathcal{D}_0\hat{\Theta}\cos\left(\Delta_{\text{p}}t - \phi_0\right), \tag{6.50}$$

and the steady-state cavity field reads

$$\hat{a} = \frac{1}{\tilde{\Delta}_{\text{c}} + i\kappa}\left[\eta_0\hat{\Theta} + \beta e^{i(\Delta_{\text{p}}t-\phi_0)}\right]. \tag{6.51}$$

We note that for $\beta = 0$, we recover the equations presented in the first section. Considering the additional drive term in equation (6.50) as a weak perturbation we can once more write the Kubo formula to calculate the response of $\hat{\Theta}$ under this perturbation, such that

$$\left\langle\hat{\Theta}(t)\right\rangle = \left\langle\hat{\Theta}\right\rangle_0 + \frac{2\beta\mathcal{D}_0}{\eta_0}\int_{-\infty}^{\infty} dt'\chi(t-t')\cos\left(\Delta_{\text{p}}t' - \phi_0\right), \tag{6.52}$$

where the index 0 refers to the expectation value with $\beta = 0$, so that $\left\langle\hat{\Theta}\right\rangle_0 = 0$ below the critical point. The finite detuning between the pump and drive imposes the time dependence of the problem and the time dependent density response is defined with

$$\chi(t-t') = -i\theta(t-t')\left\langle[\hat{\Theta}(t),\hat{\Theta}(t')]\right\rangle_0. \tag{6.53}$$

Its temporal Fourier transform gives the dynamical response function, defined by

$$\chi(\Delta_{\text{p}}) = -\int_{-\infty}^{\infty} dt\chi(t)e^{i\Delta_{\text{p}}t}, \tag{6.54}$$

which is an extension to finite frequencies to the density response of the system derived in section 6.1 and thus verifies equation (6.32). Equation (6.52) can then be recast as

$$\left\langle\hat{\Theta}(t)\right\rangle = \left\langle\hat{\Theta}\right\rangle_0 + \frac{2\beta\mathcal{D}_0}{\eta_0}\text{Re}\left[\chi(\Delta_{\text{p}})e^{-i(\Delta_{\text{p}}t-\phi_0)}\right]. \tag{6.55}$$

Taking the low frequency limit $\Delta_{\text{p}} \ll c_{\text{s}}|\mathbf{k}_-|$, where c_{s} is the speed of sound, the dynamical response function is purely real and $\chi(\Delta_{\text{p}}) \simeq \chi(0) + O((\Delta_{\text{p}}/c_{\text{s}}|\mathbf{k}_-|)^2)$. Below the critical point, using the mapping of the order parameter onto the cavity field given by equation (6.51), the intracavity photon number reads, to first order

$$\left\langle\hat{a}^\dagger\hat{a}\right\rangle = \frac{\beta^2}{\tilde{\Delta}_{\text{c}}^2}\left[1 + 4\mathcal{D}_0\chi(0)\cos^2(\Delta_{\text{p}}t - \phi_0)\right]. \tag{6.56}$$

This equation explicitly relates the amplitude of the oscillations of the intracavity field to the static density wave susceptibility $\chi(0)$ below the critical point. It also features the importance of probing the system with a finite detuning Δ_p. Should $\Delta_\mathrm{p} = 0$ we would only observe a constant signal for each repetition of the experiment with an amplitude varying due the uncontrolled initial phase ϕ_0. Setting $\Delta_\mathrm{p} \neq 0$ thus forces the signal to oscillate and allows to measure its amplitude on a single realization of the experiment.

6.3.2 Measurement of the density response in the presence of long-range interactions

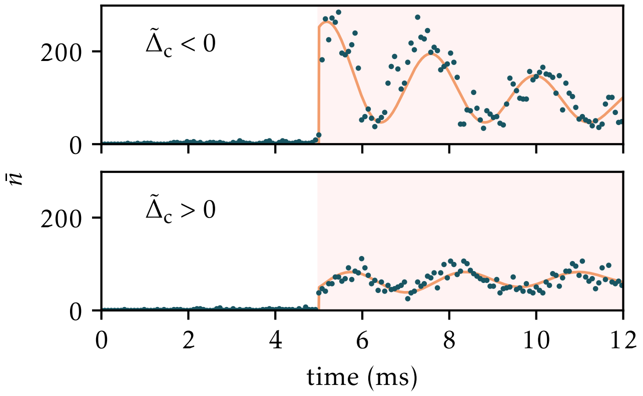

Figure 6.14: Photon traces obtained in the presence of the weak on-axis drive. The first 5 ms correspond to the ramp-up of the pump lattice depth. Since it remains below the critical point, the cavity mode doesn't get populated. Once the setpoint is reached, we shine the on-axis drive as depicted by the shaded area in both panels. Both for attractive and repulsive long-range interactions we observe the predicted oscillatory behavior of the intracavity field, with an amplitude given by the density wave susceptibility.

Experimentally, we first fix the long-range interaction strength by ramping up the pump lattice depth to a value below the critical point and then shine the on-axis drive for 10 ms with $\Delta_\mathrm{p} = 2\pi \times 200\,\mathrm{Hz}$ as to work in the low-frequency limit. Typical signals are shown in figure 6.14 for $\tilde{\Delta}_\mathrm{c} = -2\pi \times 1.7\,\mathrm{MHz}$ and $\tilde{\Delta}_\mathrm{c} = 2\pi \times 1.7\,\mathrm{MHz}$, and for a pump lattice depth of $V_0 = 0.75\,E_\mathrm{R}$. Both signals exhibit the oscillatory behavior expected from equation (6.56) at a frequency of $2\Delta_\mathrm{p}$ together with damping, likely due to heating resulting from the large oscillating signal. However, we observe that the density response is lower for $\tilde{\Delta}_\mathrm{c} > 0$ which corresponds to repulsive interactions compared with attractive ones for $\tilde{\Delta}_\mathrm{c} < 0$.

In both cases, as displayed on the figure, the amplitude of the initial oscillations can be directly fitted to yield the value of $\chi(0)$. For attractive photon-mediated interactions, the intracavity photon number is strongly enhanced by the presence of the atoms, as the gas forms a Bragg grating and coherently transfers photons form the pump to the cavity, similar to an optical parametric amplifier [263]. For repulsive interactions, we instead observe a reduced susceptibility.

Divergence of the static density wave susceptibility

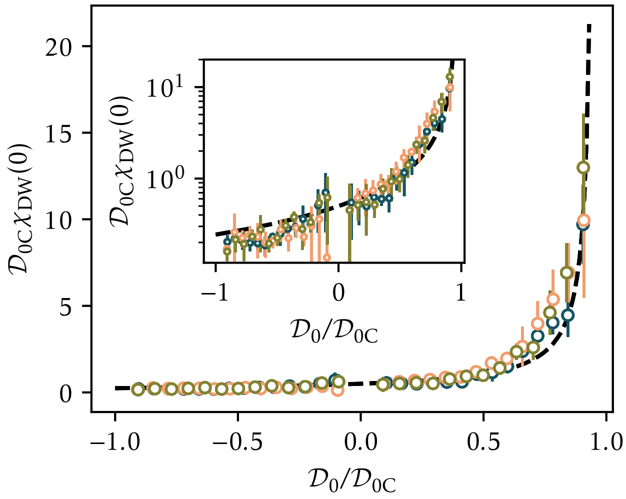

Figure 6.15: Divergence of the density wave susceptibility when the strength of the long-range interactions approaches the critical value. Each color corresponds to a value of the contact interaction parameter for extreme points of the BEC–BCS crossover and the overlapping data suggest an identical variation of the density response with the long-range interaction strength for all short-range interactions. The scaling of the susceptibility is, up to $\mathcal{D}_0/\mathcal{D}_{0\mathrm{C}} = 0.9$, well captured by equation (6.58) displayed as the dashed black line. The gap around $\mathcal{D}_0/\mathcal{D}_{0\mathrm{C}} = 0$ comes from the inability to resolve oscillations of the cavity field for low values of $\chi(0)$. The inset shows the same data in log scale to further emphasize the divergent scaling of the susceptibility.

To observe the divergence of the susceptibility as the critical point is approached, we repeat the measurement from above by systematically varying the strength of the long-range interactions $\mathcal{D}_0$ up to $0.9\mathcal{D}_{0\mathrm{C}}$, both for attractive and repulsive interactions. In the repulsive case $\mathcal{D}_{0\mathrm{C}}$ is not defined, but we still consider its value to correspond to the same absolute value of the pump power as for the attractive case. We perform the measurements for $\Delta_{\mathrm{c}} = \pm 6\delta_{\mathrm{c}}$ and $1/k_{\mathrm{F}}a = -0.75$, 0, and 0.69 and present the results in figure 6.15. There, we display the rescaled quantity

$$\mathcal{D}_{0\mathrm{C}}\chi(0) = \frac{4\mathcal{D}_0\chi(0)}{4\frac{\mathcal{D}_0}{\mathcal{D}_{0\mathrm{C}}}}, \tag{6.57}$$

which features, from equation (6.32), a surprisingly simple and universal form

$$\mathcal{D}_{0\mathrm{C}}\chi(0) = \frac{1}{2\left(1 - \frac{\mathcal{D}_0}{\mathcal{D}_{0\mathrm{C}}}\right)}, \tag{6.58}$$

where we used $\mathcal{D}_{0\mathrm{C}} = -1/2\chi_0$. We observe an increase of the susceptibility over more than one order of magnitude with increasing $\mathcal{D}_0$, which is the expected feature of second order phase transitions. This was observed for self-organization and supersolid transitions in non-interacting BECs [262, 264]. For repulsive photon-mediated interactions, no ordering is expected nor observed, and we observe a reduction of the susceptibility by up to a factor of ~ 3 over the same range of $|\mathcal{D}_0|$. Up to normalization of $\chi(0)$ and $\mathcal{D}_0$ by $\mathcal{D}_{0C}$, we observe that for attractive or repulsive long-range interactions, the variations of the susceptibility are identical within error bars for all scattering lengths in the BCS-BEC crossover. This highlights the versatility of our system in independently tuning the short- and long-range interactions, therefore addressing separately pairing and particle-hole channels. We have therefore demonstrated that attractive (repulsive) photon-mediated interactions lower (raise) the energy cost of such particle-hole excitations.

Extension of the measurement for finite frequencies

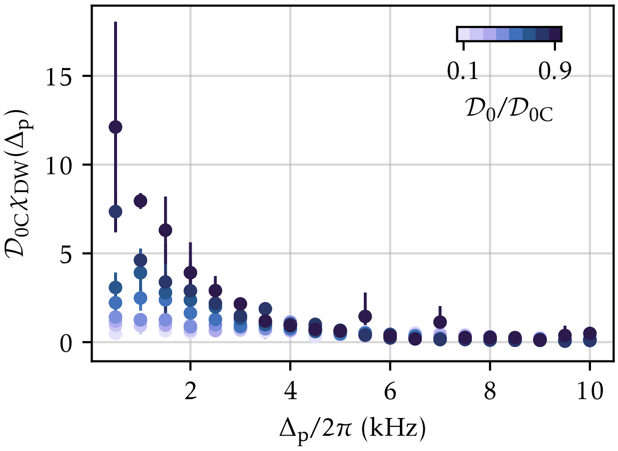

Figure 6.16: Measurement of the density wave response of a unitary Fermi gas as a function of Δ_p and for values of $\mathcal{D}_0/\mathcal{D}_{0C}$ between 0.1 and 0.9. The absence of structure at finite frequency confirms the absence of mode softening. The data is taken for $\Delta_c = -2\pi \times 2\,\text{MHz}$.

Similar experiments for bosons with a sharp single-frequency excitation spectrum observed that the long-range interactions lead to a mode softening of the corresponding excitation mode, touching zero at the critical point [262, 265]. Free fermions at low momenta in contrast feature a continuous, incoherent gapless particle-hole spectrum [258], such that no soft mode is expected.

Following up on the last remark we now extend our susceptibility measurements to finite frequencies, by systematically scanning Δ_p up to $2\pi \times 10$ kHz, larger than $\hbar^2\mathbf{k}_-^2/2m = h \times 7.2\,\text{kHz}$, the recoil energy associated with $\mathbf{k}_-$. We then extract $\chi(\Delta_p)$ from the amplitude of the photon trace oscillations at $2\Delta_p$. In that case, we note that $\chi(\Delta_p)$ is not necessarily real-valued anymore so that taking the real part of equation (6.55) actually amounts to measuring $|\chi(\Delta_p)|$. For the unitary Fermi gas the results are presented in figure 6.16, and we observe that, for $\mathcal{D}_0$ up to $0.9\mathcal{D}_{0C}$, $|\chi(\Delta_p)|$ monotonically decreases with frequency Δ_p. The low-frequency susceptibility increases upon approaching the transition, while the higher-frequencies parts of the spectrum remain unchanged. We observe such a behavior for all accessible scattering lengths in the BCS-BEC crossover.

These results contrast with the mode softening observed with weakly interacting BECs. While it would also be expected in our geometry for free fermions, due to the broad particle-hole spectrum, it is surprising that this feature is also present for the unitary Fermi gas which is known to also display a phonon spectrum at low momentum [266, 267]. This might be due to the strongly-interacting nature of the system leading to the damping of the excitations, but could also originate from the combination of finite temperature and trap averaging.

6.4 Long-range interactions between pairs of atoms, an outlook

As a natural follow-up of the results presented above and in chapter 4, one could think of operating the pump in the vicinity of a photoassociation transition, inducing long-range pair-pair interactions in addition to the atom-atom interactions. If the analogy with the atoms-only case holds, this system would also exhibit a critical point above which the density of pairs becomes unstable towards acquiring a spatial modulation: realizing a pair density wave.

Here we lay down a basic theoretical model to describe such an experiment by expressing the light-matter interaction Hamiltonian for the pairs in the dispersive regime, and in the presence of the transverse pump. We then present preliminary experimental observations in such a regime which show that the coupling to pairs induces a modification of the critical point for the ordered phase.

6.4.1 Dispersive regime for the pairs

We recall the expression of the total Hamiltonian describing the light-matter interaction between the atoms and a light field, in the vicinity of a photoassociation transition given by equation (4.6). In the dispersive regime for the pairs and single atoms, we perform the adiabatic elimination of their respective excited states following the method presented in section 2.1.3. In a frame rotating at the pump frequency the Hamiltonian reads

$$\hat{H} = \hat{H}_0 + \hat{H}_{\mathrm{cav}} + \hat{H}_{\mathrm{lm}} + \frac{1}{\Delta_{\mathrm{m}}} \int d\mathbf{R}\, \hat{G}^{\dagger}(\mathbf{R}) \hat{G}(\mathbf{R}) \hat{\phi}_{\mathrm{m}}^{\dagger}(\mathbf{R}) \hat{\phi}_{\mathrm{m}}(\mathbf{R}) \tag{6.59}$$

where the first three terms are given by equations (6.2) to (6.4). The additional term comes from the dispersive coupling of the pairs to both the pump and cavity fields with

$$\hat{G}(\mathbf{R}) = \int d\mathbf{r}\, f(\mathbf{r}) \hat{\psi}_1(\mathbf{R} - \frac{\mathbf{r}}{2}) \hat{\psi}_2(\mathbf{R} + \frac{\mathbf{r}}{2}) \tag{6.60}$$

where f is the radial part of the excited molecular wavefunction. $\hat{\phi}_{\mathrm{m}}(\mathbf{R})$ is the total light field interacting with the pairs with a definition similar to that of equation (6.5) and Δ_{m} is the detuning between the photoassociation transition and the pump frequency. The spatial structure of the interaction is the same as the one described by equation (6.6), acting on the two-body density $\hat{G}^{\dagger}\hat{G}$.

By defining an order parameter $\hat{\Theta}_{\mathrm{m}}$ for the pair density with

$$\hat{\Theta}_{\mathrm{m}} = \int d\mathbf{R}\, \hat{G}^{\dagger}(\mathbf{R}) \hat{G}(\mathbf{R}) \cos \mathbf{k}_{\mathrm{c}}\mathbf{r} \cos \mathbf{k}_{\mathrm{p}}\mathbf{r}, \tag{6.61}$$

one can think of applying the same reasoning as presented in section 6.1.2 to study the instabilities of the system, accounting for the extra contribution coming from the pairs. Since the strength of the long-range interaction for the pairs scales with Δ_{m}^{-1}, one can expect a sizeable contribution to the free energy when the cavity resonance frequency approaches the photoassociation transition.

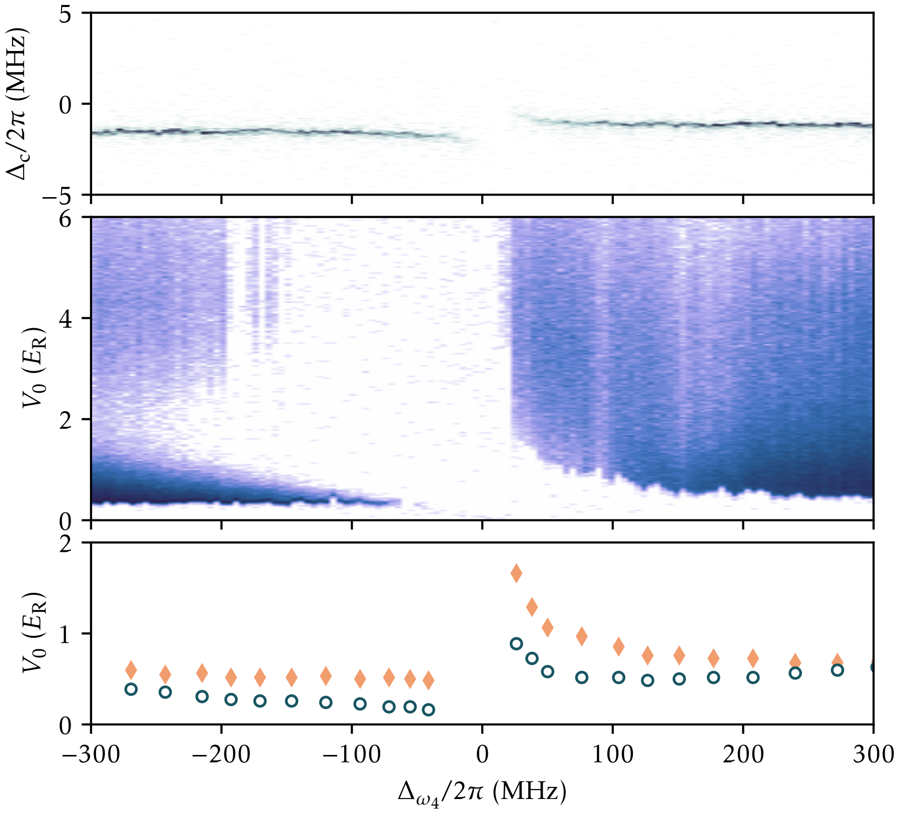

Figure 6.17: Phase diagram in the V_0–Δ_{ω_4} plane. Top, dispersive shift measurements indicating the location of the photoassociation transition. Center, aggregated photon traces obtained when ramping up the pump power. Bottom, location of the critical point extracted from the photon traces for a few selected detunings (orange diamonds). The blue circles depict the same data, accounting for the atomic losses before the critical point is reached and the varying dispersive shift.

Without pushing the theoretical modelling further, we performed this experiment by proceeding exactly as described in section 6.2, but tuning the cavity and pump frequencies in the vicinity of a photoassociation transition. We chose the transition located $-2\pi \times 25.99$ GHz from the D_2 π transition at 832 G studied in chapter 4. We fix $\Delta_c = -2\pi \times 4$ MHz and linearly ramp up the pump power for different values of the cavity resonance frequency ω_c around the photoassociation transition. In total, we explore $\Delta_{\omega_4} = \omega_c - \omega_4 \in 2\pi \times [-300, 300]$ MHz, or equivalently $\Delta_{a,2} \in -2\pi \times [26.29, 25.69]$ GHz. The aggregated photon traces are presented in figure 6.17. Away from the transition, the atomic contribution dominates, and the critical point is systematically located around $V_0 \approx 0.5\,E_R$. When the transition is approached we observe an additional contribution to the critical point. We confirm the effect by subtracting the effect of both atomic losses and a variation of the dispersive shift, as displayed on the last panel.

6.4.2 Interpretation as an optical Feshbach resonance

One interesting consequence of expressing the coupling to pairs in the dispersive regime is an interpretation of the system as realizing an optical Feshbach resonance [268], where the coupling to excited molecular states leads to a modification of the scattering length. Here we present a quick argument based on Tan's relations to motivate the interpretation.

In the absence of light-matter coupling, Tan's energy relation [147] reads, neglecting the trapping potential

$$\left\langle \hat{H}_0 \right\rangle = \sum_\sigma \int \frac{d^3k}{(2\pi)^3} \frac{\hbar^2 k^2}{2m} \left[n_\sigma(\mathbf{k}) - \frac{\mathcal{C}}{k^4} \right] + \frac{\hbar^2 \mathcal{I}}{4\pi m a} \tag{6.62}$$

In this expression, the sum of the terms proportional to the contact gives the interaction energy and one of them has been combined with the kinetic energy part to make the integral ultraviolet-convergent. The idea here is to show that in the presence of long-range interactions between pairs, the above expression is modified and accounts for an additional term. In that case, the expectation value of the total energy reads

$$\left\langle \hat{H} \right\rangle = \left\langle \hat{H}_0 \right\rangle + \left\langle \hat{H}_{\mathrm{cav}} \right\rangle + \left\langle \hat{H}_{\mathrm{lm}} \right\rangle + \frac{\hbar}{\Delta_{\mathrm{m}}} \int d\mathbf{R} \left\langle \hat{G}^\dagger(\mathbf{R}) \hat{G}(\mathbf{R}) \hat{\phi}^\dagger_{\mathrm{m}}(\mathbf{R}) \hat{\phi}_{\mathrm{m}}(\mathbf{R}) \right\rangle. \tag{6.63}$$

The last term of this expression is reminiscent of expressions for the two-body correlation functions obtained in chapter 4. By using a mean-field approximation for the photons, we are led to calculate $\left\langle \hat{G}^\dagger \hat{G} \right\rangle$. Using equation (4.16) we get

$$\left\langle \hat{G}^\dagger(\mathbf{R}) \hat{G}(\mathbf{R}) \right\rangle = B(a) \mathcal{C}(\mathbf{R}, a) \tag{6.64}$$

where B is a function which depends on both the scattering length and on the Condon radius R_C of the excited molecular state. We remind that $\mathcal{C}(\mathbf{R})$ is the local contact density which verifies $\mathcal{I} = \int d\mathbf{R} \mathcal{C}(\mathbf{R})$.

By considering the field to be homogeneous, the last term of equation (6.63) simplifies to

$$\frac{\hbar}{\Delta_{\mathrm{m}}} B(a) \mathcal{I} \left\langle \phi^\dagger_{\mathrm{m}} \phi_{\mathrm{m}} \right\rangle \tag{6.65}$$

and leads to a modification of the contact contribution compared to the case without interaction of equation (6.62), with

$$\frac{\hbar^2 \mathcal{I}}{4\pi m a} \to \frac{\hbar^2 \mathcal{I}}{4\pi m} \left[\frac{1}{a} + \frac{4\pi m}{\hbar \Delta_{\mathrm{m}}} B(a) \left\langle \phi^\dagger_{\mathrm{m}} \phi_{\mathrm{m}} \right\rangle \right], \tag{6.66}$$

or in terms of scattering length

$$\frac{1}{a} \to \frac{1}{a} + \frac{4\pi m}{\hbar \Delta_{\mathrm{m}}} B(a) \left\langle \phi^\dagger_{\mathrm{m}} \phi_{\mathrm{m}} \right\rangle. \tag{6.67}$$

This last expression indicates that in the presence of long range interactions between pairs in the dispersive regime, the pump field can be used to tune the effective scattering length of the gas. Indeed, variations of the pump field intensity or detuning, with respect to either the cavity resonance or the photossociation transitions, yield effective variations of the scattering length. Similarly to how modulation [269] or quenches [270–272] of the scattering length were employed to observe the excitations of strongly interacting Fermi gases, one can now think about either quenching or modulating the long-range interaction strength for the pairs in our system to induce changes in the scattering length.

Conclusion

We have shown that for a wide range of the short-range interaction strength, our strongly interacting Fermi gas with long-range interactions features a phase transition to a density ordered phase upon increasing the photon-mediated interaction strength. Given our temperature data, the gas returns to the superfluid phase when the long-range interaction is ramped back to zero, with limited heating. However, this leaves open the fascinating question whether the system remains paired and superfluid in the presence of strong long-range interactions and in the density ordered state.

Compared to condensed-matter systems showing an interplay of charge-density-wave and superfluidity [273, 274] which is not well understood to this day[275, 276], our system has a fully-controllable microscopic Hamiltonian. The photon-induced density order shares similarities with type II charge-density-wave compounds [277] in which the phase transition is mainly driven by the electron-phonon coupling. For us, cavity photons playing the role of phonons in real materials. In this context, the real-time weakly destructive measurement channel through the cavity field opens the possibility of gaining insight into the interplay of structural effects and strong interactions in complex quantum materials.

Conclusion and outlooks

> Le laurier du poète est souvent un cyprès.
>
> Louise Michel

In this manuscript, we have presented the first experiments performed with strongly interacting, superfluid Fermi gases strongly coupled to light by a high finesse optical cavity.

All the results contained in this work were obtained with the experimental apparatus presented in chapter 1. There, we discussed the main choices which motivated the specificities of the design of the machine. It was kept simple yet innovative: it is the first experimental setup which aimed to investigate the physics of strongly interacting fermions coupled to light in a high-finesse cavity. To that end, we proved with a first series of cavity spectroscopy measurements presented in chapter 2 that the atoms-light coupled system was evolving in the strong coupling regime. On the other hand, using absorption imaging, we demonstrated via an efficient thermometry method that the strongly interacting gases we routinely produce were indeed operating in the deeply degenerate, superfluid regime.

Along with the observation of the strong coupling regime for the atoms came a surprise: pairs of interacting atoms were also getting strongly coupled to the cavity field, via photoassociation transitions. Since the existence of short-range pairs is a purely many-body effect, we dedicated chapter 3 to the explanation of the mechanisms inducing the strong atom-atom interactions in our system. We showed how these strong interactions lead to the existence of short-range pairs, and how the many-body physics of the gas can be captured by a universal thermodynamical quantity: the contact. In chapter 4 we put our knowledge of both the strong coupling of atoms to light and of the short-range physics of the gas to use, and studied in details the coupling of pairs to light. We proved that the measured light-matter coupling strengths for the pair-polaritons were directly controlled by the contact. This result is significant, for the first time the many-body nature of strongly interacting Fermi gases was getting imprinted onto cavity spectra. We reached a similar conclusion albeit with a different method following the experiments presented in chapter 5. By performing slow, steady-state, transmission spectroscopy measurements in the dispersive regime we were able to modulate the atomic density during the measurement. Via the nonlinear Kerr effect, the modulation got translated into distorted cavity transmission spectra. The strength of the nonlinearity was linked to a ground-state property of the gas: the density-density response function. Using an operator product expansion technique, we showed that this response function is controlled by the contact, again linking cavity spectra with universal many-body physics.

In the remaining part of the manuscript, embodied by chapter 6, we studied the effects of engineering long-range interactions, mediated by cavity photons. To the contrary of the other experiments, the cavity field was now actively driving the system. Above a critical strength for the long-range interactions, we proved and observed that the atoms exhibit a phase transition to a density-modulated, superradiant state: a density wave. We observed the onset of the density wave via its superradiant light scattering properties, in the ordered phase the cavity mode gets spontaneously populated with photons. The critical strength for the phase transition is again given by the density-density response of the unperturbed gas, which in turn depends on the short-range interaction strength. By measuring the excitation spectrum of the gas in the presence of long-range interactions, we observed the divergence of its density response as the critical point was approached, confirming the phase transition interpretation. In addition, we proved that the gas remained superfluid after the long-range interactions were ramped back down to zero, with limited heating.

In the following we present some natural extensions of and remaining questions about the experiments described above.

Investigation of the density-wave ordered phase

Besides what we have presented in the scope of this manuscript, a few questions remain unanswered regarding the density-wave phase transition.

Is the density-wave superfluid ? We have shown that the temperature of the gas *after* having crossed the transition and turning off the long-range interaction strength was still below the critical point for superfluidity. However, we do not know for sure what happens to superfluidity *in* the ordered phase. Since the density of the gas is highly modulated, one cannot resort to in-situ fits of trapped density profiles for thermometry.

What happens to Cooper pairing ? The short wavevector $\mathbf{k}_-$ of the density ordered pattern nests points of the Fermi surface together, locally distorting it. Since Cooper pairing occurs on top of the Fermi surface, one can wonder what happens to it in these nested regions. What would then be the impact of a modified, anisotropic superfluid order ?

How much of a role quantum correlations play in the onset of the phase transition ? We discarded the quantum correlation terms in the derivation of the free energy of the gas in chapter 6. Given the fact that the resulting prediction for the critical point do not match our observations by a systematic factor of 2, one could assume that these neglected terms actually play a sizeable role. Even for simple condensed matter systems exhibiting phase transitions, quantum correlations are known to play a dramatic role: accurate predictions for the onset of the spontaneous magnetization of an Ising magnet have to account for such beyond mean-field terms [253].

What is the order of the phase transition ? A question perhaps linked to the previous one, for which the formal answer lies again in a finer calculation of the free energy. One of the early theory work on the phase transition for fermions actually predicted the transition to be of first order in some particular regime of parameters [250]. One characteristic of first order transitions is their hysteretic nature, which measurement would most likely require a better stabilization of atomic losses and heating in the presence of the pump beam. In addition, the measurement of the critical exponent for the order parameter is expected to give insight about the universality class of the transition.

What role does the geometry of the system play ? Assuming that our description of the critical point for the phase transition in terms of density response is correct, one should expect a drastic modification of the critical behavior when the dimensionality of the system is reduced. Indeed, Lindhard function drastically changes behavior when going from 3D to 2D and 1D systems [216], with the emergence of a divergence at the Fermi wavevector, absent in 3D. When reducing the dimension of the system, a single wavevector connects proportionally more points of the Fermi surface together. If the Fermi surface is completely nested, Umklapp processes are expected to lead to a thresholdless phase transition [233]. This could be achieved either by directly reducing the dimensionality of the gas, or more simply by distorting the Fermi surface to increase the total area connected by the density order wavevectors, for example by trapping the gas in a lattice.

The answer to some of these questions demands a significant theoretical effort while some others can be tackled directly in the lab. To that end, there is an ongoing effort to implement a high-resolution imaging setup on the experiment. With it, we hope to be able to resolve the in-situ density modulations in the ordered phase and therefore the expected translational symmetry breaking associated with the phase transition. In addition, the high-resolution optics would be used to project arbitrary potentials on the atoms, paving the way to the production of a homogeneous cloud. Later, it might even be used to tune the dimensionality of the system.

Simulation of pair density waves

As discussed in section 6.4, we have recently proven our ability, by addressing the dispersive regime for the pairs, to engineer long-range interactions between them and observe an effective modification of the critical behavior for the phase transition process. Similarly to how photonic signals for the atoms-only phase transition were mapped to density modulations, we are currently trying to find a good observable to which a pair modulation operator would map. One interpretation of the system, as shown in the text, would be in terms of an optical Feshbach resonance [278, 279]. Similarly to how the coupling to a molecular channel in the resonance model might be employed to tune the scattering length [131, 153], the coupling to a molecular level of a pair of atoms via a photoassociation transition should lead to a similar result. We sketched a tentative model in the main text for the process.

The addressing of pair density waves is an interesting perspective for the experiment, adding yet another strongly correlated matter system to the list of what can be simulated. In itself, studying pair density waves is also expected to grant insight about the not-so-well understood phase diagrams of the cuprate high temperature superconductors in which they emerge [280].

Cavity-enabled nondemolition transport measurements

The weakly destructive nature of cavity-based measurements makes them attractive to investigate the dynamics of quantum systems under continuous observation. While we have demonstrated the ability to probe the system a discrete number of times without disturbing it with cavity transmission spectroscopy, continuous measurement of the cavity field would require the implementation of a finer detection scheme such as a homodyne[4] setup. With it, continuous nondemolition measurement schemes of transport processes were proposed [106, 281] and could be implemented in the experiment.

---

[4] Homodyning the cavity field would also grant us insight about the phase of scattered light in the density-ordered state: another potential observable of the symmetry breaking process.

Bibliography

1. Ashcroft, N. & Mermin, N. *Solid State Physics* (Cengage Learning, 2011) (cit. on p. 1).
2. Bardeen, J., Cooper, L. N. & Schrieffer, J. R. Theory of Superconductivity. *Physical Review* **108,** 1175–1204 (Dec. 1, 1957) (cit. on pp. 1, 54).
3. Hwang, H. Y. *et al.* Emergent Phenomena at Oxide Interfaces. *Nature Materials* **11,** 103–113 (2 Feb. 2012) (cit. on p. 1).
4. Imada, M., Fujimori, A. & Tokura, Y. Metal-Insulator Transitions. *Reviews of Modern Physics* **70,** 1039–1263 (Oct. 1, 1998) (cit. on p. 1).
5. Kotliar, G. & Vollhardt, D. Strongly Correlated Materials: Insights From Dynamical Mean-Field Theory. *Physics Today* **57,** 53–59 (Mar. 2004) (cit. on p. 1).
6. Bednorz, J. G. & Müller, K. A. Possible highTc Superconductivity in the Ba-La-Cu-O System. *Zeitschrift für Physik B Condensed Matter* **64,** 189–193 (June 1, 1986) (cit. on p. 1).
7. Cao, Y. *et al.* Unconventional Superconductivity in Magic-Angle Graphene Superlattices. *Nature* **556,** 43–50 (7699 Apr. 2018) (cit. on p. 1).
8. Drozdov, A. P. *et al.* Superconductivity at 250 K in Lanthanum Hydride under High Pressures. *Nature* **569,** 528–531 (7757 May 2019) (cit. on p. 1).
9. Privman, V., Vagner, I. D. & Kventsel, G. Quantum Computation in Quantum-Hall Systems. *Physics Letters A* **239,** 141–146 (Mar. 2, 1998) (cit. on p. 1).
10. Bravyi, S. Universal Quantum Computation with the Nu=5/2 Fractional Quantum Hall State. *Physical Review A* **73,** 042313 (Apr. 12, 2006) (cit. on p. 1).
11. Schulz, T. *et al.* Emergent Electrodynamics of Skyrmions in a Chiral Magnet. *Nature Physics* **8,** 301–304 (4 Apr. 2012) (cit. on p. 1).
12. Feynman, R. P. Simulating Physics with Computers. *International Journal of Theoretical Physics* **21,** 467–488 (June 1, 1982) (cit. on p. 2).
13. Lloyd, S. Universal Quantum Simulators. *Science* **273,** 1073–1078 (Aug. 23, 1996) (cit. on p. 2).
14. Arute, F. *et al.* Quantum Supremacy Using a Programmable Superconducting Processor. *Nature* **574,** 505–510 (7779 Oct. 2019) (cit. on p. 2).
15. Zhong, H.-S. *et al.* Quantum Computational Advantage Using Photons. *Science* **370,** 1460–1463 (Dec. 18, 2020) (cit. on p. 2).
16. Daley, A. J. *et al.* Practical Quantum Advantage in Quantum Simulation. *Nature* **607,** 667–676 (7920 July 2022) (cit. on p. 2).
17. Buluta, I. & Nori, F. Quantum Simulators. *Science* **326,** 108–111 (Oct. 2, 2009) (cit. on p. 2).

18. Kendon, V. M., Nemoto, K. & Munro, W. J. Quantum Analogue Computing. *Philosophical Transactions of the Royal Society A: Mathematical, Physical and Engineering Sciences* **368,** 3609–3620 (Aug. 13, 2010) (cit. on p. 2).
19. Cirac, J. I. & Zoller, P. Goals and Opportunities in Quantum Simulation. *Nature Physics* **8,** 264–266 (4 Apr. 2012) (cit. on p. 2).
20. Schaetz, T., Monroe, C. R. & Esslinger, T. Focus on Quantum Simulation. *New Journal of Physics* **15,** 085009 (Aug. 2013) (cit. on p. 2).
21. Georgescu, I. M., Ashhab, S. & Nori, F. Quantum Simulation. *Reviews of Modern Physics* **86,** 153–185 (Mar. 10, 2014) (cit. on p. 2).
22. Bloch, I., Dalibard, J. & Zwerger, W. Many-Body Physics with Ultracold Gases. *Reviews of Modern Physics* **80,** 885–964 (July 18, 2008) (cit. on p. 2).
23. Bloch, I., Dalibard, J. & Nascimbène, S. Quantum Simulations with Ultracold Quantum Gases. *Nature Physics* **8,** 267–276 (4 Apr. 2012) (cit. on pp. 2, 51).
24. Chevy, F. in *Many-Body Physics with Ultracold Gases: Lecture Notes of the Les Houches Summer School: Volume 94, July 2010* (eds Salomon, C., Shlyapnikov, G. V. & Cugliandolo, L. F.) 0 (Oxford University Press, Nov. 15, 2012) (cit. on pp. 2, 51).
25. Garreau, J.-C. Quantum Simulation of Disordered Systems with Cold Atoms. *Comptes Rendus Physique. Prizes of the French Academy of Sciences 2015 / Prix de l'Académie Des Sciences 2015* **18,** 31–46 (Jan. 1, 2017) (cit. on p. 2).
26. Gross, C. & Bloch, I. Quantum Simulations with Ultracold Atoms in Optical Lattices. *Science* **357,** 995–1001 (Sept. 8, 2017) (cit. on p. 2).
27. Browaeys, A. & Lahaye, T. Many-Body Physics with Individually Controlled Rydberg Atoms. *Nature Physics* **16,** 132–142 (2 Feb. 2020) (cit. on p. 2).
28. Aidelsburger, M. *et al.* Cold Atoms Meet Lattice Gauge Theory. *Philosophical Transactions of the Royal Society A: Mathematical, Physical and Engineering Sciences* **380,** 20210064 (Dec. 20, 2021) (cit. on p. 2).
29. Amico, L. *et al.* Roadmap on Atomtronics: State of the Art and Perspective. *AVS Quantum Science* **3,** 039201 (Sept. 2021) (cit. on p. 2).
30. Anderson, M. H., Ensher, J. R., Matthews, M. R., Wieman, C. E. & Cornell, E. A. Observation of Bose-Einstein Condensation in a Dilute Atomic Vapor. *Science* **269,** 198–201 (July 14, 1995) (cit. on p. 2).
31. Davis, K. B. *et al.* Bose-Einstein Condensation in a Gas of Sodium Atoms. *Physical Review Letters* **75,** 3969–3973 (Nov. 27, 1995) (cit. on p. 2).
32. Zwierlein, M. W., Abo-Shaeer, J. R., Schirotzek, A., Schunck, C. H. & Ketterle, W. Vortices and Superfluidity in a Strongly Interacting Fermi Gas. *Nature* **435,** 1047–1051 (7045 June 2005) (cit. on p. 2).
33. Hofstetter, W. & Qin, T. Quantum Simulation of Strongly Correlated Condensed Matter Systems. *Journal of Physics B: Atomic, Molecular and Optical Physics* **51,** 082001 (Mar. 2018) (cit. on p. 2).
34. Billy, J. *et al.* Direct Observation of Anderson Localization of Matter Waves in a Controlled Disorder. *Nature* **453,** 891–894 (7197 June 2008) (cit. on p. 2).
35. Roati, G. *et al.* Anderson Localization of a Non-Interacting Bose–Einstein Condensate. *Nature* **453,** 895–898 (7197 June 2008) (cit. on p. 2).

36. Krinner, S., Stadler, D., Husmann, D., Brantut, J.-P. & Esslinger, T. Observation of Quantized Conductance in Neutral Matter. *Nature* **517,** 64–67 (Jan. 2015) (cit. on p. 2).

37. Valtolina, G. *et al.* Josephson Effect in Fermionic Superfluids across the BEC-BCS Crossover. *Science (New York, N.Y.)* **350,** 1505–1508 (2015) (cit. on p. 2).

38. Luick, N. *et al.* An Ideal Josephson Junction in an Ultracold Two-Dimensional Fermi Gas. *Science (New York, N.Y.)* **369,** 89–91 (2020) (cit. on p. 2).

39. Chin, C., Grimm, R., Julienne, P. & Tiesinga, E. Feshbach Resonances in Ultracold Gases. *Reviews of Modern Physics* **82,** 1225–1286 (Apr. 29, 2010) (cit. on pp. 2, 47).

40. Greiner, M., Mandel, O., Esslinger, T., Hänsch, T. W. & Bloch, I. Quantum Phase Transition from a Superfluid to a Mott Insulator in a Gas of Ultracold Atoms. *Nature* **415,** 39–44 (6867 Jan. 2002) (cit. on p. 2).

41. Jördens, R., Strohmaier, N., Günter, K., Moritz, H. & Esslinger, T. A Mott Insulator of Fermionic Atoms in an Optical Lattice. *Nature* **455,** 204–207 (7210 Sept. 2008) (cit. on p. 2).

42. Paredes, B. *et al.* Tonks–Girardeau Gas of Ultracold Atoms in an Optical Lattice. *Nature* **429,** 277–281 (6989 May 2004) (cit. on p. 2).

43. Jotzu, G. *et al.* Experimental Realization of the Topological Haldane Model with Ultracold Fermions. *Nature* **515,** 237–240 (7526 Nov. 2014) (cit. on p. 2).

44. Gross, C. & Bakr, W. S. Quantum Gas Microscopy for Single Atom and Spin Detection. *Nature Physics* **17,** 1316–1323 (12 Dec. 2021) (cit. on p. 2).

45. Zwerger, W. *The BCS-BEC Crossover and the Unitary Fermi Gas* 543 pp. (Springer Science & Business Media, Oct. 22, 2011) (cit. on pp. 2, 35, 51, 54, 90).

46. Heiselberg, H. Fermi Systems with Long Scattering Lengths. *Physical Review A* **63,** 043606 (Mar. 14, 2001) (cit. on pp. 2, 55).

47. Ketterle, W. & Zwierlein, M. W. Making, Probing and Understanding Ultracold Fermi Gases. *La Rivista del Nuovo Cimento* **31,** 247–422 (May 1, 2008) (cit. on pp. 2, 7, 31, 34, 93, 119).

48. Randeria, M. & Taylor, E. Crossover from Bardeen-Cooper-Schrieffer to Bose-Einstein Condensation and the Unitary Fermi Gas. *Annual Review of Condensed Matter Physics* **5,** 209–232 (2014) (cit. on pp. 2, 54).

49. Parish, M. M. in *Quantum Gas Experiments Cold Atoms* Volume 3, 179–197 (IMPERIAL COLLEGE PRESS, May 5, 2014) (cit. on pp. 2, 54).

50. Holten, M. *et al.* Observation of Cooper Pairs in a Mesoscopic Two-Dimensional Fermi Gas. *Nature* **606,** 287–291 (7913 June 2022) (cit. on p. 2).

51. Vale, C. J. & Zwierlein, M. Spectroscopic Probes of Quantum Gases. *Nature Physics* **17,** 1305–1315 (12 Dec. 2021) (cit. on p. 2).

52. Biss, H. *et al.* Excitation Spectrum and Superfluid Gap of an Ultracold Fermi Gas. *Physical Review Letters* **128,** 100401 (Mar. 8, 2022) (cit. on pp. 2, 86).

53. Mivehvar, F., Piazza, F., Donner, T. & Ritsch, H. Cavity QED with Quantum Gases: New Paradigms in Many-Body Physics. *Advances in Physics* **70,** 1–153 (Jan. 2, 2021) (cit. on p. 2).

54. Raimond, J. M., Brune, M. & Haroche, S. Manipulating Quantum Entanglement with Atoms and Photons in a Cavity. *Reviews of Modern Physics* **73,** 565–582 (Aug. 28, 2001) (cit. on p. 2).

55. Tanji-Suzuki, H. *et al.* in *Advances In Atomic, Molecular, and Optical Physics* (eds Arimondo, E., Berman, P. R. & Lin, C. C.) 201–237 (Academic Press, Jan. 1, 2011) (cit. on pp. 2, 18, 26, 72).
56. Colombe, Y. *et al.* Strong Atom–Field Coupling for Bose–Einstein Condensates in an Optical Cavity on a Chip. *Nature* **450,** 272–276 (7167 Nov. 2007) (cit. on p. 2).
57. Brennecke, F., Ritter, S., Donner, T. & Esslinger, T. Cavity Optomechanics with a Bose-Einstein Condensate. *Science* **322,** 235–238 (Oct. 10, 2008) (cit. on pp. 2, 82).
58. Münstermann, P., Fischer, T., Maunz, P., Pinkse, P. W. H. & Rempe, G. Observation of Cavity-Mediated Long-Range Light Forces between Strongly Coupled Atoms. *Physical Review Letters* **84,** 4068–4071 (May 2000) (cit. on pp. 2, 101, 104).
59. Ritsch, H., Domokos, P., Brennecke, F. & Esslinger, T. Cold Atoms in Cavity-Generated Dynamical Optical Potentials. *Reviews of Modern Physics* **85,** 553–601 (Apr. 2, 2013) (cit. on pp. 2, 85).
60. Baumann, K., Guerlin, C., Brennecke, F. & Esslinger, T. Dicke Quantum Phase Transition with a Superfluid Gas in an Optical Cavity. *Nature* **464,** 1301–1306 (Apr. 2010) (cit. on pp. 3, 100).
61. Klinder, J., Keßler, H., Wolke, M., Mathey, L. & Hemmerich, A. Dynamical Phase Transition in the Open Dicke Model. *Proceedings of the National Academy of Sciences* **112,** 3290–3295 (2015/03/17, 2015-03) (cit. on pp. 3, 100).
62. Landig, R. *et al.* Quantum Phases from Competing Short- and Long-Range Interactions in an Optical Lattice. *Nature* **532,** 476–479 (2016/04/28/print, 2016-04-28) (cit. on pp. 3, 100).
63. Vaidya, V. D. *et al.* Tunable-Range, Photon-Mediated Atomic Interactions in Multimode Cavity QED. *Physical Review X* **8,** 011002 (Jan. 8, 2018) (cit. on p. 3).
64. Dogra, N. *et al.* Dissipation-Induced Structural Instability and Chiral Dynamics in a Quantum Gas. *Science* **366,** 1496–1499 (Dec. 20, 2019) (cit. on p. 3).
65. Ferri, F. *et al.* Emerging Dissipative Phases in a Superradiant Quantum Gas with Tunable Decay. *Physical Review X* **11,** 041046 (Dec. 7, 2021) (cit. on p. 3).
66. Keßler, H. *et al.* Observation of a Dissipative Time Crystal. *Physical Review Letters* **127,** 043602 (July 19, 2021) (cit. on p. 3).
67. Guo, Y. *et al.* An Optical Lattice with Sound. *Nature* **599,** 211–215 (7884 Nov. 2021) (cit. on pp. 3, 101).
68. Dreon, D. *et al.* Self-Oscillating Pump in a Topological Dissipative Atom–Cavity System. *Nature* **608,** 494–498 (7923 Aug. 2022) (cit. on p. 3).
69. Kollath, C., Sheikhan, A., Wolff, S. & Brennecke, F. Ultracold Fermions in a Cavity-Induced Artificial Magnetic Field. *Physical Review Letters* **116,** 060401 (Feb. 2016) (cit. on pp. 3, 26, 100).
70. Mivehvar, F., Ritsch, H. & Piazza, F. Superradiant Topological Peierls Insulator inside an Optical Cavity. *Physical Review Letters* **118,** 073602 (Feb. 2017) (cit. on pp. 3, 26, 100).
71. Schlawin, F. & Jaksch, D. Cavity-Mediated Unconventional Pairing in Ultracold Fermionic Atoms. *Physical Review Letters* **123,** 133601 (Sept. 2019) (cit. on pp. 3, 26, 100).
72. Curtis, J. B., Raines, Z. M., Allocca, A. A., Hafezi, M. & Galitski, V. M. Cavity Quantum Eliashberg Enhancement of Superconductivity. *Physical Review Letters* **122,** 167002 (Apr. 26, 2019) (cit. on pp. 3, 26).

73. Bloch, J., Cavalleri, A., Galitski, V., Hafezi, M. & Rubio, A. Strongly Correlated Electron–Photon Systems. *Nature* **606,** 41–48 (7912 June 2022) (cit. on p. 3).
74. Gehm, M. E. *Preparation of an Optically-Trapped Degenerate Fermi Gas of 6 Li: Finding the Route to Degeneracy* (Duke University, 2003) (cit. on pp. 7, 14, 19, 27).
75. Zimmermann, B. *Microscopy of Ultra-Cold Fermionic Lithium* Doctoral Thesis (ETH Zurich, 2010) (cit. on p. 7).
76. Weimer, W. *Probing Superfluid Properties in Strongly Correlated Fermi Gases with High Spatial Resolution* (Universität Hamburg, 2014) (cit. on p. 7).
77. Valtolina, G. *Superfluid and Spin Dynamics of Strongly Interacting Atomic Fermi Gases* (Scuola Normale Superiore di Pisa, 2016) (cit. on p. 7).
78. Chin, C., Grimm, R., Julienne, P. & Tiesinga, E. Feshbach Resonances in Ultracold Gases. *Reviews of Modern Physics* **82,** 1225–1286 (Apr. 2010) (cit. on p. 8).
79. Roux, K. E. R. *Cavity Quantum Electrodynamics with Strongly Correlated Fermions* (EPFL, Lausanne, 2022). 249 pp. (cit. on pp. 8, 12, 13, 18, 21, 23, 24, 30, 31, 35, 150, 153).
80. Roux, K., Cilenti, B., Helson, V., Konishi, H. & Brantut, J.-P. Compact Bulk-Machined Electromagnets for Quantum Gas Experiments. *SciPost Physics* **6,** 048 (Apr. 24, 2019) (cit. on pp. 8, 10).
81. Roux, K., Helson, V., Konishi, H. & Brantut, J. P. Cavity-Assisted Preparation and Detection of a Unitary Fermi Gas. *New Journal of Physics* **23,** 043029 (Apr. 2021) (cit. on p. 8).
82. Ricci, L., Martini, L. M., Franchi, M. & Bertoldi, A. A Current-Carrying Coil Design with Improved Liquid Cooling Arrangement. *Review of Scientific Instruments* **84,** 065115 (June 2013) (cit. on p. 10).
83. Mosk, A. *et al.* Resonator-Enhanced Optical Dipole Trap for Fermionic Lithium Atoms. *Optics Letters* **26,** 1837–1839 (Dec. 1, 2001) (cit. on p. 11).
84. Siegman, A. *Lasers* (University Science Books, 1986) (cit. on pp. 11, 19).
85. Drever, R. W. P. *et al.* Laser Phase and Frequency Stabilization Using an Optical Resonator. *Applied Physics B* **31,** 97–105 (June 1, 1983) (cit. on pp. 11, 12).
86. Black, E. D. An Introduction to Pound–Drever–Hall Laser Frequency Stabilization. *American Journal of Physics* **69,** 79–87 (Jan. 2001) (cit. on pp. 11, 12).
87. Phillips, W. D. & Metcalf, H. Laser Deceleration of an Atomic Beam. *Physical Review Letters* **48,** 596–599 (Mar. 1, 1982) (cit. on p. 14).
88. *Laser Cooling and Trapping* () (cit. on p. 14).
89. Roux, K., Helson, V., Konishi, H. & Brantut, J.-P. Cavity-Assisted Preparation and Detection of a Unitary Fermi Gas. *New Journal of Physics* **23,** 043029 (2021) (cit. on pp. 15, 18, 30, 31).
90. Luo, L. *et al.* Evaporative Cooling of Unitary Fermi Gas Mixtures in Optical Traps. *New Journal of Physics* **8,** 213 (Sept. 2006) (cit. on p. 15).
91. Cox, K. C., Greve, G. P., Wu, B. & Thompson, J. K. Spatially Homogeneous Entanglement for Matter-Wave Interferometry Created with Time-Averaged Measurements. *Physical Review A* **94,** 061601 (Dec. 2, 2016) (cit. on p. 15).
92. Roux, K., Konishi, H., Helson, V. & Brantut, J.-P. Strongly Correlated Fermions Strongly Coupled to Light. *Nature Communications* **11,** 2974 (1 June 12, 2020) (cit. on pp. 18, 31).

93. Jaynes, E. & Cummings, F. Comparison of Quantum and Semiclassical Radiation Theories with Application to the Beam Maser. *Proceedings of the IEEE* **51,** 89–109 (Jan. 1963) (cit. on p. 18).

94. Haroche, S. & Raimond, J. *Exploring the Quantum: Atoms, Cavities, and Photons* (OUP Oxford, 2006) (cit. on pp. 18, 21).

95. Tavis, M. & Cummings, F. W. Exact Solution for an N-Molecule—Radiation-Field Hamiltonian. *Physical Review* **170,** 379–384 (June 10, 1968) (cit. on p. 19).

96. Moore, M. G., Zobay, O. & Meystre, P. Quantum Optics of a Bose-Einstein Condensate Coupled to a Quantized Light Field. *Physical Review A* **60,** 1491–1506 (Aug. 1, 1999) (cit. on p. 19).

97. Gardiner, C., Zoller, P. & Zoller, P. *Quantum Noise: A Handbook of Markovian and Non-Markovian Quantum Stochastic Methods with Applications to Quantum Optics* (Springer, 2004) (cit. on pp. 21, 85).

98. Dicke, R. H. Coherence in Spontaneous Radiation Processes. *Physical Review* **93,** 99–110 (Jan. 1, 1954) (cit. on p. 24).

99. Holstein, T. & Primakoff, H. Field Dependence of the Intrinsic Domain Magnetization of a Ferromagnet. *Physical Review* **58,** 1098–1113 (Dec. 15, 1940) (cit. on pp. 25, 72).

100. Mazza, G. & Georges, A. Superradiant Quantum Materials. *Physical Review Letters* **122,** 017401 (Jan. 9, 2019) (cit. on p. 26).

101. Cohen-Tannoudji, C., Dupont-Roc, J. & Grynberg, G. *Atom-Photon Interactions: Basic Processes and Applications* (Wiley, 1998) (cit. on pp. 26, 27).

102. Zhang, H. *et al.* Collective State Measurement of Mesoscopic Ensembles with Single-Atom Resolution. *Physical Review Letters* **109,** 133603 (Sept. 27, 2012) (cit. on p. 28).

103. Horikoshi, M. *et al.* Appropriate Probe Condition for Absorption Imaging of Ultracold 6Li Atoms. *Journal of the Physical Society of Japan* **86,** 104301 (Oct. 15, 2017) (cit. on pp. 28, 31).

104. Sawyer, B. J., Horvath, M. S. J., Tiesinga, E., Deb, A. B. & Kjærgaard, N. Dispersive Optical Detection of Magnetic Feshbach Resonances in Ultracold Gases. *Physical Review A* **96,** 022705 (Aug. 18, 2017) (cit. on p. 30).

105. Zeiher, J., Wolf, J., Isaacs, J. A., Kohler, J. & Stamper-Kurn, D. M. Tracking Evaporative Cooling of a Mesoscopic Atomic Quantum Gas in Real Time. *Physical Review X* **11,** 041017 (Oct. 25, 2021) (cit. on pp. 30, 79).

106. Uchino, S., Ueda, M. & Brantut, J.-P. Universal Noise in Continuous Transport Measurements of Interacting Fermions. *Physical Review A* **98,** 063619 (Dec. 17, 2018) (cit. on pp. 30, 131).

107. Zwierlein, M. W., Schunck, C. H., Schirotzek, A. & Ketterle, W. Direct Observation of the Superfluid Phase Transition in Ultracold Fermi Gases. *Nature* **442,** 54–58 (7098 July 2006) (cit. on p. 30).

108. *Pairing and Phase Separation in a Polarized Fermi Gas | Science* `https://www.science.org/doi/10.1126/science.1122876` (cit. on p. 30).

109. Spiegelhalder, F. M. *et al.* Collisional Stability of 40K Immersed in a Strongly Interacting Fermi Gas of 6Li. *Physical Review Letters* **103,** 223203 (Nov. 25, 2009) (cit. on p. 31).

110. Nascimbène, S., Navon, N., Jiang, K. J., Chevy, F. & Salomon, C. Exploring the Thermodynamics of a Universal Fermi Gas. *Nature* **463,** 1057–1060 (7284 Feb. 2010) (cit. on pp. 31, 33, 34, 55).

111. Shin, Y.-i., Schunck, C. H., Schirotzek, A. & Ketterle, W. Phase Diagram of a Two-Component Fermi Gas with Resonant Interactions. *Nature* **451,** 689–693 (7179 Feb. 2008) (cit. on p. 31).

112. Luo, L., Clancy, B., Joseph, J., Kinast, J. & Thomas, J. E. Measurement of the Entropy and Critical Temperature of a Strongly Interacting Fermi Gas. *Physical Review Letters* **98,** 080402 (Feb. 21, 2007) (cit. on p. 31).

113. Reinaudi, G., Lahaye, T., Wang, Z. & Guéry-Odelin, D. Strong Saturation Absorption Imaging of Dense Clouds of Ultracold Atoms. *Optics Letters* **32,** 3143–3145 (Nov. 1, 2007) (cit. on p. 31).

114. Hueck, K. *et al.* Calibrating High Intensity Absorption Imaging of Ultracold Atoms. *Optics Express* **25,** 8670–8679 (Apr. 17, 2017) (cit. on p. 31).

115. Amico, A. *Andrea Amico Probing the Many Body Dynamics of Ultracold Repulsive Fermi Gases of Lithium Atoms* (University of Firenze, Florence, 2019). ¨ (cit. on p. 32).

116. Guajardo, E. R. S., Tey, M. K., Sidorenkov, L. A. & Grimm, R. Higher-Nodal Collective Modes in a Resonantly Interacting Fermi Gas. *Physical Review A* **87,** 063601 (June 3, 2013) (cit. on p. 33).

117. Del Pace, G., Kwon, W. J., Zaccanti, M., Roati, G. & Scazza, F. Tunneling Transport of Unitary Fermions across the Superfluid Transition. *Physical Review Letters* **126,** 055301 (Feb. 4, 2021) (cit. on p. 33).

118. Horikoshi, M., Nakajima, S., Ueda, M. & Mukaiyama, T. Measurement of Universal Thermodynamic Functions for a Unitary Fermi Gas. *Science* **327,** 442–445 (Jan. 22, 2010) (cit. on p. 33).

119. Nascimbène, S., Navon, N., Chevy, F. & Salomon, C. The Equation of State of Ultracold Bose and Fermi Gases: A Few Examples. *New Journal of Physics* **12,** 103026 (Oct. 2010) (cit. on p. 33).

120. Ku, M. J. H., Sommer, A. T., Cheuk, L. W. & Zwierlein, M. W. Revealing the Superfluid Lambda Transition in the Universal Thermodynamics of a Unitary Fermi Gas. *Science (New York, N.Y.)* **335,** 563–567 (2012) (cit. on pp. 33, 120).

121. Ku, M. J. H., Sommer, A. T., Cheuk, L. W. & Zwierlein, M. W. Revealing the Superfluid Lambda Transition in the Universal Thermodynamics of a Unitary Fermi Gas. *Science* **335,** 563–567 (Feb. 3, 2012) (cit. on pp. 34, 55).

122. Liu, X.-J., Hu, H. & Drummond, P. D. Virial Expansion for a Strongly Correlated Fermi Gas. *Physical Review Letters* **102,** 160401 (Apr. 22, 2009) (cit. on p. 34).

123. Hou, Y.-H., Pitaevskii, L. P. & Stringari, S. First and Second Sound in a Highly Elongated Fermi Gas at Unitarity. *Physical Review A* **88,** 043630 (Oct. 21, 2013) (cit. on p. 34).

124. Yan, Z.-C., Babb, J. F., Dalgarno, A. & Drake, G. W. F. Variational Calculations of Dispersion Coefficients for Interactions among H, He, and Li Atoms. *Physical Review A* **54,** 2824–2833 (Oct. 1, 1996) (cit. on p. 41).

125. Walraven, J. T. M. Quantum Gases Lectures University of Amsterdam, 363 (cit. on p. 41).

126. Landau, L. & Lifshitz, E. *Quantum Mechanics: Non-relativistic Theory* (Elsevier Science, 1981) (cit. on p. 43).

127. Huang, K. & Yang, C. N. Quantum-Mechanical Many-Body Problem with Hard-Sphere Interaction. *Physical Review* **105,** 767–775 (Feb. 1, 1957) (cit. on p. 46).

128. Bethe, H. & Peierls, R. Quantum Theory of the Diplon. *Proceedings of the Royal Society of London. Series A, Mathematical and Physical Sciences* **148,** 146–156 (1935) (cit. on p. 46).

129. Ma, Z.-Q. The Levinson Theorem. *Journal of Physics A: Mathematical and General* **39,** R625 (Nov. 2006) (cit. on p. 46).

130. Taylor, J. *Scattering Theory: The Quantum Theory of Nonrelativistic Collisions* (Dover Publications, 2012) (cit. on p. 47).

131. Naidon, P. & Pricoupenko, L. Width and Shift of Fano-Feshbach Resonances for van Der Waals Interactions. *Physical Review A* **100,** 042710 (Oct. 28, 2019) (cit. on pp. 48, 49, 131).

132. Mies, F. H. A Multichannel Quantum Defect Analysis of Diatomic Predissociation and Inelastic Atomic Scattering. *The Journal of Chemical Physics* **80,** 2514–2525 (Mar. 15, 1984) (cit. on p. 48).

133. Schunck, C. H. *et al.* Feshbach Resonances in Fermionic \$\hat{}{6}\mathrm{Li}\$. *Physical Review A* **71,** 045601 (Apr. 5, 2005) (cit. on p. 50).

134. Zürn, G. *et al.* Precise Characterization of 6Li Feshbach Resonances Using Trap-Sideband-Resolved RF Spectroscopy of Weakly Bound Molecules. *Physical Review Letters* **110,** 135301 (Mar. 25, 2013) (cit. on pp. 50, 55).

135. Giorgini, S., Pitaevskii, L. P. & Stringari, S. Theory of Ultracold Atomic Fermi Gases. *Reviews of Modern Physics* **80,** 1215–1274 (Oct. 2, 2008) (cit. on p. 51).

136. Ho, T.-L. & Mueller, E. J. High Temperature Expansion Applied to Fermions near Feshbach Resonance. *Physical Review Letters* **92,** 160404 (Apr. 20, 2004) (cit. on p. 52).

137. Pricoupenko, L. & Castin, Y. One Particle in a Box: The Simplest Model for a Fermi Gas in the Unitary Limit. *Physical Review A* **69,** 051601 (May 18, 2004) (cit. on pp. 52, 53).

138. Cooper, L. N. Bound Electron Pairs in a Degenerate Fermi Gas. *Physical Review* **104,** 1189–1190 (Nov. 15, 1956) (cit. on p. 54).

139. Bardeen, J., Cooper, L. N. & Schrieffer, J. R. Microscopic Theory of Superconductivity. *Physical Review* **106,** 162–164 (Apr. 1, 1957) (cit. on p. 54).

140. Haussmann, R., Rantner, W., Cerrito, S. & Zwerger, W. Thermodynamics of the BCS-BEC Crossover. *Physical Review A* **75,** 023610 (Feb. 8, 2007) (cit. on p. 55).

141. Eagles, D. M. Possible Pairing without Superconductivity at Low Carrier Concentrations in Bulk and Thin-Film Superconducting Semiconductors. *Physical Review* **186,** 456–463 (Oct. 10, 1969) (cit. on p. 54).

142. Leggett, A. J. *Diatomic Molecules and Cooper Pairs* in *Modern Trends in the Theory of Condensed Matter* (eds Pękalski, A. & Przystawa, J. A.) (Springer, Berlin, Heidelberg, 1980), 13–27 (cit. on p. 54).

143. Nozières, P. & Schmitt-Rink, S. Bose Condensation in an Attractive Fermion Gas: From Weak to Strong Coupling Superconductivity. *Journal of Low Temperature Physics* **59,** 195–211 (May 1, 1985) (cit. on p. 54).

144. Zwierlein, M. W. *et al.* Condensation of Pairs of Fermionic Atoms near a Feshbach Resonance. *Physical Review Letters* **92,** 120403 (Mar. 25, 2004) (cit. on p. 54).

145. Regal, C. A., Greiner, M. & Jin, D. S. Observation of Resonance Condensation of Fermionic Atom Pairs. *Physical Review Letters* **92,** 040403 (Jan. 28, 2004) (cit. on p. 54).

146. Ketterle, W., Shin, Y., Schirotzek, A. & Schunk, C. H. Superfluidity in a Gas of Strongly Interacting Fermions. *Journal of Physics: Condensed Matter* **21,** 164206 (Mar. 2009) (cit. on p. 56).

147. Tan, S. Energetics of a Strongly Correlated Fermi Gas. *Annals of Physics* **323,** 2952–2970 (Dec. 2008) (cit. on pp. 56, 59, 127).

148. Tan, S. Generalized Virial Theorem and Pressure Relation for a Strongly Correlated Fermi Gas. *Annals of Physics* **323,** 2987–2990 (Dec. 2008) (cit. on pp. 56, 57).

149. Tan, S. Large Momentum Part of Fermions with Large Scattering Length. *Annals of Physics* **323,** 2971–2986 (Dec. 2008) (cit. on pp. 56, 57).

150. Zhang, S. & Leggett, A. J. Universal Properties of the Ultracold Fermi Gas. *Physical Review A* **79,** 023601 (Feb. 2, 2009) (cit. on pp. 56, 58).

151. Leggett, A. & Leggett, M. *Quantum Liquids: Bose Condensation and Cooper Pairing in Condensed-Matter Systems* (OUP Oxford, 2006) (cit. on p. 56).

152. Yu, Z., Bruun, G. M. & Baym, G. Short-Range Correlations and Entropy in Ultracold-Atom Fermi Gases. *Physical Review A* **80,** 023615 (Aug. 20, 2009) (cit. on pp. 56, 58).

153. Braaten, E., Kang, D. & Platter, L. Universal Relations for a Strongly Interacting Fermi Gas near a Feshbach Resonance. *Physical Review A* **78,** 053606 (Nov. 4, 2008) (cit. on pp. 58, 90, 131).

154. Mukherjee, B. *et al.* Spectral Response and Contact of the Unitary Fermi Gas. *Physical Review Letters* **122,** 203402 (May 23, 2019) (cit. on pp. 58, 59).

155. Stewart, J. T., Gaebler, J. P., Drake, T. E. & Jin, D. S. Verification of Universal Relations in a Strongly Interacting Fermi Gas. *Physical Review Letters* **104,** 235301 (June 7, 2010) (cit. on p. 58).

156. Braaten, E., Kang, D. & Platter, L. Short-Time Operator Product Expansion for Rf Spectroscopy of a Strongly Interacting Fermi Gas. *Physical Review Letters* **104,** 223004 (June 4, 2010) (cit. on p. 59).

157. Shkedrov, C., Florshaim, Y., Ness, G., Gandman, A. & Sagi, Y. High-Sensitivity Rf Spectroscopy of a Strongly Interacting Fermi Gas. *Physical Review Letters* **121,** 093402 (Aug. 30, 2018) (cit. on p. 59).

158. Hoinka, S. *et al.* Precise Determination of the Structure Factor and Contact in a Unitary Fermi Gas. *Physical Review Letters* **110,** 055305 (Jan. 30, 2013) (cit. on pp. 59, 74, 76, 86).

159. Son, D. T. & Thompson, E. G. Short-Distance and Short-Time Structure of a Unitary Fermi Gas. *Physical Review A* **81,** 063634 (June 25, 2010) (cit. on pp. 59, 91).

160. Hu, H. & Liu, X.-J. Universal Dynamic Structure Factor of a Strongly Correlated Fermi Gas. *Physical Review A* **85,** 023612 (Feb. 9, 2012) (cit. on p. 59).

161. Carcy, C. *et al.* Contact and Sum Rules in a Near-Uniform Fermi Gas at Unitarity. *Physical Review Letters* **122,** 203401 (May 23, 2019) (cit. on pp. 59, 86).

162. Partridge, G. B., Strecker, K. E., Kamar, R. I., Jack, M. W. & Hulet, R. G. Molecular Probe of Pairing in the BEC-BCS Crossover. *Physical Review Letters* **95,** 020404 (July 7, 2005) (cit. on pp. 59, 62, 64, 67).

163. Werner, F., Tarruell, L. & Castin, Y. Number of Closed-Channel Molecules in the BEC-BCS Crossover. *The European Physical Journal B* **68,** 401–415 (Apr. 1, 2009) (cit. on pp. 59, 62).

164. Konishi, H., Roux, K., Helson, V. & Brantut, J.-P. *Universal Pair-Polaritons in a Strongly Interacting Fermi Gas* Mar. 3, 2021 (cit. on p. 61).

165. Stwalley, W. C. & Wang, H. Photoassociation of Ultracold Atoms: A New Spectroscopic Technique. *Journal of Molecular Spectroscopy* **195,** 194–228 (June 1, 1999) (cit. on p. 61).

166. Jones, K. M., Tiesinga, E., Lett, P. D. & Julienne, P. S. Ultracold Photoassociation Spectroscopy: Long-range Molecules and Atomic Scattering. *Reviews of Modern Physics* **78,** 483–535 (May 22, 2006) (cit. on pp. 61, 64).

167. Abraham, E. R. I., Ritchie, N. W. M., McAlexander, W. I. & Hulet, R. G. Photoassociative Spectroscopy of Long-range States of Ultracold 6Li2 and 7Li2. *The Journal of Chemical Physics* **103,** 7773–7778 (Nov. 8, 1995) (cit. on pp. 62, 65, 66, 70).

168. Yasuda, M., Kishimoto, T., Takamoto, M. & Katori, H. Photoassociation Spectroscopy of 88Sr: Reconstruction of the Wave Function near the Last Node. *Physical Review A* **73,** 011403 (Jan. 27, 2006) (cit. on p. 62).

169. Ulmanis, J., Deiglmayr, J., Repp, M., Wester, R. & Weidemüller, M. Ultracold Molecules Formed by Photoassociation: Heteronuclear Dimers, Inelastic Collisions, and Interactions with Ultrashort Laser Pulses. *Chemical Reviews* **112,** 4890–4927 (Sept. 12, 2012) (cit. on p. 62).

170. *Cold Molecules: Progress in Quantum Engineering of Chemistry and Quantum Matter | Science* `https://www.science.org/doi/10.1126/science.aam6299` (cit. on pp. 62, 79).

171. Yan, M., DeSalvo, B. J., Huang, Y., Naidon, P. & Killian, T. C. Rabi Oscillations between Atomic and Molecular Condensates Driven with Coherent One-Color Photoassociation. *Physical Review Letters* **111,** 150402 (Oct. 10, 2013) (cit. on p. 62).

172. Taie, S., Watanabe, S., Ichinose, T. & Takahashi, Y. Feshbach-Resonance-Enhanced Coherent Atom-Molecule Conversion with Ultranarrow Photoassociation Resonance. *Physical Review Letters* **116,** 043202 (Jan. 27, 2016) (cit. on p. 62).

173. Cohen-Tannoudji, C., Diu, B. & Laloë, F. *Quantum Mechanics, Volume 2: Angular Momentum, Spin, and Approximation Methods* (Wiley, 2020) (cit. on p. 62).

174. Brown, J. & Carrington, A. *Rotational Spectroscopy of Diatomic Molecules* (Cambridge University Press, 2003) (cit. on p. 63).

175. McAlexander, W. I. *et al.* Precise Atomic Radiative Lifetime via Photoassociative Spectroscopy of Ultracold Lithium. *Physical Review A* **51,** R871–R874 (Feb. 1, 1995) (cit. on p. 63).

176. Zilio, S. C. *et al.* Polarization Dependence of Optical Suppression in Photoassociative Ionization Collisions in a Sodium Magneto-optic Trap. *Physical Review Letters* **76,** 2033–2036 (Mar. 18, 1996) (cit. on p. 63).

177. Julienne, P. S. Cold Binary Atomic Collisions in a Light Field. *Journal of Research of the National Institute of Standards and Technology* **101,** 487–503 (1996) (cit. on p. 64).

178. Kinoshita, T., Wenger, T. & Weiss, D. S. Local Pair Correlations in One-Dimensional Bose Gases. *Physical Review Letters* **95,** 190406 (Nov. 3, 2005) (cit. on p. 64).

179. Semczuk, M., Gunton, W., Bowden, W. & Madison, K. W. Anomalous Behavior of Dark States in Quantum Gases of 6Li. *Physical Review Letters* **113,** 055302 (July 29, 2014) (cit. on pp. 64, 67).

180. Paintner, T. *et al.* Pair Fraction in a Finite-Temperature Fermi Gas on the BEC Side of the BCS-BEC Crossover. *Physical Review A* **99,** 053617 (May 28, 2019) (cit. on p. 64).

181. Liu, X.-P. *et al.* Observation of the Density Dependence of the Closed-Channel Fraction of a 6Li Superfluid. *National Science Review* **9,** nwab226 (Oct. 1, 2022) (cit. on p. 64).

182. LeRoy, R. J. & Bernstein, R. B. Dissociation Energy and Long-Range Potential of Diatomic Molecules from Vibrational Spacings of Higher Levels. *The Journal of Chemical Physics* **52,** 3869–3879 (Apr. 15, 1970) (cit. on p. 65).

183. Le Roy, R. J. Theory of Deviations from the Limiting Near-dissociation Behavior of Diatomic Molecules. *The Journal of Chemical Physics* **73,** 6003–6012 (Dec. 15, 1980) (cit. on p. 65).

184. Jasik, P. & Sienkiewicz, J. E. Calculation of Adiabatic Potentials of Li2. *Chemical Physics* **323,** 563–573 (Apr. 21, 2006) (cit. on p. 66).

185. Semczuk, M. *et al.* High-Resolution Photoassociation Spectroscopy of the ${}{̂6}$Li${}_{2}$ ${1}{̂3}{\ensuremath{\Sigma}}_{g}{̂+}$ State. *Physical Review A* **87,** 052505 (May 9, 2013) (cit. on p. 66).

186. Linton, C., Murphy, T. L., Martin, F., Bacis, R. & Verges, J. Fourier Transform Spectroscopy of the $13̂\Sigma+̂_g–a3̂\Sigma+̂_u$ Transition of the 6Li2 Molecule. *The Journal of Chemical Physics* **91,** 6036–6041 (Nov. 15, 1989) (cit. on p. 66).

187. Hu, H., Liu, X.-J. & Drummond, P. D. Universal Contact of Strongly Interacting Fermions at Finite Temperatures. *New Journal of Physics* **13,** 035007 (Mar. 2011) (cit. on pp. 74, 76).

188. Ritsch, H., Domokos, P., Brennecke, F. & Esslinger, T. Cold Atoms in Cavity-Generated Dynamical Optical Potentials. *Reviews of Modern Physics* **85,** 553–601 (Apr. 2013) (cit. on pp. 79, 101).

189. *Universal Spin Transport and Quantum Bounds for Unitary Fermions | Annual Review of Condensed Matter Physics* `https://www.annualreviews.org/doi/10.1146/annurev-conmatphys-031218-013732` (cit. on p. 79).

190. Amico, A. *et al.* Time-Resolved Observation of Competing Attractive and Repulsive Short-Range Correlations in Strongly Interacting Fermi Gases. *Physical Review Letters* **121,** 253602 (Dec. 19, 2018) (cit. on p. 79).

191. Krinner, S., Esslinger, T. & Brantut, J.-P. Two-Terminal Transport Measurements with Cold Atoms. *Journal of Physics: Condensed Matter* **29,** 343003 (July 2017) (cit. on p. 79).

192. Eisele, M., Maier, R. A. W. & Zimmermann, C. Fast In Situ Observation of Atomic Feshbach Resonances by Photoassociative Ionization. *Physical Review Letters* **124,** 123401 (Mar. 24, 2020) (cit. on p. 79).

193. Flick, J., Ruggenthaler, M., Appel, H. & Rubio, A. Atoms and Molecules in Cavities, from Weak to Strong Coupling in Quantum-Electrodynamics (QED) Chemistry. *Proceedings of the National Academy of Sciences* **114,** 3026–3034 (Mar. 21, 2017) (cit. on p. 79).

194. Kampschulte, T. & Denschlag, J. H. Cavity-Controlled Formation of Ultracold Molecules. *New Journal of Physics* **20,** 123015 (Dec. 2018) (cit. on p. 79).

195. Wellnitz, D., Schütz, S., Whitlock, S., Schachenmayer, J. & Pupillo, G. Collective Dissipative Molecule Formation in a Cavity. *Physical Review Letters* **125,** 193201 (Nov. 2, 2020) (cit. on p. 79).

196. Helson, V. *et al. Optomechanical Response of a Strongly Interacting Fermi Gas* Nov. 4, 2021 (cit. on p. 81).

197. Stamper-Kurn, D. M. in *Cavity Optomechanics: Nano- and Micromechanical Resonators Interacting with Light* (eds Aspelmeyer, M., Kippenberg, T. J. & Marquardt, F.) 283–325 (Springer, Berlin, Heidelberg, 2014) (cit. on p. 81).

198. Gupta, S., Moore, K. L., Murch, K. W. & Stamper-Kurn, D. M. Cavity Nonlinear Optics at Low Photon Numbers from Collective Atomic Motion. *Physical Review Letters* **99,** 213601 (Nov. 20, 2007) (cit. on p. 82).

199. Purdy, T. P. *et al.* Tunable Cavity Optomechanics with Ultracold Atoms. *Physical Review Letters* **105,** 133602 (Sept. 22, 2010) (cit. on p. 82).

200. Ritter, S. *et al.* Dynamical Coupling between a Bose–Einstein Condensate and a Cavity Optical Lattice. *Applied Physics B* **95,** 213–218 (May 1, 2009) (cit. on p. 82).

201. Keßler, H., Klinder, J., Wolke, M. & Hemmerich, A. Optomechanical Atom-Cavity Interaction in the Sub-Recoil Regime. *New Journal of Physics* **16,** 053008 (May 2014) (cit. on p. 82).

202. Kanamoto, R. & Meystre, P. Optomechanics of a Quantum-Degenerate Fermi Gas. *Physical Review Letters* **104,** 063601 (Feb. 9, 2010) (cit. on p. 82).

203. Boyd, R. W. *Nonlinear Optics* 636 pp. (Academic Press, Mar. 30, 2020) (cit. on pp. 82, 86).

204. Maschler, C. & Ritsch, H. Cold Atom Dynamics in a Quantum Optical Lattice Potential. *Physical Review Letters* **95,** 260401 (Dec. 19, 2005) (cit. on pp. 85, 104).

205. Mivehvar, F., Piazza, F., Donner, T. & Ritsch, H. Cavity QED with Quantum Gases: New Paradigms in Many-Body Physics. *Advances in Physics* **70,** 1–153 (Jan. 2, 2021) (cit. on pp. 85, 102).

206. Kubo, R. The Fluctuation-Dissipation Theorem. *Reports on Progress in Physics* **29,** 255 (Jan. 1966) (cit. on pp. 85, 109).

207. Fetter, A. L. & Walecka, J. D. *Quantum Theory of Many-Particle Systems* (Dover Publications, Mineola, N.Y., 2003) (cit. on p. 86).

208. Pitaevskii, L. & Stringari, S. *Bose-Einstein Condensation and Superfluidity* 576 pp. (Oxford University Press, Oxford, 2016) (cit. on pp. 86, 92, 155, 156).

209. Wilson, K. G. Non-Lagrangian Models of Current Algebra. *Physical Review* **179,** 1499–1512 (Mar. 25, 1969) (cit. on p. 90).

210. Braaten, E. & Platter, L. Exact Relations for a Strongly Interacting Fermi Gas from the Operator Product Expansion. *Physical Review Letters* **100,** 205301 (May 21, 2008) (cit. on p. 90).

211. Hofmann, J. Current Response, Structure Factor and Hydrodynamic Quantities of a Two- and Three-Dimensional Fermi Gas from the Operator-Product Expansion. *Physical Review A* **84,** 043603 (Oct. 4, 2011) (cit. on p. 91).

212. Goldberger, W. D. & Rothstein, I. Z. Structure-Function Sum Rules for Systems with Large Scattering Lengths. *Physical Review A* **85,** 013613 (Jan. 9, 2012) (cit. on p. 91).

213. Hofmann, J. & Zwerger, W. Deep Inelastic Scattering on Ultracold Gases. *Physical Review X* **7,** 011022 (Mar. 1, 2017) (cit. on p. 91).

214. Combescot, R., Giorgini, S. & Stringari, S. Molecular Signatures in the Structure Factor of an Interacting Fermi Gas. *EPL (Europhysics Letters)* **75,** 695 (July 21, 2006) (cit. on p. 92).

215. Hoinka, S., Lingham, M., Delehaye, M. & Vale, C. J. Dynamic Spin Response of a Strongly Interacting Fermi Gas. *Physical Review Letters* **109,** 050403 (Aug. 1, 2012) (cit. on p. 92).

216. Mihaila, B. *Lindhard Function of a D-Dimensional Fermi Gas* Nov. 1, 2011 (cit. on pp. 92, 130).

217. Navon, N., Nascimbène, S., Chevy, F. & Salomon, C. The Equation of State of a Low-Temperature Fermi Gas with Tunable Interactions. *Science* **328,** 729–732 (May 7, 2010) (cit. on p. 93).

218. Horikoshi, M., Koashi, M., Tajima, H., Ohashi, Y. & Kuwata-Gonokami, M. Ground-State Thermodynamic Quantities of Homogeneous Spin-$1/2$ Fermions from the BCS Region to the Unitarity Limit. *Physical Review X* **7,** 041004 (Oct. 11, 2017) (cit. on p. 93).

219. Kuhnle, E. D. *et al.* Studies of the Universal Contact in a Strongly Interacting Fermi Gas Using Bragg Spectroscopy. *New Journal of Physics* **13,** 055010 (May 2011) (cit. on p. 93).

220. Kuhnle, E. D. *et al.* Universal Behavior of Pair Correlations in a Strongly Interacting Fermi Gas. *Physical Review Letters* **105,** 070402 (Aug. 9, 2010) (cit. on p. 93).

221. Sagi, Y., Drake, T. E., Paudel, R., Chapurin, R. & Jin, D. S. Breakdown of the Fermi Liquid Description for Strongly Interacting Fermions. *Physical Review Letters* **114,** 075301 (Feb. 19, 2015) (cit. on p. 93).

222. Ness, G. *et al.* Observation of a Smooth Polaron-Molecule Transition in a Degenerate Fermi Gas. *Physical Review X* **10,** 041019 (Oct. 27, 2020) (cit. on p. 93).

223. Leroux, I. D., Schleier-Smith, M. H. & Vuletić, V. Implementation of Cavity Squeezing of a Collective Atomic Spin. *Physical Review Letters* **104,** 073602 (Feb. 17, 2010) (cit. on p. 96).

224. Black, A. T., Chan, H. W. & Vuletićć, V. Observation of Collective Friction Forces Due to Spatial Self-Organization of Atoms: From Rayleigh to Bragg Scattering. *Physical Review Letters* **91,** 203001 (Nov. 2003) (cit. on p. 100).

225. Klinder, J., Keßler, H., Bakhtiari, M. R., Thorwart, M. & Hemmerich, A. Observation of a Superradiant Mott Insulator in the Dicke-Hubbard Model. *Physical Review Letters* **115,** 230403 (Dec. 2015) (cit. on p. 100).

226. Zhang, X. *et al.* Observation of a Superradiant Quantum Phase Transition in an Intracavity Degenerate Fermi Gas. *Science (New York, N.Y.)* **373,** 1359–1362 (2021) (cit. on pp. 100, 111).

227. Léonard, J., Morales, A., Zupancic, P., Esslinger, T. & Donner, T. Supersolid Formation in a Quantum Gas Breaking a Continuous Translational Symmetry. *Nature* **543,** 87–90 (Mar. 2017) (cit. on p. 100).

228. Landini, M. *et al.* Formation of a Spin Texture in a Quantum Gas Coupled to a Cavity. *Physical Review Letters* (2018) (cit. on p. 100).

229. Kroeze, R. M., Guo, Y., Vaidya, V. D., Keeling, J. & Lev, B. L. Spinor Self-Ordering of a Quantum Gas in a Cavity. *Physical Review Letters* **121,** 163601 (2018) (cit. on p. 100).

230. Kroeze, R. M., Guo, Y. & Lev, B. L. Dynamical Spin-Orbit Coupling of a Quantum Gas. *Physical Review Letters* **123,** 160404 (Oct. 2019) (cit. on p. 100).

231. Guo, Y. *et al.* An Optical Lattice with Sound. *Nature* **599,** 211–215 (Nov. 1, 2021) (cit. on p. 100).

232. Keeling, J., Bhaseen, M. J. & Simons, B. D. Fermionic Superradiance in a Transversely Pumped Optical Cavity. *Physical Review Letters* **112,** 143002 (Apr. 2014) (cit. on p. 100).

233. Piazza, F. & Strack, P. Umklapp Superradiance with a Collisionless Quantum Degenerate Fermi Gas. *Physical Review Letters* **112,** 143003 (Apr. 2014) (cit. on pp. 100, 105, 131).

234. Chen, Y., Yu, Z. & Zhai, H. Superradiance of Degenerate Fermi Gases in a Cavity. *Physical Review Letters* **112,** 143004 (Apr. 2014) (cit. on pp. 100, 105).

235. Yang, S., Al-Amri, M. & Zubairy, M. S. Dicke Quantum Phase Transition with a Degenerate Fermi Gas in an Optical Cavity. *Journal of Physics B: Atomic, Molecular and Optical Physics* **47,** 135503 (June 2014) (cit. on p. 100).

236. Chen, Y., Zhai, H. & Yu, Z. Superradiant Phase Transition of Fermi Gases in a Cavity across a Feshbach Resonance. *Physical Review A* **91,** 021602 (Feb. 2015) (cit. on p. 100).

237. Zheng, Z. & Wang, Z. D. Cavity-Induced Fulde-Ferrell-Larkin-Ovchinnikov Superfluids of Ultracold Fermi Gases. *Physical Review A* **101,** 023612 (Feb. 19, 2020) (cit. on p. 100).

238. Helson, V. *et al. Density-Wave Ordering in a Unitary Fermi Gas with Photon-Mediated Interactions* `http://arxiv.org/abs/2212.04402`. preprint (cit. on p. 100).

239. Defenu, N. *et al. Long-Range Interacting Quantum Systems* 2021 (cit. on p. 101).

240. Chomaz, L. *et al. Dipolar Physics: A Review of Experiments with Magnetic Quantum Gases* 2022 (cit. on p. 101).

241. Pupillo, G., Micheli, A., Boninsegni, M., Lesanovsky, I. & Zoller, P. Strongly Correlated Gases of Rydberg-Dressed Atoms: Quantum and Classical Dynamics. *Physical Review Letters* **104,** 223002 (June 1, 2010) (cit. on p. 101).

242. Balewski, J. B. *et al.* Rydberg Dressing: Understanding of Collective Many-Body Effects and Implications for Experiments. *New Journal of Physics* **16,** 063012 (June 2014) (cit. on p. 101).

243. Guardado-Sanchez, E. *et al.* Quench Dynamics of a Fermi Gas with Strong Nonlocal Interactions. *Physical Review X* **11,** 021036 (May 17, 2021) (cit. on p. 101).

244. Moses, S. A., Covey, J. P., Miecnikowski, M. T., Jin, D. S. & Ye, J. New Frontiers for Quantum Gases of Polar Molecules. *Nature Physics* **13,** 13–20 (2017) (cit. on p. 101).

245. Mivehvar, F., Piazza, F., Donner, T. & Ritsch, H. Cavity QED with Quantum Gases: New Paradigms in Many-Body Physics. *Advances in Physics* **70,** 1–153 (2021/01/02, 2021-01) (cit. on p. 101).

246. Vaidya, V. D. *et al.* Tunable-Range, Photon-Mediated Atomic Interactions in Multimode Cavity QED. *Physical Review X* **8,** 011002 (Jan. 2018) (cit. on pp. 101, 102).

247. Asbóth, J. K., Domokos, P. & Ritsch, H. Correlated Motion of Two Atoms Trapped in a Single-Mode Cavity Field. *Physical Review A* **70,** 013414 (July 29, 2004) (cit. on p. 104).

248. Bukov, M., D'Alessio, L. & Polkovnikov, A. Universal High-Frequency Behavior of Periodically Driven Systems: From Dynamical Stabilization to Floquet Engineering. *Advances in Physics* **64,** 139–226 (Mar. 4, 2015) (cit. on p. 105).

249. Baumann, K., Guerlin, C., Brennecke, F. & Esslinger, T. Dicke Quantum Phase Transition with a Superfluid Gas in an Optical Cavity. *Nature* **464,** 1301–1306 (7293 Apr. 2010) (cit. on p. 105).

250. Keeling, J., Bhaseen, M. J. & Simons, B. D. Fermionic Superradiance in a Transversely Pumped Optical Cavity. *Physical Review Letters* **112,** 143002 (Apr. 8, 2014) (cit. on pp. 105, 130).

251. Landau, L. On the Theory of Phase Transitions. **7,** 19–32 (1927) (cit. on p. 105).

252. Georges, A. & Yedidia, J. S. How to Expand around Mean-Field Theory Using High-Temperature Expansions. *Journal of Physics A: Mathematical and General* **24,** 2173 (May 1991) (cit. on p. 106).

253. Georges, A. in *Strongly Correlated Fermions and Bosons in Low-Dimensional Disordered Systems* (eds Lerner, I. V., Althsuler, B. L., Fal'ko, V. I. & Giamarchi, T.) 375–394 (Springer Netherlands, Dordrecht, 2002) (cit. on pp. 106, 130).

254. Georges, A. Le Modèle de Hubbard Fermionique : Introduction et Progrès Récents (2021) (cit. on p. 106).

255. *Making Sense of the Legendre Transform: American Journal of Physics: Vol 77, No 7* `https://aapt.scitation.org/doi/10.1119/1.3119512` (cit. on p. 107).

256. Navon, N., Nascimbène, S., Chevy, F. & Salomon, C. The Equation of State of a Low-Temperature Fermi Gas with Tunable Interactions. *Science (New York, N.Y.)* **328,** 729–732 (2010) (cit. on p. 110).

257. Horikoshi, M., Koashi, M., Tajima, H., Ohashi, Y. & Kuwata-Gonokami, M. Ground-State Thermodynamic Quantities of Homogeneous Spin-1/2 Fermions from the BCS Region to the Unitarity Limit. *Physical Review X* **7,** 041004 (Oct. 2017) (cit. on p. 110).

258. Mihaila, B. *Lindhard Function of a D-Dimensional Fermi Gas* 2011 (cit. on pp. 111, 124).

259. Watanabe, G., Orso, G., Dalfovo, F., Pitaevskii, L. P. & Stringari, S. Equation of State and Effective Mass of the Unitary Fermi Gas in a One-Dimensional Periodic Potential. *Physical Review A: Atomic, Molecular, and Optical Physics* **78,** 063619 (Dec. 2008) (cit. on p. 113).

260. Morsch, O. & Oberthaler, M. Dynamics of Bose-Einstein Condensates in Optical Lattices. *Reviews of Modern Physics* **78,** 179–215 (Feb. 27, 2006) (cit. on p. 117).

261. Gadway, B., Pertot, D., Reimann, R., Cohen, M. G. & Schneble, D. Analysis of Kapitza-Dirac Diffraction Patterns beyond the Raman-Nath Regime. *Optics Express* **17,** 19173–19180 (Oct. 2009) (cit. on p. 118).

262. Mottl, R. *et al.* Roton-Type Mode Softening in a Quantum Gas with Cavity-Mediated Long-Range Interactions. *Science (New York, N.Y.)* **336,** 1570–1573 (2012) (cit. on pp. 120, 123, 124).

263. Weidemüller, M., Hemmerich, A., Görlitz, A., Esslinger, T. & Hänsch, T. W. Bragg Diffraction in an Atomic Lattice Bound by Light. *Physical Review Letters* **75,** 4583–4586 (Dec. 18, 1995) (cit. on p. 122).

264. Brennecke, F. *et al.* Real-Time Observation of Fluctuations at the Driven-Dissipative Dicke Phase Transition. *Proceedings of the National Academy of Sciences* **110,** 11763–11767 (2013) (cit. on p. 123).

265. Léonard, J., Morales, A., Zupancic, P., Donner, T. & Esslinger, T. Monitoring and Manipulating Higgs and Goldstone Modes in a Supersolid Quantum Gas. *Science (New York, N.Y.)* **358,** 1415–1418 (2017) (cit. on p. 124).

266. Patel, P. B. *et al.* Universal Sound Diffusion in a Strongly Interacting Fermi Gas. *Science (New York, N.Y.)* **370,** 1222–1226 (2020) (cit. on p. 125).

267. Biss, H. *et al.* Excitation Spectrum and Superfluid Gap of an Ultracold Fermi Gas. *Physical Review Letters* **128,** 100401 (Mar. 2022) (cit. on p. 125).

268. Nicholson, T. L. *et al.* Optical Feshbach Resonances: Field-dressed Theory and Comparison with Experiments. *Physical Review A* **92,** 022709 (Aug. 24, 2015) (cit. on p. 127).

269. Greiner, M., Regal, C. A. & Jin, D. S. Probing the Excitation Spectrum of a Fermi Gas in the BCS-BEC Crossover Regime. *Physical Review Letters* **94,** 070403 (Feb. 24, 2005) (cit. on p. 127).

270. Behrle, A. *et al.* Higgs Mode in a Strongly Interacting Fermionic Superfluid. *Nature Physics* **14,** 781–785 (8 Aug. 2018) (cit. on p. 127).

271. Harrison, T. *et al.* Decay and Revival of a Transient Trapped Fermi Condensate. *Physical Review Research* **3,** 023205 (June 11, 2021) (cit. on p. 127).

272. Dyke, P. *et al.* Dynamics of a Fermi Gas Quenched to Unitarity. *Physical Review Letters* **127,** 100405 (Aug. 31, 2021) (cit. on p. 127).

273. Fradkin, E., Kivelson, S. A. & Tranquada, J. M. Colloquium: Theory of Intertwined Orders in High Temperature Superconductors. *Reviews of Modern Physics* **87,** 457–482 (May 2015) (cit. on p. 128).

274. *Density Waves In Solids* (CRC Press, Mar. 8, 2018) (cit. on p. 128).

275. Gabovich, A. M., Voitenko, A. I., Annett, J. F. & Ausloos, M. Charge- and Spin-Density-Wave Superconductors. *Superconductor Science and Technology* **14,** R1 (Apr. 2001) (cit. on p. 128).

276. Kusmartseva, A. F., Sipos, B., Berger, H., Forró, L. & Tutiš, E. Pressure Induced Superconductivity in Pristine $1T\mathrm{\text{\ensuremath{-}}}{\mathrm{TiSe}}_{2}$. *Physical Review Letters* **103,** 236401 (Nov. 30, 2009) (cit. on p. 128).

277. Zhu, X., Cao, Y., Zhang, J., Plummer, E. W. & Guo, J. Classification of Charge Density Waves Based on Their Nature. *Proceedings of the National Academy of Sciences* **112,** 2367–2371 (Feb. 24, 2015) (cit. on p. 128).

278. Theis, M. *et al.* Tuning the Scattering Length with an Optically Induced Feshbach Resonance. *Physical Review Letters* **93,** 123001 (Sept. 15, 2004) (cit. on p. 131).

279. Bauer, D. M., Lettner, M., Vo, C., Rempe, G. & Dürr, S. Control of a Magnetic Feshbach Resonance with Laser Light. *Nature Physics* **5,** 339–342 (5 May 2009) (cit. on p. 131).

280. Agterberg, D. F. *et al.* The Physics of Pair-Density Waves: Cuprate Superconductors and Beyond. *Annual Review of Condensed Matter Physics* **11,** 231–270 (2020) (cit. on p. 131).

281. Laflamme, C., Yang, D. & Zoller, P. Continuous Measurement of an Atomic Current. *Physical Review A* **95,** 043843 (Apr. 28, 2017) (cit. on p. 131).

282. *Labscript Suite* (cit. on p. 149).

283. Starkey, P. T. *et al.* A Scripted Control System for Autonomous Hardware-Timed Experiments. *Review of Scientific Instruments* **84,** 085111 (Aug. 2013) (cit. on p. 149).

284. Starkey, P. T. *A Software Framework for Control and Automation of Precisely Timed Experiments* thesis (Monash University, July 4, 2019) (cit. on p. 149).

285. Billington, C. J. *State-Dependent Forces in Cold Quantum Gases* thesis (Monash University, Apr. 3, 2019) (cit. on p. 149).

286. Ueda, M. *Fundamentals and New Frontiers of Bose-Einstein Condensation* (WORLD SCIENTIFIC, July 2010) (cit. on p. 157).

Appendix A

Experiment control

All the gas preparation and probing procedures are completely automatized thanks to a powerful computer control software: Labscript [282]. It is an open-source experiment control system designed to fully supervize shot-based, time-resolved experiments. We cannot stress how convenient this software was to interface all the various hardware required to run a cold atoms machine together. It is entirely Python-based with a rich documentation [283–285], making any modification straightforward to implement.

Within the framework of Labscript, every experiment is described by a series of explicit, time-resolved hardware instructions in a Python script. For example, the following piece of code turns on and off the Zeeman slower beam during the MOT loading phase

```
t = 0

# Open the flag
Li_shutter.constant(t, value = 10)

# Turn on the beam
ZS_amp.constant(t, value = ZeemanSlower_amp)

t += MOT_loading_time

# Stop loading
Li_shutter.constant(t, value = 0)
ZS_amp.constant(t, value = 0)
...
```

where each Python object relates to a physical element of the experiment. Labscript then makes use of three different interconnected software

- RUNMANAGER compiles a sequence Python script into a series of time-tagged hardware instructions. Its interface allows to specify values for variables called in the Python script, in the example above one can specify the value `ZeemanSlower_amp` to change the value of `ZS_amp` which corresponds to the voltage of one of the outputs of an analog output card.
- BLACS receives the series of hardware instructions and takes care of the communication with the various instruments. It then sequentially executes all the compiled shots. At the

end of a shot, it retrieves data from the various measurement instruments and saves them in a single file.

- LYSE allows for easy, on-the-fly post-processing of the data. One can load custom analysis scripts to be executed directly once a BLACS run is over, displaying for example absorption images or cavity spectra almost in real time. It also permits the use of "multi-shot" scripts which compile the results of single-shot ones together, for example for averaging purposes or to systematically display the results of scanning one parameter.

Hardware and data acquisition

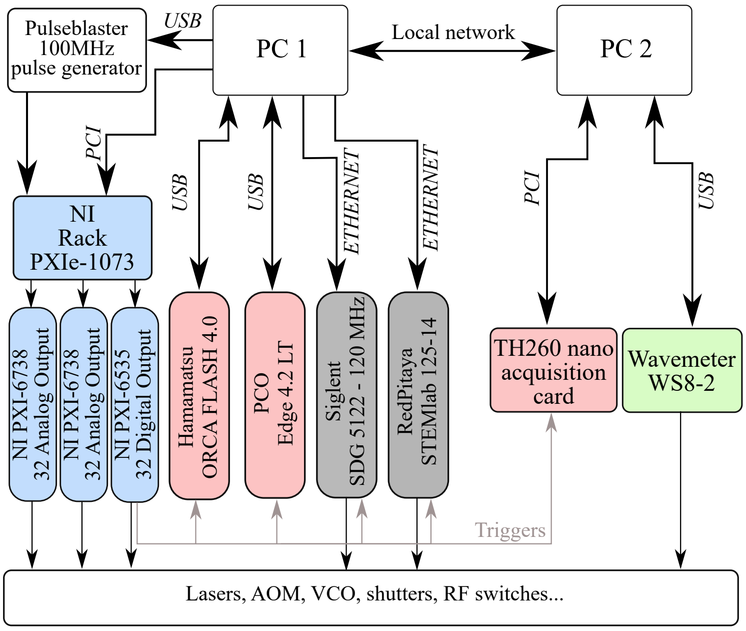
Pulseblaster 100MHz pulse generator
USB
PC 1
Local network
PC 2
PCI
NI Rack PXIe-1073
USB
USB
ETHERNET
ETHERNET
PCI
USB
NI PXI-6738 32 Analog Output
NI PXI-6738 32 Analog Output
NI PXI-6535 32 Digital Output
Hamamatsu ORCA FLASH 4.0
PCO Edge 4.2 LT
Siglent SDG 5122 - 120 MHz
RedPitaya STEMlab 125-14
TH260 nano acquisition card
Wavemeter WS8-2
Triggers
Lasers, AOM, VCO, shutters, RF switches...

Figure A.1: Hardware architecture for experiment control and data acquisition. The figure is reproduced from [79]. Blue boxes generate analog and digital control signal, gray ones generate RF signals, red ones are used for data acquisition and the wavemeter is depicted in green.

The architecture of the hardware for its control with Labscript is presented in figure A.1. The control software is installed on a computer (PC1) and for each shot it produces a series of instructions communicated to a programmable arbitrary waveform generator, the pulseblaster (PB24-100-4k-PCIe from SpinCore). This device provides a main clockline to a rack of digital and analog output cards (National Instruments PXIe-1073), allowing to control the cards outputs during the experimental sequence with a time resolution of $2.5\,\mu$s. The same computer also controls two CMOS cameras (Hamamatsu Orca Flash 4.0 and pco.edge 4.2 LT) which are used to acquire absorption images at the end of a sequence, respectively from the vertical and horizontal directions. In addition, it hosts an ethernet hub on which are connected numerous arbitrary waveform generators from Siglent and RedPitaya devices.

A second computer accommodates a high-speed, time-resolved single photon acquisition card with 250 ps temporal resolution (TimeHarp 260 NANO from PicoQuant). This acquisition card is used to time-tag each photon detected by a single-photon counting module (Excelitas ARQH-14-FC) at the output of the cavity and send the resulting photon trace to Labscript for processing. The wavemeter is also connected to this computer and integrated with Labscript, allowing to automatically tune the frequency of any laser at the beginning of every experimental cycle.

Appendix B

Optical setups for the cavity probe and transverse pump beams

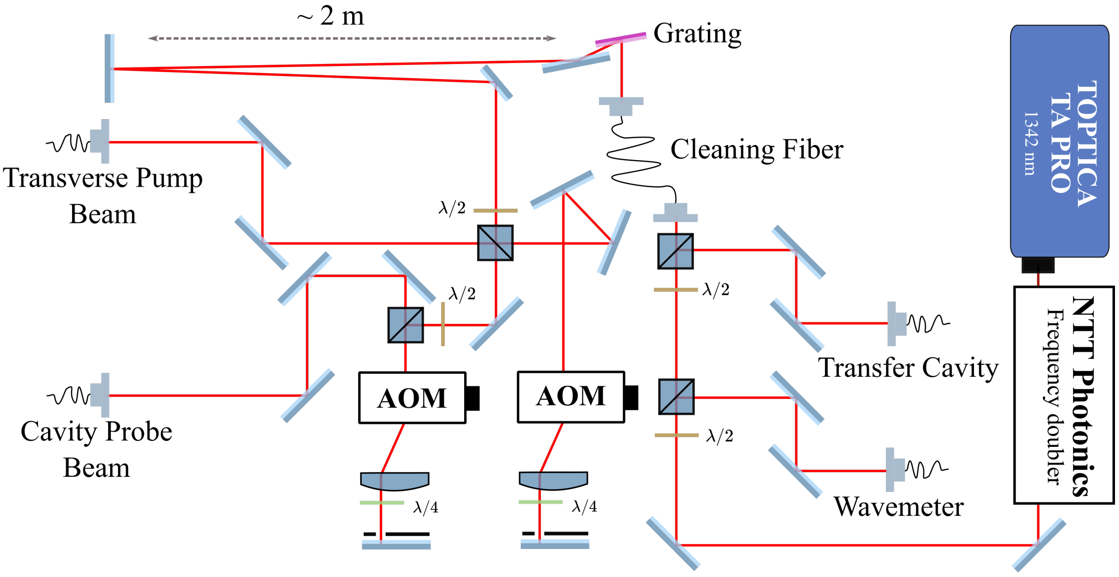
~ 2 m
Grating
Cleaning Fiber
TOPTICA
TA PRO
1342 nm
Transverse Pump
Beam
λ/2
λ/2
λ/2
λ/2
NTT Photonics
Frequency doubler
Transfer Cavity
AOM
AOM
Cavity Probe
Beam
Wavemeter
λ/4
λ/4

Figure B.1: Pump-probe laser setup on the laser table. Compared with the previous iteration presented in [79], the 671 nm light required to address the atomic transitions with the cavity is now generated by a frequency doubled diode at 1342 nm.

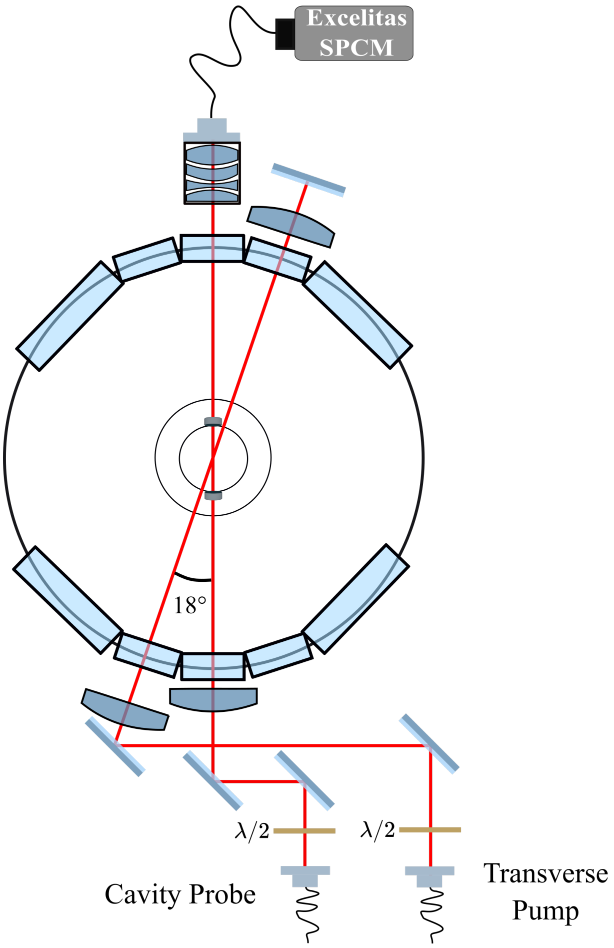
Excelitas
SPCM
18°
λ/2
λ/2
Cavity Probe
Transverse
Pump

Figure B.2: Pump-probe setup on the science table. Light leaking out of the cavity is collected by a microscope objective and fiber coupled to the photon counter.

Appendix C

Properties of the density response function

In this appendix, we present and derive some useful formal properties of the density-density response function – or susceptibility – which we heavily refer to throughout this manuscript. Most of the results and derivations presented here can be obtained following chapter 7 of the staple book reference [208].

C.1 Definitions and spectral representation

We start from the definition of the time retarded density response function for a perturbation of the gas at wavevector $\mathbf{q}$ and frequency ω which we use in the main text

$$\chi^{\mathrm{R}}(\mathbf{q},\omega) = -i\int_{-\infty}^{+\infty} dt\theta(t)e^{i\omega t}\left\langle\left[\hat{n}_{\mathbf{q}}(t),\hat{n}_{-\mathbf{q}}(0)\right]\right\rangle \tag{C.1}$$

with θ the Heaviside function and $\hat{n}_{\mathbf{q}}$ the time-dependent $\mathbf{q}$ Fourier components of the density operator. For convenience and to be consistent with the literature, we work here with the full density response function and not the one per particle, as in the main text. Its real and imaginary parts are connected by the Kramers-Kronig relations

$$\begin{aligned}\mathrm{Re}\left[\chi^{\mathrm{R}}(\mathbf{q},\omega)\right] &= -\frac{1}{\pi}\int_{-\infty}^{+\infty} d\omega'\frac{\mathrm{Im}\left[\chi^{\mathrm{R}}(\mathbf{q},\omega)\right]}{\omega-\omega'}\\ \mathrm{Im}\left[\chi^{\mathrm{R}}(\mathbf{q},\omega)\right] &= -\frac{1}{\pi}\int_{-\infty}^{+\infty} d\omega'\frac{\mathrm{Re}\left[\chi^{\mathrm{R}}(\mathbf{q},\omega)\right]}{\omega-\omega'}.\end{aligned} \tag{C.2}$$

We introduce its spectral representation using the following definitions

$$\begin{aligned}\hat{n}_{\mathbf{q}}(t) &= e^{iHt}\hat{n}_{\mathbf{q}}e^{-iHt}\\ \theta(t) &= \int_{-\infty}^{+\infty} d\omega\frac{1}{2\pi i}\frac{e^{i\omega t}}{\omega-i\eta}\end{aligned} \tag{C.3}$$

where $\eta \to 0^+$. Explicitly developing the expectation value in equation (C.1) we get

$$\begin{aligned}\chi^{\mathrm{R}}(\mathbf{q},\omega) &= -i\int_{-\infty}^{+\infty} dt\theta(t)e^{i\omega t}\mathrm{Tr}\left[\frac{e^{-\beta H}}{Z}\left[\hat{n}_{\mathbf{q}}(t),\hat{n}_{-\mathbf{q}}(0)\right]\right]\\ &= \sum_{n,m}\frac{e^{-\beta E_n}}{Z}\left[\frac{|\langle n|\hat{n}_{\mathbf{q}}|m\rangle|^2}{\omega+E_n-E_m+i\eta}-\frac{|\langle n|\hat{n}_{-\mathbf{q}}|m\rangle|^2}{\omega-E_n+E_m+i\eta}\right]\end{aligned} \tag{C.4}$$

where we have introduced the partition function $Z=\sum_n e^{-\beta E_n}$ and the inverse temperature β. Similarly, the corresponding time-ordered density response used in chapter 5 is defined with

$$\chi^{\mathrm{T}}(\mathbf{q},\omega) = \sum_{n,m}\frac{e^{-\beta E_n}}{Z}\left[\frac{|\langle n|\hat{n}_{\mathbf{q}}|m\rangle|^2}{\omega+E_n-E_m+i\eta}-\frac{|\langle n|\hat{n}_{-\mathbf{q}}|m\rangle|^2}{\omega-E_n+E_m-i\eta}\right]. \tag{C.5}$$

Each term of the sums above can be developed in the limit $\eta \to 0^+$ using the canonical Dirac relation

$$\frac{1}{\omega \pm i\eta} = \mp i\pi\delta(\omega) + \mathcal{P}\left(\frac{1}{\omega}\right) \tag{C.6}$$

where $\mathcal{P}$ denotes Cauchy's principal value. It directly yields the relation

$$\mathrm{Re}\left[\chi^{\mathrm{R}}(\mathbf{q},\omega)\right] = \mathrm{Re}\left[\chi^{\mathrm{T}}(\mathbf{q},\omega)\right] \tag{C.7}$$

used in the main text.

C.2 Structure factor and sum rules

The density response function is intimately linked to the dynamical structure factor, defined by

$$\begin{aligned}S(\mathbf{q},\omega) &= \frac{1}{2\pi}\int_{-\infty}^{+\infty} dte^{i\omega t}\left\langle \hat{n}_{\mathbf{q}}(t)\hat{n}_{-\mathbf{q}}(0)\right\rangle\\ &= \sum_{n,m}\frac{e^{-\beta E_n}}{Z}|\langle n|\hat{n}_{\mathbf{q}}|m\rangle|^2\delta(\omega+E_n-E_m)\end{aligned} \tag{C.8}$$

so that

$$\chi^{\mathrm{R}}(\mathbf{q},\omega) = \int_{-\infty}^{+\infty} d\omega'\left[\frac{S(\mathbf{q},\omega')}{\omega-\omega'+i\eta}-\frac{S(-\mathbf{q},\omega')}{\omega+\omega'+i\eta}\right], \tag{C.9}$$

again with $\eta \to 0^+$. Equation C.6 then gives the real and imaginary parts of the density response in terms of the structure factor

$$\begin{aligned}\mathrm{Re}\left[\chi^{\mathrm{R}}(\mathbf{q},\omega)\right] &= \int_{-\infty}^{+\infty} d\omega'\left[S(\mathbf{q},\omega')\mathcal{P}\left(\frac{1}{\omega-\omega'}\right)-S(-\mathbf{q},\omega')\mathcal{P}\left(\frac{1}{\omega+\omega'}\right)\right]\\ \mathrm{Im}\left[\chi^{\mathrm{R}}(\mathbf{q},\omega)\right] &= \pi(S(\mathbf{q},\omega)-S(-\mathbf{q},-\omega)).\end{aligned} \tag{C.10}$$

Under the assumption that the unperturbed system is invariant with respect to either parity or time-reversal transformations [208], the identity $S(\mathbf{q},\omega) = S(-\mathbf{q},\omega)$ holds so that at zero frequency

$$\mathrm{Im}\left[\chi^{\mathrm{R}}(\mathbf{q},0)\right] = \pi(S(\mathbf{q},0)-S(-\mathbf{q},0)) = 0, \tag{C.11}$$

and the density response function is purely real.

At zero frequency, the real part then reads

$$\operatorname{Re}\left[\chi^{\mathrm{R}}(\mathbf{q},0)\right] = -\int_{-\infty}^{+\infty} d\omega' \frac{S(\mathbf{q},\omega') + S(-\mathbf{q},\omega')}{\omega'} \tag{C.12}$$

$$= -2m_{-1}(\mathbf{q}) \tag{C.13}$$

where m_p is the p^{th} moment of the structure factor with $m_p(\mathbf{q}) = \int d\omega\omega^p S(\mathbf{q},\omega)$. The calculation of these moments gives a series of convenient sum rules. For instance, the inverse energy-weighted moment of equation C.13 yields the compressibility sum rule in the limit $|\mathbf{q}| \to 0$

$$\lim_{|\mathbf{q}|\to 0} 2m_{-1}(\mathbf{q}) = \int d^3r \frac{\partial n}{\partial \mu} = \int d^3r n^2 \kappa \tag{C.14}$$

where n is the density, κ the isothermal compressibility and μ its chemical potential of the gas [286]. Similarly, the calculation of the first moment gives the f-sum rule

$$m_1(\mathbf{q}) = \frac{\hbar^2 |\mathbf{q}|^2}{2m} N, \tag{C.15}$$

for an ensemble of N particles of mass m.

Appendix D

Molecular term symbols

Here we explicitly describe the structure of some diatomic molecular spectroscopy symbols used in the main text and the literature. The molecular symbol

$$ {}^{2|\mathbf{S}|+1}|\Lambda|^{\pm}_{\Omega,g/u} \tag{D.1} $$

corresponds to a state $|L\Lambda S\Sigma\sigma\rangle$ with

- Σ the value of the projection of the total spin $\mathbf{S}$ on the internuclear axis.
- Λ the value of the projection of the total orbital angular momentum $\mathbf{L}$ on the same axis.
- $\sigma = 0$ or 1 indicating whether the wavefunction is symmetric with respect to the inversion of the nuclei about the center of charge of the system. This inversion symmetry is called gerade or ungerade for $\sigma = 0$ or 1 respectively and labelled with a g/u subscript.[1]
- The ± superscript referring to the reflection symmetry of the electronic part of the wavefunction about any plane containing the internuclear axis.

The value of $|\Lambda|$ is commonly replaced by a capital Greek letter $\Sigma, \Pi, \Delta, \Phi, \ldots$ for $|\Lambda| = 0, 1, 2, 3, \ldots$ respectively. We have also introduced the projection of the total angular momentum on the internuclear axis Ω for the sake of completeness. In addition, an extra single-symbol label is often added as a prefix to the above notation. Usually, the letter X denotes the ground state while excited states with the same value of $|\mathbf{S}|$ as the ground state are labelled in increasing order of energy with capital letters $A, B, C, \ldots$. Lower case letters are then used to denote states where the value of $|\mathbf{S}|$ differs from the ground state; $a, b, c, \ldots$.

---

[1] For obvious reasons, the gerade symmetry only holds for homonuclear diatomic molecules.

Contents

Abstract vii

Remerciements ix

Contents xi

Introduction 1

I Production and Interrogation of Strongly Interacting Fermi Gases Coupled to Light 5

1 An experimental platform to study strongly interacting fermions coupled to light 7
- 1.1 A high finesse cavity inside a single-chamber experiment 8
  - 1.1.1 Overview of the ultra-high vacuum system 8
  - 1.1.2 Compact, bulk-machined electromagnets 10
  - 1.1.3 The high-finesse optical cavity 11
- 1.2 From hot vapor to quantum degenerate gas: production of a Fermi gas of ^{6}Li . . 13
  - 1.2.1 Laser cooling 14
  - 1.2.2 Evaporative cooling in cavity dipole traps 15
  - 1.2.3 Evaporative cooling in a running wave dipole trap 15

2 Probing strongly interacting Fermi gases strongly coupled to light 17
- 2.1 Probing the strong light-matter coupling 18
  - 2.1.1 Light-matter interaction and the strong coupling regime 18
  - 2.1.2 Strong light-matter coupling from near-resonance transmission spectroscopy 21
  - 2.1.3 Transmission spectroscopy in the dispersive limit 26
- 2.2 Absorption imaging for the thermometry of unitary Fermi gases 30
  - 2.2.1 High-intensity absorption imaging 31
  - 2.2.2 Temperature measurement using the equation of state 33

II Quantum Optical Signatures of the Short Range Two-Body Correlation Function 37

3 Two-body scattering for the many-body physics of interacting Fermi gases 39
- 3.1 Theoretical description of cold collisions 40
  - 3.1.1 Origin of the interaction 40

3.1.2 The two-body scattering problem 41
3.1.3 Feshbach resonances 47
3.2 Going from two- to many-body fermionic systems 51
3.2.1 Energy spectrum of the interacting Fermi gas 51
3.2.2 BEC–BCS crossover 53
3.2.3 The two-body contact 56

4 Fermionic pair-polaritons, magnifiers for two-body correlations 61
4.1 From two interacting dipoles to a photoassociated pair 62
4.1.1 Interacting dipoles 62
4.1.2 Molecular spectroscopy 64
4.1.3 The case of ^{6}Li$_2$ 66
4.2 Observation of strong light-matter coupling on photoassociation transitions . . 67
4.2.1 Experimenta scheme 67
4.2.2 Mapping out photoassociation transitions close to dissociation limits . . . 68
4.3 Many-body physics from vacuum Rabi splitting 70
4.3.1 Rabi frequency of pairs coupled to light 71
4.3.2 Many-body physics from the optical spectrum 74
4.3.3 Continuous measurement of the two-body contact 77

5 Optomechanical response of strongly interacting Fermi gases 81
5.1 Observation of a Kerr nonlinearity in a unitary Fermi gas coupled to light . . . 82
5.1.1 Kerr nonlinearities and optical bistability 82
5.1.2 Response function from light-matter coupling 83
5.1.3 Experimental realization 86
5.2 The connection between light-matter coupling and the universal thermodynamics of strongly interacting fermions 90
5.2.1 The Operator Product Expansion 91
5.2.2 Density response in the BEC–BCS crossover 94

III Cavity Mediated Long Range Interactions and Their Interplay with Short Range Physics 97

6 Density-wave ordering induced by photon-mediated long-range interactions 99
6.1 Engineering photon-mediated long-range interactions in a strongly correlated Fermi gas 101
6.1.1 Effective photon-mediated atom-atom interactions from strong light-matter coupling 101
6.1.2 Phase transition to a density ordered state 105
6.1.3 Density response function 108
6.2 Observation and characterization of density wave ordering 111
6.2.1 Experimental procedure and observation of the phase transition 111
6.2.2 Mapping the phase diagram 113
6.2.3 Variation of the interaction parameter 114
6.2.4 Experimental calibrations 116
6.3 Measurement of the density wave susceptibility 120
6.3.1 Implementation of fixed-**q** Bragg spectroscopy 120
6.3.2 Measurement of the density response in the presence of long-range interactions 122

6.4 Long-range interactions between pairs of atoms, an outlook 125
6.4.1 Dispersive regime for the pairs 125
6.4.2 Interpretation as an optical Feshbach resonance 127

Conclusion and outlooks **129**
Investigation of the density-wave ordered phase 130
Simulation of pair density waves 131
Cavity-enabled nondemolition transport measurements 131

Bibliography **133**

A Experiment control **149**

B Optical setups for the cavity probe and transverse pump beams **153**

C Properties of the density response function **155**
C.1 Definitions and spectral representation 155
C.2 Structure factor and sum rules 156

D Molecular term symbols **159**

Contents **161**
Curriculum Vitae 166

This much I'm certain of: it doesn't happen immediately. You'll finish the book and that will be that, until a moment will come, maybe in a month, maybe a year, maybe even several years. You'll be sick or feeling troubled or deeply in love or quietly uncertain or even content for the first time in your life. It won't matter. Out of the blue, beyond any cause you can trace, you'll suddenly realize things are not how you perceived them to be at all. For some reason, you will no longer be the person you believed you once were. You'll detect slow and subtle shifts going on all around you, more importantly shifts in you. Worse, you'll realize it's always been shifting, like a shimmer of sorts, a vast shimmer, only dark like a room. But you won't understand why or how. You'll have forgotten what granted you this awareness in the first place.

...

You might try then, as I did, to find a sky so full of stars it will blind you again. Only no sky can blind you now. Even with all that iridescent magic up there, your eye will no longer linger on the light, it will no longer trace constellations. You'll care only about the darkness and you'll watch it for hours, for days, maybe even for years, trying in vain to believe you're some kind of indispensable, universe-appointed sentinel, as if just by looking you could actually keep it all at bay. It will get so bad you'll be afraid to look away, you'll be afraid to sleep.

Then no matter where you are, in a crowded restaurant or on some desolate street or even in the comforts of your own home, you'll watch yourself dismantle every assurance you ever lived by. You'll stand aside as a great complexity intrudes, tearing apart, piece by piece, all of your carefully conceived denials, whether deliberate or unconscious. And then for better or worse you'll turn, unable to resist, though try to resist you still will, fighting with everything you've got not to face the thing you most dread, what is now, what will be, what has always come before, the creature you truly are, the creature we all are, buried in the nameless black of a name. And then the nightmares will begin.

Mark Danielewski

CURRICULUM VITAE

PERSONAL

Born May 5, 1993, in La Louvière, Belgium
Rue du Lac 6, 1007 Lausanne, Switzerland
helson.victor@gmail.com
+41 78 798 51 77

EDUCATION

2018–2023 PhD thesis under the supersivsion of Prof. Jean-Philippe Brantut: *Many-body physics with strongly interacting fermions coupled to light*. EPFL Switzerland.

2017 Master thesis under the supersivsion of Prof. Jean-Philippe Brantut: *Frequency stabilization and narrowing of lasers on a Fabry-Pérot cavity*. EPFL Switzerland.

2015–2017 Master of Science in Applied Physics. EPFL Switzerland.